Title

Highly Selective Roles of Key Transcription Factors in Genome-Wide Toll-Like Receptor-Induced Nucleosome Remodeling in Activated Macrophages

Author

Feng, An-Chieh

Publication Date

2021

Peer reviewed|Thesis/dissertation

UNIVERSITY OF CALIFORNIA

Los Angeles

Highly Selective Roles of Key Transcription Factors in Genome-Wide Toll-Like Receptor-Induced Nucleosome Remodeling in Activated Macrophages

A dissertation submitted in partial satisfaction of the requirements for the degree Doctor of Philosophy in Molecular Biology

by

An-Chieh Feng

2021

ABSTRACT OF THE DISSERTATION

Highly Selective Roles of Key Transcription Factors in Genome-Wide Toll-Like Receptor-Induced Nucleosome Remodeling in Activated Macrophages

by

An-Chieh Feng

Doctor of Philosophy in Molecular Biology

University of California, Los Angeles, 2021

Professor Stephen T. Smale, Chair

Macrophages play a critical role in bridging the innate and adaptive immune systems, which requires timely and precise transcription control when responding to danger signals. Gene expression networks in macrophages have been profiled extensively in recent decades with the advancement of high-throughput sequencing technologies. However, unveiling critical mechanistic insights into control of diverse transcriptional networks has proven to be challenging. Recent evidence has suggested that the accessibility of chromatin structure can provide an integral means of transcription regulation. We have used the relatively recent Assay for Transposase-Accessible Chromatin using Sequencing (ATAC-seq) method to assess chromatin accessibility with optimal resolution in mouse bone marrow derived macrophages during the course of lipid-A stimulation. This advanced method enabled us to characterize the chromatin state of genome-wide regulatory regions. By applying a quantitative systematic approach, we obtained mechanistic insights into the highly selective role of the major transcription factors, NF-κB and IRF3, in nucleosome remodeling and transcription regulation.

The dissertation of An-Chieh Feng is approved.

Steven J. Bensinger

Douglas L. Black

Michael F. Carey

Peter Tontonoz

Stephen T. Smale, Committee Chair

University of California, Los Angeles

2021

DEDICATION

To my parents, Da-Than Feng and Jui-Mei Ma;

for being my strongest support always and forever

To my grandfather, Jing-Lan Ma;

for blessing me no matter where you are

TABLE OF CONTENTS

LIST OF FIGURES AND TABLES

FIGURES

TABLES

ACKNOWLEDGEMENTS

I have looked at the dictionary for days but still hardly find a word much stronger than “thank” to express my deepest gratefulness. I am lucky to have Dr. Michael Lai introducing me to the foundation of biological science and guiding me with great patience even when I am terribly distracted by clinical training. With his inspiration, I have a completely different career path which brings me the most satisfying self-fulfillment ever.

Four years ago, UCLA MBI home area director Dr. Peter Bradley recruited me and made me believe that IMMP would be the perfect fit for me. During my days at UCLA, I have kept wondering if he is right because IMMP is way more than just a perfect fit for me, it is fantastic. I really appreciate his support and valuable advice in my junior years, especially his recommendation of my mentor, Dr. Stephen T. Smale. Dr. Smale guides and builds me into a critical thinker and a gentle communicator. Most importantly, as an extraordinary scientist, his humbleness greatly affects and shapes me into a better person. I am fortunate to learn and work in the Smale lab together with a group of amazing colleagues and scientists: Philip O. Scumpia, Prabhat Kumar Purbey, Xin Liu, Brandon J. Thomas, Peter Kim, Hung-Hao Lo, Amber R. Ruccia, Vasileios Ragkousis, Allison Daly, Ariel Floro and Lijing Chen. I will always cherish the days we laughed, struggled, learned, and “happy houred” together. You lighted up and added a lot of spice to my life at UCLA.

I would also like to present my gratefulness to my colleagues and mentors in Tri-Service General Hospital, Taipei, Taiwan. Special thanks to Dr. Sheng-I Hu and Dr. Chin-Sheng Lin, who take care of my family while I am not around. Dr. Chi-young Liao not only takes care of my family but also constantly sends me warm regards as well as tons of home-missing snacks. Without your help and support, there is no way I can survive.

Lastly, I cannot be even luckier to have the most supportive family in the world. Even though they know the choice I made is not an easy path for their daughter, my parents encourage me to pursue whatever I believe in and persevere until the moment of achieving it. Thank you for being my strongest backup and having such great faith in me.

Chapter 1 contains reprints of figures and tables from published manuscripts with permission for Figure 1-1, Figure 1-4 and Table 1 by Elsevier (License Number: 4977430791125, 4977440444381, 4978500546350); Figure 1-2, Figure 1-5 and Figure 1-3 by Springer Nature (4977450413544, 4979240805221).

Chapter 2 is version of a manuscript titled “Toll-Like Receptor-Induced Nucleosome Remodeling Achieved by Broadly Acting NF-kB in Collaboration with Transcription Factors Conferring Selectivity”. **An-Chieh Feng***, Brandon J Thomas*, Fei Sun, Michael F. Carey, Philip O Scumpia, Stephen T Smale

B.J.T. and A.-C.F designed and performed most of the experiments. B.J.T and A.-C.F performed bioinformatic analysis. F.S. provided technical support to the 4C and Hi-C experiments. M.F.C and P.O.S provided intellectual inputs. A.-C.F. and S.T.S wrote the manuscript.

Appendix A is a reprint of an article published in Nature Materials.

Griffin, D. R., Archang, M. M., Kuan, C. H., Weaver, W. M., Weinstein, J. S., **Feng, A. C.**, Ruccia, A., Sideris, E., Ragkousis, V., Koh, J., Plikus, M. V., Di Carlo, D., Segura, T.,

Scumpia, P. O. (2020). Activating an adaptive immune response from a hydrogel scaffold imparts regenerative wound healing. *Nat. Mater.* DOI: 10.1038/s41563-020-00844-w

D.R.G., P.O.S. and T.S. conceived the experiments. D.R.G., W.M.W., E.S., M.M.A. and J.K. carried out the microfluidic design and fabrication, and D.D.C. oversaw the microfluidic design and fabrication. D.R.G., M.M.A., C.-H.K., W.M.W, J.S.W., **A.C.F.**, E.S., A.R., V.R. and P.O.S. performed the experiments. D.R.G., M.M.A., J.S.W., A.R., M.V.P., T.S. and P.O.S. analyzed and interpreted the data. D.R.G., M.M.A., P.O.S. and T.S. wrote the manuscript and all the authors discussed the results and contributed to writing portions of the manuscript and editing the manuscript. D.R.G. and M.M.A. contributed equally to this work. The co-principal investigators are P.O.S. and T.S.

Appendix B is a reprint of an article published in Nature Immunology.

Zhou, Q.D., Chi, X., Lee, M.S., Hsieh, W.Y., Mkrtchyan, J.J., **Feng, A.C.**, He, C., York, A.G., Bui, V.L., Kronenberger, E.B., Ferrari, A., Xiao, X., Daly, A.E., Tarling, E.J., Damoiseaux, R., Scumpia, P.O., Smale, S.T., Williams, K.J., Tontonoz, P., Bensinger, S.J. (2020). Interferon-mediated reprogramming of membrane cholesterol to evade bacterial toxins. *Nat Immunol 21*, 746-755. DOI: 10.1038/s41590-020-0695-4

S.J.B. conceived the study. Q.D.Z. led the design and execution of experiments. X.C. codesigned and performed all flow cytometry experiments and data analysis. V.L.B., W.Y.H. and J.J.M. contributed to flow cytometry experiments. J.J.M. and M.S.L. contributed to protein purification and staining experiments. Q.D.Z., M.S.L. and R.D. developed and performed live-cell imaging assays. C.H. performed NanoSIMS analysis and contributed to protein purification. J.J.M. and E.B.K. contributed to RNA analysis.

W.Y.H. and A.G.Y. performed GC–MS analysis with help from Q.D.Z. and E.B.K. K.J.W. conducted lipidomic studies. X.X., A.F., P.T. and E.J.T. contributed to *Abcg1*, *Abca1* and SCAP KO studies. A.E.D. analyzed gene expression data. **A.-C.F.**, P.O.S., M.S.L. and S.T.S. conceptualized and developed the in vivo SLO challenge assay. W.Y.H. contributed to data visualization. S.J.B., Q.D.Z., W.Y.H., X.C. and P.T. contributed to construction of the manuscript.

Appendix C is a reprint of an article published in Nature Communication.

Zhang, Z., **Feng, A.C.**, Salisbury, D., Liu, X., Wu, X., Kim, J., Lapina, I., Wang, D., Lee, B., Fraga, J., Pan, C., Williams, K.J., Lusis, A.J., Scumpia, P., Sallam, T. (2020). Collaborative interactions of heterogenous ribonucleoproteins contribute to transcriptional regulation of sterol metabolism in mice. *Nat Commun 11*, 984. DOI: 10.1038/s41467-020-14711-4

T.S. supervised and conceived the study, guided the interpretation of results, and the preparation of the manuscript. Z.Z. and T.S. designed the studies and wrote the manuscript. Z.Z. performed the majority of experiments and data analysis. X.W., J.K., and J.F. assisted with mouse experiments. D.S., B.L., and I.L. assisted with molecular in vitro studies. **A.F.**, X.L., D.W., and P.S. assisted with ChIP and ATAC studies, including data analysis and results interpretation. K.J.W. performed lipidomics and data analysis. C.P. and A.J.L. assisted with gene expression data of RALY from human tissues. All authors listed have made a substantial, direct, and intellectual contribution to the work, and approved it for publication.

Appendix D is a reprint of an article published in eLife.

Rajbhandari, P., Arneson, D., Hart, S.K., Ahn, I.S., Diamante, G., Santos, L.C., Zaghari, N., **Feng, A.C.**, Thomas, B.J., Vergnes, L., Lee, S.D., Rajbhandari, A.K., Reue, K., Smale, S.T., Yang, X., Tontonoz, P. (2019). Single cell analysis reveals immune cell-adipocyte crosstalk regulating the transcription of thermogenic adipocytes. *Elife 8*. DOI: 10.7554/eLife.49501

Contribution: Formal analysis, Investigation

Appendix E is a reprint of an article published in Small with permission by John Wiley and Sons (License Number: 4978550437551).

Koh, J., Griffin, D.R., Archang, M.M., **Feng, A.C.**, Horn, T., Margolis, M., Zalazar, D., Segura, T., Scumpia, P.O., and Di Carlo, D. (2019). Enhanced In Vivo Delivery of Stem Cells using Microporous Annealed Particle Scaffolds. *Small 15*, e1903147. DOI: 10.1002/smll.201903147

This work was supported by the Presidential Early Career Award for Scientists and Engineers (N00014-16-1-2997). J.K. was supported by the Kwanjeong Educational Foundation, Korea. P.O.S. was supported by the Mentored Clinical Scientist Development Award (K08-AR066545) through NIAMS. M.A. was supported by NIH NIGMS training grant (GM008042). The authors would like to thank Weikun Xiao and Dr. Stephanie Seidlits for technical assistance and comments, Dr. Jason Lee at the Crump Institute in California NanoSystems Institute (CNSI) for discussions and assistant for IVIS, Dr. Matt Schibler and Dr. Laurent Bentolila at Advanced Light Microscopy/Spectroscopy in CNSI for confocal imaging consultation, Dr. Westbrook Weaver, Joseph de Rutte, Dr. Maria Antfolk and Wei Yang for helpful discussions. J.K., D.R.G., T.S., P.O.S., and D.D.C.

conceived the study and designed the experiment. J.K., M.A. performed in vitro studies, J.K., D.R.G., **A.F.**, P.O.S. performed in vivo studies. J.K., T.H., M.M., D.Z. characterized the MAP scaffold. J.K. designed and fabricated the microfluidic device. J.K., D.D.C. analyzed and interpreted the data. J.K., P.O.S. and D.D.C. wrote the manuscript with input from all the authors.

Appendix F is a reprint of an article published in Cell.

Rajbhandari, P., Thomas, B.J., **Feng, A.C**., Hong, C., Wang, J., Vergnes, L., Sallam, T., Wang, B., Sandhu, J., Seldin, M.M., Lusis, A.J., Fong, L.G., Katz, M., Lee, R., Young, S.G., Reue, K., Smale, S.T., Tontonoz, P. (2018). IL-10 Signaling Remodels Adipose Chromatin Architecture to Limit Thermogenesis and Energy Expenditure. *Cell 172*, 218-233.e217. DOI: 10.1016/j.cell.2017.11.019

P.R., B.J.T, **A.-C.F.**, J.S., C.H., L.V., T.S., J.W., B.W., and L.G.F. performed the experiments. M.M.S. and A.J.L. performed the HMDP and the METSIM correlation meta-analysis. M.K. and R.L. designed and validated the IL-10Rα ASO. P.R., S.G.Y., K.R., S.T.S., and P.T. designed the experiments and interpreted the data. P.R. and P.T. wrote the manuscript. P.T. and S.T.S. supervised the study.

VITA

Education

M.D., National Defense Medical Center, Taipei, Taiwan 2002-2009

Honor

UCLA Grad Slam, 1st Place 2020

Roy & Dorothy John, Fred Eiserling & Judith Lengyel Awards for Teaching Excellence 2019

Full Scholarship for Ph.D. study abroad 2016-2021

Publications

- Griffin, D. R., Archang, M. M., Kuan, C. H., Weaver, W. M., Weinstein, J. S., **Feng, A. C.**, Ruccia, A., Sideris, E., Ragkousis, V., Koh, J., Plikus, M. V., Di Carlo, D., Segura, T., Scumpia, P. O. (2020). Activating an adaptive immune response from a hydrogel scaffold imparts regenerative wound healing. *Nat. Mater.* doi: 10.1038/s41563-020-00844-w. Online ahead of print.
- Zhou, Q.D., Chi, X., Lee, M.S., Hsieh, W.Y., Mkrtchyan, J.J., **Feng, A.C.**, He, C., York, A.G., Bui, V.L., Kronenberger, E.B.*, et al.* (2020). Interferon-mediated reprogramming of membrane cholesterol to evade bacterial toxins. *Nat Immunol 21*, 746-755.
- Zhang, Z., **Feng, A.C.**, Salisbury, D., Liu, X., Wu, X., Kim, J., Lapina, I., Wang, D., Lee, B., Fraga, J.*, et al.* (2020). Collaborative interactions of heterogenous ribonucleoproteins contribute to transcriptional regulation of sterol metabolism in mice. *Nat Commun 11*, 984.
- Rajbhandari, P., Arneson, D., Hart, S.K., Ahn, I.S., Diamante, G., Santos, L.C., Zaghari, N., **Feng, A.C.**, Thomas, B.J., Vergnes, L.*, et al.* (2019). Single cell analysis reveals immune cell-adipocyte crosstalk regulating the transcription of thermogenic adipocytes. *Elife 8*.
- Koh, J., Griffin, D.R., Archang, M.M., **Feng, A.C.**, Horn, T., Margolis, M., Zalazar, D., Segura, T., Scumpia, P.O., and Di Carlo, D. (2019). Enhanced In Vivo Delivery of Stem Cells using Microporous Annealed Particle Scaffolds. *Small 15*, e1903147.
- Rajbhandari, P., Thomas, B.J., **Feng, A.C.**, Hong, C., Wang, J., Vergnes, L., Sallam, T., Wang, B., Sandhu, J., Seldin, M.M.*, et al.* (2018). IL-10 Signaling Remodels Adipose Chromatin Architecture to Limit Thermogenesis and Energy Expenditure. *Cell 172*, 218-233.e217.
- Shiu, T.Y., Shih, Y.L., **Feng, A.C.**, Lin, H.H., Huang, S.M., Huang, T.Y., Hsieh, C.B., Chang, W.K., and Hsieh, T.Y. (2017). HCV core inhibits hepatocellular carcinoma cell replicative senescence through downregulating microRNA-138 expression. *J Mol Med (Berl) 95*, 629-639.

- Wu, S.Y., Chen, T.W., **Feng, A.C.**, Fan, H.L., Hsieh, C.B., and Chung, K.P. (2016). Comprehensive risk assessment for early neurologic complications after liver transplantation. *World J Gastroenterol 22*, 5548-5557.
- **Feng, A.C.**, Chen, T.W., Fan, H.L., Yu, J.C., and Hsieh, C.B. (2015). The Correlation of Hepatic and Systemic Hemodynamics During Liver Transplantation: Quantification of Hepatic Resistance as an Actual Value. *Medicine (Baltim) 94*, e1815.
- **Feng, A.C.**, Liao, C.Y., Fan, H.L., Chen, T.W., and Hsieh, C.B. (2015). The modified Sugiura procedure as bridge surgery for liver transplantation: a case report. *J Med Case Rep 9*, 50.
- **Feng, A.C.**, Liao, C.Y., Fan, H.L., Chen, T.W., and Hsieh, C.B. (2015). A successful child-to-adult deceased donor liver transplantation: a case report and literature review. *Ann Transplant 20*, 21-24.
- **Feng, A.C.**, Fan, H.L., Chen, T.W., and Hsieh, C.B. (2014). Hepatic hemodynamic changes during liver transplantation: a review. *World J Gastroenterol 20*, 11131-11141.
- **Feng, A.C.**, Hsieh, C.B., and Fan, H.L. (2013). Ramsay Hunt syndrome with an unusual clinical presentation in a liver transplant recipient: a case report and literature review. *Transpl Int 26*, e77-78.
- Dai, N.T., Yeh, M.K., Chiang, C.H., Chen, K.C., Liu, T.H., **Feng, A.C.**, Chao, L.L., Shih, C.M., Sytwu, H.K., Chen, S.L.*, et al.* (2009). Human single-donor composite skin substitutes based on collagen and polycaprolactone copolymer. *Biochem Biophys Res Commun 386*, 21-25.

Posters

- Annual I3T (The Immunology, Inflammation, Infection, and Transplantation Research Theme) Scientific Retreat, 12th June 2018: “Highly Selective Roles of Key Transcription Factors in Chromatin Remodeling at both Promoters and Intergenic Regions in Activated Macrophages” UC Los Angeles, CA.
- UCLA Biomedical / Life Science Innovation Day, 13th June 2018: “Highly Selective Roles of Key Transcription Factors in Chromatin Remodeling at both Promoters and Intergenic Regions in Activated Macrophages” UC Los Angeles, CA.

Oral Presentations

- I3T Research Seminar Series, February 12th, 2019: “Molecular mechanisms regulating selective transcription in the innate immune system” UC Los Angeles, CA.
- MBIDP Student Seminar Series, May 29th, 2019: “Molecular mechanisms regulating selective transcription in the innate immune system” UC Los Angeles, CA.
- Gene Reg Tuesday Seminar Series, December 3rd, 2019 “Highly Selective Roles of Key Transcription Factors in Chromatin Remodeling in Activated Macrophages” UC Los Angeles, CA.

CHAPTER 1

INTRODUCTION

PART 1: Chromatin Contribution to Immune Gene Regulation

PART 2: High Throughput Sequencing Technologies in Studying Gene Regulation

PART 1

Genetic Code and Central Dogma

Deoxyribonucleic acid (DNA) is the genetic material that carries the fundamental instructions of all organisms on Earth and is known as “the molecule of life”. DNA is a double-stranded molecule composed of two polynucleotide chains held together by hydrogen bonds between base pairs of nucleotides. There are four nucleotides containing one of the following bases: adenine (A), guanine (G), cytosine (C), or thymine (T). The base pairs only form between A and T, and between C and G; therefore, only the two polynucleotide strands with complementary base pairing can coil together to form the double-helix DNA molecule (Franklin and Gosling, 1953; Watson and Crick, 1953; Wilkins et al., 1953).

The double-stranded DNA molecules are stable and located in the nucleus of eukaryotic cells. The human genome contains 3 billion base pairs (bp) of nucleotides and if we stretch out the entire genome, it is over 6 feet long. How can this possibly fit into a tiny nucleus? The DNA of eukaryotic cells is tightly bound to histone proteins and folded to form chromatin. The basic structural unit of chromatin is called the nucleosome (Kornberg and Thomas, 1974), which consists of 147 bp of DNA wrapped around two molecules of each histone proteins H2A, H2B, H3, H4, and one molecule of histone H1. The nucleosomal DNA can be further folded and coiled into chromatin structure which allows the long DNA molecule to be packaged within the confines of the nucleus with proper organization.

A DNA molecule is not just a long string of nucleotides. It is divided into functional units known as genes. The genetic information is stored in the DNA base sequence in

triplets which can be converted into another form of information-storing molecules, ribonucleic acid (RNA), by RNA polymerase. The RNA molecules are single-stranded and have the same bases used in DNA except for T, which is replaced with the demethylated form, Uracil (U). The process of RNA synthesis from DNA templates is called transcription. The transcribed RNA molecules, or transcripts, are further classified into many different RNA species that perform a wide variety of functions. Mainly, the messenger RNA (mRNA) molecules, which code for protein, will be transported into cytoplasm and serve as the template for subsequent polypeptide synthesis by ribosomes. The RNA sequence is complementary to the DNA template and the nucleotide triplet codes for the corresponding amino acid or acts as a specific signal in the process of polypeptide synthesis. For example, AUG codes for methionine and also serves as the start codon in RNA to polypeptide translation. The polypeptides then transform into functional proteins with proper folding and modifications. Proteins are the basic building blocks, or functional units, of organisms and serve various functions.

Regulation of Gene Expression

The development of organisms depends on specific gene expression in distinct cells to establish different cell types of various functions. In addition to cell development, all living organisms have to interact with the environment and make proper responses, such as activating genes to produce defensive substances when encountering pathogens. To achieve this, intricate regulation of gene expression is required, which occurs to a large extent during the transcription of genes into RNA. Transcriptional regulation in eukaryotes is the combined effects of structural properties (will be discussed

later) and interactions of proteins called transcription factors (TFs) that bind to specific DNA elements.

On the DNA side, there are several functional DNA elements that can contribute to gene regulation in eukaryotes. These include the core promoter (Smale and Kadonaga, 2003), regulatory promoter and enhancer sequences, which will be discussed in detail later. The core promoter serves as an initial binding site for the RNA polymerase II (RNA Pol II) and the composing elements include the TATA box (25-30 bp upstream of the transcription start site [TSS]) (Lifton et al., 1978), the initiator (Inr, flanking the TSS) (Smale, 1997) and the downstream promoter element (DPE, about 30 bp downstream of the TSS) (Burke and Kadonaga, 1997). The core promoter can include either a TATA box or Inr alone, or both together; whereas the DPE is found in many promoters that do not contain a TATA box. Although the core promoter is sufficient to correctly initiate transcription *in vitro*, most gene expression *in vivo* is dependent on additional regulatory sequences located within a few hundred base pairs upstream of the core promoter, often referred to as the regulatory promoter. Enhancers are regulatory sequences that increase transcription and can be at a great distance located either upstream or downstream of the core promoter (will be discussed later). Both the regulatory promoter and enhancer contain many TFs binding sites. To begin transcription, RNA Pol II requires a number of additional factors known as general transcription factors (GTFs) to load onto the core promoter and together assemble the pre-initiation complex (PIC). The associated regulatory sequences (regulatory promoter and/or enhancer) bound by TFs can facilitate transcription initiation by various mechanisms, such as stabilizing the PIC (Gill, 2001).

TFs are proteins that regulate the transcription of genes by binding to specific DNA sequences. A basic feature of TFs is that they contain DNA-binding domains (DBDs) that recognize specific sequence patterns, known as motifs, within the promoter and/or enhancers of the regulated gene. TFs are categorized into different families based on the structure of their DBDs. In addition to the DBDs, TFs possess other domains involved in activating or repressing expression, dimerization, and establishing protein-protein interactions. There are up to 1600 TFs found in the human genome that serve various functions and play important roles in almost all kinds of cellular processes; thus, their activity is tightly regulated. One feature of a subset of stimulus-responsive TFs is their translocation to the nucleus when activated. Many other forms of TF regulation have been documented, such as posttranslational modifications, dimerization and cleavage.

Enhancers

Though *cis*-acting regulatory sequences are frequently found to be located upstream of promoters, they can be farther away from the TSS. In 1981, Walter Schaffner identified two 72-base-sequence repeats in the simian virus 40 (SV40) genome that were required for efficient transcription and were located farther away from the TSS (Benoist and Chambon, 1981; Gruss et al., 1981; Moreau et al., 1981). Surprisingly, these sequences were active when placed several kilobases either upstream or downstream from the TSS, in either a forward or backward orientation. In mammalian cells, many genes are controlled by these regulatory sequences, called enhancers.

Enhancers function like promoters by binding TFs; the TF-bound enhancers then interact with co-activators, GTFs, and/or RNA Pol II to facilitate the PIC assembly and

transcription initiation. The DNA looping model has been proposed to allow for direct contact of promoters and distant enhancers (Jiang and Peterlin, 2008; Miele and Dekker, 2008; Vakoc et al., 2005). In this model, the enhancer and promoter make contact by looping out the intervening chromatin. The resulting chromatin loops are stabilized by protein-protein interactions. A number of large proteins and protein complexes have been proposed to bridge and direct physical contact between enhancers and promoters, such as Mediator, CTCF, and Cohesin (Kagey et al., 2010) (Figure 1-1). There are several proposed models to describe the nature and forces that generate and stabilize the looping structure. Though the cause or consequence for transcriptional regulation in these models is still uncertain, they all point to crucial roles of enhancers in transcriptional regulation.

The mammalian genome contains approximately 23,000 genes; however, it is estimated that there are more than 1 million enhancers (Andersson et al., 2014; de Laat and Duboule, 2013). Considerable effort has been devoted to characterizing enhancers and unveiling their functional roles since their discovery. There is an increasing appreciation of their importance not only in developmental processes but also in evolution and disease. However, our knowledge of these elements has remained incomplete. The vast majority of enhancers in any animal genome and their spatiotemporal activities are unknown, as suggested by the small number of gene expression patterns that have been linked to specific enhancers, the many disease-associated single-nucleotide polymorphisms in non-coding regions of unknown function and the large number of genomic regions with enhancer-like chromatin features. One of the major unanswered questions about enhancers is why an excessive number of enhancers is required and maintained in the genome? It has been reported that the enhancers responsible for limb

development are still preserved in the genome of snakes. Surprisingly, the number of enhancers in snakes is close to the number present in lizard DNA. After 80 million years, the DNA segments would not still be intact unless they serve an essential purpose. From the perspective of a complicated gene expression network, the huge number of regulatory elements in the genome may be the reservoir to achieve the need for diverse and specific expression control, such as immune response.

Chromatin remodeling in Gene Regulation

In eukaryotic cells, DNA is packaged in the tiny nucleus in the form of chromatin. Though transcription initiation is considered as an important step of transcription control, the interaction between proteins and *cis*-regulatory elements cannot happen if the DNA is tightly wrapped around the histones and inaccessible to TFs. Chromatin can also provide a barrier to transcription itself. Indeed, before TFs bind to regulatory elements, PIC assembly, and the start of transcription, the underlying DNA sequences have to be made accessible for protein binding (Li et al., 2007). Dynamic modulation of chromatin structure is now widely appreciated as a key component in regulating individual gene expression.

Chromatin regulators are usually multi-subunit complexes that can be grouped broadly into two classes, those that covalently modify histones or DNA and those that use the energy of ATP to mobilize nucleosome (Becker and Workman, 2013; Roberts and Orkin, 2004). Complexes of those covalently modify histones can acetylate, methylate, phosphorylate and ubiquitylate specific amino acid residues on the N-terminus of histone proteins. Recently, large-scale mapping of histone modifications and related structures

have characterized and emphasized the functional consequences of chromatin structure and transcription activity among various sequence features, such as promoters, enhancers, and gene bodies (Zhou et al., 2011) (Table 1).

ATP-dependent chromatin remodeling complexes (remodelers) influence chromatin dynamics in various ways and contribute to gene expression (Figure 1-2). Remodelers include enzymes that ensure proper density and spacing of nucleosomes. Another set of remodelers cooperates with nucleosome-avid TFs (known as “pioneer factors”) (Zaret and Carroll, 2011) and histone modification enzymes to move or eject histones and make the DNA accessible for TFs binding. In addition, another set of remodelers is involved in replacing canonical histones with histone variants to create specialized chromosomal regions.

All remodeler ATPases are classified within the RNA/DNA helicase superfamily 2, which can be divided into four subfamilies: imitation switch (ISWI), chromatin helicase DNA-binding (CHD), switch/sucrose non-fermentable (SWI/SNF) and INO80. Each subfamily is characterized by ATPase structure and is specialized to preferentially achieve particular chromatin outcomes including nucleosome assembly (ISWI and CHD), access (SWI/SNF) or editing (INO80) (Becker and Workman, 2013; Clapier et al., 2017; Hargreaves and Crabtree, 2011).

Chromatin access can be accomplished by specialized remodelers in all four subfamilies, but it is most strongly associated with the SWI/SNF remodeler. The SWI/SNF complex was identified in yeast by defects in mating type switching and/or sucrose fermentation (Cairns et al., 1994; Côté et al., 1994; Peterson et al., 1994). It is highly conserved in eukaryotes and homologous complexes have been purified from *Drosophila*

and humans (Kingston and Narlikar, 1999). It uses energy generated from ATP hydrolysis to break and reform the histone-DNA contacts followed by nucleosome repositioning, ejecting full nucleosomes or evicting nucleosome components (such as H2A-H2B dimers) (Narlikar et al., 2013). In addition, structural studies with the SWI/SNF remodeler reveal a binding pocket with almost perfect mononucleosome dimensions (Tang et al., 2010). Access of the nucleosome to this pocket may involve conformational changes and can be regulated by histone tail modifications (Skiniotis et al., 2007), which may be recognized by one of the many histone-interacting domains in SWI/SNF complexes. This observation emphasizes the crosstalk and cooperation between two broad classes of chromatin regulators (Becker and Workman, 2013; Hargreaves and Crabtree, 2011).

The above remodeling processes contribute to transcriptional regulation at the level of chromatin organization before transcription initiation. Increasing evidence has emphasized the importance of chromatin contribution to shaping cell-specific and stimulus-specific transcription.

Immune gene regulation

The mammalian immune system has two components, the innate and adaptive immune systems. Innate immunity recognizes foreign molecules and stimulates immune responses such as inflammation and phagocytosis. It provides a timely first line of defense against pathogens, which is critical in preventing infection, maintaining homeostasis and also activating the adaptive immune system. Innate immunity is semi-specific and does not adapt to specific external stimulus or a prior infection but relies on genetically encoded recognition of particular patterns. Adaptive immunity, or acquired

immunity, is the active immune component of host immune response operated by programmed antigen-specific lymphocytes, such as T- and B-cells. Different from innate immunity, adaptive immunity is highly specific and can confer memory.

Given the highly interactive immune network, timely and precise signaling is required. In the past decade, considerable progress has been made toward elucidating the nature of the signaling and transcriptional pathways and associated genomic control circuits that underlie the development of distinct immune cell lineages, as well as their differentiation and activation in response to sensing of pathogens or non-self antigens. The gene control circuits involve receptors that sense particular stimuli and transduce them via signaling cascades to regulators of gene expression. In a given circuit, the developmental or activation signals elicit distinct cascades of coordinately activated and repressed gene expression states, thereby enabling cell fate or effector state transitions. Numerous factors contribute to the signaling circuit to ensure the precise and controlled information flow in the immune development and response. Considerable effort has been devoted in the field in the past 40 years with great achievement. However, given the complexity of the immune system and the progress of genome-wide research platforms, an understanding of global regulatory logic is needed in addition to revealing the gene-specific centralized logic.

Key transcription factors in the immune response

Nuclear Factor -κB

Numerous transcription factors contribute to immune responses. Nuclear factor kappa-light-chain-enhancer of activated B cells (NF-κB) was originally discovered in the

study of the Ig κ light chain enhancer and found to be the central inflammatory mediator in immune responses that controls cytokine production and cell survival (Sen and Baltimore, 1986). NF-κB is an inducible dimeric TF family composed of members that share a Rel homology domain in the N-terminus which recognize a common sequence motif (Gilmore, 2006). RelA, RelB, and c-Rel have a C-terminal transactivation domain and the other two members, NF-κB1 and NF-κB2, are synthesized as large precursors, p105 and p100. Both the p105 and p100 precursors undergo selective cleavage of the C-terminal region containing ankyrin repeats to generate the mature p50 and p52. However, the process of generating p52 from p100 is tightly regulated and p50 is produced constitutively from p105. NF-κB factors usually exert their function by dimerization and bind to 9-10 base pairs DNA sites (κB sites), which have a great variability (5'-GGGRNWYYCC-3′; R, A or G; N, any nucleotide; W, A or T; Y, C or T) (Hoffmann and Baltimore, 2006). The five NF-κB family members can form homodimers and heterodimers in a great diversity which contributes to different degrees of specificity and redundancy in regulating sets of genes.

NF-κB is found in almost all animal cell types and contributes to activation of an exceptionally large number of genes in responses to harmful situations which required timely reprogramming of gene expression, such as bacterial or viral infection, inflammation, stress, free radicals, and ultraviolet irradiations (Ghosh et al., 1998). In unstimulated cells, NF-κB is latent in the cytoplasm and sequestered by binding to inhibitor NF-κB family proteins (IκBs) (Jacobs and Harrison, 1998). When encountering stimuli, there are two well-described pathways leading to the activation of NF-κB: canonical and non-canonical pathways (or the classical and alternative pathways) and

both of them are important in regulating immune and inflammatory responses (Karin and Delhase, 2000; Oeckinghaus and Ghosh, 2009; Sun, 2011; Vallabhapurapu and Karin, 2009). The canonical pathway responses to diverse stimuli. Upon activation, Inhibitor Kappa kinases (IKKs) phosphorylates IκBα, triggers ubiquitin-dependent IκBα degradation, resulting rapid and transient nuclear localization of canonical NF-κB members such as p50/RelA and p50/c-Rel dimers. On the other hand, the non-canonical pathway selectively responds to a subset of TNF receptor superfamily members. In the non-canonical pathway, NF-κB inducing kinase (NIK) activates and cooperates with IKKα to mediate p100 phosphorylation, which in turns induces p100 ubiquitination. The ubiquitinated p100 undergoes degradation of its C-terminal IκB-like structure, resulting in generation of mature NF-κB2 p52 and nuclear translocation of the non-canonical p52/RelB dimer. Once NF-κB TFs translocate into the nucleus, they exert their function by binding to the DNA elements and regulate the associated genes transcription.

The regulation of NF-κB is crucial for the physiology of inflammation and immune activation, and dysregulation of NF-κB has been linked to inflammatory and autoimmune diseases, cancer, septic shock, and improper immune development. Since its discovery, NF-κB regulation has been the major focus of biomedical studies. Though the main components of the signaling pathways that activate NF-κB have been identified and mapped, the interactive and dynamic network is still incompletely understood. With advanced high throughput and computing technologies, researchers are able to gain greater understanding of the amazing complexity of the NF-κB signaling network. Mathematical models are applied to understand the regulation of NF-κB dynamics based on the experimental results, including the multiple feedback loops to ensure steady NF-

κB activity, different IKK dynamics to enable stimulus-specific responses, the crosstalk between the IκB-NF-κB module and other pathways, and NF-κB oscillations (Lipniacki et al., 2004). Such computational approaches provide broader insights into the network of signal transduction. However, unveiling the critical mechanistic insights into the control of diverse transcription networks remains challenging.

Interferon Regulatory Factors

Interferon regulatory factors (IRFs) are another major transcription factor family modulating the immune signaling. There are nine members in the family, IRF1 to IRF9, which possess an N-terminal DBD characterized by a series of five well-conserved tryptophan-rich repeats (Honda and Taniguchi, 2006; Tamura et al., 2008). The DBD forms a helix-turn-helix structure and recognizes a consensus DNA sequence (A/GNGAAANNGAAACT) known as the IFN-stimulated response element (ISRE). The C-terminal region is more diverse among members and mediates specific interactions between family members, other TFs, or cofactors (Chen and Royer, 2010; Panne et al., 2007). The C-terminal domain of each IRF member contains a nuclear export sequence, an autoinhibitory sequence, and an IRF-association domain which for most family members contains serine residues that are phosphorylated to regulate activity. IRF family members can both homodimerize and heterodimerize, forming both transcriptionally active and repressive complexes. IRF3, IRF5, and IRF7, are critical to type I interferon (IFN) production downstream of pathogen recognition receptors that detect viral RNA and DNA (Honda et al., 2006). IRF4, IRF8 and IRF5 regulate myeloid cell development and phenotype, while IRF9 regulates interferon-driven gene expression. Given their central

role as transcription regulators of type I IFN (IFN-α and IFN-β) biology, IRFs play pivotal roles in many aspects of the immune responses to pathogens, immune cell development and differentiation. Thus, understanding how their levels and activity is regulated is of critical importance given the perturbations in either can result in dysregulated immune responses and autoimmune disease or oncogenesis.

Regulation of Innate Immune Response by IRFs and NF-κB

The initial sensing of infection is mediated by innate pattern recognition receptors (PRRs), which include Toll-like receptors (TLRs), C-type lectin receptors (CLRs), RIG-I-like receptors (RLRs), and NOD-like receptors (NLRs) (Takeuchi and Akira, 2010). These receptors recognize diverse pathogen-associated molecular patterns (PAMPs) and danger-associated molecular patterns (DAMPs). Responding to various PAMPs/DAMPs, PRRs trigger different signaling cascade accordingly and induced transcription of type I IFNs, pro-inflammatory cytokines, and chemokines that eliminate pathogens and infected cells but meanwhile poise the uninfected cells. IRFs are essential mediators that transmit PRR signals to chromatin for immune cell activation (Ikushima et al., 2013). The innate immunity utilizes different PRRs to detect pathogens depending on their modes of infection. TLRs are present on the cell membrane and are the most well-characterized receptors among PRRs. They initiate key inflammatory responses in addition to shaping the adaptive immune response (Kawai and Akira, 2011).

All TLRs comprise an extracellular domain with leucine-rich repeats, which is responsible for ligand recognition, and a cytoplasmic Toll/IL-1R (TIR) homology domain, which is required for the signaling initiation. TLR1, TLR2, TLR4, TLR5, and TLR6 are

located on the cell surface and are responsible for recognizing microbial membrane components, whereas TLR3, TLR7, TLR8, and TLR9 are expressed within intracellular vesicles and recognize nucleic acids. TLRs initiate shared and distinct signaling pathways by recruiting different combinations of four TIR domain-containing adaptor molecules: MyD88, TIRAP, TRIF, and TRAM (Kawai and Akira, 2010).

Broadly, signaling through TLRs can be categorized into two pathways: the MyD88-dependent pathway and the TRIF-dependent pathway (Kawai and Akira, 2010) (Figure 1-3). All TLRs, except TL3, activate the MyD88-dependent pathway (O'Neill et al., 2013). In contrast, TLR3 and TLR4 activate the TRIF-dependent pathway. Both TLR3 and TLR4 use a TRIF adapter to activate IRF3 and induce type I IFNs. TLR4 recognizes lipopolysaccharide (LPS) from gram-negative bacteria and also a variety of other PAMPs and DAMPs. TLR4 is the only TLR that recruits all four adaptor proteins and activates two distinct signaling pathways (Figure 1-3). TLR4 initially recruits TIRAP and MyD88; then MyD88 recruits IRAKs, TRAF6, and the TAK1 complex, which lead to the early-phase activation of NF-κB and MAP kinase. TLR4 is then endocytosed and delivered to intracellular vesicles to form a complex with TRAM and TRIF. The complex then recruits TRAF3 and the protein kinase TBK1, which catalyze the phosphorylation of IRF3. The phosphorylated IRF3 then translocates into the nucleus to induce type I IFNs and related gene expression by binding to ISRE. TRAM-TRIF also recruits TRAF6 and TAK1 to mediate late phase activation of NF-κB and MAP kinase.

In the TLR4 signaling cascade, IRF3 serves as the final effector which translocates into the nucleus and induces type I interferons expression. Among the IRF family members, IRF3 and IRF7 share the greatest structural homology and are known to be

the principal mediators of IFN production. However, IRF3 is ubiquitously expressed, whereas IRF7 is expressed only at a very low level, except in plasmacytoid DCs. IRF7 expression is induced by type I IFNs resulting in a secondary feedforward loop that maximally drives type I IFNs expression (Yanai et al., 2012).

Macrophages

Macrophages were first identified by the Russian zoologist, Élie Metchnikoff, in 1884. Soon after their discovery, they became a great interest for immunologists. Because their capacity to phagocytose inert particles, bacteria, parasites or other harmful organisms, macrophages are a first-line defense against foreign invaders. After internalization, microbes are degraded within phagolysosomes. Macrophages then release recruitment signals for and present antigens from the degraded microbes to other immune cells such as T lymphocytes. Macrophages are able to detect products of bacteria and other microorganisms using PRRs (TLRs, CLRs, RLRs, and NLRs). These PRRs can bind specifically to different pathogen components like LPS, RNA, DNA or extracellular proteins (for example, flagellin from bacterial flagella). The PRRs then initiate the signaling networks through selected adaptors and protein complexes to activate transcription factors, such as NF-κB and IRFs, with designed dynamics which result in precise production of IFNs, cytokines and related genes.

Macrophages play a crucial role not only in serving as the first line defense but also in bridging the innate and adaptive immunity; therefore, timely and precise transcription control is required. In the past decades, remarkable effort has been made to understand transcription regulation in macrophages when responding to various stress

and danger signals. The well-profiled macrophage signaling cascades and transcriptome provide the optimal platform in studying the critical details of immune gene regulation.

Mouse bone marrow derived macrophage

Macrophages are derived from monocytes. Monocytes arise in the bone marrow from myeloid stem cells and migrate to peripheral blood and various tissues where they differentiate into macrophages. Currently, the majority of the research in the field is done on macrophage cell lines, such as RAW264.7 and J774, which differ from primary macrophages in their phagocytic activity, cytokine production and the regulation of the oxidative burst (Ralph et al., 1980). To study macrophage-pathogen interactions as well as the immune signaling networks, primary macrophages are recommended, such as Bone Marrow Derived Macrophages (BMDMs), which exhibit more physiological features. It is also possible to work on genetically modified BMDMs by isolating the macrophages directly from genetically engineered mouse models, such as knockout mouse models. The procedure of differentiating mouse bone marrow cells into macrophages is well-established and widely used by research groups (Trouplin et al., 2013). By treating BMDMs with receptor-specific stimulus, we can focus on the targeted signal cascades. Therefore, the BMDM model provides us the possibility of understanding complicated immune networks.

PART 2

High throughput sequencing technology

The advancement of high throughput sequencing technologies in recent decades enables us to profile genome-wide characteristics comprehensively. The human genome sequence was drafted in 2001 with Sanger DNA sequencing, which was limited in throughput and high cost (Lander et al., 2001; Venter et al., 2001). The National Human Genome Research Institute then created the initiative of DNA sequencing technology aimed at achieving lower cost human genome sequences in 10 years, which resulted in the emergence of various high-throughput sequencing (HTS) technologies. Though there was a great improvement of the traditional Sanger sequencing, the biggest leap involved commercial HTS platforms, which follow a general paradigm: template preparation, clonal amplification, and cyclical rounds of massively parallel sequencing. As sequencing costs have dropped, HTS machines have become accessible and enable researchers to develop various applications in addition to simply sequencing genomes (Figure 1-4).

High Throughput Sequencing in Profiling Genome-Wide Characteristics

One of the highest impact areas by HTS is the genome-wide mapping of DNA elements and chromatin landscapes at high-resolution. Nucleosome positions along with histone variants and modifications make up the primary structure of the chromatin landscape. The first of these technologies was ChIP-seq (chromatin immunoprecipitation followed by sequencing) in which DNA associated with a TF, histone variant or modification is immune-selected with specific antibodies and then sequenced using HTS (Johnson et al., 2007). Mapping the sequences back to the genome reveals the location of bound regions, histone variant, or modifications. The pioneering study done by Barski et al. highlighted the value of comprehensive and HTS approaches to map histone modifications (Barski

et al., 2007). Evidence has revealed the association of particular modifications with gene activation or repression and with various genomic features, including promoters, transcribed regions, enhancers and insulators (Figure 1-5, Table 1-1). Typically, protein-coding gene promoters exhibit histone H3 lysine 4 trimethylation (H3K4me3). On the contrary, the presence of H3K27ac accompanied by high levels of H3K4me1 and low H3K4me3 is broadly used to identify enhancers. However, this methodology possesses considerable false positives and false negatives (Kim and Shiekhattar, 2015). Recent work has demonstrated that H3K4me1 is not a requirement for enhancer function and H3K4me2 and H3K4me3 are compatible with enhancer activity (Dorighi et al., 2017; Rickels et al., 2017). Another drawback of applying histone modification ChIP-seq to define regulatory regions is the broad modification size, often thousands of base pairs, which greatly reduces the signal sharpness in comparison to DNA binding protein ChIP-seq, ~400 bp, such as coactivator p300/CBP (Ostuni et al., 2013).

Another method in identifying putative regulatory regions is to target the “open” chromatin regions. The first applied method was DNase I digestion and followed by DNA sequencing of the fragments (DNase-seq) (Crawford et al., 2006). Other similar assays for chromatin accessibility include FAIRE-seq (formaldehyde-assisted isolation of regulatory elements) (Giresi et al., 2007), Sono-seq (sonification followed by sequencing) (Auerbach et al., 2009), and MNase-seq (micrococcal nuclease digestion) (Schones et al., 2008). In 2013, Assay for Transposase-Accessible Chromatin using sequencing (ATAC-seq) was first described as an alternative advanced method which quickly became the most widely used application in profiling the genome-wide “open” regions (Buenrostro et al., 2013). Compared to DNase-seq, MNase-seq and FAIRE-seq, ATAC-seq can be

performed with smaller numbers of cells, or even single cells, and the protocol is much simpler. In brief, hyperactive Tn5 transposase is used to tag the genomic regions of accessible chromatin with a sequencing adapter. Followed by PCR amplification, a library can be generated for high throughput sequencing. Recently, the modified ATAC-seq protocol, Omni-ATAC, was presented by Corces et. al. which works across multiple applications with substantial improvement of signal-to-background ratio and information content (Corces et al., 2017). Unlike the prediction of the chromatin organization by various histone modifications indirectly, ATAC-seq profiles chromatin accessibility directly with much sharper signals and resolution.

Three-dimensional Organization of the Genome

To fit into the tiny nucleus, the 6-feet long DNA molecule has to wrap around the histones and fold into a compartmental and well-organized structure. HTS technologies can also profile the three dimensional chromatin organization using assays such as Hi-C and ChIA-PET (chromatin interaction analysis by paired-end tag sequencing) (Fullwood et al., 2009; Lieberman-Aiden et al., 2009). These methods rely upon proximal ligation of cross-linked, digested chromatin followed by sequencing to derive contact maps. Hi-C is the first technique that can profile the unbiased, genome-wide chromatin organization. Lieberman-Aiden et al. revealed the dynamic conformation of the whole genome which broadly partitions into open and closed chromatin state. By applying Hi-C, Dixon et al. demonstrated that the genome is organized into topological associating domains (TADs), within which high amounts of intra-domain interactions are noticed but infrequent interactions across domain boundaries (Dixon et al., 2012). Recent ultra-deep Hi-C

sequencing provides higher resolution contact maps of about 1 kb and refines TAD size from 1 Mb to 200 kb. The high-resolution contact map demonstrates that intrachromosomal loops often contain promoter-enhancer contacts associated with gene activation. Most loops are anchored with CTCF protein binding sites and are occupied by the cohesin complex and form an insulated neighborhood. Recent evidence showed that the integrity of an insulated neighborhood is essential for maintaining normal gene expression (Dowen et al., 2014; Ji et al., 2016). Thus, insulated neighborhoods are considered to be the structural and functional units of gene regulation.

One major drawback of Hi-C assay is the requirement of very deep sequencing depth to obtain enough resolution. Recently, the Promoter Capture Hi-C (PCHi-C) method has been proposed to enable genome-wide promoter-based detection of distal promoter-interaction regions (Schoenfelder et al., 2018). By hybridizing a set of designed biotinylated RNA probes containing promoter sequences, the DNA fragments containing the promoter and its interacting partner will be captured and enriched specifically for sequencing. The capture method can achieve satisfying resolution which reveals the functional interactions between promoter and enhancer.

Profiling the transcriptome

RNA transcripts are the readout of gene activity and serve various functions. HTS applications enable systematic identification of various RNA classes. RNA-seq have been utilized extensively to characterize transcriptomes, providing precise, quantitative measurements of message abundance, isoform usage, RNA-editing and allele-specific expression (Nagalakshmi et al., 2008). To profile transcriptomes, the most widely used

method is selecting RNA with a poly-A tail using oligo-dT beads for the downstream sequencing. This method can profile the pool of processed, semi-processed as well as the unprocessed RNA transcripts, which can be used for broader multi-purpose analysis. To study primary transcripts and RNA splicing, nascent RNA sequencing (Nascent-seq) provides a more reflective, timely and native measurement of transcription (Khodor et al., 2011). Another modified RNA-seq method was described by fractionating the cells to obtain chromatin associated, nucleoplasmic, and cytoplasmic transcripts for sequencing (Bhatt et al., 2012). Sequencing of the chromatin-associated transcripts is beneficial for studying primary gene regulation because it snapshots the newly transcribed RNA molecules at the moment but not the combinatorial result of RNA synthesis, processing, and degradation. In addition, because there is no poly-A selection, any species of RNA actively transcribed on the genome will be captured, such as enhancer RNAs.

Enhancer RNAs (eRNAs) are transcripts derived from active *cis*-regulatory regions (Ashe et al., 1997; Collis et al., 1990; Tuan et al., 1992). They generally lack splicing and polyadenylation (poly-A tail), which renders them unstable and susceptible to rapid degradation. Though it is a debate whether eRNAs are functional, emerging evidence has shown they can facilitate transcription initiation by stabilizing the PIC. Nonetheless, eRNA transcription is correlated with enhancer activity, and mapping of eRNAs is an appealing method to define putative regulatory sites (Natoli and Andrau, 2012).

Significance

During the past 40 years, there has been great progress in understanding transcriptional regulation in immune cell development and the response of immune

system cells to various stimuli. In the pre-genomics era, our understanding was mainly limited to gene-specific logic. In the genomics era, the completion of genome sequences, along with the advancement of HTS technologies and computational methodologies, have facilitated broader analyses, which have revealed the amazing complexity of transcription regulation networks in the immune system. However, much remains to be learned.

In the well-characterized TLR4 response, two major TFs, NF-κB and IRF3, together with optimized mouse BMDMs, provide us the opportunity to obtain critical insights into immune regulation networks under manageable complexity. The HTS assays enable the global event characterization, such as ChIP-seq to identify TFs binding events, ATAC-seq to profile the nucleosome remodeling, chromatin-associated RNA-seq to obtain the dynamic transcriptome and Hi-C to capture the three-dimensional chromatin interactions. All these strategies and methods together hold the promise to fill the knowledge gap between global and gene-specific logics of transcription control. We aim to systematically elucidate the mechanistic principles that allow immune and environmental stimuli to elicit highly selective transcriptional responses.

Figure Legends

Figure 1-1: Mechanisms of Enhancer-Promoter Interactions

The enhancer is brought in close contact with the promoter by forming the lopping structure. The Mediator/Cohesin complex is involved in stable formation of enhancer/promoter looping. Some eRNAs facilitate the looping through interaction with the subunit(s) of the Mediator/Cohesin complex.

Figure 1-2: Layers of Chromatin Organization in the Mammalian Cell Nucleus

Features at different levels of chromatin organization are generally associated with inactive or active transcription. The genomic DNA either with (inactive) or without (active) methylated on cytosine is wrapped around histone octamers and forms nucleosomes. The nucleosomes vary in histone composition and histone modifications; these features constitute the primary layer of chromatin structure. DNA in chromatin may remain accessible to DNA-binding proteins such as TFs and RNA polymerase II or may be further compacted. Chromatin can also organize into higher-order structures such as nuclear lamina-associated domains and transcription factories. Each layer of organization reflects aspects of gene and genome regulation.

Figure 1-3: Mammalian TLR Signaling Pathways

There are nine TLRs identified which recognize different components of the pathogens. TLR signaling is initiated by ligand-induced dimerization of receptors. The TIR domains of TLRs engage the adaptor proteins such as MyD88, MAL, TRIF and TRAM. Engagement of the signaling adaptors stimulate the downstream signaling pathways

involving the interactions between IRAKs and TRAF which leads to the activation of the MAPKs, JNK and p38, and to the activation of TFs. There are two major TFs, NF-kB and IRFs, activated downstream of TLR signaling; however, other TFs such as CREB and AP1 are also important. The activated TFs translocate into the nucleus and exert their function by binding to the associated DNA element to induce pro-inflammatory cytokines and type I INFs production. Specifically, TLR4 initially recruits MAL and MyD88 for the early phase activation of NF-κB; then it moves from the plasma membrane to the endosomes to switch signaling from MyD88 to TRIF resulting in IRF3 and late-phase NF-κB activation.

Figure 1-4: Broad Overview of HTS Applications

The advancement of HTS and its wide applications. Publication date of a founding article describing a method versus the number of citations that the article received. Methods are colored by category, and the size of the data point is proportional to publication rate.

Figure 1-5: Histone Modifications Demarcate Functional Elements in Mammalian Genomes

The distribution of histone variants and modifications on the promoter, gene body, enhancer and boundary element from a transcription perspective.

Figure 1-1

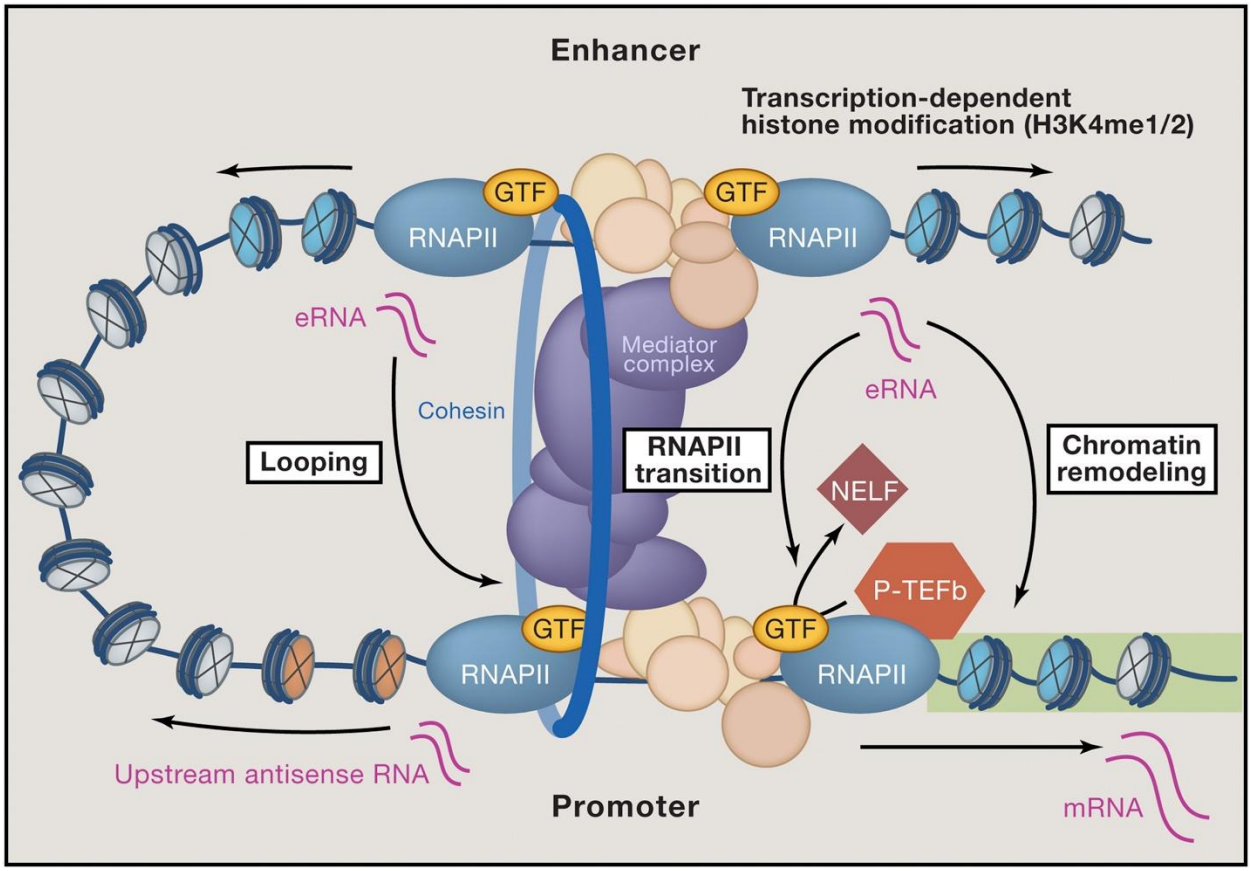

(Kim et al., 2015)

Figure 1-2

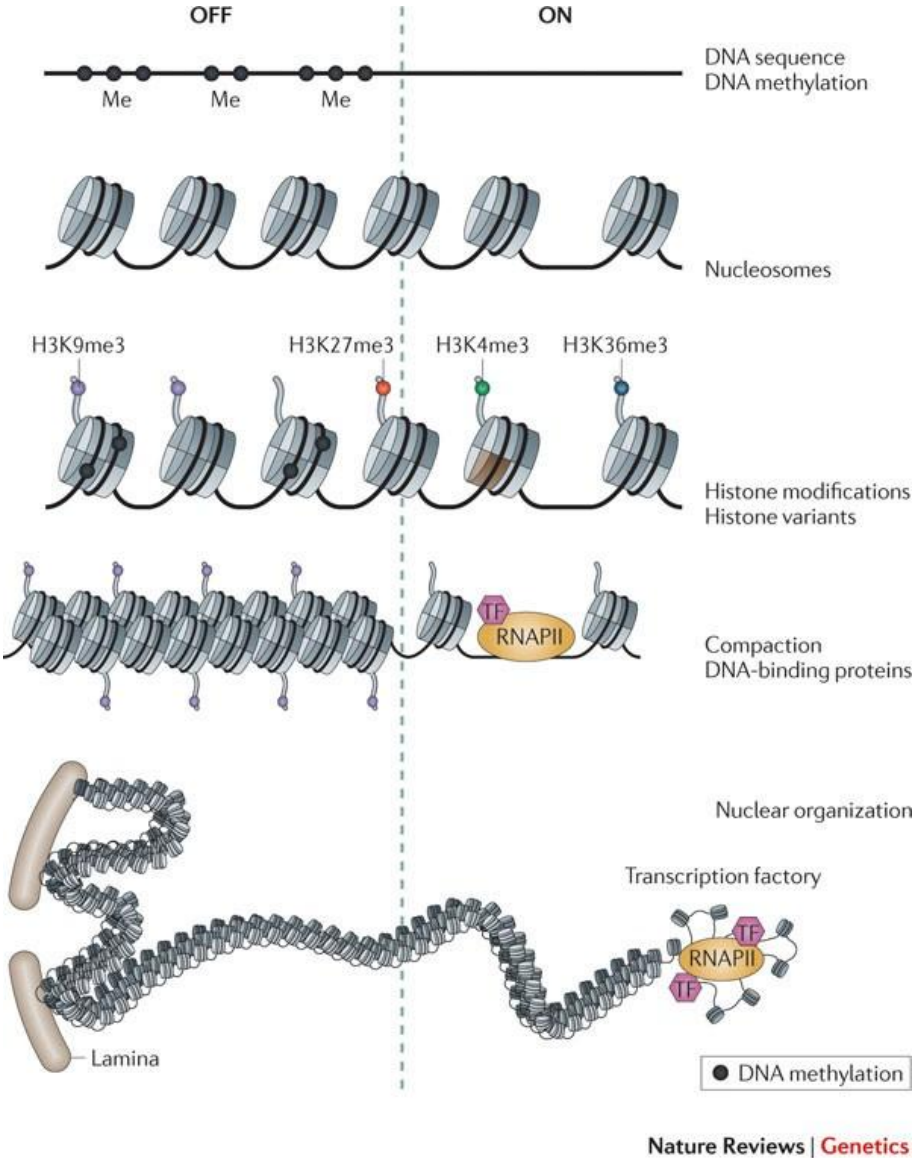

(Zhou et al., 2011)

Figure 1-3

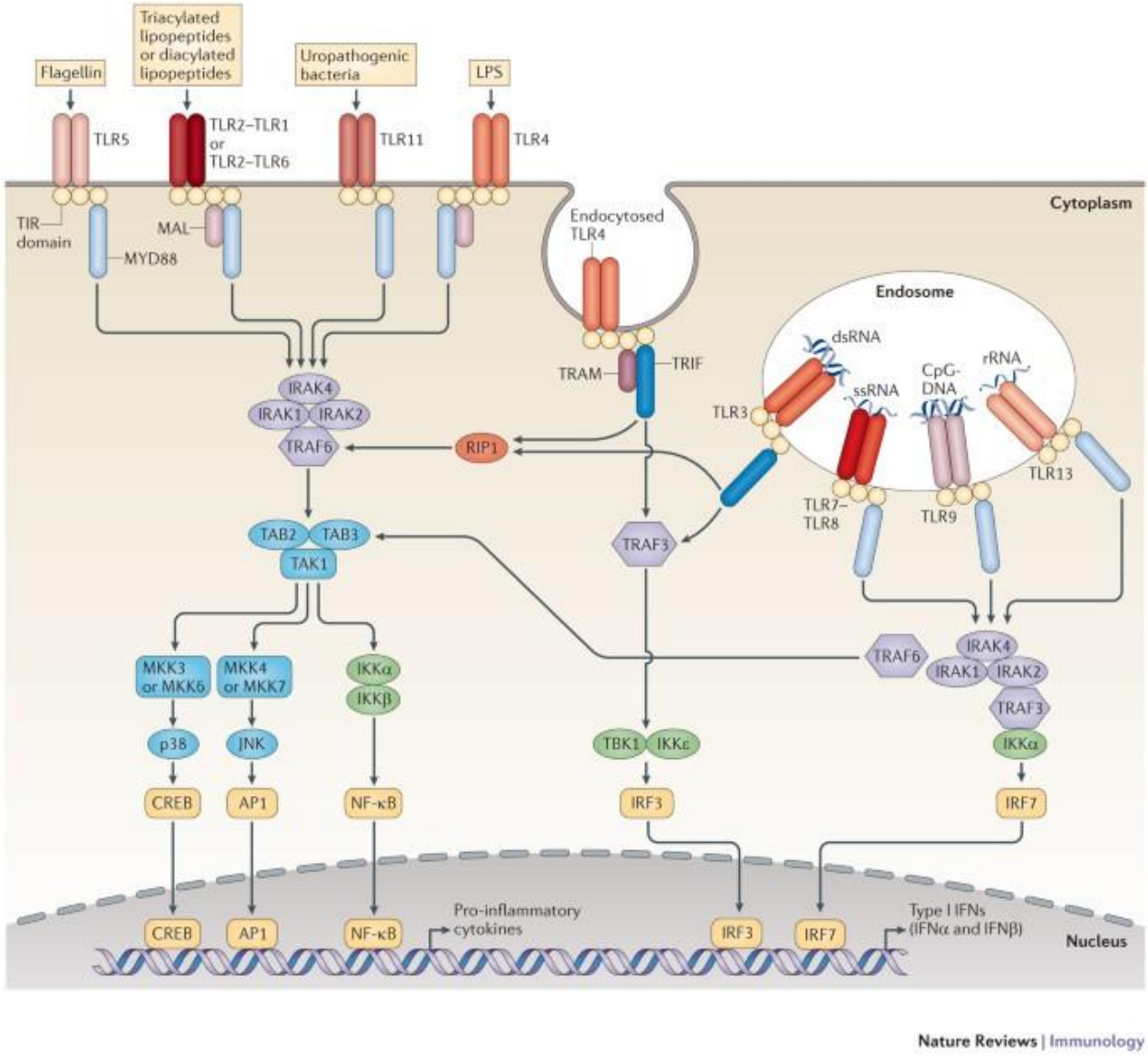

(O'Neill et al., 2013)

Figure 1-4

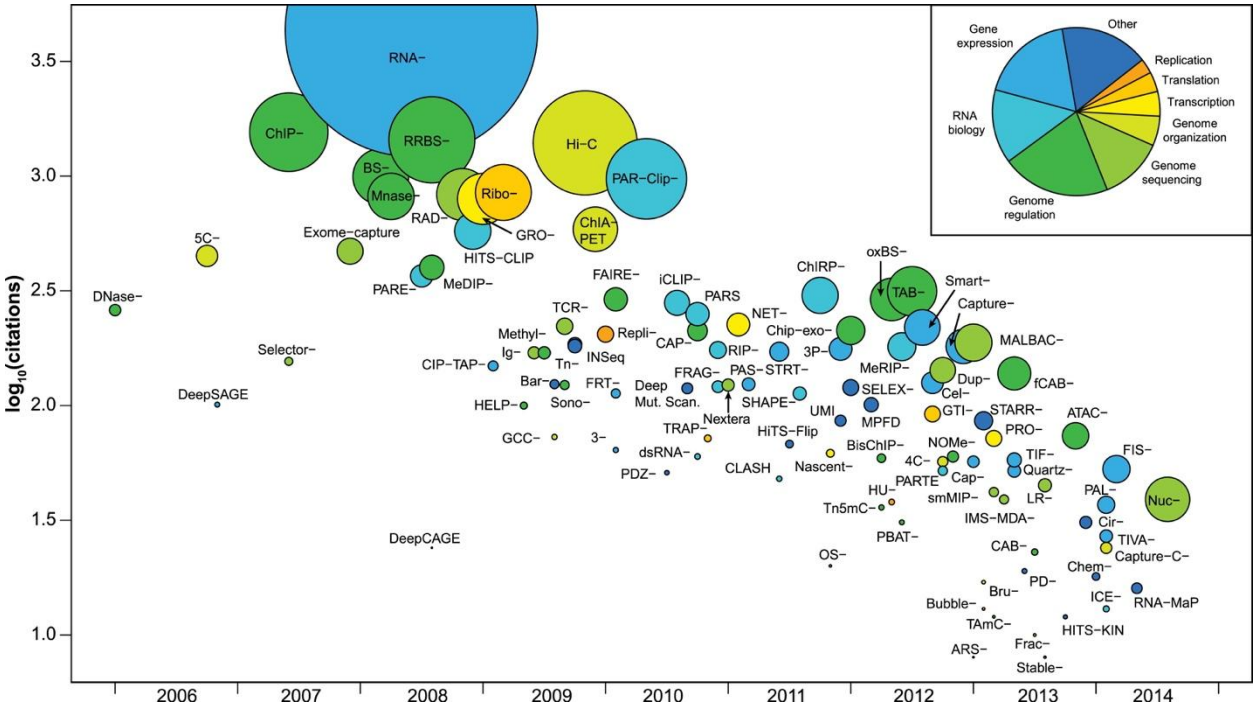

(Reuter et al., 2015)

Figure 1-5

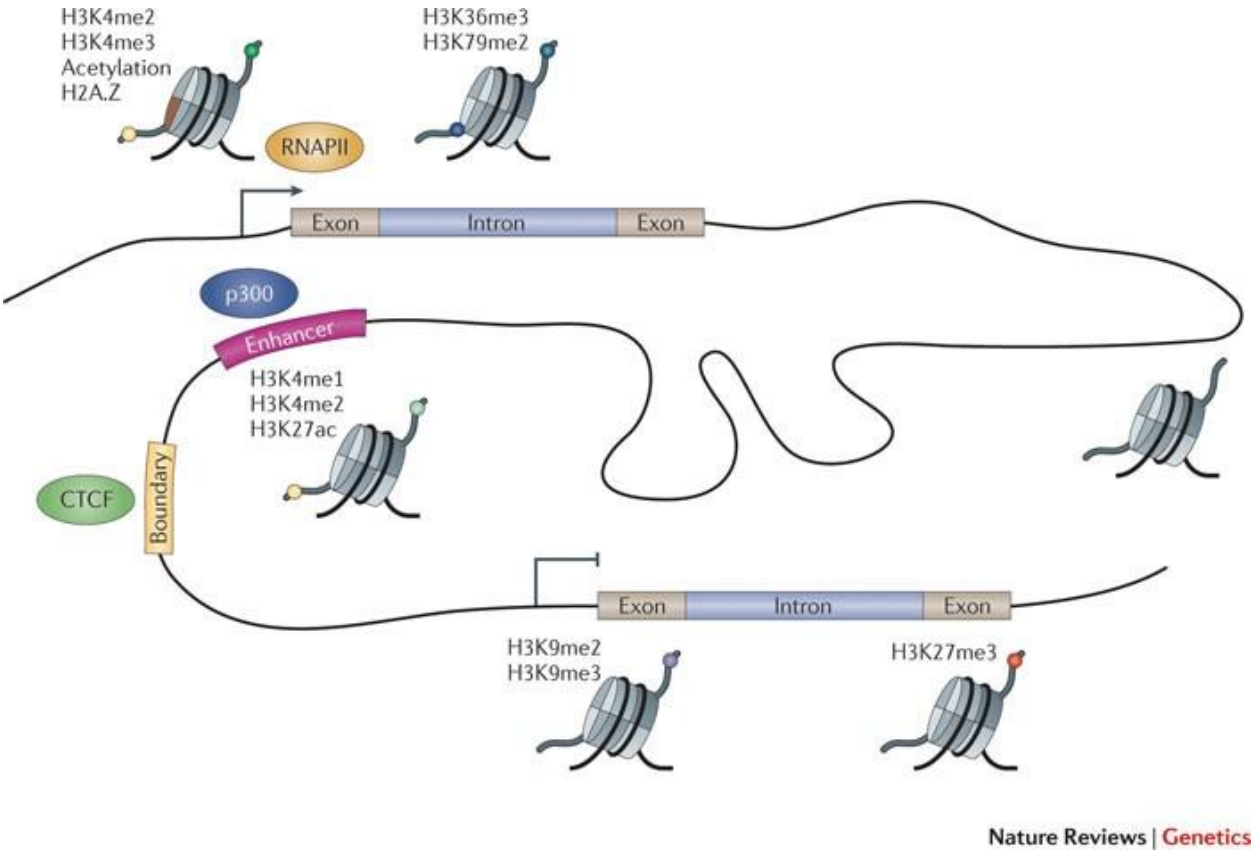

(Zhou et al., 2011)

Table 1-1

Table 1. Histone Modifications Associated with Transcription

Modifications	Position		Enzymes				Recognition Module(s)[a]	Functions in Transcription
			S. cerevisiae	*S. pombe*	*Drosophila*	Mammals		
Methylation	H3	K4	Set1	Set1	Trx, Ash1	MLL, ALL-1, Set9/7, ALR-1/2, ALR, Set1	PHD, Chromo, WD-40	Activation
		K9	n/a	Clr4	Su(var)3-9, Ash1	Suv39h, G9a, Eu-HMTase I, ESET, SETBD1	Chromo (HP1)	Repression, activation
		K27				E(Z)	Ezh2, G9a	Repression
		K36	Set2			HYPB, Smyd2, NSD1	Chromo(Eaf3), JMJD	Recruiting the Rpd3S to repress internal initiation
		K79	Dot1			Dot1L	Tudor	Activation
	H4	K20		Set9	PR-Set7, Ash1	PR-Set7, SET8	Tudor	Silencing
Arg Methylation	H3	R2				CARM1		Activation
		R17				CARM1		Activation
		R26				CARM1		Activation
	H4	R3				PRMT1	(p300)	Activation
Phosphorylation	H3	S10	Snf1				(Gcn5)	Activation
Ubiquitination	H2B	K120/123	Rad6, Bre1	Rad6		UbcH6, RNF20/40	(COMPASS)	Activation
	H2A	K119				hPRC1L		Repression
Acetylation	H3	K56					(Swi/Snf)	Activation
	H4	K16	Sas2, NuA4		dMOF	hMOF	Bromodomain	Activation
	Htz1	K14	NuA4, SAGA					Activation

[a] The proteins that are indicated within the parentheses are shown to recognize the corresponding modifications but specific domains have yet to be determined.

(Li et al., 2007)

CHAPTER 2

Highly Selective Roles of Key Transcription Factors in Genome-Wide Toll-Like Receptor-Induced Nucleosome Remodeling in Activated Macrophages

Summary

Macrophages play a critical role in bridging the innate and adaptive immune systems, which requires timely and precise transcription control when responding to danger signals. Gene expression networks in macrophages have been profiled extensively in recent decades with the advancement of high throughput sequencing technologies. However, unveiling critical mechanistic insights into the control of diverse transcriptional networks has proven to be challenging. Recent evidence has suggested that chromatin accessibility can provide an integral means of transcription regulation. We have applied the relatively recent Assay for Transposase-Accessible Chromatin using Sequencing (ATAC-seq) method to assess chromatin accessibility with optimal resolution in mouse bone marrow derived macrophages (BMDMs) responding to a pro-inflammatory stimulus, lipid A. By applying systematic quantitative analysis, we found that NF-kB motifs are the only identifiable transcription factor binding motifs that are strongly and preferentially enriched at genomic regions showing the strongest evidence of inducible nucleosome remodeling during the primary response to lipid A. This observation was further supported by RelA ChIP-seq binding enrichment. Our finding suggests that NF-κB may be a key inducer of nucleosome remodeling, either alone or in combination with diverse collaborating transcription factors. Furthermore, we utilized IRF3 as the model factor and showed that only Ccl5 promoter and a very small subset of putative enhancers are significantly IRF3-dependent for their primary nucleosome remodeling in response to lipid A. The highly selective role of IRF3 in nucleosome remodeling reveals that the large enhancer reservoir can provide diversity and specificity in regulating the complicated inflammatory network.

Introduction

The rapid activation of transcriptional cascades is required for innate immune cells, such as macrophages, to fight off invading pathogens. Upon activation of a specific pattern recognition receptor (PRRs) by a pathogen-associated molecular pattern (PAMP) or danger-associated molecular pattern (DAMP), the timely and precise transcriptional response is achieved by a diverse set of signaling pathways and transcription factors (TFs), tailored to activate immune response genes that can directly combat the environmental threats (Mogensen, 2009; O'Neill et al., 2013). While transcriptional reprogramming to a broad range of stimuli (bacteria, virus, radiation, hypoxia, etc.) displays common elements, a high degree of selectivity of specific subsets of genes can be seen to each individual stimulus. This phenomenon is particularly interesting because most of the environmental stimuli activate the same similar signaling pathways and TFs that do not display a great degree of selectivity.

Macrophages play a critical role in bridging the innate and adaptive immune systems. Gene expression networks in macrophages have been profiled extensively in recent decades with the advancement of high-throughput technologies. However, unveiling critical mechanistic insights into the control of diverse transcriptional networks has proven to be challenging. Recent evidence has suggested that the accessibility of chromatin can provide an integral means of transcription regulation (Li et al., 2007; Smale et al., 2014; Zhou et al., 2011).

Chromatin structure can be profiled indirectly by monitoring epigenetic marks using methods such as histone modification chromatin immunoprecipitation (ChIP-seq) (Johnson et al., 2007) and bisulfite sequencing (BS-seq)(Cokus et al., 2008) or directly

by monitoring nucleosome positioning using methods such as micrococcal nuclease digestion (MNase-seq) (Schones et al., 2008), formaldehyde-assisted isolation of regulatory elements (FAIRE-seq) (Giresi et al., 2007), and DNase I hypersensitive sites sequencing (DNase-seq) (Crawford et al., 2006). Histone marks have been widely used to identify and characterize regulatory elements, such as enhancers. However, using histone modifications as an approach possesses limitations, including an incomplete understanding of the relationship between these modifications and chromatin accessibility (Kim and Shiekhattar, 2015). We have applied the relatively recent Assay for Transposase-Accessible Chromatin using Sequencing (ATAC-seq) (Buenrostro et al., 2013; Buenrostro et al., 2015) method to assess chromatin accessibility directly with optimal resolution in the mouse bone marrow derived macrophages (BMDMs) during the course of lipid A stimulation. This advanced method enables us to characterize the chromatin state of regulatory regions quantitatively for systematic analysis.

The main objective of this study is to understand the mechanistic principles of inflammatory gene regulation from the perspective of nucleosome remodeling. Nucleosome remodeling is carried out by a group of ATP-dependent remodeler complexes including four subfamilies: ISWI, CHD, SWI/SNF, and ISO8 (Becker and Workman, 2013; Clapier et al., 2017; Hargreaves and Crabtree, 2011). SWI/SNF is the primary remodeler complex that renders the chromatin more accessible involving sliding nucleosomes along DNA, evicting nucleosome components, or ejecting full nucleosomes (Narlikar et al., 2013). Access remodelers can expose binding sites for TFs at gene promoters or enhancers. SWI/SNF functions as a global transcription regulator and plays a crucial role in the regulation of eukaryotic gene expression (Reisman et al., 2009).

Multiple attempts have been made to generate mouse models containing the loss of function mutation of core subunit in SWI/SNF complex, such as *Snf5* or *Brg1*, and shown to be embryonic lethal and cancer prone (Bultman et al., 2000; Guidi et al., 2001; Klochendler-Yeivin et al., 2000; Roberts et al., 2000). The technical challenges impede us from using SWI/SNF as a model to obtain mechanistic insights into nucleosome remodeling in immune gene induction.

Alternatively, we profiled genome-wide accessible sites in BMDMs treated with lipid A using ATAC-seq. The extent of accessibility increased after stimulation is quantified by the fold change of RPKM (Reads Per Kilobase Per Million Reads) at each site before and after stimulation. It is impractical to consider that induced accessibility is simply the result of nucleosome remodeling. Hence, applying the criteria to identify sites that underwent nucleosome remodeling with confidence is the most critical step in this study. The induction of chromatin accessibility in the activated BMDMs ranged from 1.4 to 68.3-fold. This continuum of fold accessibility likely indicates that some induced peaks occur in regions of pre-existing open chromatin that undergo small structural changes of the nucleosome. These small changes are not reflective of the nucleosome remodeling and instead may represent increased accessibility due to TFs binding or transcription machinery. Moreover, the small fold induction may be derived from nucleosome remodeling in a small population of the pooled cells. Therefore, it is challenging to determine the threshold of the induction fold range to better capture regions that undergo nucleosome remodeling in the simulated BMDMs. We found that half of the 2-fold induced regions were already accessible before stimulation. In contrast, more than 95% of the 5-fold induced regions were inaccessible at the baseline. We, therefore, focused our

analysis on the 5-fold induced regions which are more likely to reflect nucleosome remodeling events. The broader systematic motif analysis revealed that regions with inducible accessibility were preferentially enriched with NF-κB TF motifs. This surprising observation was further strengthened with the genome-wide RelA binding profile (ChIP-seq) and suggests the potential role of NF-κB in nucleosome remodeling.

In this study, we utilized the well-established lipid A-stimulated BMDMs, which were previously optimized to study inducible gene transcription. This tightly controlled and simplified system provided us a chance to understand complex regulatory networks. Toll-like receptor 4 (TLR4) is responsible for detecting Gram-negative bacteria through the non-nucleic acid ligand such as lipopolysaccharide. TLR4 activates two distinct signaling pathways: the MyD88-dependent and TRIF-dependent pathways (Kawai and Akira, 2006). The MyD88-dependent pathway results in the early-phase activation of NF-κB and MAP kinases. The TRIF-dependent pathway results in IRF3 activation, which, in macrophages, leads to the expression of IFN-β. The secreted IFN-β will bind to IFNAR through autocrine or paracrine pathways and activate the IFN signaling pathway, which triggers second wave IRF activation and IFN stimulated gene expression (O'Neill et al., 2013; Zhao et al., 2015). By treating BMDMs with cycloheximide (CHX), the synthesis of IFN-β is blocked and the compensation effects from the other IRF members, mainly IRF7, will be eliminated. Therefore, we can exclusively unveil the Ccl5 promoter and a small subset of enhancers whose nucleosome remodeling depends on IRF3 significantly during the primary response to TLR4 signaling.

Overall, we not only profiled a fundamental chromatin property in lipid A-stimulated BMDMs globally but also applied a systematic and stepwise focused approach by using

IRF3 and NF-κB as model factors to understand the role of nucleosome remodeling in immune gene regulation. Our results provided critical insights into the innate immune gene regulation from the perspective of nucleosome remodeling.

Result

Profiling Global Chromatin Accessibility Change During Stimulation

To understand how global chromatin accessibility changes in macrophages responding to pro-inflammatory stimuli, we first performed ATAC-seq in BMDMs stimulated with lipid A for 0, 30, 60, and 120 minutes. With at least two biological replicates per time point, we used MACS2 to identify regions enriched with sequencing reads (FDR < 0.01) (Zhang et al., 2008). In total, there were 101,448 accessible sites before or during the time course of stimulation, which were designated “peak” in the following context (Figure 2-1A). The vast majority of peaks were constitutive within the 2-fold repression (i.e. 0.5-fold induction) to 2-fold induction range (72.8%), and only a very small percentage were repressed more than 2-fold (2.7%). Since lipid A is a pro-inflammatory stimulus, 19.4% of the peaks were induced 2 to 5-fold and 5.1% induced more than 5-fold. The majority of these accessible sites resided in intronic and intergenic regions, which accounted for 44.5% and 39.4%, respectively, with 10.1% in the promoter region (Figure 2-1B). Examples of the repressed, constitutive, and induced peaks are shown in Figure 2-1C. By visually scrutinizing the induced peaks, several actively transcribed genes were found to have intense and continuous signals over the gene body, which are more likely the signals derived from active transcription (Figure 2-1C, *Tnf*). We therefore carefully performed the downstream analysis on the peaks located at the promoter or intergenic regions to avoid induced signals associated with active transcription.

To gain insight of chromatin accessibility changes in the genome, we categorized the peaks as repressed, constitutive, and induced based on the maximum accessibility induction fold range (<0.5, 0.5 to 2, and >2-fold). In Figure 2-1D, though the constitutive

peaks accounted for the largest portion among all genomic locations, the promoter region was less associated with dynamic peaks compared to the intronic and intergenic regions (6.4% vs 16.7 and 17.0%). We further ranked the peaks based on their maximum accessibility induction fold and generated 40 bins with an equal number of peaks (2,536 Peaks/ Bin). The promoter peaks were enriched in constitutive Bins 7 to 16, with a maximum of 24.5% in Bin 11. In contrast, the most repressed (Bins 1 and 2) and induced bins (Bins 39 and 40) comprised dominantly intronic and intergenic peaks (Figure 2-1E). This observation reflects the fact that promoters are more accessible and poised at the basal state to ensure timely response when activated. In contrast, the regulatory elements in the intergenic and intronic regions are more dynamic, and more likely to undergo chromatin remodeling upon stimulation.

The goal of this study is to understand how nucleosome remodeling contributes to the inducible gene transcription regulation. Therefore, we would like to focus our attention on the regions that undergo inducible nucleosome remodeling. However, it is challenging to determine the cutoff of ATAC accessibility induction fold which can reflect the nucleosome remodeling events. We divided all peaks equally into 40 bins based on the accessibility induction fold from the most repressed (Bin 1) to the most induced (Bin 40), the percentage of peaks without basal ATAC signal increased as the fold induction increased (Figure 2-1F). In Bin 30, around 2-fold induction range, half of the peaks had a basal ATAC signal and half did not. As the fold induction range increased, especially in the last two bins (Bins 39 and 40), greater than 5-fold induction range, 95% of the peaks showed no basal ATAC signal. The ATAC signal represents the chromatin accessibility; thus, sites with no ATAC signal are considered as inaccessible or “closed” chromatin

state. Based on this observation, almost all the peaks induced greater than 5-fold were "closed" before stimulation and became "open" after stimulation. Therefore, we considered 5-fold accessibility induction as the cutoff for the sites underwent nucleosome remodeling.

The peaks with weak induction (2 to 5-fold) also bear greater uncertainty of true nucleosome remodeling. The small increase in ATAC signal after stimulation may be due to increased TF binding, slight remodeling, or heterogeneity of the entire cell population evening out the strong induction in a small subset of cells. Instead, the stringent fold induction cutoff, 5-fold, can give us the greatest confidence in capturing the regions (peaks) that underwent nucleosome remodeling. For better phrasing, the peaks induced greater than 5-fold were called inducible peaks in the following context. We show an example of the *Ccl9* promoter peaks, which were induced 2.2-fold after stimulation but accessible at the basal state (Figure 2-1G). The increased ATAC signal could be the result of TF binding, increased transcription, a minor change in chromatin structure, or nucleosome remodeling in a small percentage of cells within the population. In contrast, the intergenic peak upstream of *Ccl9* promoter showed 14-fold induction without basal ATAC signal, which is more likely to represent a robust, inducible nucleosome remodeling event, accompanied by nucleosome eviction, sliding, or the transition of a nucleosome from a closed to an open conformational state in most or all cells within the population.

Global Motif Enrichment Across the Accessibility Induction Range

To identify TFs associated with accessible regions across the spectrum of inducibility, peaks were grouped into 40 bins from the most repressed to the most

induced, with 2,356 peaks per bin. We then performed motif analysis by using HOMER tools (Heinz et al., 2010). The enrichment of each motif across the inducibility ranges was shown in Figure 2-2A in the heatmap. Each column represented one bin from the most repressed to the most induced and the fold induction range was marked on the top. Each row represented one TF motif and was shown as the grouped motif family. The enrichment was colored according to the -log(p-value). There were 364 non-redundant TF motif matrices from the Homer motif database and were categorized into major motif families. The bZIP and IRF motifs were enriched in the bins across the weakly induced to the strongly induced fold range, while the NF-κB motifs were strongly and preferentially enriched in the last four bins with the greatest induction fold range. The POU/Homeobox family was similar to NF-κB but with much weaker enrichment. In contrast, the ETS family was enriched in the bins with repressed accessibility and the CTCF motif, which belongs to the Zf family, was enriched in the bins with constitutive accessibility.

There were four motif families showing enrichment in the induced bins with different strengths and distribution (Figure 2-3A), which are bZIP, IRF, NF-κB, and POU/Homeobox. One representative TF motif from each family was shown in Figure 2-2B as the line graphs of p-value significance and percentage of peaks with the target motif within each bin from the most repressed to the most induced. Though all four motifs had the enrichment trend toward the more induced bins; it is clear that the NF-κB motif showed the strongest and preferential enrichment in the last two bins, which are the inducible peaks (> 5-fold).

TFs can participate in primary and/or secondary responses to stimuli. We next separated primary and secondary nucleosome remodeling by performing ATAC-seq in

BMDMs stimulated with lipid A in the presence of cycloheximide (CHX), which can block new protein synthesis and the secondary response to stimulation, including the synthesis of and response to IFN-β. The CHX resistance was calculated as the percent accessibility in CHX pre-treated and lipid A stimulated cells compared to the lipid A treated cells. The primary response was defined as a maximum percent accessibility during the stimulation course greater than 33%. We grouped the inducible peaks equally into 8 bins based on the CHX percent accessibility from the most CHX sensitive (Bin 1) to the most resistant (Bin 8) and performed motif analysis. The result was presented as the heatmap of -log(p-value) (Figure 2-2C). NF-κB motifs were preferentially enriched in the primary response bins while the IRF, as well as POU/Homeobox family motifs, were in the secondary bins. The AP-1 like motifs in the bZIP family showed equal enrichment across the spectrum of CHX resistance.

NF-κB motifs are the only identifiable TF binding motifs that are strongly and preferentially enriched at inducible ATAC sites showing the strongest evidence of inducible nucleosome remodeling during the primary response to lipid A. This result suggests that NF-κB may be a key inducer of nucleosome remodeling, either alone or in combination with diverse collaborating TFs. This observation is surprising since in vitro studies suggested that NF-κB cannot bind nucleosomal DNA by itself (Chen et al., 1998; Saccani et al., 2001), leading to a previous hypothesis that NF-κB does not promote nucleosome remodeling.

To gain better an understanding of the collaboration between TFs, the inducible peaks were grouped as primary and secondary. The motif analysis was performed on the peaks with and without the representative inducing factor motif from each of the four

inducing motif families, which were Atf3 (AP-1 like) motif in bZIP family, all NF-κB motifs in NF-κB family (NFκB-p65; NFκB-p65-Rel; NFκB-p50,p52), IRF3 motif in IRF family and Oct4 in POU/Homeobox family. The results show that TF motifs are enriched at inducible ATAC-seq peaks in a variety of different combinations, with no clear preferences (Figure 2-3B). For example, bZIP, IRF, and POU motifs are enriched at ATAC-seq peaks that both lack and contain NF-kB motifs (Figure 2-3B, data columns 5 and 6, respectively). This observation is consistent with the well-established view that different combinations of TFs regulate distinct control regions, and further suggests that different combinations of TFs may promote inducible nucleosome remodeling.

NF-κB Motif and Binding Enrichment over the Strongly Induced ATAC Sites

Among the four motif families, the NF-κB family revealed unique preferential enrichment over the inducible ATAC peaks. To validate this surprising finding, we integrated RelA ChIP-seq data to correlate the genome-wide RelA binding sites and ATAC sites. We grouped the ATAC peaks into 40 bins based on their fold induction and the percentage of ATAC peaks with RelA binding increased considerably in the last few bins, which contained the most strongly induced ATAC peaks (2,356 Peaks/ Bin, 14%) (Figure 2-4A, navy dots, and line). Moreover, when bins were created on the basis of induction p-value as opposed to fold-induction, an event greater enrichment of RelA binding (34%) was observed in the bin with the smallest p-value. (Figure 2-4A, blue dots, and line). These results confirm the preferential enrichment of both NF-κB motifs and binding over the inducible ATAC peaks.

We then separated the inducible peaks (>5-fold) into primary and secondary response groups by a maximum CHX percent accessibility of 33%. The primary and secondary response peaks were subsequently divided into 10 bins based on the statistical significance (-log(p-value)) of accessibility induction (Figure 2-4B). RelA binding showed increased enrichment as the significance of accessibility induction increased both in the primary and secondary peaks. However, the primary response peaks had much higher enrichment over the most consistently induced primary response peaks. Among the 329 most consistently and strongly induced primary response peaks, 205 (62.5%) had defined RelA binding. Moreover, when carefully scrutinizing the 124 peaks without defined RelA binding, 69 had indeed transient RelA binding, 10 had RelA binding but not called by the program, 23 had reproducible but weak RelA binding (peak score < 19), 19 were transcriptional noise, and only 3 had no RelA binding signal. Thus, RelA may bind to all or almost all the genomic regions that exhibit primary nucleosome remodeling in response to lipid A (Figure 2-4C). These results suggest that NF-κB may play an essential role in inducible nucleosome remodeling during the primary response to lipid A stimulation.

Functional Roles of NF-κB in Nucleosome Remodeling

To functionally evaluate the role of NF-κB in nucleosome remodeling, we performed ATAC-seq on three independent NF-κB depletion models: IKK inhibitor (Bay11) treated BMDMs, NF-κB motif editing BMDM cell line, and $RelA^{-/-}C\text{-}Rel^{-/-}$ BMDM cell line. Bay11 is an NF-κB inhibitor that inhibits IKK related I-κB phosphorylation and suppresses NF-κB activation upon stimulation (as well as the activation of other IKK-

induced TFs). We observed that Bay11 potently suppressed nucleosome remodeling at almost all the inducible sites (data not shown). It is known that Bay11 is not a selective inhibitor for IKK and exhibit a broad spectrum of inhibitory activity against inflammation, including inhibition of cytokines, induction of heme oxygenase-1, suppression of ICAM-1 expression, reduction of ATPase activity of NLRP3 inflammasome, and increase neutrophil apoptosis (Lee et al., 2012). Therefore, it is not surprising to see the non-selective global suppression by Bay11.

To obtain a cleaner system, we used CRISPR-Cas9 ribonucleoprotein (cRNP) genomic editing to modify the NF-κB motifs and prevent NF-κB binding without disrupting other factor bindings to the candidate peak. Peak45836 contains two NF-κB motif clusters at the peak center and shows early RelA binding but late accessibility induction (Figure2-5A, top, and Figure 2-5B). The edited peak completely lost its accessibility in response to the stimulus (Figure 2-5B). The raw read counts containing different sequence segments (30 bp) were listed (Figure 2-5A) to avoid alignment bias. Because of the redundancy between NF-κB members as well as the critical roles of NF-κB in cell survival, we attempted to eliminate most of the NF-κB activity by knocking out the two major members RelA and C-Rel in the BMDM cell line. The ATAC-seq performed on $RelA^{-/-}C\text{-}Rel^{-/-}$ cell line also shows a remarkable decrease in chromatin accessibility in response to lipid A (Figure 2-5B). These functional experiments further support the hypothesis that NF-κB plays a critical role in promoting inducible nucleosome remodeling.

Nucleosome Remodeling at Promoters

Our previous study of a limited set of strongly induced genes showed that strong nucleosome remodeling in promoters of potently induced genes is rare (Tong et al., 2016). Consistent with those results, our current experiments showed that there are only 40 promoter ATAC peaks with inducible chromatin accessibility (> 5-fold). To compare ATAC changes with transcriptional changes, we utilized previously published chromatin-associated RNA-seq (caRNA-seq) data. Only thirteen promoters (32.5%) are associated with potently induced genes, whereas the majority are assigned to genes that are weakly induced or expressed (67.5%). The heatmap of normalized expression suggested that inducible promoters correlate with inducible transcription (Figure 2-6A). To further evaluate the magnitude of induction among the two datasets, we compared the promoter ATAC fold accessibility to caRNA-seq fold induction for all primary response genes (PRGs) and secondary response genes (SRGs). Both PRGs and SRGs with strong promoter ATAC fold induction exhibited high levels of transcriptional induction (Figure 2-6B, left). When comparing ATAC induction to promoter CpG content, we observed a very similar trend with low CpG density correlating with strong ATAC induction (Figure 2-6B, right). *Ccl5*, as an example, demonstrates the highest transcriptional induction, largest ATAC fold change, and low CpG content. This trend can be readily seen among SRGs as well, but with a less strict association with caRNA-seq fold induction.

To understand the regulation of these promoter accessibility changes, we performed ATAC-seq in cells that were pretreated with CHX before stimulation. None of the primary response promoters were inhibited during CHX treatment, while 2 of the secondary response gene promoters had diminished accessibility (*Il12b* and *Ifi47*, <30%). The other 4 SRGs maintained induction of accessibility in the presence of CHX

suggesting that the secondary response component required for activation of these 4 SRGs might proceed after promoter accessibility has been established (Figure 2-6A).

Interestingly, IRF3 was previously reported to be exclusively required for the nucleosome remodeling and subsequent RelA association at the *Ccl5* promoter. To expand upon our previous finding and to address whether we can detect IRF3 dependent promoter induction across the additional 39 promoters, we performed ATAC-seq in WT and *Irf3*$^{-/-}$ BMDMs stimulated for 0, 30, 60, and 120 minutes with lipid A in the presence or absence of CHX. We used CHX treatment to limit the potential compensatory effects on transcription and/or remodeling by the other IRF family members that can be induced as part of the secondary response to type I interferon. By directly comparing the ATAC-seq maximum RPKM of CHX-pretreated WT and *Irf3*$^{-/-}$ BMDMs through the time course or at each time point of stimulation (Figure 2-6C and Figure 2-7A), both the *Ccl5* and *Rnase10* promoters (Figure 2-7B) showed decreased accessibility. However, the *Ccl5* promoter stood out to be the only promoter whose nucleosome remodeling is significantly IRF3-dependent (Figure 2-7D). Strong IRF3 binding (peak score > 90, red) of the *Ccl5* promoter was also observed in the IRF3 ChIP-seq (Figure 2-7E).

Nucleosome Remodeling at Putative Enhancers

It is challenging to identify the associated gene promoters with which enhancers interact. While intergenic regulatory elements tend to interact with the promoters of proximity, they can also associate with distant promoters through looping (Jiang and Peterlin, 2008; Miele and Dekker, 2008; Vakoc et al., 2005). To understand the characteristics of putative enhancers, we first analyzed the proximity of intergenic ATAC

peaks and genes. We calculated the percentage of intergenic ATAC peaks located within the distance range of every 10 kb to the transcription start site (TSS) of genes induced greater than 10-fold. There are four ATAC categories: repressed, constitutive, weakly induced (2 to 5-fold), and strongly induced (> 5-fold). In addition to a direct comparison between different ATAC groups, we also shuffled the ATAC peaks for 100 times randomly and averaged the percentage of peaks located within each 10 kb bin as the expected values. By comparing the observed to the expected existence of the ATAC peaks at each of the 10 kb distance range to the nearest 10-fold induced genes, the strongly and weakly induced ATAC peaks are more likely to exist in the first 10 bins which is a total of 100 kb range (Figure 2-8A, Figure 2-9A). Among the four ATAC peak categories, strongly induced ATAC peaks were greatly enriched in the 100 kb region of the nearest 10-fold induced genes and followed by weakly induced ATAC peaks. There was no enrichment of the constitutive and repressed peaks located within the 100 kb range of the nearest 10-fold induced genes.

We next performed a kinetic analysis on the strongly induced intergenic peaks (n=2,356). The intergenic peaks with inducible chromatin accessibility were classified into six clusters based on their induction kinetics (Figure 2-8B, left). The average RPKM at each time point of these 6 clusters is also shown as a line graph (Figure 2-8B, right). Consistent with the kinetic analysis, the clusters with early accessibility induction are enriched with primary response elements (orange portion) while the secondary response elements are enriched in the clusters with late induction kinetics (white portion).

The promoter analysis shows a striking selectivity of IRF3 in chromatin remodeling which regulates the expression of an individual gene, *Ccl5*. Visual inspection of the region

upstream of *Ccl5* TSS demonstrates several other inducible peaks showing diminished accessibility in the *Irf3*$^{-/-}$ BMDMs. These observations made us wonder whether specific factors such as IRF3 maintain a similar degree of selectivity in mediating rare remodeling events at a small number of intergenic elements.

The motif analysis of the strongly induced intergenic peaks grouped based on CHX resistance revealed that IRF motifs are enriched mainly in the secondary response bins while the NF-κB motifs in the primary response bins (Figure 2-8C). We next examine whether a subset of intergenic peaks require IRF3 for their primary nucleosome remodeling in response to lipid A. To address this question, we focused on the 1,494 primary response peaks and compared the maximum RPKM of CHX-pretreated WT and *Irf3*$^{-/-}$ BMDMs during the time course of lipid A stimulation (Figure 2-8D and Figure 2-9B). Surprisingly, among the 1,494 inducible primary response peaks, only 107 peaks displayed 67% dependence on IRF3 with the enrichment of strong binding (peak score ≥ 90, red) by IRF3 ChIP-seq (Figure 2-8D). Notably, one of the intergenic peaks upstream of the Ccl5 promoter showed the most significant IRF3 dependence for its primary nucleosome remodeling in response to lipid A (Figure 2-9C). Though the motif analysis showed no IRF family enrichment in the primary response peaks (Figure 2-8C), we asked whether the IRF motif would be enriched in peaks exhibiting functional IRF3-dependence. The IRF3 motif was indeed enriched in IRF3-dependent primary response peaks, consistent with the strong IRF3 binding to most of these peaks (Figure 2-8C, rightmost bin).

We next targeted these 107 peaks and 22 of them reached statistical significance (Figure 2-8E). Thirteen of the 22 significant IRF3-dependent peaks have strong IRF3

binding (56.5%), 5 have weak binding (26.1%) and 4 have no IRF3 binding (13%). Visual inspection reveals the 2 peaks without IRF3 binding are derived from readthrough effects of *Ccl4* and *Ccl5*. Among the 18 intergenic peaks with IRF3 binding (either strong or weak), 15 peaks have transcribed genes located within 100 kb region, 2 have genes located at 100 kb to 200 kb region, and 1 peak is isolated without any genes within the nearby 200 kb distance (peak57514, Figure 2-11). Among the 15 peaks with genes nearby, 4 peaks have strongly induced genes (> 10-fold, n=8) and 2 peaks have weakly induced genes (5 to 10-fold, n=2). The 8 strongly induced genes with 1 or 2 strongly induced IRF3-dependent primary response intergenic peaks nearby have different transcriptional characteristics profiled by caRNA-seq previously, including 5 PRGs and 3 SRGs. *Ccl5*, *Peli1*, and *2610024D14Rik* are IRF3-dependent PRGs, while *IL27* and *Heatr9* are SRGs with borderline IRF3 dependence. These results suggest that IRF3 is required for nucleosome remodeling at a remarkably small number of inducible enhancers associated with IRF3-dependent inducible genes, reminiscent of our prior finding that IRF3 is critical for remodeling at only one inducible promoter.

Functional Significance of Target Enhancer Elements

We have identified a small subset of selective IRF3-dependent primary response intergenic elements. The next step was to evaluate their functional relevance. We performed two experiments to determine (a) the direct physical contact between target enhancers and associated promoters and (b) the expression of the associated genes after cRNP mediated deletion of the entire accessible intergenic region (~400 bp). We first conducted the circularized chromosome conformation capture (4C) experiment (Simonis

et al., 2006) and capture Hi-C (high throughput conformation capture) experiment (Hughes et al., 2014) to detect the direct physical contacts between target enhancers and their interacting elements. In the 4C experiment, we used two candidate intergenic peaks (peak68866 and peak57514) as the viewpoints (baits) and designed the primers to capture genome-wide interaction to the viewpoints. Peak68866 is the IRF3-dependent primary response intergenic peak located 10 kb upstream of the *Ccl5* promoter and peak57514 is the isolated peak without any gene in the nearby 200 kb region. Peak68866 showed increased interaction to the *Ccl5* promoter after lipid A stimulation (Figure 2-10A). Peak57514 interacted with Jarid2, the nearest gene but 200 kb away, which is also an IRF3 dependent gene (Figure 2-11).

We additionally performed the promoter capture HiC (CHi-C) experiment to capture the interactions with the promoters. The biotinylated RNA probe set was designed to capture and enrich the proximal ligated DNA fragments containing the promoter elements. The CHi-C showed an increased interaction between peak68866 to not only *Ccl5* but also to *Ccl3* and *Ccl4* (Figure 2-10A).

Next, we used cRNP to delete the entire target enhancer, peak68866 (~ 400 bp), with two designed guide RNAs (gRNAs) (Figure 2-10B). We then checked the expression of genes associated with the target enhancer before and/or after lipid-A stimulation by qPCR. The 4C and CHi-C results show that *Ccl5*, *Ccl3*, and *Ccl4* promoters are associated with peak68866. We also remove the *Ccl5* promoter as a positive control (PC) ensuring the efficiency of cRNP deletion. We selected at least three CRISPR clones for each deletion (Target and PC). The PC clones showed that *Ccl5* transcription was completely blocked 2 hours after lipid-A treatment (Figure 2-10C). However, there was

only a slight decrease of *Ccl5* expression in the target deletion clones compared to the WT clones at 2 and 6 hours of treatment (Figure 2-10C). There was no difference either in the *Ccl3*, or *Ccl4* transcript level, kinetics or to different stimuli such as TNFβ or TNFγ (data not shown). More experiments are needed to elucidate the complex and redundant roles of enhancers.

Discussion

Chromatin structure plays a crucial role in gene regulation and transcription control. With the advancement of high throughput sequencing technologies, we are able to characterize genome-wide chromatin structure indirectly by epigenetic marks such as histone ChIP-seq, BS-seq or directly by nucleosome positioning, such as MNase-seq, FAIRE-seq, and DNase-seq. Recently, histone marks have been widely used to identify and characterize regulatory elements genome-widely, such as enhancers. However, using histone modifications as an approach to identify regulatory elements possesses limitations, including considerable false positive and false negative marks with low resolution (Kim and Shiekhattar, 2015; Ostuni et al., 2013). In this study, we used ATAC-seq to profile the chromatin state directly and also identify the active regulatory regions during the time course of stimulation with better confidence and higher resolution. In brief, ATAC-seq uses hyperactive Tn5 transposase to tag accessible chromatin regions and the sequencing library can be generated with one simple PCR step. This advanced method enables us to characterize the chromatin state of regulatory regions quantitatively for systematic analysis.

The core of this study is to understand gene regulation from the aspect of nucleosome remodeling. It is challenging to define nucleosome remodeling based on the change of ATAC-seq signals. We calculated the ATAC RPKM induction fold across the treatment course and correlated it with the presence of basal ATAC signals (called peaks). We found that 95% of the genomic regions with induction fold greater than 5-fold have no basal ATAC signals indicating inaccessible chromatin structure before stimulation and become accessible afterward. However, 50% of the regions with 2-fold

induction have basal ATAC signals and are accessible before stimulation but become more accessible after stimulation. The moderate increase of chromatin accessibility may be due to increased transcription factors binding, active transcription, nucleosome sliding, or nucleosome remodeling in a small population of cells. The characteristics in the regions with weak to moderate accessibility fold induction increase the uncertainty and complexity in unveiling the regulating principles. Therefore, we focused our attention on regions with strong accessibility fold induction of greater than 5-fold. This strategy increases our probability of capturing true nucleosome remodeling and provides a chance to gain critical mechanistic insights.

In the global motif analysis, we surprisingly observed that NF-κB motifs are the only identifiable transcription factor binding motifs that are strongly and preferentially enriched at the regions that show the strongest evidence of inducible nucleosome remodeling during the primary response to lipid A. By applying stepwise dissection, we have found that almost all of the significantly induced ATAC peaks undergoing primary nucleosome remodeling were bound by RelA. Interestingly, while inspecting the representative regions, we noticed the regions underwent nucleosome remodeling at the later time point after RelA binding occurred. The loss of accessibility in response to lipid A stimulation in NF-κB motif edited clones and *RelA*$^{-/-}$*C-Rel*$^{-/-}$ clones provide functional evidence of NF-κB in nucleosome remodeling. Others have proposed a role for NF-κB in binding to nucleosomal DNA (Angelov et al., 2004; Lone et al., 2013), but structural studies and other in-vitro experiments have demonstrated a low affinity of NF-κB to nucleosomal DNA (Chen et al., 1998; Saccani et al., 2001), leading to a previous hypothesis that NF-κB does not promote nucleosome remodeling. Our observations

suggest that NF-κB may be a key inducer of nucleosome remodeling, either alone or in combination with diverse collaborating transcription factors.

Our recent gene-centric analysis revealed that even a small subset of five genes required both NF-κB and IRF3 for their activation but the mechanism by which these factors collaborate can be entirely gene-specific. Based on these findings, we aim to understand the mechanistic principles of inflammatory gene regulation from the aspect of nucleosome remodeling using IRF3 as the model factor. We performed a systematic approach to examine the global nucleosome remodeling events over the promoters and intergenic regions (putative enhancers). Consistent with the gene-centric analysis, there are only 40 promoters undergoing nucleosome remodeling after lipid A stimulation; however, the Ccl5 promoter appears to be the only one whose nucleosome remodeling significantly depends on IRF3. The observation of promoters made us wonder among many intergenic regions showing different degrees of IRF3 dependence for their primary nucleosome remodeling, how many of them are significantly IRF3 dependent? Surprisingly, only a small number of 22 intergenic regions showed significant IRF3 dependence.

The observation of imbalanced numbers between genes and enhancers has been discussed extensively. Scientists have tried to better characterize enhancers with different histone marks and DNA binding factors. In our system, even when responding to one stimulus, lipid A, there are 41,003 accessible intergenic regions found during stimulation. Though there are only 2,358 sites that underwent nucleosome remodeling, it is still around ten times more than the 226 strongly induced genes. There are several explanations for this phenomenon: 1) they are functionally redundant to ensure crucial

transcription (Barolo, 2012; Frankel et al., 2010; Osterwalder et al., 2018), 2) multiple enhancers work in concert to modulate the same gene target, 3) some regulatory regions are the anchors in maintaining the boundary of a cluster of genes such as insulating neighborhoods (Hnisz et al., 2016; Ji et al., 2016), 4) some may be non-functional. Our enhancer analysis using IRF3 as the model factor reveals that despite the large enhancer reservoir, there is only a small subset of enhancers that are significantly dependent on IRF3 for their primary nucleosome remodeling in response to lipid A. This result suggests that the large enhancer reservoir can provide variety and selectivity in regulating the complex inflammatory network.

Based on the mechanistic insights gained from this analysis, we aim to continue exploring the regulatory roles of NF-κB in nucleosome remodeling, and the collaboration between major inducing factors by applying quantitative systematic approaches. To evaluate functional relevance, extensive cRNP genome editing and the creation of deletion clones are the near future tasks. Additionally, in-depth analysis of the recently generated capture Hi-C data in combination with the ATAC-seq, chromatin RNA-seq, and a wide variety of DNA binding factors, such as CTCF, Cohesin, and p300, will provide regulatory insights of a higher structural level.

Experimental Procedures

Cell Culture

C57BL/6 was purchased from Jackson Laboratory (Bar Harbor, ME), and *Irf3*$^{-/-}$ mice were a gift from Genhong Cheng. Experiments were performed under the written approval of the UCLA Chancellor's Animal Research Committee (ARC) in accordance with all federal, state, and local guidelines. BMDMs were prepared from 8 to 10-week-old C57BL/6 and *Irf3*$^{-/-}$ male mice. BMDMs were cultured with the media containing CMG for macrophage differentiation. The cells were scraped and re-seeded on day 4 and activated with 100 ng/ml lipid A (Sigma, L6895) on day 6 for the indicated time course. When indicated, cells were preincubated with 10 ug/mL CHX (Sigma, 239765) for 15 minutes or with 10uM Bay11(Sigma, B5556) for one hour. J2 virus-immortalized macrophages were also from C57BL/6 mouse and named as B16#5 by former colleague Xin Liu. B16#5 cells were cultured in the same media for BMDMs and treated accordingly with the same dose of lipid A and CHX for downstream assays.

ATAC-seq

ATAC-seq libraries were prepared using the Nextera Tn5 Transposase kit (Illumina) as described (Buenrostro et al., 2015) with slight modifications. Libraries were single-end sequenced (50 bp) on Illumina Hiseq2000 or Hiseq3000. Reads were mapped to the mouse genome (NCBI37/mm9) using Bowtie2. Unwanted reads were removed from the subsequent analysis if they were duplicated, mapped to mitochondrial genome, or aligned to unmapped contiguous sequences. All samples include at least two biological replicates, and replicates were merged prior to peak calling with MACS2 (Zhang et al.,

2008). Overlapping peaks were merged together and used as annotation probes for quantifying reads by using SeqMonk (http://www.bioinformatics.babraham.ac.uk/projects/seqmonk/). The reads were quantified as RPKM by normalizing to the probe length and read depth for the downstream analysis.

Motif Analysis

The accessible sites identified by ATAC-seq were used for motif analysis using Homer tools (Heinz et al., 2010) with provided motif matrices (n=364).

CRISPR-Cas9 Ribonucleoprotein (cRNP) Genome Editing and Deletion

A. Guide RNA Design

Two guide RNAs were designed for each deletion or edit site by using CRISPOR online tool (Concordet and Haeussler, 2018). The gRNAs were ranked from highest to lowest specificity score (Hsu et al., 2013) and gRNAs satisfied our need with the highest specificity score were selected. The selected gRNAs were synthesized and purchased from SYNTHEGO.

Peak68866 (Intergenic peak 10 kb upstream of *Ccl5* TSS):

gRNA1-TCCTCACACTTAATAGCAGG gRNA2-CAGCTGAGGTGTCCCCGCTG

Peak68862 (*Ccl5* promoter):

gRNA1- ATGACAGGGTAGCCGTGTCA gRNA2-TCTCTGGCCAAATACAGTAG

Peak45837(NF-κB motif editing):

gRNA1- TCCCCATTGGGGAAACCCCT gRNA2- TGAGGGGATTCCCCTAAGCA

B. HDR Template Design and Preparation

The HDR template was designed as sense single-stranded DNA containing 300 nucleotides flanking the replaced sequence and purchased from IDT in the amount of 9 µg. The dry synthesized DNA oligo was dissolved in 4 µL resuspension buffer R provided with Neon™ Transfection System 10 µL kit (Thermo Fisher Scientific, Catalog #MPK1025) right before electroporation.

C. Assemble of cRNP complex

Cas9 2NLS nuclease (*S. Pyrogenes*) was purchased from SYNTHEGO as 20 uM stock and the dry synthetic gRNAs (sgRNAs) were prepared into 30 µM stock. We assembled cRNP complexes by mixing Cas9 10 pmol and sgRNAs 90 pmol in 3.5 µL of resuspension buffer R, then incubated the mixture for 10 minutes at room temperature. For NF-κB motif editing, Cas9 and sgRNAs were added in 3.5 µL of resuspension buffer R containing HDR templates.

D. Prepare Cells

B16#5 cells were subcultured one day before electroporation in an appropriate number to that they were about 60-70% confluence on the day of transfection. Before electroporation, the cells were scraped off from the 10 cm plate and counted to obtain 1.5 x 10^6 cells enough for 10 transfections. The cells were washed with 1x PBS and resuspended in 50 µL of resuspension buffer R.

E. Electroporation

To prepare for a cell-RPN solution, 5 µL of cell suspension was added into the 7 µL RNP mix (total 12 µL). Electroporation was performed using the Neon Transfection System at pulse code (10 ms x 4 pulses) using 10 µL Neon tips at 1,900V. Immediately the following

electroporation, cells were pipetted into a 6-well plate containing prewarmed culture media.

F. Single Cell Colony Expansion

Fresh cell culture media was added to replace the media containing dead cells 24 hours after electroporation. 48 hours after electroporation, cells were scraped off from the plate, counted, and seeded 2 cells/well in the 96-well plates. Wells containing single-cell colony were selected under a microscope and replaced with fresh media every four days until wells turned yellow. Cells were then detached from the wells with trypsin and collected for freezing storage and DNA extraction.

G. Screening and Sequencing

Enhancer and promoter deletion clones: DNA was extracted from the single-cell colonies and PCR amplified regions containing deleted sites followed by gel electrophoresis. Clones with successful deletion were selected based on the size of the amplified fragment and confirmed by Sanger sequencing.

NF-κB motif edited clones: The regions containing the edited sites were PCR amplified and successfully edited clones were confirmed by Sanger sequencing directly.

qRT-PCR

RNA was extracted using TRI-reagent (Molecular Research Center, TR118), and treated with DNase I (Qiagen, 79254), and purified using the RNeasy kit (Qiagen, 74106). 1ug of RNA was reverse-transcribed using random hexamers and primers targeting mRNA of *Ccl5*, *Ccl3*, and *Ccl4* designed to amplify products quantified by SYBR-green.

Ccl3: F- CCAGCCAGGTGTCATTTTCC R- AGGAGATGGAGCTATGCAGG

Ccl5: F- TGCCCACGTCAAGGAGTATT R- AGAGCAAGCAATGACAGGGA

Ccl4: F- TCTGCCCTCTCTCTCCTCTT R- ATGTACTCAGTGACCCAGGG

4C Assay

The 4C library was prepared as described (Krijger et al., 2020). In brief, we crosslinked the lipid-A treated BMDMs with 1% Formaldehyde for 10 minutes and quenched them with 2M Tris (0.125M final concentration) for 10 minutes at room temperature. Cells were lysed for 30 minutes in 1 mL cold lysis buffer (10 mM Tris-HCl pH 8.0, 10 mM NaCl, and 0.2% NP-40 supplemented with protease inhibitor). Nuclei were pelleted and resuspended in 500 µL of 1st restriction enzyme buffer with 0.1% SDS and incubated for 1 hour at 37^{o}C at 1200rpm. SDS was then quenched by adding Triton-X 100 (final concentration 0.8%) for another 1 hour. 400 units of 1st restriction enzyme (DpnII, NEB R0543M) was added to samples, incubated at 37 ^{o}C for 6 hours following by adding additional 400 units for overnight digestion. The 1st restriction enzyme was inactivated by incubating at 65^{o}C for 10 minutes and placed samples on iced immediately. Ligation buffer (66 mM Tris-HCl pH 7.5, 5 mM $MgCl_2$, 5 mM DTT, 1 mM ATP) was added to dilute samples to a total volume of 7 mL. 2,000 units of T4 DNA ligase was added to each sample and incubated at 16^{o}C overnight to achieve proximal ligation. Reverse crosslinking and RNA digestion were performed and followed by phenol/chloroform DNA extraction. Ligation efficiency was confirmed by running the samples before and after ligation on 1% agarose gel. The ligated DNA was digested overnight in a volume of 500 uL with 200 units of 2nd restriction enzyme (CviQI, NEB R0639L). The digested samples were diluted in the ligation buffer into a total volume of 7 mL. Proximal ligation was

performed by adding 4000 units of T4 DNA ligase and incubated overnight at 16°C. The 4C template DNA was extracted by phenol/chloroform and ethanol precipitation. The extracted DNA was further cleaned up using the QIAquick PCR Cleanup kit (QIAGEN, 28104).

To generate the library for subsequent sequencing, reading and non-reading primers were designed for each viewpoint. Choice-Taq™ DNA Polymerase (Denville, CB4050-2) was used to PCR amplify 4C DNA templates containing the viewpoints in four of 25 μL reactions. The PCR products were purified with the illustra™ GFX PCR DNA and Gel Band Purification kit (Sigma, GE28-9034-66) to remove primer dimers. Libraries were sequenced for 50 bp single-end reads on the Illumina Hiseq2000 platform.

Peak68866 Reading Primers

R1	AATGATACGGCGACCACCGAGATCTACACTCTTTCCCTACACGACGCTCTTCCGATCTTCCTAGGTTGTTATATTCTAAGCATGGATC
R2	AATGATACGGCGACCACCGAGATCTACACTCTTTCCCTACACGACGCTCTTCCGATCTACCTAGGTTGTTATATTCTAAGCATGGATC
R3	AATGATACGGCGACCACCGAGATCTACACTCTTTCCCTACACGACGCTCTTCCGATCTCCCTAGGTTGTTATATTCTAAGCATGGATC
R4	AATGATACGGCGACCACCGAGATCTACACTCTTTCCCTACACGACGCTCTTCCGATCTGCCTAGGTTGTTATATTCTAAGCATGGATC
R5	AATGATACGGCGACCACCGAGATCTACACTCTTTCCCTACACGACGCTCTTCCGATCTCACTAGGTTGTTATATTCTAAGCATGGATC
R6	AATGATACGGCGACCACCGAGATCTACACTCTTTCCCTACACGACGCTCTTCCGATCTAACTAGGTTGTTATATTCTAAGCATGGATC

Peak68866 Non-reading Primer

NR	CAAGCAGAAGACGGCATACGAAAGAGAGACCCAGCTGTTCTCAG

Peak57514 Reading Primers

R1	AATGATACGGCGACCACCGAGATCTACACTCTTTCCCTACACGACGCTCTT CCGATCTCGGTTTGTTTGTTTGTTTTTAGCAGATC
R2	AATGATACGGCGACCACCGAGATCTACACTCTTTCCCTACACGACGCTCTT CCGATCTAGGTTTGTTTGTTTGTTTTTAGCAGATC
R3	AATGATACGGCGACCACCGAGATCTACACTCTTTCCCTACACGACGCTCTT CCGATCTTGGTTTGTTTGTTTGTTTTTAGCAGATC
R4	AATGATACGGCGACCACCGAGATCTACACTCTTTCCCTACACGACGCTCTT CCGATCTGGGTTTGTTTGTTTGTTTTTAGCAGATC
R5	AATGATACGGCGACCACCGAGATCTACACTCTTTCCCTACACGACGCTCTT CCGATCTTAGTTTGTTTGTTTGTTTTTAGCAGATC
R6	AATGATACGGCGACCACCGAGATCTACACTCTTTCCCTACACGACGCTCTT CCGATCTGAGTTTGTTTGTTTGTTTTTAGCAGATC

Peak57514 Non-reading Primer

NR	CAAGCAGAAGACGGCATACGACACACGTAATTATGTTTACTCAGACTCTG

Promoter Capture Hi-C Assay

The CHi-C library was prepared as described (Schoenfelder et al., 2018) with slight modifications. Cells were crosslinked in 1% formaldehyde for 10 minutes at room temperature and quenched with 2M Tris-HCl pH 8.0 (final 0.125M) for 10 minutes at room

temperature. Cells then were lysed in 300 µL of cold lysis buffer (10 mM Tris-HCl pH 8.0, 10 mM NaCl, 0.2% Igepal supplemented with protease inhibitor). The nuclei were digested in 1x NEBuffer 2 containing 100 units of MboI (NEB, R0147L) and incubated for 6 hours at 37 °C followed by heat inactivation (65°C for 10 minutes). DNA polymerase I, Large (Klenow) fragment (NEB, M0210L), and biotin-14-dATP (ThermoFisher, 19524016) were used to fill in restriction fragment overhangs and biotinylate DNA ends. 4000 units of T4 DNA ligase then added for proximate ligation and incubated at 16°C overnight. After reverse crosslinking, DNA was extracted with phenol/chloroform and ethanol precipitation. Sonication was then performed to make the biotinylated DNA size suitable for high-throughput sequencing (300-500 bp). DNA was dissolved in 130 µL 10 mM Tris-HCl pH 8.0 and transferred to microTUBE (Covaris, 520045) for sonication (Peak Incidence Power 50W, Duty Factor 10%, 200 Cycle per Burst, 60 seconds). Sonicated DNA was size selected for fragments in the range of 300-500 bp by AMPure XP purification beads (VWR, 75803-122). The fragments marked with biotin were pulled down with Dynabeads™ MyOne™ Streptavidin T1 beads (ThermoFisher, 65601). End repair, A-tailing, and paired-end Agilent adaptor ligation (SureSelect XT Library Prep Kit ILM) were performed and followed by on-bead PCR amplification before hybridizing to the customized probe library (Custom 6-11.9 Mb library for 16 samples). The samples were prepared and hybridized to the capture library according to the protocol provided by Agilent (https://www.agilent.com/cs/library/usermanuals/Public/G7530-90000.pdf). The final PCR amplification was carried out for 9 cycles and purified by using AMPure XP beads. The library was paired-end sequenced for 150 bp on the Illumina Novaseq platform.

Figure Legends

Figure 2-1: Accessible DNA Dynamics During the Lipid A Response

BMDMs were stimulated with Lipid A over the time course of 0, 30, 60, and 120 minutes, and ATAC-seq was utilized to profile the genome-wide chromatin accessibility.

(A) The distribution of the maximum fold accessibility over the two-hour stimulation period is shown for the 101,448 regions (called peaks) in WT BMDMs. Dashed black lines indicate 1, 2, and 5-fold cutoffs.

(B) The accessible sites (ATAC peaks) were annotated according to a genomic location using Homer.

(C) Bedgraph visualization of representative promoter peaks from repressed, constitutive, induced, and transcript-associate ATAC-peak categories. The time of stimulation is indicated at the left of each panel.

(D) The responsiveness of ATAC peaks at different genomic locations. The induced ATAC sites are shown in orange, repressed in grey, and constitutive in blue.

(E) The genomic distributions of ATAC peaks across the inducibility. The ATAC peaks are ranked and grouped into 40 bins with equivalent size based on the maximum fold induction from the most repressed to the most induced.

(F) The percentage of ATAC peaks with (blue) and without basal signal (orange) across the inducibility of ATAC peaks from the most repressed to the most induced.

(G) The bedgraph visualization of ATAC peaks with different inducibility before and after two-hours of stimulation.

Figure 2-2: Global Transcription Factor Motif Analysis

(A) The Motif enrichment across the 40 ATAC peaks bins of equivalent size from the most repressed to the most induced. The motif analysis was done by Homer with 256 motif matrices from the database. The motifs were grouped and annotated as motif families.
(B) Four representative motifs from four motif families (AP-1 like of bZIP, NF-κB, IRF, and POU/Homeobox) enriched in the induced bins. Major axis: -log(p-value), blue dot and line. Secondary axis: % of peaks with the motif in each bin, orange dot and line.
(C) Four induced motif family's enrichment of the strongly induced ATAC peaks. The strongly induced ATAC peaks were binned into 8 bins with equal size based on the CHX percent accessibility from the most CHX sensitive to CHX resistant.

Figure 2-3: Four Overrepresented Motif Families in the Inducible Sites and Their Collaboratively

(A) Motif enrichment of the four inducing motif families across the 40 ATAC peaks bins of equivalent size from the most repressed to the most induced. The motif analysis was done using Homer with 364 motif matrices in the database. The color scheme was adjusted for each motif family.
(B) Motif enrichment of the inducible peaks (1^{o}, primary; 2^{o} secondary) with (Y) and without (N) the representative motif from each inducing family.

Figure 2-4: Preferential Enrichment of NF-κB Binding in the Most Significantly Induced Primary Response Peaks

(A) Percentage of ATAC peaks with RelA binding in 40 bins of ATAC peaks across the accessibility of fold induction or induction significance (-log(p-value)).

(B) Percentage of ATAC peaks with RelA binding in 10 bins of primary (yellow) and secondary (purple) response ATAC peaks.

(C) Summary of RelA binding in 154 most significantly induced primary response ATAC peaks.

Figure 2-5: Functional Validation of NF-κB in Nucleosome Remodeling

(A) Top: NF-κB motif editing sites and the designed homology-directed repair template. Bottom: List of raw read counts containing the sequence fragments (1-7, 30 bp each).

(B) Peak45837 genome browser tracks of ATAC-seq on WT BMDM cell line, NF-κB motif edited clone and *RelA*$^{-/-}$*C-Rel*$^{-/-}$ clone as well as RelA ChIP-seq of the WT BMDM.

Figure 2-6: Properties of Inducible Promoter Sites

(A) Heatmap of 40 promoters with inducible accessibility on the corresponding gene expression, CHX percent accessibility, percent accessibility in the lipid A treated *Irf3*$^{-/-}$, CHX and lipid A treated *Irf3*$^{-/-}$ BMDMs, and Irf3 binding score.

(B) Scatter plots of maximum accessibility fold induction versus maximum RNA expression fold induction and CpG content in the promoters of primary response genes (PRG) and secondary response genes (SRG).

(C) Scatter plot of maximum ATAC RPKM in the WT BMDMs versus *Irf3*$^{-/-}$ BMDMs pretreated with CHX followed by a time course of lipid A stimulation of the promoters with nucleosome remodeling.

(D) Volcano plot of ATAC RPKM fold change to induction significance in the WT BMDMs versus *Irf3*$^{-/-}$ BMDMs treated with CHX and lipid A for 2 hours in promoters with nucleosome remodeling.

(E) Genome browser tracks of chromatin accessibility, Irf3 binding, and chromatin associated transcripts of *Ccl5* gene.

Figure 2-7: Properties of Inducible Promoter Sites (Supplemental Figures)

(A) Scatter plot of ATAC RPKM in the WT BMDMs versus *Irf3*$^{-/-}$ BMDMs pretreated with CHX and different lipid A stimulation durations of the promoters with nucleosome remodeling.

(B) Genome browser tracks of chromatin accessibility, Irf3 binding, and chromatin-associated transcript of *Rnase10* gene.

Figure 2-8: Properties of Inducible Intergenic Sites

(A) Top: Distance distribution of inducible intergenic ATAC peaks to the nearest 10-fold induced genes. Second: Distance distribution of weakly induced intergenic ATAC peaks to the nearest 10-fold induced genes. Third: Distance distribution of constitutive intergenic ATAC peaks to the nearest 10-fold induced genes. Bottom: Distance distribution of repressed intergenic ATAC peaks to the nearest 10-fold induced genes.

(B) Left: Heatmap of chromatin accessibility among the time course of lipid A treatment in the inducible intergenic peaks grouped into 6 clusters based on the accessibility kinetics. Maximum CHX percent accessibility was also shown in the last column (white: secondary; orange: primary). Right: Average RPKM at each time point of the 6 clusters.

(C) IRF and RHD motif enrichment in the inducible intergenic peaks binned equally based on CHX percent accessibility. The enrichment of IRF and RHD motifs in the defined primary Irf3 dependent intergenic peaks.

(D) Scatter plot of maximum ATAC RPKM in the WT BMDMs versus *Irf3*$^{-/-}$ BMDMs treated with CHX and a time course of lipid A stimulation of the intergenic sites with nucleosome remodeling.

(E) Volcano plot of ATAC RPKM fold change to induction significance in the WT BMDMs versus *Irf3*$^{-/-}$ BMDMs treated with CHX and lipid A for 2 hours in the intergenic sites with nucleosome remodeling.

Figure 2-9: Properties of Inducible Intergenic Sites (Supplemental Figures)

(A) Observed and expected occurrence of different groups of peaks (repressed, constitutive, weakly induced, and strongly induced) in every 10 kb distance to the nearest TSS of strongly induced genes (> 10-fold).

(B) Scatter plot of ATAC RPKM in the WT BMDMs versus *Irf3*$^{-/-}$ BMDMs pretreated with CHX and different lipid A stimulation durations of intergenic peaks with nucleosome remodeling.

(C) Genome browser tracks of chromatin accessibility, Irf3 binding, and chromatin-associated transcript of the intergenic peaks upstream of *Ccl5*.

Figure 2-10: Functional Relevance of IRF3-dependent Primary Response Intergenic Peaks (peak68866)

(A) Interacting genome browser tracks (4C and CHi-C) of peak68866 before and after lipid A stimulation.

(B) Design of CRISPR-Cas9 deletion sites (PC: positive control; Target: peak68866).

(C) *Ccl5*, *Ccl3*, and *Ccl4* qPCR results of Target and PC clones.

Figure 2-11: Physical Contacts of the Isolated IRF3-dependent Primary Response Intergenic Peaks (Peak57514)

Interacting genome browser tracks (4C and CHi-C) of peak57514 before and after lipid A stimulation.

Figure 2-1: Accessible DNA Dynamics During the Lipid A Response

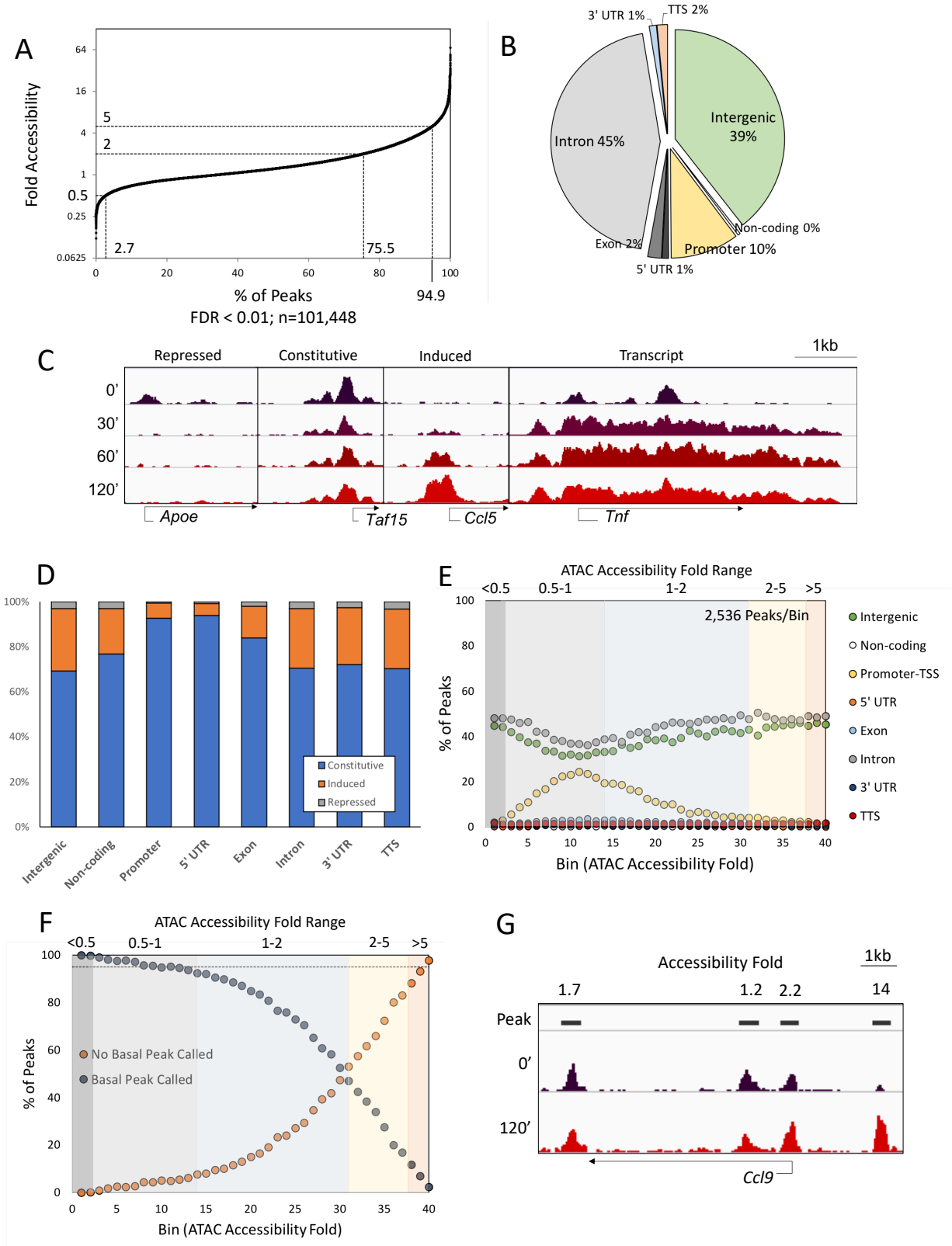

Figure 2-2: Global Transcription Factor Motif Analysis

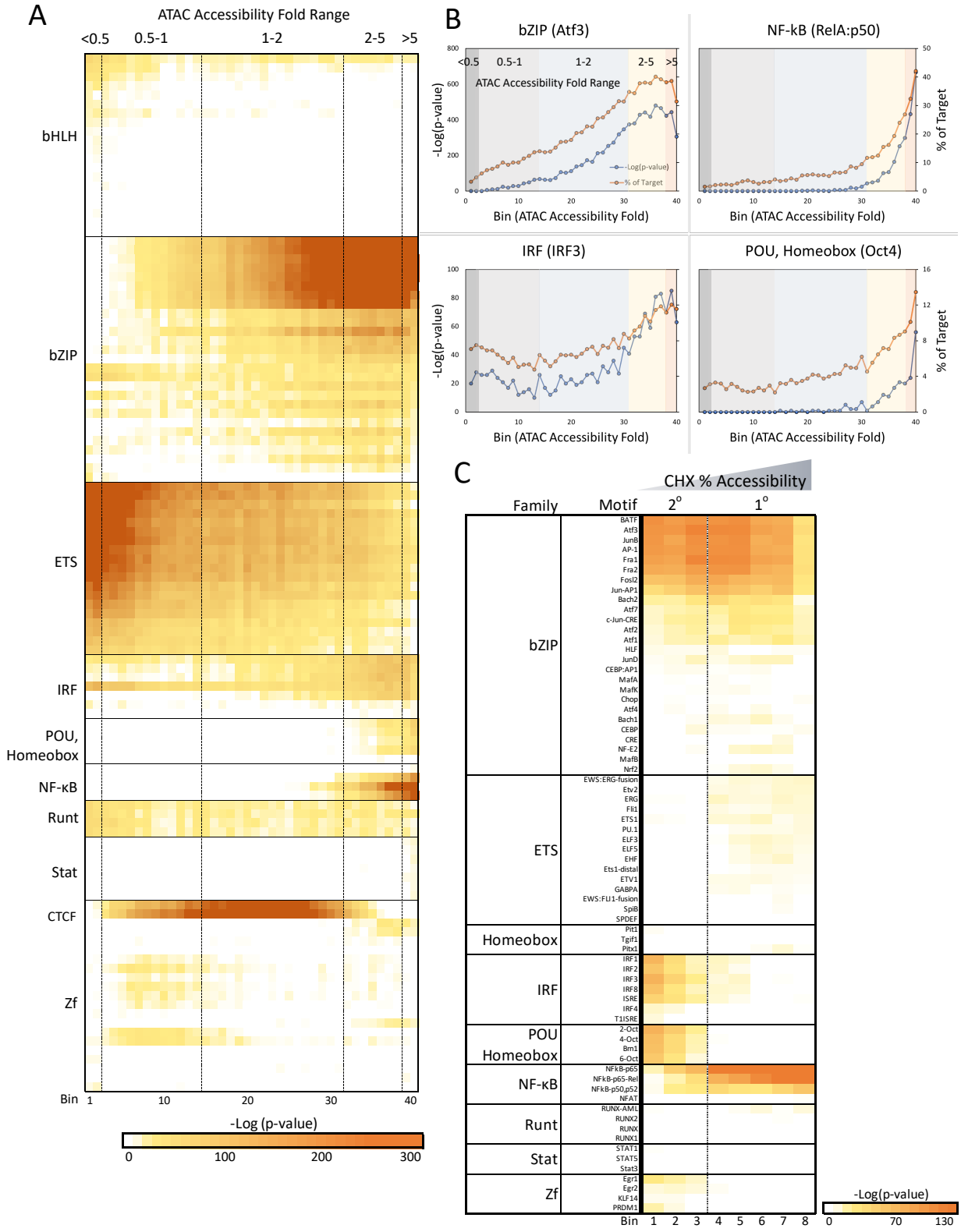

Figure 2-3: Four Overrepresented Motif Families in the Inducible Sites and Their Collaboratively

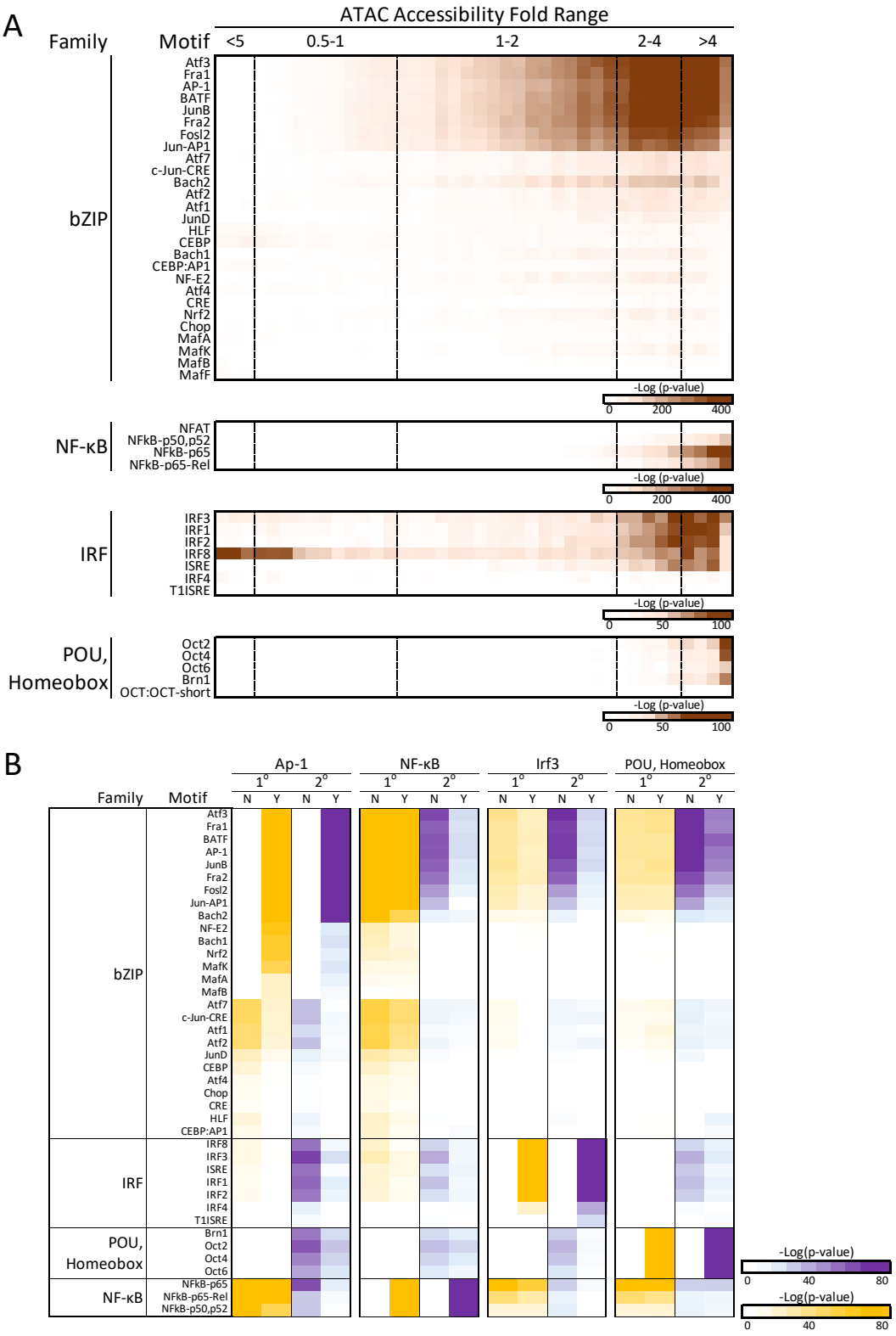

Figure 2-4: Preferential Enrichment of NF-κB Binding in the Most Significantly Induced Primary Response Peaks

A

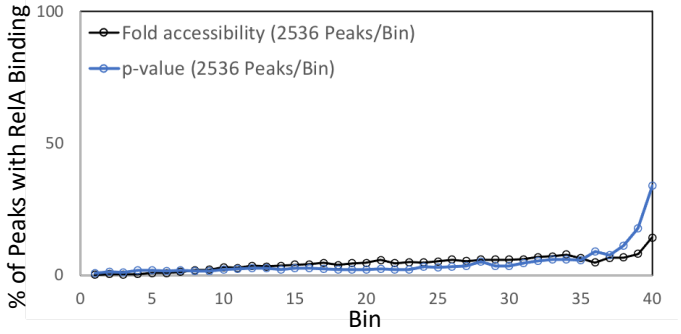

B

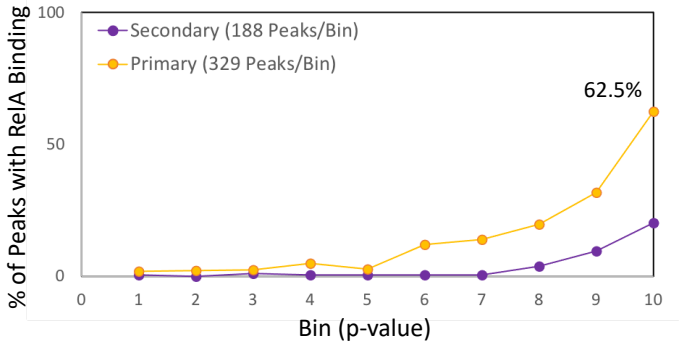

C

329 most significant primary response ATAC peaks

• 205 have defined RelA binding
• 102 have no defined RelA binding
  ○ 69 have transient RelA binding
  ○ 23 have reproducible but weak RelA binding
  ○ 10 have RelA signal but not called by the program
• 19 are transcriptional noise
• 3 have no RelA binding

Figure 2-5: Functional Validation of NF-κB in Nucleosome Remodeling

	Seq1	Seq2	Seq3	Seq4	Seq5	Seq6	Seq7	Total reads
WT_0	5	1	0	0	0	0	2	35,794,772
WT_15	17	14	0	4	3	0	7	35,738,973
WT_30	46	12	0	8	4	0	13	42,701,952
WT_60	37	11	0	9	5	0	11	41,676,140
WT_120	29	7	0	8	3	0	6	34,348,773
DKO_0	2	1	0	1	0	0	0	24,423,149
DKO_15	3	4	0	1	1	0	2	31,502,927
DKO_30	3	3	0	1	0	0	1	29,789,571
DKO_60	3	0	0	1	0	0	1	30,777,515
DKO_120	5	0	0	0	0	0	1	30,771,543
N3_0	0	0	0	0	0	0	0	25,678,270
N3_15	0	0	0	0	0	0	0	28,271,549
N3_30	0	0	0	0	0	1	1	21,934,904
N3_60	0	0	1	1	0	0	0	29,440,559
N3_120	1	0	0	0	0	0	0	27,280,072

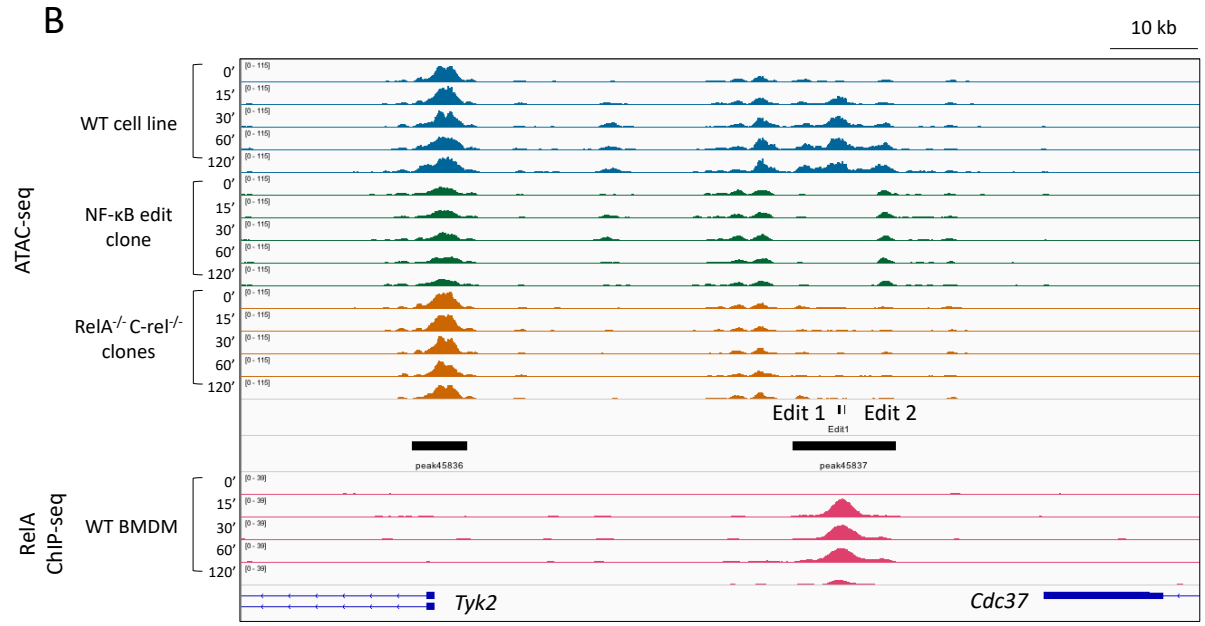

Figure 2-6: Properties of Inducible Promoter Sites

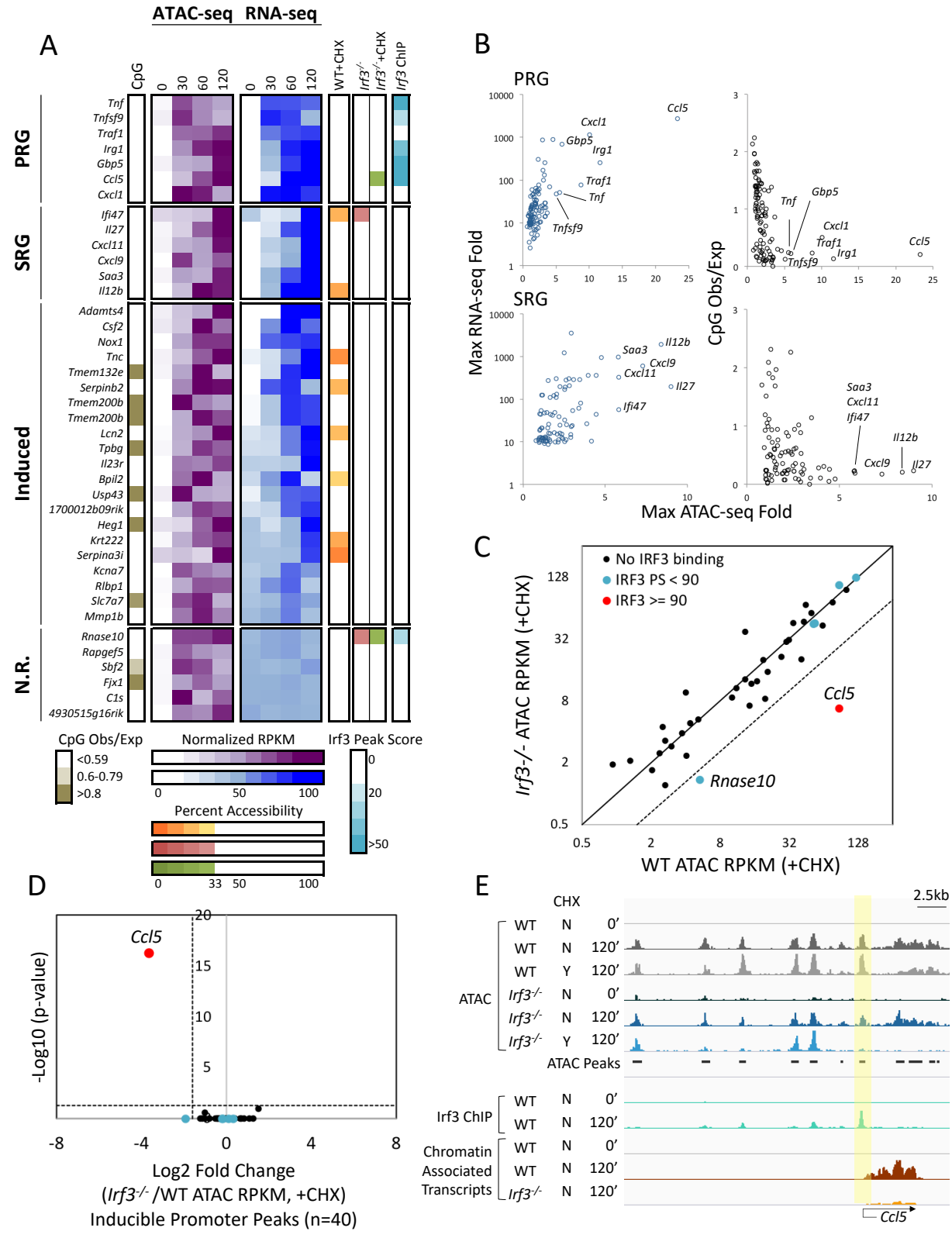

Figure 2-7: Properties of Inducible Promoter Sites (supplemental figures)

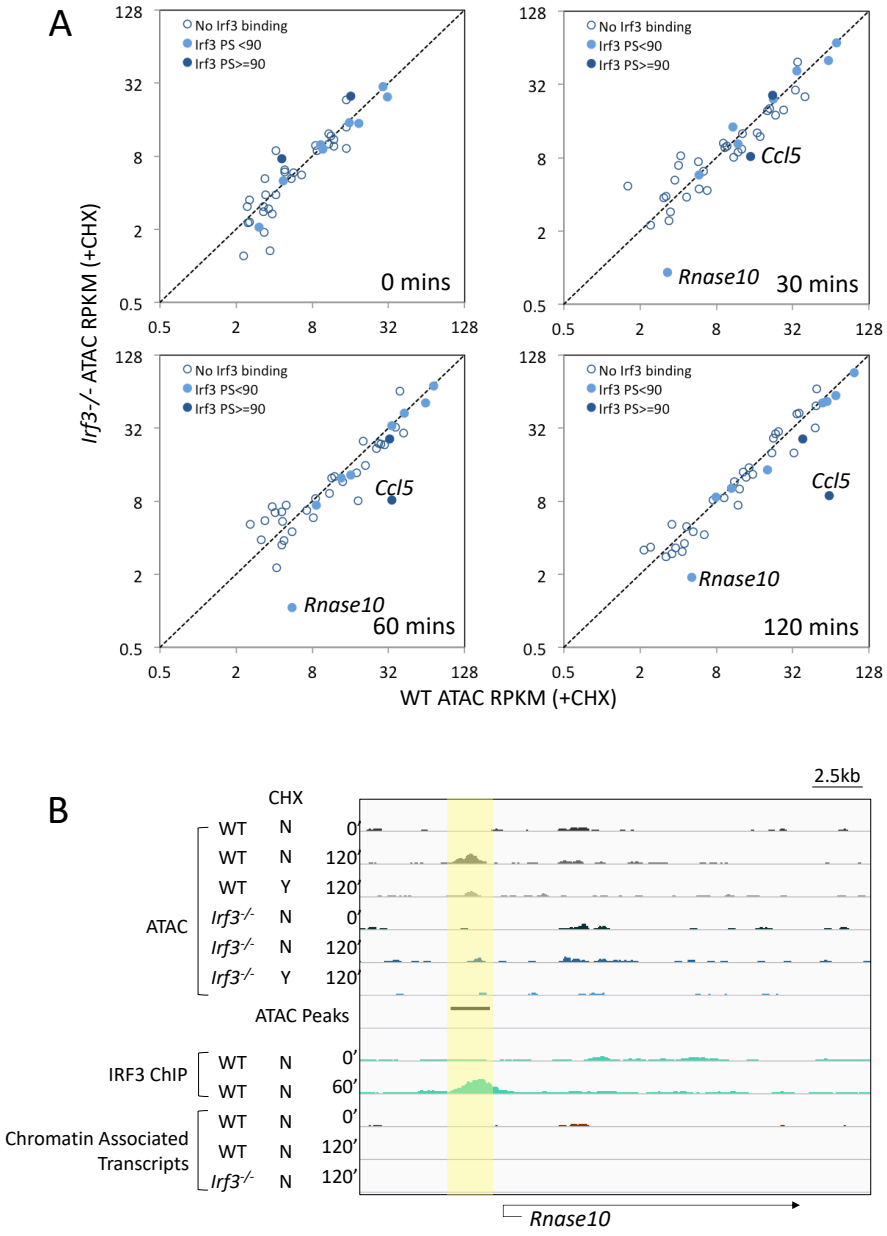

Figure 2-8: Properties of Inducible Intergenic Sites

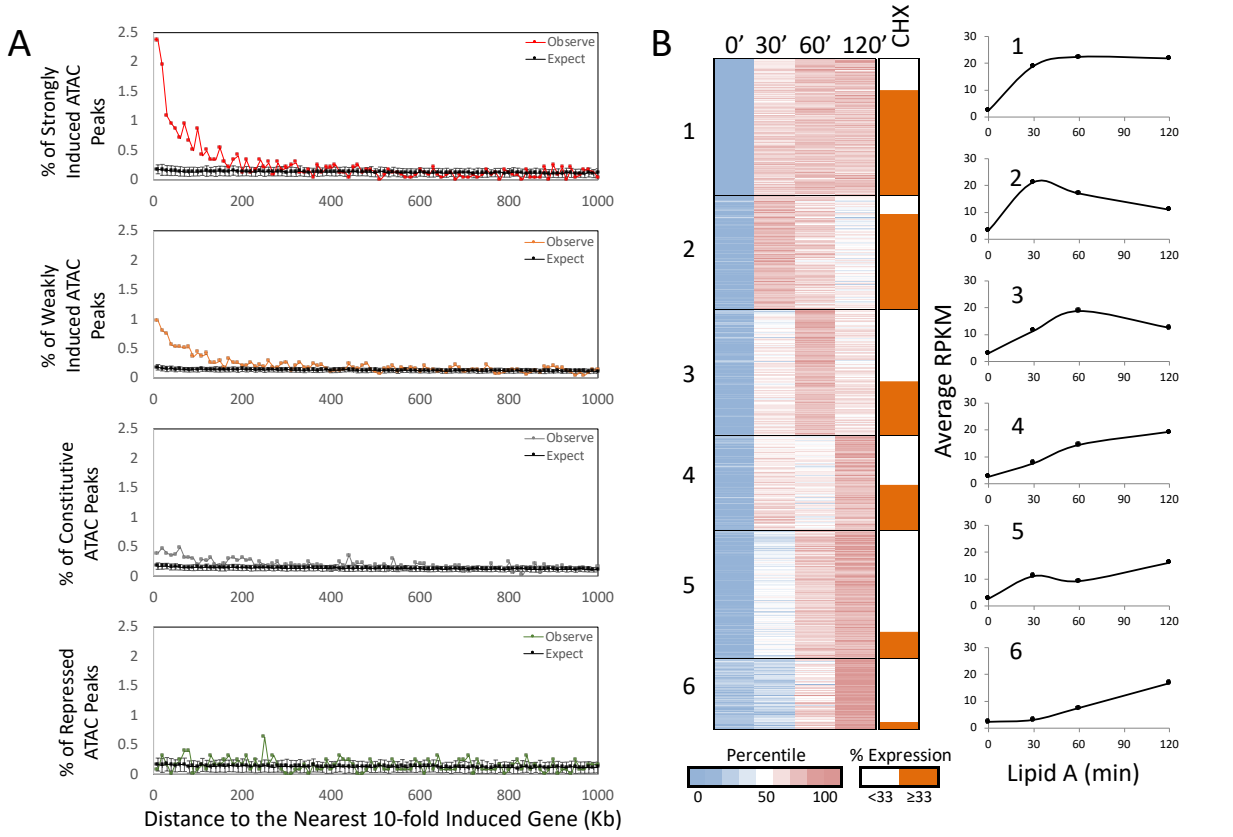

C

Primary Irf3 dependent peaks

Family	Motif Name	Secondary								Primary														
IRF	IRF1	17	12	11	13	2	1	4	3	2	5	3	4	1	0	0	0	0	2	0	0	0	3	7
	IRF3	15	20	14	12	4	3	7	6	6	3	1	3	4	1	0	1	4	2	1	2	0	1	22
	IRF8	15	10	8	8	1	1	6	5	2	4	2	2	3	0	0	0	0	1	0	0	1	4	3
	IRF2	13	9	9	13	2	2	4	5	3	2	3	1	1	0	0	0	0	1	1	0	1	3	8
	ISRE	8	10	9	12	1	2	8	4	2	4	3	2	1	0	0	0	0	4	0	0	0	3	10
	T1ISRE	4	3	0	0	0	0	0	0	0	0	0	0	0	0	0	0	0	0	0	0	0	0	0
	IRF4	3	4	1	1	0	3	0	0	1	0	0	1	0	0	1	0	0	0	0	1	0	1	2
RHD	NFkB-p65	1	5	9	5	11	7	11	12	17	25	22	35	30	30	33	39	41	42	45	32	48	39	12
	NFkB-p65-Rel	0	3	4	0	2	7	8	8	7	21	18	21	13	15	17	21	16	26	29	27	22	25	2
	NFAT	0	0	0	1	1	0	0	0	0	1	0	1	0	0	0	1	1	0	0	1	1	3	2
	NFkB-p50,p52	0	2	2	0	6	5	3	8	7	5	9	11	4	8	2	6	7	8	6	7	14	15	5

-Log(p-value) 0 25 50

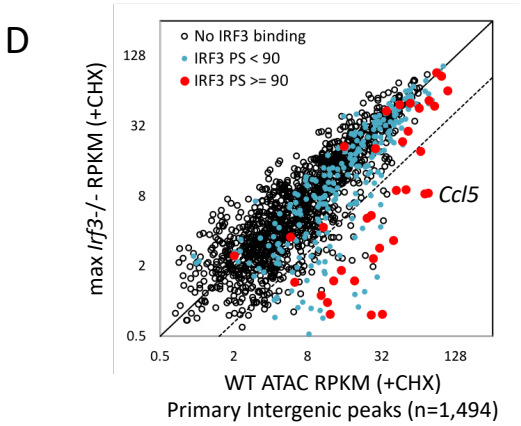

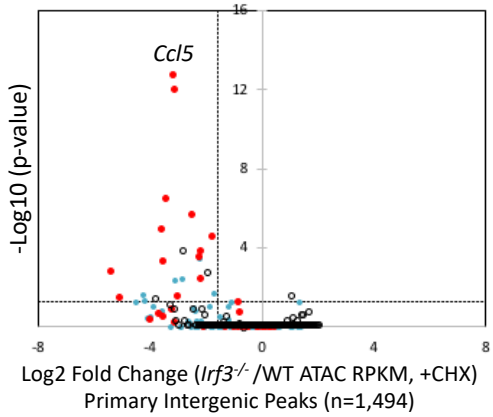

Figure 2-9: Properties of Inducible Intergenic Sites (supplemental figures)

A

Percent of ATAC Peaks

		Distance Range									
		<10 Kb	10-20 Kb	20-30 Kb	30-40 Kb	40-50 Kb	50-60 Kb	60-70 Kb	70-80 Kb	80-90 Kb	90-100 Kb
Repressed	Observe	0.08	0.32	0.16	0.00	0.16	0.24	0.40	0.40	0.00	0.08
	Expect	0.17	0.15	0.17	0.16	0.14	0.16	0.16	0.12	0.14	0.12
	SD	0.11	0.12	0.11	0.11	0.10	0.11	0.11	0.10	0.10	0.10
Constitutive	Observe	0.39	0.47	0.39	0.35	0.37	0.49	0.32	0.32	0.30	0.19
	Expect	0.17	0.17	0.17	0.16	0.16	0.15	0.14	0.14	0.14	0.15
	SD	0.05	0.05	0.05	0.05	0.05	0.05	0.04	0.05	0.05	0.05
Weakly Induced	Observe	0.98	0.80	0.75	0.56	0.53	0.53	0.51	0.52	0.36	0.43
	Expect	0.18	0.16	0.15	0.16	0.15	0.15	0.14	0.14	0.14	0.14
	SD	0.05	0.04	0.05	0.04	0.04	0.04	0.04	0.04	0.04	0.04
Strongly Induced	Observe	2.37	1.96	1.08	0.96	0.87	0.71	0.96	0.67	0.50	0.87
	Expect	0.18	0.17	0.16	0.16	0.15	0.14	0.14	0.14	0.14	0.14
	SD	0.08	0.09	0.08	0.08	0.08	0.08	0.08	0.08	0.08	0.07

B

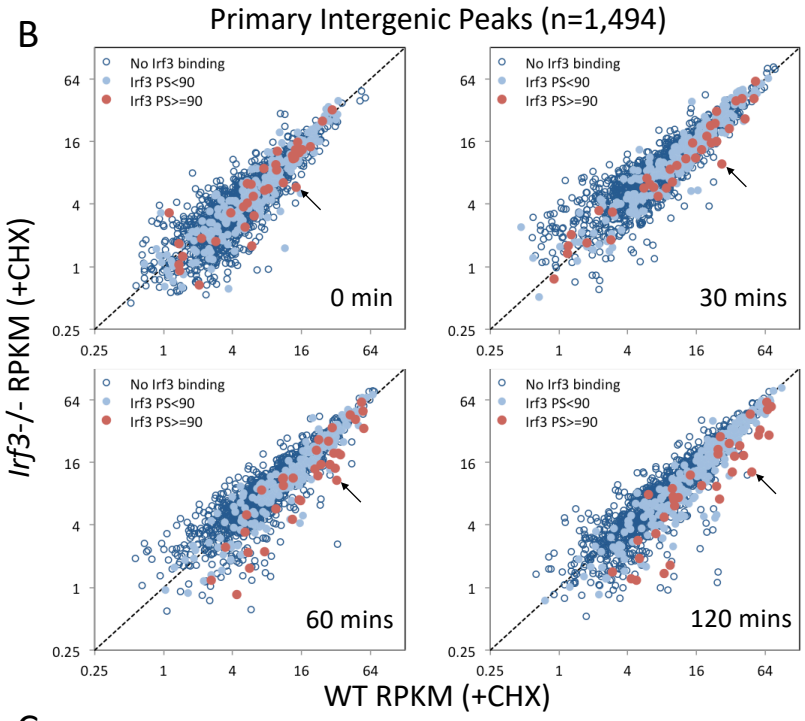

C

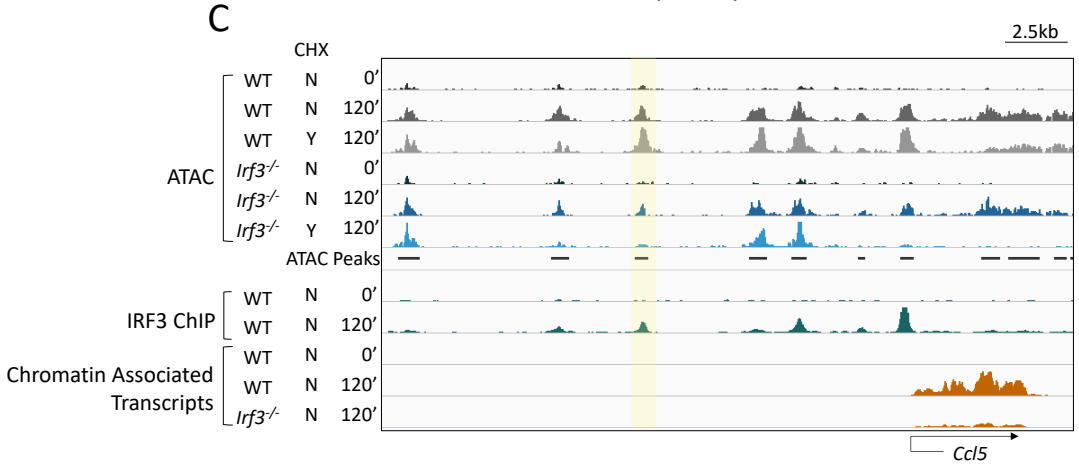

Figure 2-10: Functional Relevance of IRF3-dependent Primary Response Intergenic Peaks (peak68866)

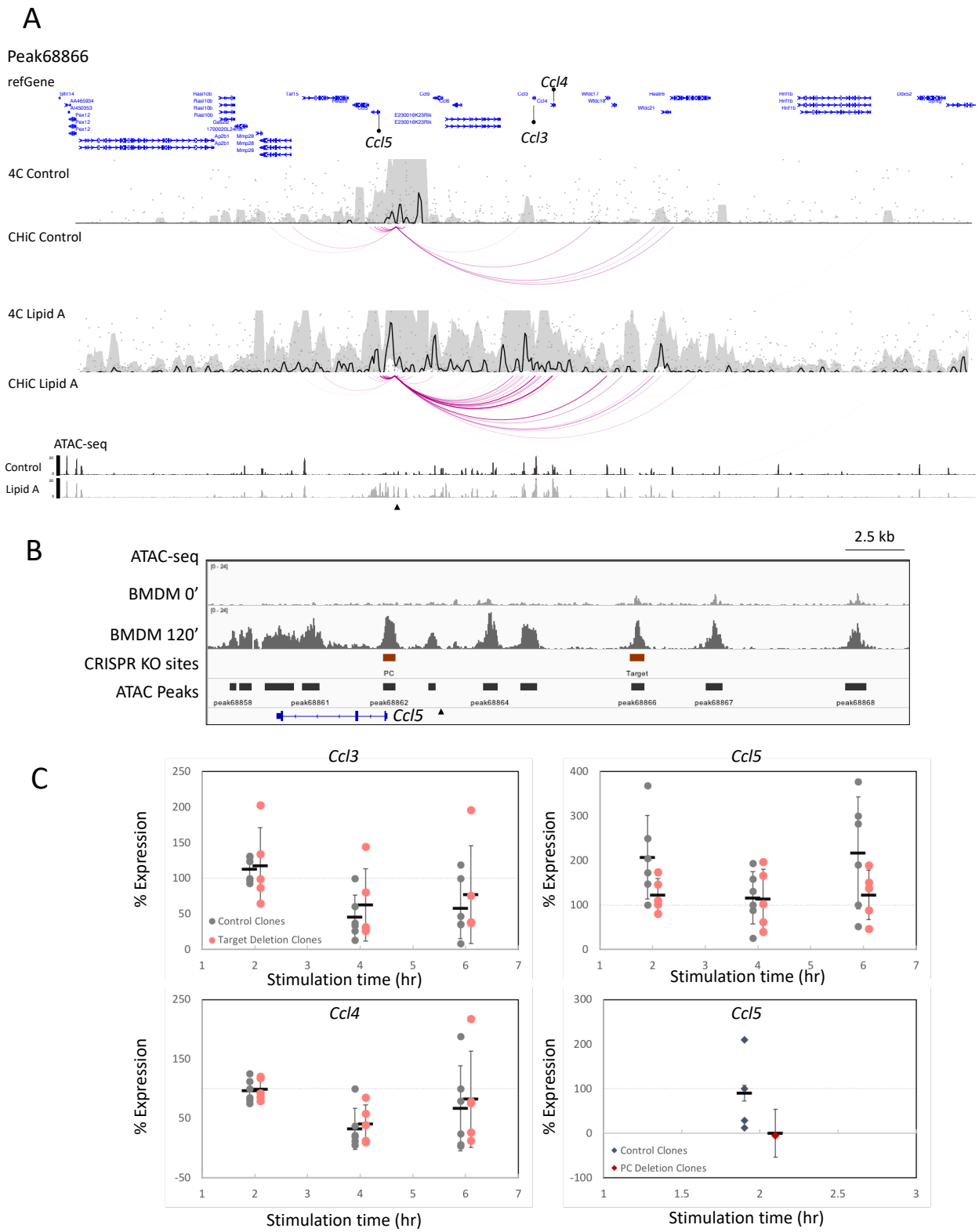

Figure 2-11: : Physical Contacts of the Isolated IRF3-dependent Primary Response Intergenic Peaks (peak57514)

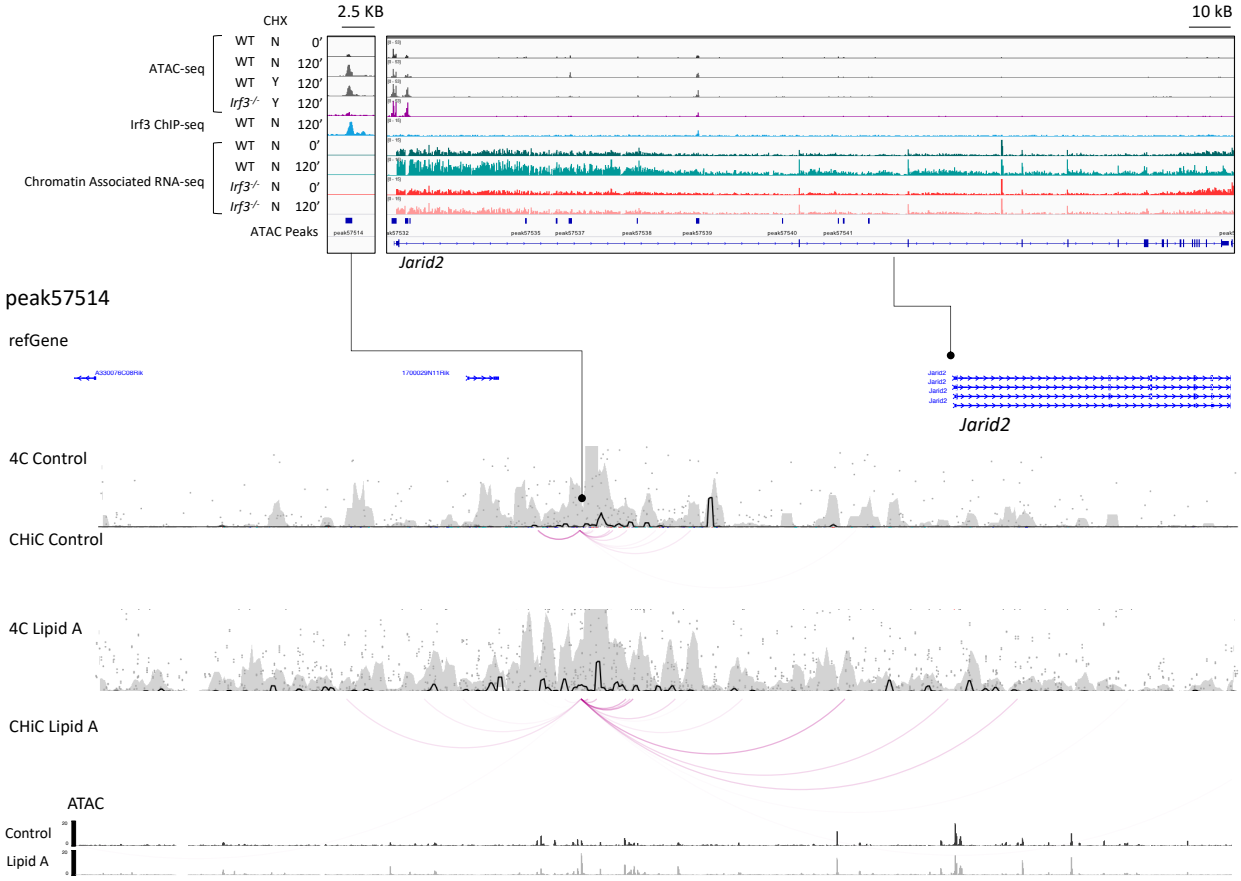

CHAPTER 3

CONCLUDING DISCUSSION

The advancement of HTS technologies greatly enhances our understanding of gene regulation. Numerous genome-wide studies have revealed the overwhelming complexity of gene regulatory networks. However, it is challenging to unveil the critical mechanistic insights from the broader analysis given the large number and diverse dynamics of transcription factors as well as the large number of post-translational modifications. In eukaryotes, regulation of gene expression is inherently more complicated because the transcription machinery must gain access to chromatin templates instead of naked DNA. Emerging evidence has suggested chromatin structure dynamics can provide an integral means of transcription regulation. This study provides valuable mechanistic insights into nucleosome remodeling and inducible gene regulation using the following strategies: (1) simplified and reproducible mouse primary macrophage model; (2) multi-modalities HTS assays; (3) systematic, sequential, and quantitative approach.

We recapitulate the native innate immune response in BMDMs with great reproducibility. We focus our attention on the well-documented TLR4 signaling cascade by treating BMDMs with lipid A. Another attempt to simplify the model is the use of CHX in examining IRF3 dependent remodeling. CHX can eliminate new protein synthesis, thus block type I IFNs production and reduce compensation from other IRF family members.

We performed ATAC-seq to profile the genome-wide DNA accessibility across the time course of lipid A treatment as well as IRF3 and RelA ChIP-seq to identify genome-wide TFs binding events. Chromatin associated RNA-seq was applied to snapshot the timely transcription. HTS assays were done on WT and different knockout strains with and without CHX pretreatment. The intense genome-wide profiling of the molecular and

transcriptional events provides the basis for systematic analysis from multiple aspects, such as remodeling dynamics and TF dependence.

In the broader analysis, we characterized the accessible DNA regions by their dynamics, primary versus secondary response nature, TF motifs and binding enrichment. Our research aims to understand how nucleosome remodeling contributes to transcriptional control of the innate immune response. In addition to the global characterization of accessible DNA regions, we applied a stringent accessibility fold induction (more than 5-fold) before and after lipid A stimulation to capture the nucleosome remodeling events with better confidence. We then targeted regions that underwent primary and consistent nucleosome remodeling. Together with major TF bindings, knockout BMDMs accessibility profiling, and CRISPR-Cas9 genome editing of selected targets, we are able to dive in and unveil critical mechanistic details.

By applying the above strategies, we can systematically layer off the complicated networks from the broader analysis and narrow the analysis to unveil the selectivity of the major TFs involving the TLR4-induced chromatin remodeling. Though, arguably, our approach method provided less information of the sites that underwent repressed, constitutive, and weakly induced accessibility changes, these regions hold more uncertainty given the various minor TFs involvement and the post-translational modifications. Our future goal is to extend this study to the regions with different chromatin dynamics and broaden our knowledge of chromatin regulation in the immune response.

References

Andersson, R., Gebhard, C., Miguel-Escalada, I., Hoof, I., Bornholdt, J., Boyd, M., Chen, Y., Zhao, X., Schmidl, C., Suzuki, T.*, et al.* (2014). An atlas of active enhancers across human cell types and tissues. *Nature 507*, 455-461.

Angelov, D., Lenouvel, F., Hans, F., Müller, C.W., Bouvet, P., Bednar, J., Moudrianakis, E.N., Cadet, J., and Dimitrov, S. (2004). The histone octamer is invisible when NF-kappaB binds to the nucleosome. *J Biol Chem 279*, 42374-42382.

Ashe, H.L., Monks, J., Wijgerde, M., Fraser, P., and Proudfoot, N.J. (1997). Intergenic transcription and transinduction of the human beta-globin locus. *Genes Dev 11*, 2494-2509.

Auerbach, R.K., Euskirchen, G., Rozowsky, J., Lamarre-Vincent, N., Moqtaderi, Z., Lefrançois, P., Struhl, K., Gerstein, M., and Snyder, M. (2009). Mapping accessible chromatin regions using Sono-Seq. *Proc Natl Acad Sci U S A 106*, 14926-14931.

Barolo, S. (2012). Shadow enhancers: frequently asked questions about distributed cis-regulatory information and enhancer redundancy. *Bioessays 34*, 135-141.

Barski, A., Cuddapah, S., Cui, K., Roh, T.Y., Schones, D.E., Wang, Z., Wei, G., Chepelev, I., and Zhao, K. (2007). High-resolution profiling of histone methylations in the human genome. *Cell 129*, 823-837.

Becker, P.B., and Workman, J.L. (2013). Nucleosome remodeling and epigenetics. *Cold Spring Harb Perspect Biol 5*.

Benoist, C., and Chambon, P. (1981). In vivo sequence requirements of the SV40 early promotor region. *Nature 290*, 304-310.

Bhatt, D.M., Pandya-Jones, A., Tong, A.J., Barozzi, I., Lissner, M.M., Natoli, G., Black, D.L., and Smale, S.T. (2012). Transcript dynamics of proinflammatory genes revealed by sequence analysis of subcellular RNA fractions. *Cell 150*, 279-290.

Buenrostro, J.D., Giresi, P.G., Zaba, L.C., Chang, H.Y., and Greenleaf, W.J. (2013). Transposition of native chromatin for fast and sensitive epigenomic profiling of open chromatin, DNA-binding proteins and nucleosome position. *Nat Methods 10*, 1213-1218.

Buenrostro, J.D., Wu, B., Chang, H.Y., and Greenleaf, W.J. (2015). ATAC-seq: A Method for Assaying Chromatin Accessibility Genome-Wide. *Curr Protoc Mol Biol 109*, 21.29.21-21.29.29.

Bultman, S., Gebuhr, T., Yee, D., La Mantia, C., Nicholson, J., Gilliam, A., Randazzo, F., Metzger, D., Chambon, P., Crabtree, G.*, et al.* (2000). A Brg1 null mutation in the mouse reveals functional differences among mammalian SWI/SNF complexes. *Mol Cell 6*, 1287-1295.

Burke, T.W., and Kadonaga, J.T. (1997). The downstream core promoter element, DPE, is conserved from Drosophila to humans and is recognized by TAFII60 of Drosophila. *Genes Dev 11*, 3020-3031.

Cairns, B.R., Kim, Y.J., Sayre, M.H., Laurent, B.C., and Kornberg, R.D. (1994). A multisubunit complex containing the SWI1/ADR6, SWI2/SNF2, SWI3, SNF5, and SNF6 gene products isolated from yeast. *Proc Natl Acad Sci U S A 91*, 1950-1954.

Chen, F.E., Huang, D.B., Chen, Y.Q., and Ghosh, G. (1998). Crystal structure of p50/p65 heterodimer of transcription factor NF-kappaB bound to DNA. *Nature 391*, 410-413.

Chen, W., and Royer, W.E., Jr. (2010). Structural insights into interferon regulatory factor activation. *Cell Signal 22*, 883-887.

Clapier, C.R., Iwasa, J., Cairns, B.R., and Peterson, C.L. (2017). Mechanisms of action and regulation of ATP-dependent chromatin-remodelling complexes. *Nat Rev Mol Cell Biol 18*, 407-422.

Cokus, S.J., Feng, S., Zhang, X., Chen, Z., Merriman, B., Haudenschild, C.D., Pradhan, S., Nelson, S.F., Pellegrini, M., and Jacobsen, S.E. (2008). Shotgun bisulphite sequencing of the Arabidopsis genome reveals DNA methylation patterning. *Nature 452*, 215-219.

Collis, P., Antoniou, M., and Grosveld, F. (1990). Definition of the minimal requirements within the human beta-globin gene and the dominant control region for high level expression. *EMBO J 9*, 233-240.

Concordet, J.P., and Haeussler, M. (2018). CRISPOR: intuitive guide selection for CRISPR/Cas9 genome editing experiments and screens. *Nucleic Acids Res 46*, W242-w245.

Corces, M.R., Trevino, A.E., Hamilton, E.G., Greenside, P.G., Sinnott-Armstrong, N.A., Vesuna, S., Satpathy, A.T., Rubin, A.J., Montine, K.S., Wu, B.*, et al.* (2017). An

improved ATAC-seq protocol reduces background and enables interrogation of frozen tissues. *Nat Methods 14*, 959-962.

Côté, J., Quinn, J., Workman, J.L., and Peterson, C.L. (1994). Stimulation of GAL4 derivative binding to nucleosomal DNA by the yeast SWI/SNF complex. *Science 265*, 53-60.

Crawford, G.E., Holt, I.E., Whittle, J., Webb, B.D., Tai, D., Davis, S., Margulies, E.H., Chen, Y., Bernat, J.A., Ginsburg, D.*, et al.* (2006). Genome-wide mapping of DNase hypersensitive sites using massively parallel signature sequencing (MPSS). *Genome Res 16*, 123-131.

de Laat, W., and Duboule, D. (2013). Topology of mammalian developmental enhancers and their regulatory landscapes. *Nature 502*, 499-506.

Dixon, J.R., Selvaraj, S., Yue, F., Kim, A., Li, Y., Shen, Y., Hu, M., Liu, J.S., and Ren, B. (2012). Topological domains in mammalian genomes identified by analysis of chromatin interactions. *Nature 485*, 376-380.

Dorighi, K.M., Swigut, T., Henriques, T., Bhanu, N.V., Scruggs, B.S., Nady, N., Still, C.D., 2nd, Garcia, B.A., Adelman, K., and Wysocka, J. (2017). Mll3 and Mll4 Facilitate Enhancer RNA Synthesis and Transcription from Promoters Independently of H3K4 Monomethylation. *Mol Cell 66*, 568-576.e564.

Dowen, J.M., Fan, Z.P., Hnisz, D., Ren, G., Abraham, B.J., Zhang, L.N., Weintraub, A.S., Schujiers, J., Lee, T.I., Zhao, K.*, et al.* (2014). Control of cell identity genes occurs in insulated neighborhoods in mammalian chromosomes. *Cell 159*, 374-387.

Frankel, N., Davis, G.K., Vargas, D., Wang, S., Payre, F., and Stern, D.L. (2010). Phenotypic robustness conferred by apparently redundant transcriptional enhancers. *Nature 466*, 490-493.

Franklin, R.E., and Gosling, R.G. (1953). Molecular configuration in sodium thymonucleate. *Nature 171*, 740-741.

Fullwood, M.J., Liu, M.H., Pan, Y.F., Liu, J., Xu, H., Mohamed, Y.B., Orlov, Y.L., Velkov, S., Ho, A., Mei, P.H.*, et al.* (2009). An oestrogen-receptor-alpha-bound human chromatin interactome. *Nature 462*, 58-64.

Ghosh, S., May, M.J., and Kopp, E.B. (1998). NF-kappa B and Rel proteins: evolutionarily conserved mediators of immune responses. *Annu Rev Immunol 16*, 225-260.

Gill, G. (2001). Regulation of the initiation of eukaryotic transcription. *Essays Biochem 37*, 33-43.

Gilmore, T.D. (2006). Introduction to NF-kappaB: players, pathways, perspectives. *Oncogene 25*, 6680-6684.

Giresi, P.G., Kim, J., McDaniell, R.M., Iyer, V.R., and Lieb, J.D. (2007). FAIRE (Formaldehyde-Assisted Isolation of Regulatory Elements) isolates active regulatory elements from human chromatin. *Genome Res 17*, 877-885.

Gruss, P., Dhar, R., and Khoury, G. (1981). Simian virus 40 tandem repeated sequences as an element of the early promoter. *Proceedings of the National Academy of Sciences 78*, 943-947.

Guidi, C.J., Sands, A.T., Zambrowicz, B.P., Turner, T.K., Demers, D.A., Webster, W., Smith, T.W., Imbalzano, A.N., and Jones, S.N. (2001). Disruption of Ini1 leads to peri-implantation lethality and tumorigenesis in mice. *Mol Cell Biol 21*, 3598-3603.

Hargreaves, D.C., and Crabtree, G.R. (2011). ATP-dependent chromatin remodeling: genetics, genomics and mechanisms. *Cell Res 21*, 396-420.

Heinz, S., Benner, C., Spann, N., Bertolino, E., Lin, Y.C., Laslo, P., Cheng, J.X., Murre, C., Singh, H., and Glass, C.K. (2010). Simple combinations of lineage-determining transcription factors prime cis-regulatory elements required for macrophage and B cell identities. *Mol Cell 38*, 576-589.

Hnisz, D., Day, D.S., and Young, R.A. (2016). Insulated Neighborhoods: Structural and Functional Units of Mammalian Gene Control. *Cell 167*, 1188-1200.

Hoffmann, A., and Baltimore, D. (2006). Circuitry of nuclear factor kappaB signaling. *Immunol Rev 210*, 171-186.

Honda, K., Takaoka, A., and Taniguchi, T. (2006). Type I interferon [corrected] gene induction by the interferon regulatory factor family of transcription factors. *Immunity 25*, 349-360.

Honda, K., and Taniguchi, T. (2006). IRFs: master regulators of signalling by Toll-like receptors and cytosolic pattern-recognition receptors. *Nat Rev Immunol 6*, 644-658.

Hsu, P.D., Scott, D.A., Weinstein, J.A., Ran, F.A., Konermann, S., Agarwala, V., Li, Y.Q., Fine, E.J., Wu, X.B., Shalem, O.*, et al.* (2013). DNA targeting specificity of RNA-guided Cas9 nucleases. *Nat Biotechnol 31*, 827-+.

Hughes, J.R., Roberts, N., McGowan, S., Hay, D., Giannoulatou, E., Lynch, M., De Gobbi, M., Taylor, S., Gibbons, R., and Higgs, D.R. (2014). Analysis of hundreds of cis-regulatory landscapes at high resolution in a single, high-throughput experiment. *Nat Genet 46*, 205-212.

Ikushima, H., Negishi, H., and Taniguchi, T. (2013). The IRF family transcription factors at the interface of innate and adaptive immune responses. *Cold Spring Harb Symp Quant Biol 78*, 105-116.

Jacobs, M.D., and Harrison, S.C. (1998). Structure of an IkappaBalpha/NF-kappaB complex. *Cell 95*, 749-758.

Ji, X., Dadon, D.B., Powell, B.E., Fan, Z.P., Borges-Rivera, D., Shachar, S., Weintraub, A.S., Hnisz, D., Pegoraro, G., Lee, T.I.*, et al.* (2016). 3D Chromosome Regulatory Landscape of Human Pluripotent Cells. *Cell Stem Cell 18*, 262-275.

Jiang, H., and Peterlin, B.M. (2008). Differential chromatin looping regulates CD4 expression in immature thymocytes. *Mol Cell Biol 28*, 907-912.

Johnson, D.S., Mortazavi, A., Myers, R.M., and Wold, B. (2007). Genome-wide mapping of in vivo protein-DNA interactions. *Science 316*, 1497-1502.

Kagey, M.H., Newman, J.J., Bilodeau, S., Zhan, Y., Orlando, D.A., van Berkum, N.L., Ebmeier, C.C., Goossens, J., Rahl, P.B., Levine, S.S.*, et al.* (2010). Mediator and cohesin connect gene expression and chromatin architecture. *Nature 467*, 430-435.

Karin, M., and Delhase, M. (2000). The I kappa B kinase (IKK) and NF-kappa B: key elements of proinflammatory signalling. *Semin Immunol 12*, 85-98.

Kawai, T., and Akira, S. (2006). TLR signaling. *Cell Death Differ 13*, 816-825.

Kawai, T., and Akira, S. (2010). The role of pattern-recognition receptors in innate immunity: update on Toll-like receptors. *Nat Immunol 11*, 373-384.

Kawai, T., and Akira, S. (2011). Toll-like receptors and their crosstalk with other innate receptors in infection and immunity. *Immunity 34*, 637-650.

Khodor, Y.L., Rodriguez, J., Abruzzi, K.C., Tang, C.H., Marr, M.T., 2nd, and Rosbash, M. (2011). Nascent-seq indicates widespread cotranscriptional pre-mRNA splicing in Drosophila. *Genes Dev 25*, 2502-2512.

Kim, T.K., and Shiekhattar, R. (2015). Architectural and Functional Commonalities between Enhancers and Promoters. *Cell 162*, 948-959.

Kingston, R.E., and Narlikar, G.J. (1999). ATP-dependent remodeling and acetylation as regulators of chromatin fluidity. *Genes Dev 13*, 2339-2352.

Klochendler-Yeivin, A., Fiette, L., Barra, J., Muchardt, C., Babinet, C., and Yaniv, M. (2000). The murine SNF5/INI1 chromatin remodeling factor is essential for embryonic development and tumor suppression. *EMBO Rep 1*, 500-506.

Kornberg, R.D., and Thomas, J.O. (1974). Chromatin structure; oligomers of the histones. *Science 184*, 865-868.

Krijger, P.H.L., Geeven, G., Bianchi, V., Hilvering, C.R.E., and de Laat, W. (2020). 4C-seq from beginning to end: A detailed protocol for sample preparation and data analysis. *Methods 170*, 17-32.

Lander, E.S., Linton, L.M., Birren, B., Nusbaum, C., Zody, M.C., Baldwin, J., Devon, K., Dewar, K., Doyle, M., FitzHugh, W.*, et al.* (2001). Initial sequencing and analysis of the human genome. *Nature 409*, 860-921.

Lee, J., Rhee, M.H., Kim, E., and Cho, J.Y. (2012). BAY 11-7082 is a broad-spectrum inhibitor with anti-inflammatory activity against multiple targets. *Mediators Inflamm 2012*, 416036.

Li, B., Carey, M., and Workman, J.L. (2007). The role of chromatin during transcription. *Cell 128*, 707-719.

Lieberman-Aiden, E., van Berkum, N.L., Williams, L., Imakaev, M., Ragoczy, T., Telling, A., Amit, I., Lajoie, B.R., Sabo, P.J., Dorschner, M.O.*, et al.* (2009). Comprehensive mapping of long-range interactions reveals folding principles of the human genome. *Science 326*, 289-293.

Lifton, R.P., Goldberg, M.L., Karp, R.W., and Hogness, D.S. (1978). The organization of the histone genes in Drosophila melanogaster: functional and evolutionary implications. *Cold Spring Harb Symp Quant Biol 42 Pt 2*, 1047-1051.

Lipniacki, T., Paszek, P., Brasier, A.R., Luxon, B., and Kimmel, M. (2004). Mathematical model of NF-kappaB regulatory module. *J Theor Biol 228*, 195-215.

Lone, I.N., Shukla, M.S., Charles Richard, J.L., Peshev, Z.Y., Dimitrov, S., and Angelov, D. (2013). Binding of NF-κB to nucleosomes: effect of translational positioning, nucleosome remodeling and linker histone H1. *PLoS Genet 9*, e1003830.

Miele, A., and Dekker, J. (2008). Long-range chromosomal interactions and gene regulation. *Mol Biosyst 4*, 1046-1057.

Mogensen, T.H. (2009). Pathogen recognition and inflammatory signaling in innate immune defenses. *Clin Microbiol Rev 22*, 240-273, Table of Contents.

Moreau, P., Hen, R., Wasylyk, B., Everett, R., Gaub, M.P., and Chambon, P. (1981). The SV40 72 base repair repeat has a striking effect on gene expression both in SV40 and other chimeric recombinants. *Nucleic Acids Res 9*, 6047-6068.

Nagalakshmi, U., Wang, Z., Waern, K., Shou, C., Raha, D., Gerstein, M., and Snyder, M. (2008). The transcriptional landscape of the yeast genome defined by RNA sequencing. *Science 320*, 1344-1349.

Narlikar, G.J., Sundaramoorthy, R., and Owen-Hughes, T. (2013). Mechanisms and functions of ATP-dependent chromatin-remodeling enzymes. *Cell 154*, 490-503.

Natoli, G., and Andrau, J.C. (2012). Noncoding transcription at enhancers: general principles and functional models. *Annu Rev Genet 46*, 1-19.

O'Neill, L.A., Golenbock, D., and Bowie, A.G. (2013). The history of Toll-like receptors - redefining innate immunity. *Nat Rev Immunol 13*, 453-460.

Oeckinghaus, A., and Ghosh, S. (2009). The NF-kappaB family of transcription factors and its regulation. *Cold Spring Harb Perspect Biol 1*, a000034.

Osterwalder, M., Barozzi, I., Tissieres, V., Fukuda-Yuzawa, Y., Mannion, B.J., Afzal, S.Y., Lee, E.A., Zhu, Y.W., Plajzer-Frick, I., Pickle, C.S.*, et al.* (2018). Enhancer redundancy provides phenotypic robustness in mammalian development. *Nature 554*, 239-+.

Ostuni, R., Piccolo, V., Barozzi, I., Polletti, S., Termanini, A., Bonifacio, S., Curina, A., Prosperini, E., Ghisletti, S., and Natoli, G. (2013). Latent enhancers activated by stimulation in differentiated cells. *Cell 152*, 157-171.

Panne, D., Maniatis, T., and Harrison, S.C. (2007). An atomic model of the interferon-beta enhanceosome. *Cell 129*, 1111-1123.

Peterson, C.L., Dingwall, A., and Scott, M.P. (1994). Five SWI/SNF gene products are components of a large multisubunit complex required for transcriptional enhancement. *Proc Natl Acad Sci U S A 91*, 2905-2908.

Ralph, P., Spector, W.G., and van Furth, R. (1980). Functions of Macrophage Cell Lines. In Mononuclear Phagocytes: Functional Aspects, R. van Furth, ed. (Dordrecht: Springer Netherlands), pp. 439-457.

Reisman, D., Glaros, S., and Thompson, E.A. (2009). The SWI/SNF complex and cancer. *Oncogene 28*, 1653-1668.

Reuter, J.A., Spacek, D.V., and Snyder, M.P. (2015). High-throughput sequencing technologies. *Mol Cell 58*, 586-597.

Rickels, R., Herz, H.M., Sze, C.C., Cao, K., Morgan, M.A., Collings, C.K., Gause, M., Takahashi, Y.H., Wang, L., Rendleman, E.J.*, et al.* (2017). Histone H3K4 monomethylation catalyzed by Trr and mammalian COMPASS-like proteins at enhancers is dispensable for development and viability. *Nat Genet 49*, 1647-1653.

Roberts, C.W., Galusha, S.A., McMenamin, M.E., Fletcher, C.D., and Orkin, S.H. (2000). Haploinsufficiency of Snf5 (integrase interactor 1) predisposes to malignant rhabdoid tumors in mice. *Proc Natl Acad Sci U S A 97*, 13796-13800.

Roberts, C.W., and Orkin, S.H. (2004). The SWI/SNF complex--chromatin and cancer. *Nat Rev Cancer 4*, 133-142.

Saccani, S., Pantano, S., and Natoli, G. (2001). Two waves of nuclear factor kappaB recruitment to target promoters. *J Exp Med 193*, 1351-1359.

Schoenfelder, S., Javierre, B.M., Furlan-Magaril, M., Wingett, S.W., and Fraser, P. (2018). Promoter Capture Hi-C: High-resolution, Genome-wide Profiling of Promoter Interactions. *J Vis Exp*.

Schones, D.E., Cui, K., Cuddapah, S., Roh, T.Y., Barski, A., Wang, Z., Wei, G., and Zhao, K. (2008). Dynamic regulation of nucleosome positioning in the human genome. *Cell 132*, 887-898.

Sen, R., and Baltimore, D. (1986). Inducibility of kappa immunoglobulin enhancer-binding protein Nf-kappa B by a posttranslational mechanism. *Cell 47*, 921-928.

Simonis, M., Klous, P., Splinter, E., Moshkin, Y., Willemsen, R., de Wit, E., van Steensel, B., and de Laat, W. (2006). Nuclear organization of active and inactive

chromatin domains uncovered by chromosome conformation capture-on-chip (4C). *Nat Genet 38*, 1348-1354.

Skiniotis, G., Moazed, D., and Walz, T. (2007). Acetylated histone tail peptides induce structural rearrangements in the RSC chromatin remodeling complex. *J Biol Chem 282*, 20804-20808.

Smale, S.T. (1997). Transcription initiation from TATA-less promoters within eukaryotic protein-coding genes. *Biochim Biophys Acta 1351*, 73-88.

Smale, S.T., and Kadonaga, J.T. (2003). The RNA polymerase II core promoter. *Annu Rev Biochem 72*, 449-479.

Smale, S.T., Tarakhovsky, A., and Natoli, G. (2014). Chromatin contributions to the regulation of innate immunity. *Annu Rev Immunol 32*, 489-511.

Sun, S.C. (2011). Non-canonical NF-κB signaling pathway. *Cell Res 21*, 71-85.

Takeuchi, O., and Akira, S. (2010). Pattern recognition receptors and inflammation. *Cell 140*, 805-820.

Tamura, T., Yanai, H., Savitsky, D., and Taniguchi, T. (2008). The IRF family transcription factors in immunity and oncogenesis. *Annu Rev Immunol 26*, 535-584.

Tang, L., Nogales, E., and Ciferri, C. (2010). Structure and function of SWI/SNF chromatin remodeling complexes and mechanistic implications for transcription. *Prog Biophys Mol Biol 102*, 122-128.

Tong, A.J., Liu, X., Thomas, B.J., Lissner, M.M., Baker, M.R., Senagolage, M.D., Allred, A.L., Barish, G.D., and Smale, S.T. (2016). A Stringent Systems Approach Uncovers Gene-Specific Mechanisms Regulating Inflammation. *Cell 165*, 165-179.

Trouplin, V., Boucherit, N., Gorvel, L., Conti, F., Mottola, G., and Ghigo, E. (2013). Bone marrow-derived macrophage production. *J Vis Exp*, e50966.

Tuan, D., Kong, S., and Hu, K. (1992). Transcription of the hypersensitive site HS2 enhancer in erythroid cells. *Proc Natl Acad Sci U S A 89*, 11219-11223.

Vakoc, C.R., Letting, D.L., Gheldof, N., Sawado, T., Bender, M.A., Groudine, M., Weiss, M.J., Dekker, J., and Blobel, G.A. (2005). Proximity among distant regulatory elements at the beta-globin locus requires GATA-1 and FOG-1. *Mol Cell 17*, 453-462.

Vallabhapurapu, S., and Karin, M. (2009). Regulation and function of NF-kappaB transcription factors in the immune system. *Annu Rev Immunol 27*, 693-733.

Venter, J.C., Adams, M.D., Myers, E.W., Li, P.W., Mural, R.J., Sutton, G.G., Smith, H.O., Yandell, M., Evans, C.A., Holt, R.A.*, et al.* (2001). The sequence of the human genome. *Science 291*, 1304-1351.

Watson, J.D., and Crick, F.H. (1953). Molecular structure of nucleic acids; a structure for deoxyribose nucleic acid. *Nature 171*, 737-738.

Wilkins, M.H., Stokes, A.R., and Wilson, H.R. (1953). Molecular structure of deoxypentose nucleic acids. *Nature 171*, 738-740.

Yanai, H., Negishi, H., and Taniguchi, T. (2012). The IRF family of transcription factors: Inception, impact and implications in oncogenesis. *Oncoimmunology 1*, 1376-1386.

Zaret, K.S., and Carroll, J.S. (2011). Pioneer transcription factors: establishing competence for gene expression. *Genes Dev 25*, 2227-2241.

Zhang, Y., Liu, T., Meyer, C.A., Eeckhoute, J., Johnson, D.S., Bernstein, B.E., Nusbaum, C., Myers, R.M., Brown, M., Li, W.*, et al.* (2008). Model-based analysis of ChIP-Seq (MACS). *Genome Biol 9*, R137.

Zhao, G.N., Jiang, D.S., and Li, H.L. (2015). Interferon regulatory factors: at the crossroads of immunity, metabolism, and disease. *Bba-Mol Basis Dis 1852*, 365-378.

Zhou, V.W., Goren, A., and Bernstein, B.E. (2011). Charting histone modifications and the functional organization of mammalian genomes. *Nat Rev Genet 12*, 7-18.

APPENDICES

APPENDIX A

Activating an Adaptive Immune Response from a Hydrogel Scaffold Imparts Regenerative Wound Healing

nature materials

ARTICLES

https://doi.org/10.1038/s41563-020-00844-w

Activating an adaptive immune response from a hydrogel scaffold imparts regenerative wound healing

Donald R. Griffin[1,2,15], Maani M. Archang[3,15], Chen-Hsiang Kuan[4,5,6,7], Westbrook M. Weaver[3,14], Jason S. Weinstein[8], An Chieh Feng[9], Amber Ruccia[9], Elias Sideris[1], Vasileios Ragkousis[9], Jaekyung Koh[3], Maksim V. Plikus[5,6,10,11], Dino Di Carlo[3], Tatiana Segura[1,12] ✉ and Philip O. Scumpia[9,13] ✉

Microporous annealed particle (MAP) scaffolds are flowable, in situ crosslinked, microporous scaffolds composed of microgel building blocks and were previously shown to accelerate wound healing. To promote more extensive tissue ingrowth before scaffold degradation, we aimed to slow MAP degradation by switching the chirality of the crosslinking peptides from L- to D-amino acids. Unexpectedly, despite showing the predicted slower enzymatic degradation in vitro, D-peptide crosslinked MAP hydrogel (D-MAP) hastened material degradation in vivo and imparted significant tissue regeneration to healed cutaneous wounds, including increased tensile strength and hair neogenesis. MAP scaffolds recruit IL-33 type 2 myeloid cells, which is amplified in the presence of D-peptides. Remarkably, D-MAP elicited significant antigen-specific immunity against the D-chiral peptides, and an intact adaptive immune system was required for the hydrogel-induced skin regeneration. These findings demonstrate that the generation of an adaptive immune response from a biomaterial is sufficient to induce cutaneous regenerative healing despite faster scaffold degradation.

The goal of regenerative medicine is to restore tissue function back to physiological activity. For biomaterial scaffolds, the optimal strategy to achieve this requires balancing material degradation with tissue regrowth. Clinical and patient factors contribute to a wide variation in chemical and physical parameters in situ, which makes striking a degradative–regenerative balance particularly difficult. Our recent development of a flowable, granular biomaterial, that is, a microporous annealed particle (MAP) gel, provides a new approach to make the balance more feasible[1]. The MAP gel is composed of randomly packed microsphere building blocks with a continuous network of interconnected micrometre-scale void spaces that allows for the infiltration of surrounding tissue without the prerequisite of material degradation[1,2]. This unique design resulted in improved tissue closure and improved vascularization relative to a nanoporous (but chemically equivalent formulation) hydrogel in a cutaneous wound model[1].

Mechanical support to the growing tissue by scaffolds is inherently impacted by the degradation rate of the scaffold[3]. For MAP scaffolds, degradation leads to a slow loss of porosity and reduced tissue ingrowth prior to dissolution. We hypothesized that slowing the degradation rate of MAP scaffolds would maintain the porosity and influence both wound closure rate and regenerated tissue quality.

Changing the chirality of peptide moieties leads to a diminished degradation rate by endogenously present enzymes[4,5]. The use of chirality was made more attractive by the fact that polypeptides of D-enantiomeric amino acids do not typically elicit a robust immune response and are considered poorly immunogenic[5]. Previously, we used amino acid chirality to tune the proteolysis rate of peptide nanocapsules for the controlled release of encapsulated growth factors[4]. Therefore, we chose to use an analogous approach to slow the enzymatic degradation of our MAP scaffold by switching the chirality of the peptide crosslinker (for example, L- to D-chirality at the site of matrix metalloprotease (MMP)-mediated bond cleavage). We hypothesized that this approach would maintain the hydrogel microenvironment (for example, charge-based interactions and hydrophobicity) as it increased the long-term hydrogel integrity to allow a full infiltration of cells, and thus provide a greater integration of the entire construct with the host tissue.

In the current study, we investigated how MAP hydrogels crosslinked with either D- or L-amino acid crosslinking peptides affect wound healing and skin regenerative responses using murine wound models. We provide evidence that activation of specific immune responses by the D-amino acid crosslinked MAP hydrogels elicits skin regeneration. Although immunity undoubtedly activates the foreign body response and eventual fibrosis of some implanted

[1]Chemical and Biomolecular Engineering Department, University of California, Los Angeles, CA, USA. [2]Departments of Biomedical Engineering and Chemical Engineering, University of Virginia, Charlottesville, VA, USA. [3]Bioengineering Department, University of California, Los Angeles, CA, USA. [4]Graduate Institute of Clinical Medicine, College of Medicine, National Taiwan University, Taipei, Taiwan. [5]Department of Developmental and Cell Biology, University of California, Irvine, CA, USA. [6]Sue and Bill Gross Stem Cell Research Center, University of California, Irvine, CA, USA. [7]Division of Plastic Surgery, Department of Surgery, National Taiwan University Hospital, Taipei, Taiwan. [8]Department of Medicine and Center for Immunity & Inflammation, Rutgers –New Jersey Medical School, Newark, NJ, USA. [9]Division of Dermatology, Department of Medicine, David Geffen School of Medicine, University of California, Los Angeles, CA, USA. [10]Center for Complex Biological Systems, University of California, Irvine, CA, USA. [11]NSF-Simons Center for Multiscale Cell Fate Research, University of California-Irvine, Irvine, CA, USA. [12]Departments of Biomedical Engineering, Neurology, Dermatology, Duke University, Durham, NC, USA. [13]Department of Dermatology, VA Greater Los Angeles Healthcare System-West Los Angeles, Los Angeles, CA, USA. [14]Present address: Tempo Therapeutics, San Diego, CA, USA. [15]These authors contributed equally: Donald R. Griffin and Maani M. Archang.
✉e-mail: PScumpia@mednet.ucla.edu; Tatiana.segura@duke.edu

biomaterials[6,7], the activation of the correct immune responses may enhance the regenerative ability of a biomaterial[8,9].

D-chiral crosslinker peptides slow MAP degradation in vitro

We first used enantiomeric peptides to change the degradation rate without changing the initial material properties (for example, hydrophobicity, mesh size and charge) of the hydrogel[4]. All amino acids at the site of the enzymatic cleavage for the MMP-degradable peptide were changed to D-amino acids (Ac-GCRDGPQ$_a$GI$_a$W$_a$GQDRCG-NH$_2$, D-peptide). We matched the stiffness (that is, storage modulus) by rheology of both the D-peptide MAP (D-MAP) and L-peptide (L-MAP) formulations to that used in our previous MAP-based cutaneous application (~500 Pa; Fig. 1a). After formulation optimization, we generated the microsphere particles using a previously published microfluidic technique[1]. Following the application of collagenase I to L-MAP, D-MAP or a 50% mixture of D-MAP and L-MAP (1:1 L/D-MAP), the L-MAP hydrogel degraded within minutes, whereas the degradation of the D-MAP by itself or within a mixture with L-MAP was minimal even after one hour (Fig. 1b and Supplementary Fig. 1).

D-chiral crosslinker peptides enhance MAP degradation in vivo

We next examined how D-MAP compares with L-MAP in vivo in a murine splinted excisional wound model[1,10]. We did not find any difference in the wound closure rate or any increased erythema or gross signs of inflammation in wounds treated with D-MAP, L-MAP or a 1:1 mixture of L/D-MAP any time after treatment (days 3 and 6 after wounding are shown in Supplementary Fig. 1a). When comparing wound closure to sham treatment (no hydrogel), we found that a 1:1 mixture of L/D-MAP induced a more rapid wound closure (assessed on day 9 after wounding) than that of sham (Supplementary Fig. 2b), similar to previous results with L-MAP hydrogel[1].

As no differences in wound closure results were noted, we next examined whether the degradation of hydrogels that contained D-amino acid crosslinkers was slowed in vivo by examining excised tissue 21 days after the wound was completely healed. Unexpectedly, histological sections of wounds treated with D-MAP or a 1:1 L/D-MAP hydrogel mixture displayed minimal to no hydrogel persistence 21 days after wounding, near to levels seen in mice not treated with hydrogel (sham), whereas wounds treated with L-MAP hydrogel displayed large amounts of hydrogel remaining (Fig. 1c–f).

D-MAP hydrogels impart tissue regenerative properties

Of note, the initial examination of histological sections of D-MAP and 1:1 L/D-MAP displayed a much different overall appearance than that of the healed sham- or L-MAP-treated wounds. Previous reports suggest that, unlike large excisional wounds in adult mice (wounds larger than 1 × 1 cm), which result in significant regenerative healing with wound-induced hair neogenesis (WIHN)[11–13], wounds smaller than 1 × 1 cm in mice, like the punch biopsies performed in our studies, typically heal without regeneration of new hair and fat and, instead, form scars[12,14,15]. Despite these reports, when the correct regenerative cues are provided from wound fibroblasts, through transgenic activation of specific Hedgehog signals, small wounds can regenerate[16]. Consistent with these results, histological examination of 4 mm excisional splinted wounds in mice that did not receive hydrogel (sham) displayed the typical appearance of scar tissue with a flattened epidermis, a thinned dermis with horizontally oriented collagen bundles, vertically oriented blood vessels and the lack of hair follicles and sebaceous glands (Fig. 1c,g–i). Tissue from mice treated with the L-MAP hydrogel displayed a similar appearance, but with a thicker overall tissue compared with that of sham wounds, due to the substantial residual L-MAP hydrogels (Fig. 1d,g). Within the dermis that surrounds the hydrogel, fibroblasts that secreted collagen and/or extracellular matrix and blood vessels formed between the hydrogel microparticles (Fig. 1d). Only rare hair follicles and associated sebaceous glands were observed in the wound areas (Fig. 1d,h,i). Remarkably, examination of histological sections of the D-MAP- or 1:1 L/D-MAP-treated tissue revealed a de novo regenerated appearance. The overlying epidermis often displayed physiological undulation, and numerous immature-appearing hair follicles were seen to span the length of the healed full-thickness injury (Fig. 1e–i). Samples treated with D-MAP or 1:1 L/D-MAP also displayed an increased skin thickness despite less hydrogel remaining in these samples (Fig. 1f). Many samples also displayed epidermal cyst formation. In samples that displayed residual hydrogel, hair follicles that directly overlaid the degrading MAP hydrogel particles were apparent (Supplementary Fig. 2c). The presence of hair follicles in SKH1 mice was suggestive of embryonic-like tissue regeneration, a phenomenon not often observed in the murine small-wound model.

To further quantify tissue regeneration, we next performed tensile strength testing on unsplinted incisional wounds in SKH1 mice using a modified literature protocol[17]. We found that scar tissue from sham wounds revealed a tensile strength that was approximately 15% of that of unwounded skin from the same animal (Fig. 1i). Although the treatment of wounds with L-MAP hydrogel did not result in a significant increase in tissue tensile strength, treatment with either D- or L/D-MAP resulted in an ~80% improvement in tensile strength (Fig. 1j).

Hair follicles in D-MAP-treated wounds are neogenic

We next repeated wound-healing experiments in C57BL/6 (B6) mice to investigate if the regenerative phenomenon observed in D-MAP treated wounds was similar to that in WIHN. We chose sham as control and D-MAP as a treatment method that showed evidence of regeneration in SKH1 mice. Similar to the sham- and L-MAP-treated wounds in SKH1 mice, the B6 mice wounds without hydrogel (sham) displayed a typical scar appearance with haematoxylin and eosin (H&E) and Masson's trichrome staining (Fig. 2a,c,e). In contrast, histological sections of the D-MAP-treated tissue revealed clear signs of WIHN. As in SKH1 mice, D-MAP-treated B6 mice wounds displayed undulations and numerous epidermal cysts under the epidermis, whereas the dermis was thicker. Importantly, many neogenic hair follicles developed in the wound (Fig. 2b,d,f). The neogenic hair follicles were in the early anagen phases with an immature appearance, yet many of them had already formed new sebaceous glands (Fig. 2b) and featured a prominent SOX9$^+$ bulge stem cell region (Fig. 2j). In several instances, neogenic hair follicles were physically connected to epidermal cysts (a morphology not expected from pre-existing follicles). This suggests that in D-MAP-treated wounds, epidermal cysts can be the initiation sites for de novo morphogenesis for at least some of the neogenic hair follicles (Fig. 2h). Masson's trichrome staining confirmed the presence of neogenic hair follicles within the collagen matrix of the wound bed (Fig. 2b,f). Furthermore, regenerating day 18 D-MAP-treated wounds with neogenic hair follicles lacked PLIN$^+$ dermal adipocytes (Fig. 2h), which is consistent with a slower regeneration of neogenic adipocytes that occurs four weeks after wounding in the large wound-induced WIHN[18,19]. Thus, the addition of D-MAP to normally non-regenerating 4 mm excisional wounds activates hair follicle neogenesis.

D-MAP hydrogel implants enhance myeloid cell recruitment

To determine whether an enhanced immune response led to an enhanced D-MAP or 1:1 L:D-MAP degradation in the wound microenvironment, we utilized a subcutaneous implantation model that also allowed for larger amounts of hydrogel to be implanted, and

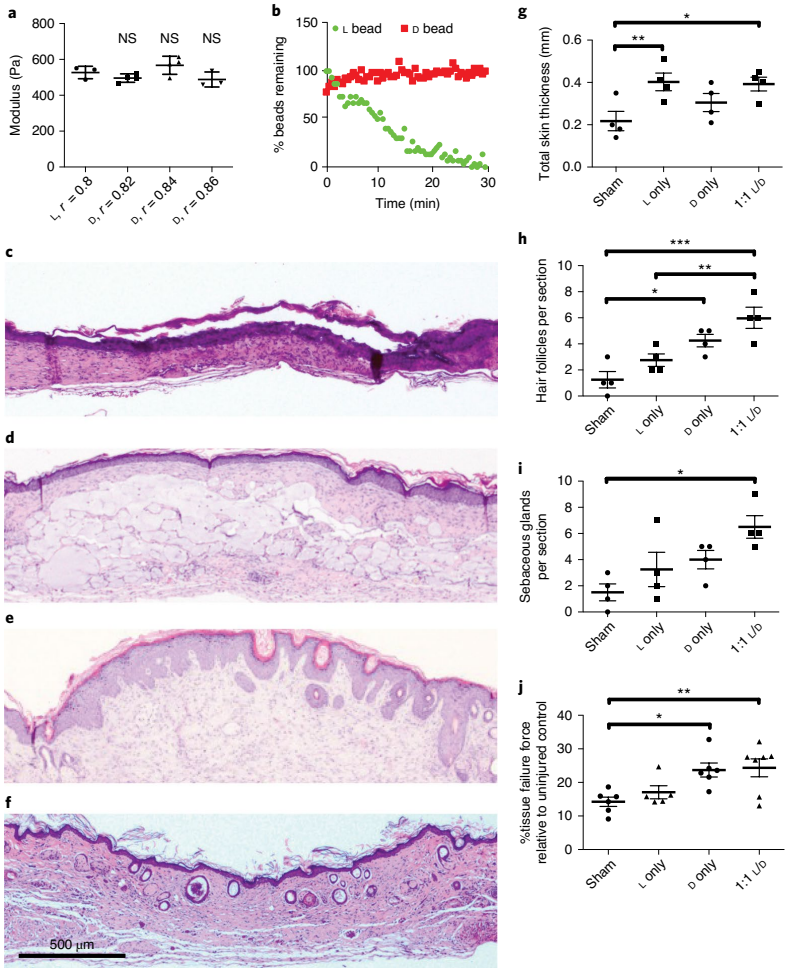

Fig. 1 | D-MAP hydrogel degradation is enhanced in wounds of SKH1 hairless mice. a, Rheological characterization of MAP hydrogels composed of L or D-peptide crosslinked microgels. The *r* ratio (ratio of sulfydryl (SH) to vinyl sulfone (VS)) used to form the microgels was changed to arrive at the same storage modulus for both L- and D-MAP scaffolds. NS, no statistical significance between the L-MAP scaffold to the D-MAP scaffold indicated using a two-tailed Student's *t*-test. **b**, Fabricated L- or D-hydrogels were tested for in vitro enzymolysis behaviour through exposure to a solution of collagenase I (5 U ml^{-1}). **c**–**f**, Representative low-power view of H&E sections from healed skin 21 days after splinted excisional wounding in SKH1 mice treated by from sham (**c**), L-MAP (**d**), D-MAP (**e**) and a 1:1 mixture of L-MAP and D-MAP (**f**). **g**–**i**, Histologic quantification of dermal thickness including gels (**g**) (mm), hair follicles (**h**) and sebaceous glands (**i**). Each point represents the average of two sections from two separate slides of one wound. Each data point represents one animal and all the analysis is by one-way analysis of variance (ANOVA) (F (3,12), 4.448 (**g**), 10.89 (**h**) and 5.074 (**i**); Tukey multiple comparisons tests, $^{*}P = 0.0460$, $^{**}P = 0.0341$ (**g**), $^{*}P = 0.0220$, $^{**}P = 0.0133$, $^{***}P = 0.0007$ (**h**), $^{*}P = 0.0110$ (**i**)). **j**, The incisional, unsplinted wounds were created and, 28 days afterwards, the healed wounds treated without or with the different hydrogels were tested against unwounded skin in the same mouse. The tensile strength was evaluated by tensiometry and reported as a percentage of the tensile strength of the scar tissue when compared with that of the normal skin of the same mouse. Each data point represents the average of two measurements from one wound, separate from wounds used in **b**–**i** with the analysis by one-way ANOVA (F (3, 20), 5.400; $^{*}P = 0.0273$, $^{**}P = 0.0131$). Data are plotted as a scatter plot showing the mean and s.d.

thus remain present for longer than in the small excisional wound model. To test whether the subcutaneous implants of the D-MAP hydrogel resulted in an enhanced immune cell recruitment, we utilized immunofluorescent microscopy with AlexaFluor488-labelled MAP hydrogel. We found that implants that contained only L-MAP displayed a background level of CD11b cells within the hydrogel, as previously observed[1], whereas D-MAP or L/D-MAP resulted in the robust accumulation of CD11b-expressing myeloid cells within and around the scaffold (Fig. 3a,b). A standard histological analysis of a repeat experiment of different formulations of subcutaneously implanted MAP hydrogel confirmed the activation of type 2 immunity with an atypical type 2 granulomatous response dominated

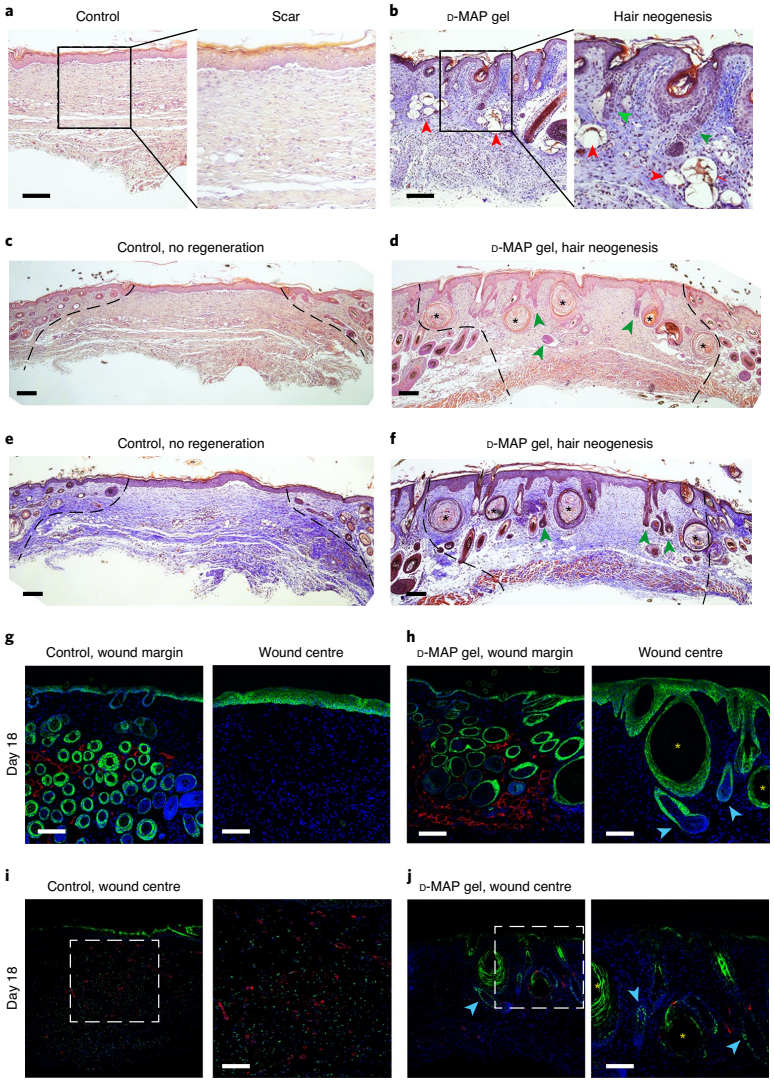

Fig. 2 | D-MAP hydrogel induces neogenesis of hair follicles in full-thickness skin wounds in B6 mice. a–f, H&E (**a**,**c**,**d**) and Masson's trichrome staining (**b**,**e**,**f**) of healed 4 mm full-thickness splinted skin wound on day 18. Control (sham-treated) wounds heal with scarring (**a**,**c**,**e**), whereas D-MAP-treated wounds form numerous epidermal cysts (asterisks) and, prominently, regenerate de novo hair follicles (green arrowheads) (**b**,**d**,**f**). In some instances, neogenic hair follicles form in close association with epidermal cysts. As compared with normal, pre-existing anagen hair follicles at the wound edges, neogenic hair follicles display early anagen stage morphology (the wound edges in **c**–**f** are outlined by dashed lines and the D-MAP hydrogel remnants in **b** are marked with red arrowheads). **g**,**h**, Immunostaining for the epithelial marker KRT5 (green) and the adipocyte marker PLIN (red) reveals normal KRT5$^+$ anagen hair follicles and many mature PLIN$^+$ dermal adipocytes (left panels in **g** and **h**). Regeneration of new KRT5$^+$ hair follicles (blue arrowheads in **h**) along with KRT5$^+$ epidermal cysts (yellow) was observed only in D-MAP-treated wounds (right panels in **g** and **h**). No neogenic adipocytes were observed in hair-forming D-MAP-treated wounds. Blue shows DAPI (4′,6-diamidino-2-phenylindole) staining. **i**,**j**, Immunostaining for SOX9 (green) and SMA (red) reveals many SOX9$^+$ epithelial cells within the bulge region of neogenic hair follicles on day 18 D-MAP-treated wounds (blue arrowheads in **j**). In contrast, in control (sham-treated) wounds that undergo scarring, the dermal wound portion contains many SOX9$^+$ cells, many of which also co-express contractile marker SMA (**i**). Expression of SMA was also seen in both control and D-MAP-treated samples in blood vessels. Scale bars, 100 μm. The images are representative of slides from four animals per group.

by the accumulation of individual macrophages within and around the D-MAP hydrogel implants, but not the L-MAP hydrogel implants (Supplementary Fig. 3a and Supplementary Discussion). Immunofluorescent staining for F4/80 and CD11b confirmed the enhanced recruitment of the macrophages, without giant cell formation, in D-MAP implants (Supplementary Fig. 3b,c and

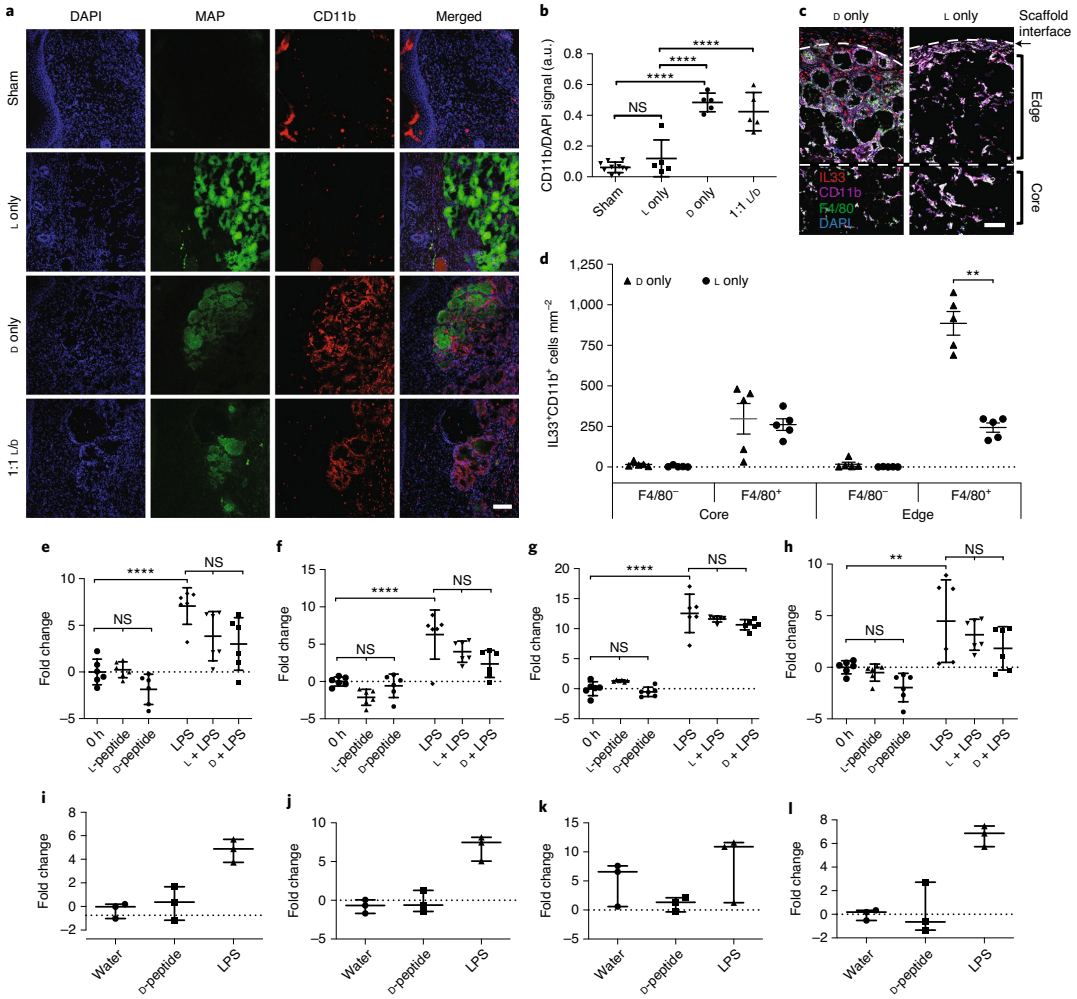

Fig. 3 | Peptide recognition by pattern recognition receptors is not required for myeloid cell recruitment. a, Representative confocal immunofluorescent images of stained myeloid cells (CD11b$^+$) within healed wounds of B6 mice in the presence of the indicated hydrogel. Scale bar, 100 μm. **b**. Localized immune response. Quantification of a CD11b$^+$ cellular infiltrate in healed tissue 21 days after wounding in the presence or absence of a hydrogel. Each point represents average of three slides for each wound. All the analyses are by one-way ANOVA (F (3,21) 41.10; $^{****}P < 0.0001$). **c**,**d**, Representative high-resolution confocal immunofluorescence imaging for CD11b, F4/80, DAPI and IL-33 from subcutaneous implants of L- or D-MAP hydrogel implants (**c**) and quantification of IL-33-producing macrophages and other myeloid cells at the hydrogel edge and core (**d**). $n = 5$ B6 mice, mean ± s.e.m., multiple t-tests adjusted for multiple comparisons using the Holm–Sidak method. $^{**}P = 0.00014$). Scale bar, 100 μm. **e**–**h**, For the uncleaved peptide, murine BMDMs from B6 mice were stimulated with 500 μg ml^{-1} of full-length L- or D-crosslinker peptide in the presence or absence of the LPS (10 ng ml^{-1}) for 6 h. Shown are the quantitative PCR results of four inflammatory genes (*Cxcl1* (**e**), *Tnf* (**f**), *Il1b* (**g**) and *Mx1* (**h**) expression) for two separate experiments performed with $n = 6$. All the analyses are by one-way ANOVA (F (5, 30), 15.66, 17.62, 107.1 and 8.229, respectively; $^{**}P = 0.009$, $^{****}P < 0.0001$). **i**–**l**, For the cleaved peptide, BMDMs were stimulated with LPS (10 ng ml^{-1}) or cleaved D-crosslinker peptide (500 μg ml^{-1}) that possessed an N-terminal D-amino acid (*Cxcl1* (**i**), *Tnf* (**j**), *Il1b* (**k**) and *Mx1* (**l**) expression). The experiment was performed in triplicate. All the analyses are by one-way ANOVA (F (2,6), 20.28, 30.86, 2.178 and 22.72, respectively). Data are plotted as a scatter plot showing the mean and s.d. a.u., arbitrary units.

Supplementary Discussion). These results confirm that D-MAP elicits a more robust immune response and degradation by the accumulated immune cells probably contributed to the enhanced degradation of D-MAP in our previous wound experiments.

Allergic responses and parasites can elicit a type 2 immune response, which includes atypical type 2 granulomatous responses, at least partially through interleukin (IL)-33 production by epithelial cells, recruited myeloid cells and resident macrophages[20–23].

Implanted, non-degradable microparticle-based materials elicit an IL-33-dependent type 2 innate immune response by circulating $CD11b^+$ myeloid cells and macrophages[24]. It is possible that MAP particles could activate this same programme, especially given the atypical type 2 foreign body responses observed in D-MAP samples. Indeed, 21 days after implantation, we found similar numbers of IL-33-expressing $F4/80^+CD11b^+$ macrophages in the centre and/or core of both L- and D-MAP implants (Fig. 3c,d), consistent with both L- and D-MAP samples activating this type 2 pathway. However, there was a dramatic increase in IL-33-producing $IL\text{-}33^+F4/80^+$ macrophages at the edges of the only D-MAP implants (Fig. 3c,d). These results confirm that the hydrogel possesses a type 2 innate 'adjuvant' effect, which may activate the adaptive immune system and contribute to the enhanced immune activation with the D-MAP hydrogel. When L-MAP scaffolds are used, the immune response remains mild as the hydrogel degrades slowly over time[25], but the presence of D-peptide accelerates the immune-mediated degradation.

Free D-chiral peptides avoid pathogen recognition receptors

We next tested whether D-peptides could directly activate innate immunity through a traditional PRR (pattern recognition receptor)-induced transcriptional response. We stimulated murine bone marrow derived macrophages (BMDMs) with L-peptide or D-peptide in the presence or absence of bacterial lipopolysaccharide (LPS), the Toll-like receptor 4 agonist that results in rapid macrophage transcriptional responses. We chose to examine genes reliably and potently induced downstream of the major signalling pathways downstream of a variety of cellular insult (AP-1, MAPK, NF-κB and type I IFN)) to simultaneously interrogate multiple PRR pathways[26–28]. To our surprise, neither L- nor D-amino acid that contained crosslinking peptides alone at high doses (1 mg ml^{-1}) induced the expression of pro-inflammatory genes *Tnf* (NF-κB dependent), *Il1b* (NF-κB and MAPK dependent), *Cxcl2* (AP-1 dependent early response) or *Mx1* (type I IFN dependent) in murine BMDMs at six hours (t_{max} of the gene induction; Fig. 3e–l). Additionally, neither L- nor D-peptides enhanced the ability of LPS to induce the expression of these same genes (Fig. 3e–h).

Previous studies showed that peptides that contain an *N*-terminal D-methionine can activate the innate immune receptor formyl peptide receptor 2 and formyl peptide-like receptor 2[29–31]. As the cleavage of a D-amino acid peptide can result in shorter peptides that contain a D-amino acid at the *N*-terminus, we next wished to examine whether a peptide that corresponded to the cleaved D-peptide could activate inflammatory responses in BMDMs. Similar to the results with the intact D-peptide, a high concentrations of cleaved D-peptide (1 mg ml^{-1}) did not induce the transcription of *Tnf*, *Il1b*, *Cxcl2* or *Mx1* at six hours (Fig. 3i–l). As there is a very low likelihood that the cleaved D-peptide will be present at such high local concentrations within the implanted hydrogel while it is being degraded in vivo, these show that D-chiral peptides are poor activators of a traditional PRR-mediated inflammatory response in macrophages and suggest that D-peptides may act as antigens to enhance immunity, which leads to the enhanced degradation of D-MAP.

D-MAP elicits antigen-specific humoral immunity

We next evaluated whether the D-MAP activated adaptive immunity. The adaptive immune system recognizes non-self-peptide antigens to induce cell mediated (T-cell) and humoral (B-cell) immunity. Peptides that contain D-amino acids were reported to activate or suppress T-cell dependent and T-cell independent adaptive immune responses[5,32]. In the context of the MAP, crosslinking peptides that are non-native may be presented to the immune system until fully degraded. D-peptides could be presented by antigen-presenting cells directly to T cells, which elicits a T-cell dependent adaptive immune response or, alternatively, the presence of D-amino acid-containing peptides on the surface of a large molecule of a MAP hydrogel could directly crosslink the B-cell receptor, which leads to a T-cell independent antibody responses similar to that of T-cell independent antigens. To test this hypothesis, we examined whether mice that were wounded or received subcutaneous implants of L-MAP, D-MAP or 1:1 L/D-MAP were able to develop T-helper cell dependent (IgG1 or IgG2a) or T-cell independent (IgG3) antibodies against L- or D-amino acid-containing crosslinkers[33–36].

Indeed, regardless of whether a D-containing MAP hydrogel was applied to wounded tissue or given via subcutaneous implants, mice developed a T-cell dependent IgG1 and IgG2a response against the D-amino acid-containing peptide, but not a T-cell independent IgG3 response. These results are more consistent with a T cell-dependent immune response against D-peptides (Fig. 4a, b). IgG1 is typically associated with a Th2 'tissue repair' type response, whereas IgG2a is typically associated with a Th1 'foreign body' response that typically requires strong adjuvants to develop, which depend on the strain of the mice[37,38]. The fact that anti-D-peptide-specific IgG2a was induced when the hydrogel was given to mice in a wound environment but not when the hydrogel was given in the subcutaneous implant model suggests that, by itself, the hydrogel does not possess sufficient adjuvant effects to induce robust Th1 responses. However, the inflammation present in the wound environment may result in a mixed Th2/Th1 response to the D-MAP (Figs. 3e and 4b). Mice that were treated with L-MAP alone did not develop antibody responses to the L-peptide.

D-MAP recruits myeloid cells via adaptive immune response

Our data suggest that the activation of adaptive immune responses to D-MAP contributes to the immune infiltration and degradation of D-MAP. To test this hypothesis further, we examined whether Balb/c.$Rag2^{-/-}\gamma c^{-/-}$ mice, which are devoid of an adaptive immune system, innate lymphoid cells and IL-2/IL-15 signalling, but possess a fully functional myeloid system, will exhibit a reduced immune infiltration[39]. Indeed, the total cellularity and specific recruitment of $CD11b^+$ myeloid cells to D-MAP hydrogel in Balb/c.$Rag2^{-/-}\gamma c^{-/-}$ mice decreased to comparable levels to those seen in L-MAP in wild-type mice (Fig. 4k,l).

D-MAP-induced skin regeneration relies on adaptive immunity

To determine whether the adaptive immune response was required for the development of neogenic hair follicles, we next performed excisional splinted wounds in B6 and B6.$Rag1^{-/-}$ mice and examined them 25 days after wounding with untreated (sham) or treated wounds with the 1:1 L/D-MAP gel. Of note, in preliminary studies scars induced by 4-mm-punch wounds healed with extremely small scars in B6 mice, so we used a 6 mm punch in this experiment.

Sham wounds in B6 mice demonstrated obvious depigmented, irregularly shaped scars, whereas scars in B6 mice treated with 1:1 L/D-MAP gel were difficult to identify visually as they displayed hair growth over the wounds and less atrophy and/or fewer surface changes typically seen in scars (representative example is shown in Fig. 5a, and all the wound images in Supplementary Fig. 4). Scars in sham-treated or 1:1 L/D-MAP-treated B6.$Rag1^{-/-}$ mice were smaller than those in sham-treated B6 mice, but were identifiable in B6.$Rag1^{-/-}$ mice regardless of whether the wounds were sham treated or hydrogel treated (Fig. 5a). All wound areas of the injuries (which included 1:1 L/D-MAP-treated B6 wound areas) were confirmed by examining the defect on the fascial side of the tissue after the excision of skin. Histological sections of the healed skin of mice displayed significant neogenic hairs and sebaceous glands only in wounds of wild-type mice treated with 1:1 L/D-MAP (Fig. 5b–d and Supplementary Fig. 5). Sham wounds in B6 and $Rag^{-/-}$ mice,

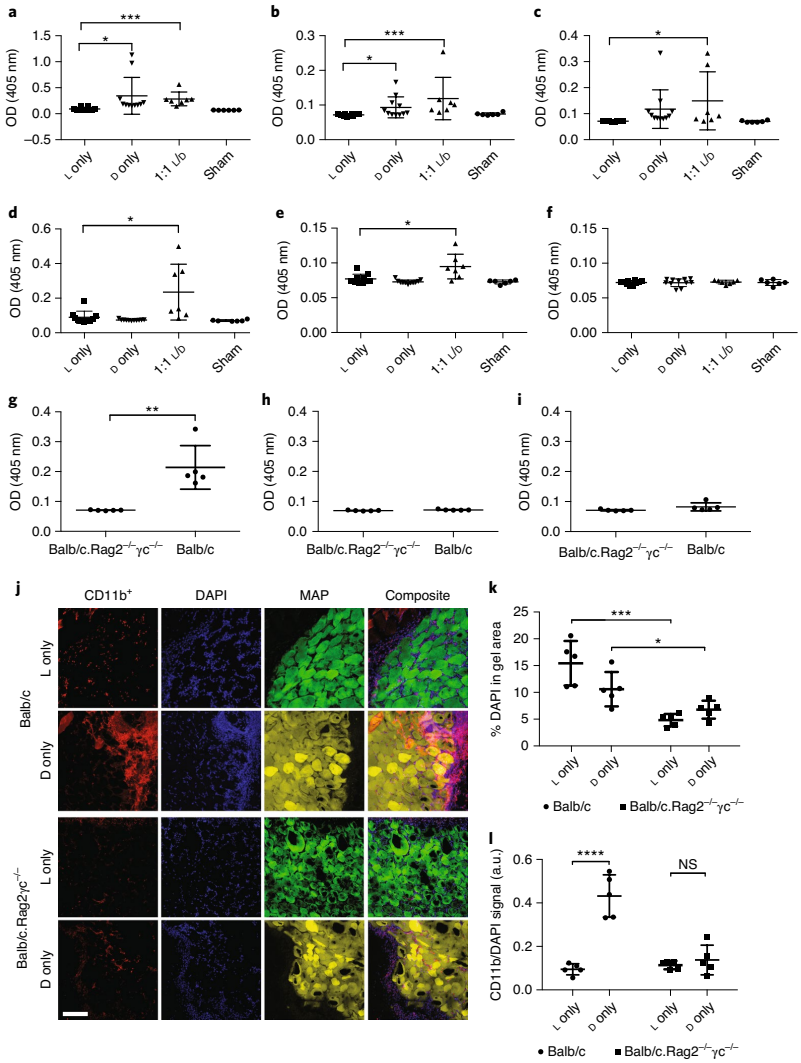

Fig. 4 | D-MAP induces antibody responses and the recruitment of myeloid cells via adaptive immunity. a–f, Wound-healing model. **a–c**, Measurement of anti-d-specific IgG subtype antibodies (anti-d peptide IgG1 (**a**, $^{*}P=0.0384$, $^{***}P=0.0004$), anti-d peptide IgG2a (**b**, $^{*}P=0.0351$, $^{***}P=0.0262$) and anti-d peptide IgG3 (**c**, $^{*}P=0.0396$)) by enzyme-linked immunosorbent assay (ELISA) 21 days after the wound healing experiments in SKH1 mice treated with the indicated hydrogels. **d–f**, Measurement of anti-l specific IgG subtype antibodies (anti-l peptide IgG1 (**d**, $^{*}P=0.0137$), anti-l peptide IgG2a (**e**, $^{*}P=0.0115$) and anti-l peptide IgG3 (**f**)) by ELISA 21 days after the wound healing experiments in SKH1 mice treated with indicated hydrogels. Each data point represents one animal and all the analyses in **a–f** are by an unpaired two-tailed t-test that compared each condition to l only. **g–i**, Subcutaneous injection model. Measurement of anti-d specific IgG subtype antibodies (anti-d peptide IgG1 (**g**, $^{**}P=0.0022$), anti-d peptide IgG2a (**h**) and anti-d peptide IgG3 (**i**)) in Balb/c or Balb/c.Rag2−/−γc−/− mice given a subcutaneous injection of d-MAP 21 days after injection. Each data point represents one animal and all the analyses in **g–i** are by an unpaired two-tailed t-test. **j–l**, Representative examples of confocal immunofluorescent imaging for CD11b, DAPI and hydrogel from subcutaneous implants of l- or d-MAP hydrogel implants in Balb/c or Balb/c.Rag2−/−γc−/− mice (**j**), and quantification of total DAPI+ cells (**k**, $^{*}P=0.0455$, $^{***}P=0.0006$) and CD11b+ myeloid cells (**l**, $^{****}P<0.0001$). Scale bar, 200 μm. Data are plotted as a scatter plot showing the mean and s.d. Each point represents the average of three slides for each wound. All the analyses are by an unpaired two-tailed t-test represent statistical significance by Student's t-test for the comparison indicated. OD, outer diameter.

and in the 1:1 L/D-MAP-treated B6.Rag1$^{-/-}$ mice, displayed prominent scars, without hairs or sebaceous glands, which confirms the requirement of an adaptive immune system in skin regeneration by a MAP gel that contains a D-peptide (Fig. 5b–d). These studies highlight that hair follicle structures can be regenerated through adaptive immune activation from MAP hydrogel scaffolds.

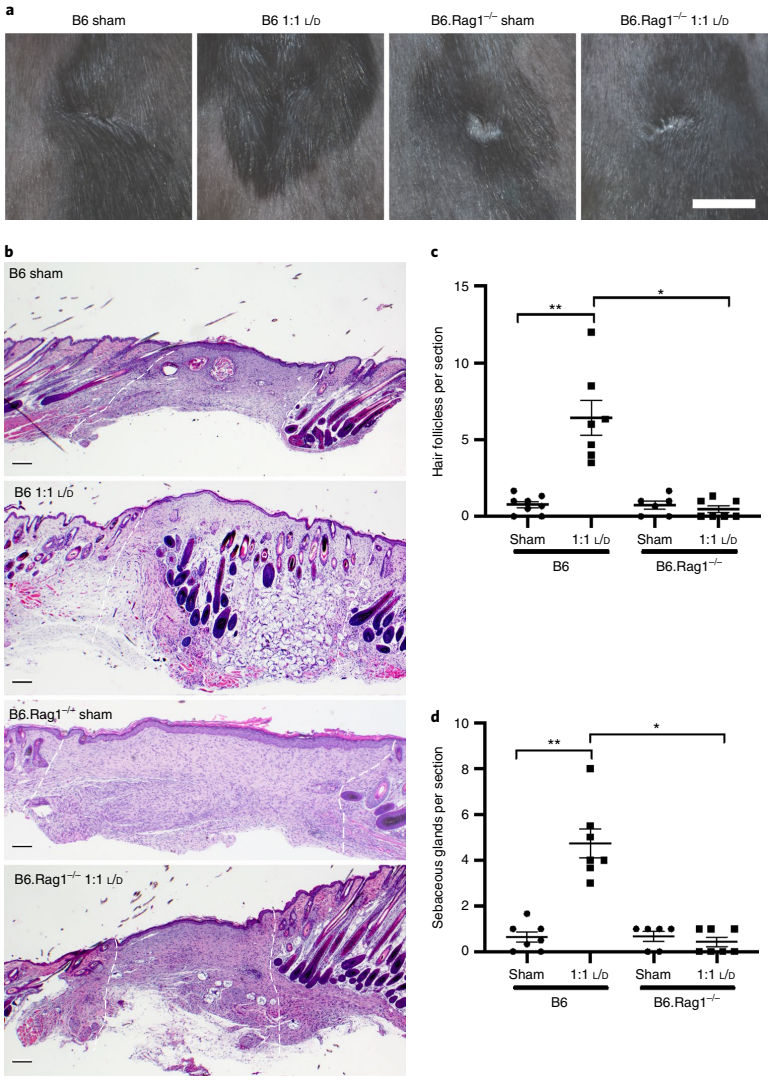

Fig. 5 | D-MAP requires an intact adaptive immunity to induce hair follicle neogenesis. a, Representative examples of gross clinical images of healed splinted excisional wounds in B6 or B6.Rag1$^{-/-}$ mice by a digital single-lens reflex camera 17 days later of sham (no hydrogel) or 1:1 L/D-MAP treatment. Scale bar, 5 mm. **b**, Histologic sections of healed tissue from B6 or B6.Rag1$^{-/-}$ mice. Scale bar, 200 μm. The white dashed lines denote wounded area. **c**,**d**, Quantification of the average numbers of hair follicles (**c**) and sebaceous glands **d**) from three histological sections per sample from B6 mice and B6.Rag1$^{-/-}$ mice. Data are plotted as a scatter plot showing the mean and s.e.m. *Two-tailed $P = 0.002$ by Mann–Whitney test for an interstrain/identical treatment comparison; **$P = 0.0039$ by a Wilcoxon test for an intrastrain/different treatment comparison.

Discussion

In most mammals, the natural process of scar formation and tissue fibrosis is highly evolved and a tissue-scale attempt to restore critical barrier functions for survival. This process, however, is ultimately a biological 'triage' that favours the rapid deposition of a fibrotic matrix to restore the barrier at the expense of a loss of function of complex tissue. In the skin, this fibrotic response results not only in a loss of functioning adnexal structures, but skin tissue that is more fragile and prone to reinjury. A major goal when engineering skin regeneration is to allow for the rapid restoration of barrier function while providing an increased tissue tensile strength and higher tissue function. Many biomaterial-based approaches, which include the addition of growth factors and decellularized extracellular matrix constructs, display limited success in restoring function in wounds. We previously showed that the MAP scaffold can accelerate wound closure in murine wounds[1]. Our findings reported

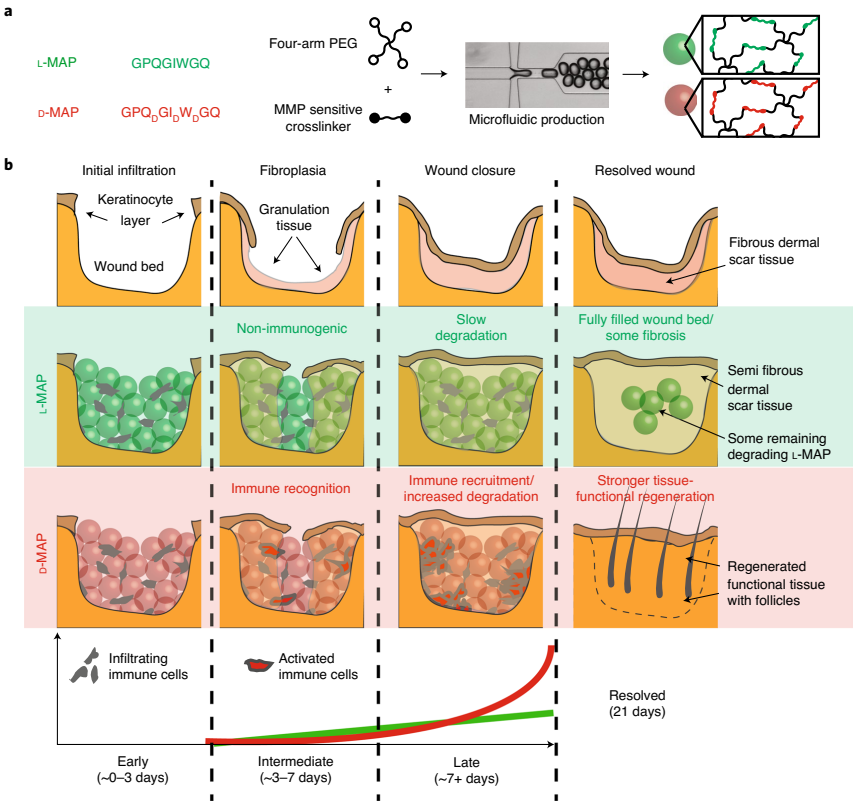

Fig. 6 | D-MAP changes the wound fate from scar formation to regeneration by type 2 immune activation. a, Representation of the MMP cleavage sequences, amino acid chirality within the crosslinking peptides and microfluidic formation of the hydrogel microbeads that incorporate L- or D-chirality peptides. **b**, The use of L- or D-MAP in a wound-healing model demonstrates that both the L-MAP (green) and D-MAP (red) hydrogels fill the wound defect. Wounds that heal in the absence of a hydrogel heal with an atrophic scar and loss of tissue (top row), whereas the epidermis forms over the scaffold with both L- and D-MAP and allows an increased dermal thickness (middle two rows). However, in the case of D-MAP, the hydrogel activates the adaptive immune system over time, which results in tissue remodelling and skin regeneration as the adaptive immune system degrades the D-MAP scaffold (bottom row). PEG, polyethylene glycol.

here further highlight that the incorporation of a modest adaptation of MAP that enhanced a type 2 innate and adaptive immune response induced skin regeneration—hair neogenesis and improved tensile strength (Fig. 6). This response was dependent on the generation of an adaptive immune response to D-enantiomeric peptides and occurred without the addition of stem cells, growth factors or adjuvants. Importantly, this regenerative response was decoupled from wound closure that begins immediately, consistent with the time needed to generate an antigen-specific immune response.

Although adaptive immunity can contribute to fibrosis, foreign body formation and the rejection of biomaterial implants[6–8], adaptive immune activation from a growth factor that contains extracellular matrices can enhance muscle regeneration[8,9]. Further, other biomaterials were created to directly activate specific components of the immune system to treat cancer as immunotherapy platforms[40,41]. In concert, these studies suggest that the role of the adaptive immune system in tissue repair is substantially more complex than previously realized. Our findings suggest that an engineered type 2 immune response to sterile, degradable microparticle-based materials can trigger regeneration rather than fibrosis and further support a role of adaptive immune cells to restore tissue function. Finally, we display the potential of the MAP scaffold as a potent immunomodulatory platform. Future identification of immune factors that tip the balance towards regeneration rather than eliciting scarring or a foreign body response may lead to improved biomaterials.

Online content

Any methods, additional references, Nature Research reporting summaries, source data, extended data, supplementary information, acknowledgements, peer review information; details of author contributions and competing interests; and statements of data and code availability are available at https://doi.org/10.1038/s41563-020-00844-w.

Received: 5 March 2019; Accepted: 25 September 2020;
Published online: 09 November 2020

References

1. Griffin, D. R., Weaver, W. M., Scumpia, P., Di Carlo, D. & Segura, T. Accelerated wound healing by injectable microporous gel scaffolds assembled from annealed building blocks. *Nat. Mater.* **14**, 737–744 (2015).
2. Nih, L. R., Sideris, E., Carmichael, S. T. & Segura, T. Injection of microporous annealing particle (MAP) hydrogels in the stroke cavity reduces gliosis and inflammation and promotes NPC migration to the lesion. *Adv. Mater.* **29**, 1606471 (2017).
3. Xu, Q. et al. Injectable hyperbranched poly(β-amino ester) hydrogels with on-demand degradation profiles to match wound healing processes. *Chem. Sci.* **9**, 2179–2187 (2018).
4. Zhu, S., Nih, L., Carmichael, S. T., Lu, Y. & Segura, T. Enzyme-responsive delivery of multiple proteins with spatiotemporal control. *Adv. Mater.* **27**, 3620–3625 (2015).
5. Sela, M. & Zisman, E. Different roles of D-amino acids in immune phenomena. *FASEB J.* **11**, 449–456 (1997).
6. Doloff, J. C. et al. Colony stimulating factor-1 receptor is a central component of the foreign body response to biomaterial implants in rodents and non-human primates. *Nat. Mater.* **16**, 671–680 (2017).
7. Mishra, P. K. et al. Sterile particle-induced inflammation is mediated by macrophages releasing IL-33 through a Bruton's tyrosine kinase-dependent pathway. *Nat. Mater.* **18**, 289–297 (2019).
8. Chung, L., Maestas, D. R., Housseau, F. & Elisseeff, J. H. Key players in the immune response to biomaterial scaffolds for regenerative medicine. *Adv. Drug Deliv. Rev.* **114**, 184–192 (2017).
9. Sadtler, K. et al. Developing a pro-regenerative biomaterial scaffold microenvironment requires T helper 2 cells. *Science* **352**, 366–370 (2016).
10. Galiano, R. D., Michaels, J., Dobryansky, M., Levine, J. P. & Gurtner, G. C. Quantitative and reproducible murine model of excisional wound healing. *Wound Repair Regen* **12**, 485–492 (2004).
11. Ito, M. et al. Wnt-dependent de novo hair follicle regeneration in adult mouse skin after wounding. *Nature* **447**, 316–320 (2007).
12. Seifert, A. W. et al. Skin shedding and tissue regeneration in African spiny mice (*Acomys*). *Nature* **489**, 561–565 (2012).
13. Nelson, A. M. et al. dsRNA released by tissue damage activates TLR3 to drive skin regeneration. *Cell Stem Cell* **17**, 139–151 (2015).
14. Guerrero-Juarez, C. F. et al. Wound regeneration deficit in rats correlates with low morphogenetic potential and distinct transcriptome profile of epidermis. *J. Invest. Dermatol.* **138**, 1409–1419 (2018).
15. Marshall, C. D. et al. Sanativo wound healing product does not accelerate reepithelialization in a mouse cutaneous wound healing model. *Plast. Reconstr. Surg.* **139**, 343–352 (2017).
16. Lim, C. H. et al. Hedgehog stimulates hair follicle neogenesis by creating inductive dermis during murine skin wound healing. *Nat. Commun.* **9**, 4903 (2018).
17. Carlson, M. A. & Chakkalakal, D. Tensile properties of the murine ventral vertical midline incision. *PLoS ONE* **6**, e24212 (2011).
18. Plikus, M. V. et al. Regeneration of fat cells from myofibroblasts during wound healing. *Science* **355**, 748–752 (2017).
19. Guerrero-Juarez, C. F. et al. Single-cell analysis reveals fibroblast heterogeneity and myeloid-derived adipocyte progenitors in murine skin wounds. *Nat. Commun.* **10**, 650 (2019).
20. Warren, K. S. A functional classification of granulomatous inflammation. *Ann. NY Acad. Sci.* **278**, 7–18 (1976).
21. Chensue, S. W. et al. Cytokine responses during mycobacterial and schistosomal antigen-induced pulmonary granuloma formation. Production of Th1 and Th2 cytokines and relative contribution of tumor necrosis factor. *Am. J. Pathol.* **145**, 1105–1113 (1994).
22. Wills-Karp, M. et al. Trefoil factor 2 rapidly induces interleukin 33 to promote type 2 immunity during allergic asthma and hookworm infection. *J. Exp. Med.* **209**, 607–622 (2012).
23. Hardman, C. S., Panova, V. & McKenzie, A. N. J. IL-33 citrine reporter mice reveal the temporal and spatial expression of IL-33 during allergic lung inflammation. *Eur. J. Immunol.* **43**, 488–498 (2013).
24. de Kouchkovsky, D. A., Ghosh, S. & Rothlin, C. V. Induction of sterile type 2 inflammation. *Nat. Mater.* **18**, 193–194 (2019).
25. Koh, J. et al. Enhanced in vivo delivery of stem cells using microporous annealed particle scaffolds. *Small* **15**, e1903147 (2019).
26. Purbey, P. K. et al. Defined sensing mechanisms and signaling pathways contribute to the global inflammatory gene expression output elicited by ionizing radiation. *Immunity* **47**, 421–434 (2017).
27. Scumpia, P. O. et al. Opposing roles of Toll-like receptor and cytosolic DNA-STING signaling pathways for *Staphylococcus aureus* cutaneous host defense. *PLoS Pathog.* **13**, e1006496 (2017).
28. Tong, A.-J. et al. A stringent systems approach uncovers gene-specific mechanisms regulating inflammation. *Cell* **165**, 165–179 (2016).
29. Kim, S. D. et al. The agonists of formyl peptide receptors prevent development of severe sepsis after microbial infection. *J. Immunol.* **185**, 4302–4310 (2010).
30. Kang, H. K. et al. The synthetic peptide Trp-Lys-Tyr-Met-Val-D-Met inhibits human monocyte-derived dendritic cell maturation via formyl peptide receptor and formyl peptide receptor-like 2. *J. Immunol.* **175**, 685–692 (2005).
31. Schepetkin, I. A. et al. 3-(1 *H*-indol-3-yl)-2-[3-(4-nitrophenyl)ureido] propanamide enantiomers with human formyl-peptide receptor agonist activity: molecular modeling of chiral recognition by FPR2. *Biochem. Pharmacol.* **85**, 404–416 (2013).
32. Zisman, E., Dayan, M., Sela, M. & Mozes, E. Ia-antigen–T-cell interactions for a thymus-independent antigen composed of D amino acids. *Proc. Natl Acad. Sci. USA* **90**, 994–998 (1993).
33. Cernysiov, V., Gerasimcik, N., Mauricas, M. & Girkontaite, I. Regulation of T-cell-independent and T-cell-dependent antibody production by circadian rhythm and melatonin. *Int. Immunol.* **22**, 25–34 (2010).
34. Honda, S. et al. Enhanced humoral immune responses against T-independent antigens in Fc alpha/muR-deficient mice. *Proc. Natl Acad. Sci. USA* **106**, 11230–11235 (2009).
35. Mongini, P. K., Stein, K. E. & Paul, W. E. T cell regulation of IgG subclass antibody production in response to T-independent antigens. *J. Exp. Med.* **153**, 1–12 (1981).
36. Weinstein, J. S. et al. Maintenance of anti-Sm/RNP autoantibody production by plasma cells residing in ectopic lymphoid tissue and bone marrow memory B cells. *J. Immunol.* **190**, 3916–3927 (2013).
37. Germann, T. et al. Interleukin-12 profoundly up-regulates the synthesis of antigen-specific complement-fixing IgG2a, IgG2b and IgG3 antibody subclasses in vivo. *Eur. J. Immunol.* **25**, 823–829 (1995).
38. Boehler, R. M., Graham, J. G. & Shea, L. D. Tissue engineering tools for modulation of the immune response. *BioTechniques* **51**, 239–254 (2011).
39. Song, J. et al. A mouse model for the human pathogen *Salmonella typhi*. *Cell Host Microbe* **8**, 369–376 (2010).
40. Park, C. G. et al. Extended release of perioperative immunotherapy prevents tumor recurrence and eliminates metastases. *Sci. Transl. Med.* **10**, eaar1916 (2018).
41. Kim, J. et al. Injectable, spontaneously assembling, inorganic scaffolds modulate immune cells in vivo and increase vaccine efficacy. *Nat. Biotechnol.* **33**, 64–72 (2015).

Methods

L-MMP and D-MMP MAP hydrogel formation. Microfluidic water-in-oil droplet generators were fabricated using soft lithography, as previously described[1]. To enable the microgel formation, two aqueous solutions were prepared. One solution contained a 10% w/v four-arm polyethylene glycol–vinyl sulfone (20 kDa, JenKem) in 300 mM triethanolamine (Sigma), pH 8.25, prefunctionalized with a 500 μM K-peptide (Ac-FKGGERCG-NH_2) (GenScript), 500 μM Q-peptide (AcNQEQVSPLGGERCG-NH_2) and 1 mM RGD (Ac-RGDSPGERCG-NH_2) (GenScript). The other solution contained either: (1) an 8 mM dicysteine-modified MMP substrate (Ac-GCRDGPQGIWGQDRCG-NH_2) (GenScript) with either all L-chirality amino acid residues for L-MMP microgel, or (2) D-chirality amino acid substitution of amino acids at the site of the MMP-mediated recognition and cleavage (Ac-GCRDGPQ_DGI$_D$W$_D$GQDRCG-NH_2) for D-MMP microgels. We matched the stiffness of the two hydrogels that required minimal changes to that of the peptide crosslinker solution (L-MAP, 8 mM; D-MAP, 8.2 mM). The oil phase was a heavy mineral oil (Fisher) that contained 0.25% v/v Span-80 (Sigma). The two solutions were mixed in the droplet generator and pinched immediately into monodisperse droplets. Downstream of the pinching region, a second oil inlet with a high concentration of Span-80 (5% v/v) was mixed with the flowing droplet emulsion. Both aqueous solution flow rates used were 0.75 μl min^{-1}, whereas both oil solutions flowed at 4 μl min^{-1}. The mixture was allowed to react overnight at room temperature and purified by repeated washes with an aqueous buffer of HEPES-buffered saline pH 7.4 and pelleting in a tabletop centrifuge at 18,000*g* for 5 min. Raw materials were purchased endotoxin free and the final hydrogels were tested for endotoxin levels prior to implantation.

Generation of MAP scaffolds from building block microgels. Fully swollen and equilibrated building block microgels were pelleted at 18,000*g* for 5 min and the excess buffer (HEPES pH 7.4 + 10 mM $CaCl_2$) was removed by aspiration. Subsequently, building blocks were split into aliquots, each of which contained 50 μl of the concentrated building blocks. An equal volume of HEPES pH 7.4 + 10 mM $CaCl_2$ was added to the concentrated building block solutions. Half of these are spiked with thrombin (Sigma) to a final concentration of 2 U ml^{-1} and the other half were spiked with FXIII (CSL Behring) to a final concentration of 10 U ml^{-1}. These solutions were then well mixed and spun down at 18,000*g*, followed by the removal of excess liquid with a cleanroom wipe (American Cleanstat).

Annealing was initiated by mixing equal volumes of the building block solutions that contained thrombin and FXIII using a positive displacement pipette (Gilson). These solutions were well mixed by pipetting up and down, repeatedly, in conjunction with stirring using the pipette tip. The mixed solution was then pipetted into the desired location (mould, well plate, mouse wound and so on) or loaded into a syringe for subcutaneous injection. The microgel fabrication was performed under sterile conditions. After particle fabrication, 20 μl of dry particles were digested in 200 μl of digestion solution (Collagenase IV 200 U ml^{-1} + DNase I 125 U ml^{-1}) and incubated in 37 °C for 30 min before testing. Endotoxin concentrations were determined with the Pierce LAL Chromogenic Endotoxin Quantitation Kit (Thermo Fisher Scientific) following the manufacturer's instructions. Particle endotoxin levels were consistently below 0.2 endotoxin U ml^{-1}.

Degradation with collagenase. Microgel degradability was confirmed with collagenase I. A 1:1 v/v mixture of microgels formed with D-MMP- or L-MMP-sensitive crosslinker was diluted in collagenase I to a final concentration of 5 U ml^{-1} collagenase. This mixture was added to 1 mm polydimethylsiloxane well and briefly allowed to settle. Images of the microgels were taken near the bottom of the well every 30 s for 2 h with a confocal microscope. Image analysis was carried out through a custom MATLAB script (script provided by S. C. Lesher-Perez) and ImageJ. MATLAB was used to determine the number of intact microgel spheres in each image. The previously mentioned script was applied with a minimum droplet radius of 30 pixels, a maximum droplet radius of 50 pixels and a sensitivity factor of 0.98 for the channel-separated images. Then, ImageJ was used to determine the area fraction that fluoresced for each channel and each image. The thresholding for each image was set to a minimum of 50 and a maximum of 255 and the fluorescing area fraction was recorded.

Mouse excisional wound-healing model. All the experiments that involved animals, animal cells or tissues were performed in accordance with the Chancellor's Animal Research Committee ethical guidelines at the University of California Los Angeles under protocol no. 10-011 (in vivo wound healing and subcutaneous implants) or no. 1999-073 (in vitro BMDM cultures). Mouse excisional wound healing experiments were performed as previously described[1,10]. Briefly, 10-week-old female SKH1 mice ($n = 6$, Charles River Laboratories) or 10-week-old female B6 or B6.Rag1$^{-/-}$ mice ($n = 4$ twice, Jackson Laboratories) were anaesthetized using a continuous application of aerosolized isoflurane (1.5 vol%) throughout the duration of the procedure and disinfected with serial washes of povidone–iodine and 70% ethanol. The nails were trimmed and buprenorphine (0.05 mg ml^{-1}) was injected intramuscularly. The mice were placed on their side and the dorsal skin was pinched along the midline. A sterile 4 mm biopsy punch was then used to create two through-and-through wounds, which resulted in four clean-cut, symmetrical, full-thickness excisional wounds on either side of the dorsal midline. A small amount of adhesive (VetBond, 3M, Inc.) was then applied to one side of a rubber splint (outer diameter, ~12 mm; outer diameter, ~8 mm) and the splint was placed centred around the wound (adhesive side down). The splint was secured with eight interrupted sutures of 5-0 non-absorbable Prolene. A second splint wrapped in Tegaderm (3M, Inc.) was attached to the initial splint via a single suture to act as a hinged cover to allow wound imaging while it acted as a physical barrier above the wound bed. After the addition of thrombin (2 U ml^{-1}) and 10 mM $CaCl_2$, the experimental material (20 μl of L-only MAP, D-only MAP or a 1:1 v/v mixture of L-MAP and D-MAP in HEPES-buffered saline that contained factor XIII (10 U ml^{-1}) and 10 mM $CaCl_2$, or no hydrogel) was then added to one of the wound beds randomly to ensure each hydrogel treatment was applied to the different regions of wounded back skin to limit the potential for site-specific effects. After treatment, a Tegaderm-coated splint was applied and wound sites were covered using a self-adhering elastic bandage (VetWrap, 3M, Inc.). Animals were housed individually to prevent wound manipulation. At the culmination of the wound-healing experiment (day 21 or day 25), the mice were killed by an isoflurane overdose and cervical dislocation and imaged with a digital camera. The skin was excised and processed via either paraffin embedding for H&E or optimal cutting temperature blocks for immunofluorescence.

Evaluation of wound closure. Wounds were imaged daily to follow their closure. Each wound site was imaged using a high-resolution camera (Nikon Coolpix). The closure fraction was determined as described previously[1]. Briefly, closure was determined by comparing the pixel area of the wound to the pixel area within the 10 mm centre hole of the red rubber splint. Closure fractions were normalized to day 0 for each mouse and/or scaffold sample. Investigators were blinded to the treatment group identity during analysis.

Wound imaging. On the specified day after the wounds were created, close-up images of the wounds were taken using a Canon Powershot A2600 or a Nikon D3400 DSLR Camera with an 18–55 mm lens, and were cropped to the wound area but not manipulated further. For wound closure, the area was obtained using ImageJ by a subject blinded to the treatment.

Tissue collection. After the wounds healed, mice were killed on the indicated day after wounding, and tissue collected with a ~5 mm margin around the healed wound. The samples were immediately submerged in Tissue-Tek optimal cutting temperature fluid and frozen into a solid block with liquid nitrogen. The blocks were then cryosectioned by a cryostat microtome (Leica) and kept frozen until use. The sections were then fixed with 4% paraformaldehyde in 1× PBS for 30 min at room temperature, washed with 1× PBS and kept at 4 °C until stained. For the antibody production analysis, was blood harvested via cardiac puncture to obtain the serum for ELISA.

Macrophage cell culture. Mouse BMDMs were generated as previously described previously[27]. Briefly, after euthanasia, the hindlimbs were removed aseptically and the bone marrow was flushed. Bone marrow cells were cultured in CMG-conditioned complete DMEM media for 6 days. Cells were then treated with intact L- or D-peptide in ultrapure H_2O at the indicated concentration in the presence or absence of LPS (10 ng ml^{-1}). Cleaved D-peptide (with an *N*-terminal D-amino acid) (W_DGQDRCG-NH_2) was also used when indicated. Cells were harvested at 6 h after treatment and the expression of cytokines and chemokines was examined by quantitative PCR using specific primers, as described previously[42].

Incisional wound model. As above, 10-week-old female B6 mice (Jackson Laboratories) were anaesthetized with isoflurane as above. The dorsal and side skin was dehaired using electric clippers followed by Nair (Church and Dwight, Inc.), then disinfected with serial washes of povidone–iodine and 70% ethanol. The nails were trimmed to lower the incidence of splint removal, and buprenorphine was injected intramuscular as above. An incisional 2 cm × 1 cm wound was made with a scalpel. Mice (five per group) were randomly assigned to receive 50 μl of L-MAP, D-MAP, 1:1 v/v mixture of L-MAP and D-MAP or no hydrogel (Aquaphor, Beiersdorf Inc.). The mice were wrapped with Tegaderm followed by VetWrap, as above.

Histology and analysis. Samples were sectioned (6–10 μm thick), then stained with H&E or Masson trichrome by the UCLA Tissue Procurement Core Laboratory using standard procedures. Sections were examined by a board-certified dermatopathologist (P.O.S.) and/or an expert in hair follicle neogenesis/regeneration (M.V.P.) who were blinded to the identity of the samples for the presence of adnexal structures in tissue sections and dermal thickness. For enumeration, two to three tissue sections from the tissue block of each wound were examined and averaged per wound to obtain the count per unit area for each sample. Wounds were splinted to prevent contraction and any sample with more than a 50% wound closure by contraction were not included.

Tensiometry. To evaluate the tensile properties of the healed incisional wounds, tensile testing was performed on an Instron model 3342 fitted with a 50 N load

cell and data recorded using the Instron Bluehill 3 software package. Tissue was collected from the wound site 28 days after wounding and treatment as a 2 cm × 4 cm 'dumbbell' shape (with a 1 cm centre width in the handle portion). The sample was oriented such that the healed wound spanned the entire middle section of the dog bone (the thinner 1 cm region) and the healed wound long axis was orthogonal to the direction of tension applied. The tissue sample was loaded into the Instron and secured with pneumatic grippers, pressurized to 276 kPa. The tissue was subjected to tensile testing at an elongation rate of 5 mm min^{-1} and ran through material failure.

For each tissue sample, stress/strain curves were calculated from force/elongation curves (provided from the Instron Bluehill software) using the known cross-sectional dimensions of the 'dog bone' samples (each measured with callipers prior to placement on the Instron), and by measuring the starting distance between pneumatic grips with a caliper. The starting distance was standardized by preloading the sample to 0.5 N, followed by measurement and then running of the tensile test to failure. This analysis enabled the calculation of yield stress, which are reported in Fig. 1j.

Subcutaneous implants of hydrogel. For subcutaneous implants, after anaesthesia, 10-week-old female Balb/c and Balb/c.Rag2$^{-/-}\gamma c^{-/-}$ mice were injected with 50 µl of L-MAP, D-MAP or 1:1 v/v mixture of L-MAP and D-MAP ($n=5$). After 21 days, the skin and subcutaneous tissue that contained the hydrogels were removed and processed for histology and immunofluorescence, and blood was collected by cardiac puncture to obtain serum for the ELISA. B6 mice were used in another batch of experiments for immunofluorescence analysis and the histology of subcutaneous implants.

Tissue section immunofluorescence, quantification of hydrogel degradation and immune infiltration. Slides that contained tissue sections (10–25 µm thickness) were blocked with 3% normal goat serum (NGS) in 1× PBS + 0.05% Tween-20 (PBST). For intracellular antigens, 0.2% triton was added to the blocking buffer. Primary antibody dilutions were prepared in 5% NGS in 1× PBST as follows: rat anti-mouse CD11b clone M1-70 (BD Pharmingen, no. 553308) 1:100, F4/80 clone A3-1 (BioRAD, MCA497G) 1:400 and IL-33 (Abcam, ab187060) 1:200. Sections were stained with primary antibodies overnight at 4 °C, and subsequently washed with 3% NGS in 1× PBST. Secondary antibodies (goat anti-rat Alexa-647; Invitrogen) were all prepared in 5% NGS in 1× PBST at a dilution of 1:500. Three 5 min washes with PBST were performed after each antibody incubation. Sections were incubated in secondary antibodies for 1 h at room temperature and subsequently washed with 1× PBST. For multicolour immunofluorescence staining for primary and secondary antibodies of each antigen were performed in sequence. Sections were either mounted with antifade mounting medium with DAPI (Fisher Scientific, H1200) or counterstained with 2 µg ml^{-1} DAPI in 1× PBST for 30 min at room temperature and then mounted in mounting medium of Antifade Gold.

Computational analysis of multicolour immunofluorescence images. A MATLAB code was used for the analysis of the multicolour immunofluorescence images. The code divided the hydrogel into an edge region (300 µm from hydrogel–tissue interface) and a core region (the centre of the hydrogel to 200 µm from the inner boundary of the edge region). For each hydrogel subregion, the code read the CD11b and F4/80 signals, and binarized each to form a mask using a similar threshold for all the samples. The code then used the nuclear stain and IL-33$^+$ stains to identify all the nuclei and IL-33$^+$ cells. The density of each cell type was then quantified by counting the number of nuclei and IL-33$^+$ cells that overlapped or evaded the masks divided by the area of the region of interest. Areas with defects caused by tissue sectioning were excluded from the analysis. Although it did not affect the code performance, the image condition was kept the same across all samples.

ELISA. To assess the anti-L- or anti-D-antibodies, sera were collected by cardiac puncture 21 days after the hydrogel application of mice (subcutaneous implant or application to wound). To detect the anti-L- and anti-D-antibodies, plates were coated with either the L-MMP or D-MMP peptide, respectively (the sequence above; GenScript). Serum samples were tested at a 1:500 dilution followed by incubation with alkaline phosphatase-labelled goat anti-mouse IgG1 or IgG2a, or IgG3 antibodies (Southern Biotechnology Associates or BD Pharmingen) and developed with *p*-nitrophenyl phosphate substrate (Sigma-Aldrich). The optical density at 405 nm was read using a Spectramax i3X microplate reader (Softmax Pro 3.1 software; Molecular Devices).

Statistics and reproducibility. All the statistical analysis was performed using Prism 6 (GraphPad, Inc.) software. Specifically, a two-tailed *t*-test or one-way ANOVA were used to determine the statistical significance, assuming an equal sample variance for each experimental group when individual groups are compared. For ANOVA, post hoc analysis with Tukey multiple comparison was used. For histological counting and the B6 and B6.Rag1$^{-/-}$ sham versus 1:1 L/D-MAP analysis, a Wilcoxon signed rank analysis was performed and for B6 versus B6.Rag1$^{-/-}$ the subcutaneous immunofluorescence analysis was performed with a *t*-test with a Mann–Whitney U test.

The hydrogel degradation test was performed on three separate occasions for each batch of L-MAP, D-MAP and 50:50 mixture of L-MAP and D-MAP for a total of nine degradation tests. In each technical replicate at least ten microgels were imaged and analysed for fluorescence intensity.

The evaluation of hair neogenesis in the B6 mice control versus D-MAP for Fig. 2 was performed on samples from $n=4$ for each group. The wound healing studies to compare wild-type to B6.Rag1$^{-/-}$ mice were repeated three times ($n=4$ each group). In the first experiment, all the Rag1-/- mice were euthanized due to the development of severe and worsening wound infections, and thus were not included in the final analysis. In addition, wounds and/or scars that showed more than a 50% contraction of the wound area from the underlying fascia from any group or histological processing results that failed to identify the wound and/or scar bed (that is, the sample was cut through) were removed from the final dataset. For the histological analysis, sham versus 1:1 L/D-MAP in B6 mice from three separate experiments were used ($n=9$ histological samples available out of an available $n=12$ wounds performed), whereas samples in the B6.Rag1$^{-/-}$ mice were obtained from the latter two experiments performed in B6 versus B6.Rag1$^{-/-}$ mice carried out at the same time ($n=6$ histological samples available out of $n=8$ wounds). The findings within this article were observed in two different mouse strains (CRL-SKH and C57BL/6) that have different adnexal structures (vellus hair only and mature and/or terminal follicles, respectively).

Reporting summary. Further information on research design is available in the Nature Research Reporting Summary linked to this article.

Data availability

The data that support the findings of this study are available from the corresponding authors upon reasonable request. Source data are provided with this paper.

References

42. Ramirez-Carrozzi, V. R. et al. A unifying model for the selective regulation of inducible transcription by CpG islands and nucleosome remodeling. *Cell* **138**, 114–128 (2009).

Acknowledgements

We thank the National Institutes of Health F32EB018713-01A1 (D.R.G.), T32-GM008042 (M.M.A.), T32AR071307 (M.M.A), U01AR073159 (M.V.P.), R01NS094599 (T.S.), R01HL110592 (T.S.), R03AR073940 (P.O.S.), K08AR066545 (P.O.S.), Pew Charitable Trust (M.V.P.), LEO Foundation (M.V.P.), the National Science Foundation grant DMS1763272, Simons Foundation Grant (594598, QN) (M.V.P.), and the Presidential Early Career Award for Scientists and Engineers (N00014-16-1-2997) (D.D.) for funding. We thank S. C. Lesher-Perez and M. Bogumil for their assistance with MATLAB coding. We thank Y. Liu for assistance with running the endotoxin texts. We also thank the Advanced Light Microscopy and Spectroscopy at California NanoSystems Institute and Electron Microscopy Core Laboratory of the Brain Research Institute at UCLA and, particularly, for the significant help of M. Cilluffo.

Author contributions

D.R.G., P.O.S. and T.S. conceived the experiments. D.R.G., W.M.W., E.S., M.M.A. and J.K. carried out the microfluidic design and fabrication, and D.D.C. oversaw the microfluidic design and fabrication. D.R.G., M.M.A., C.-H.K., W.M.W, J.S.W., A.C.F., E.S., A.R., V.R. and P.O.S. performed the experiments. D.R.G., M.M.A., J.S.W., A.R., M.V.P., T.S. and P.O.S. analysed and interpreted the data. D.R.G., M.M.A., P.O.S. and T.S. wrote the manuscript and all the authors discussed the results and contributed to writing portions of the manuscript and editing the manuscript. D.R.G. and M.M.A. contributed equally to this work. The co-principal investigators are P.O.S. and T.S.

Competing interests

D.R.G., W.M.W., D.D.C., T.S., and P.O.S. have a financial interest in Tempo Therapeutics, which aims to commercialize MAP technology.

Additional information

Supplementary information is available for this paper at https://doi.org/10.1038/s41563-020-00844-w.

Correspondence and requests for materials should be addressed to T.S. or P.O.S.

Reprints and permissions information is available at www.nature.com/reprints.

APPENDIX B

Interferon-mediated Reprogramming of Membrane Cholesterol to Evade Bacterial Toxins

ARTICLES
https://doi.org/10.1038/s41590-020-0695-4
nature immunology

Interferon-mediated reprogramming of membrane cholesterol to evade bacterial toxins

Quan D. Zhou[1,2], Xun Chi[3], Min Sub Lee[1], Wei Yuan Hsieh[3], Jonathan J. Mkrtchyan[3], An-Chieh Feng[3], Cuiwen He[4], Autumn G. York[1,5,6], Viet L. Bui[3], Eliza B. Kronenberger[3], Alessandra Ferrari[7], Xu Xiao[7], Allison E. Daly[3], Elizabeth J. Tarling[4], Robert Damoiseaux[1], Philip O. Scumpia[3,4], Stephen T. Smale[3], Kevin J. Williams[8], Peter Tontonoz[7,8] and Steven J. Bensinger[1,3] ✉

Plasma membranes of animal cells are enriched for cholesterol. Cholesterol-dependent cytolysins (CDCs) are pore-forming toxins secreted by bacteria that target membrane cholesterol for their effector function. Phagocytes are essential for clearance of CDC-producing bacteria; however, the mechanisms by which these cells evade the deleterious effects of CDCs are largely unknown. Here, we report that interferon (IFN) signals convey resistance to CDC-induced pores on macrophages and neutrophils. We traced IFN-mediated resistance to CDCs to the rapid modulation of a specific pool of cholesterol in the plasma membrane of macrophages without changes to total cholesterol levels. Resistance to CDC-induced pore formation requires the production of the oxysterol 25-hydroxycholesterol (25HC), inhibition of cholesterol synthesis and redistribution of cholesterol to an esterified cholesterol pool. Accordingly, blocking the ability of IFN to reprogram cholesterol metabolism abrogates cellular protection and renders mice more susceptible to CDC-induced tissue damage. These studies illuminate targeted regulation of membrane cholesterol content as a host defense strategy.

Cholesterol is the most abundant lipid in the plasma membrane and is an important determinant of the membrane's biochemical and biophysical properties[1–4]. Cellular cholesterol homeostasis is maintained through a combination of synthesis, import, storage and efflux pathways. While each pathway may be engaged independently, the pathways are often co-regulated to ensure that sufficient cholesterol is available for a cell and to avoid deleterious accumulation. Recent studies indicate that sterol metabolism pathways of immune cells, in particular macrophages, can be rapidly reprogrammed to support their effector functions[5–8]. Toll-like receptors (TLRs) and IFNs have been shown to mediate reprogramming of cholesterol homeostasis by rapidly decreasing cholesterol synthetic flux[9,10], increasing cholesterol ester storage in lipid droplets[11,12] and stimulating the production of cholesterol derivatives such as 25HC[5,13,14]. This reprogramming of sterol homeostasis facilitates host defense responses through a variety of mechanisms, including blockade of viral entry, regulation of innate immune receptor signaling, immune cell skewing and increasing macrophage phagocytic capacity. Thus, coordinated regulation of sterol metabolic pathways in immune cells is now viewed as a fundamental component of the host defense response.

Given the essential requirement for cholesterol in animal membranes, it is not surprising that microorganisms and viruses have evolved strategies that take advantage of cholesterol availability in membranes to facilitate pathogenesis[15–18]. CDCs are a group of secreted toxins produced mainly by Gram-positive bacteria that depend on membrane cholesterol for their pathogenic function[19–21]. CDC binding to cholesterol in the plasma membrane facilitate CDC oligomerization and pore formation, resulting in loss of membrane integrity, reduced efficacy of antimicrobial function and cell death[22,23]. Cells have repair mechanisms by which they minimize the deleterious effects of CDC toxins. Damaged plasma membranes can be internalized and resealed[24,25], or they may bleb and be subsequently shed as microvesicles[26]. However, it appears that phagocytes attempting membrane repair may become hyporesponsive to proinflammatory stimuli through shedding of TLRs and cytokine receptors[23]. Thus, host membrane repair mechanisms, which preserve phagocyte survival, also reduce their effectiveness for antimicrobial host defense. Whether phagocytes or other immune cells have evolved specific strategies that facilitate evasion from these pore-forming toxins remains less well understood.

Here we report that activation of pattern recognition receptor (PRR) signaling on macrophages influences susceptibility to CDC-induced loss of membrane integrity and function. We show that IFN signals convey resistance to CDC-mediated membrane damage on phagocytes by reprogramming their cellular cholesterol metabolism, whereas myeloid differentiation primary-response protein 88 (Myd88)-dependent TLR signals do not induce protection. Mechanistic studies revealed that IFNs mediate resistance to CDCs by decreasing their binding to the plasma membrane. The decrease in CDC binding requires coordinated inhibition of new cholesterol synthesis and an increase in the esterification of a small

[1]Department of Molecular and Medical Pharmacology, University of California, Los Angeles, Los Angeles, CA, USA. [2]Department of Surgical Oncology, The First Affiliated Hospital, School of Medicine, Zhejiang University, Hangzhou, P.R. China. [3]Department of Microbiology, Immunology and Molecular Genetics, University of California, Los Angeles, Los Angeles, CA, USA. [4]Department of Medicine, David Geffen School of Medicine, University of California, Los Angeles, Los Angeles, CA, USA. [5]Department of Immunobiology, Yale University School of Medicine, New Haven, CT, USA. [6]Howard Hughes Medical Institute, Yale University, New Haven, CT, USA. [7]Department of Pathology and Laboratory Medicine, University of California, Los Angeles, Los Angeles, CA, USA. [8]Department of Biological Chemistry, University of California, Los Angeles, Los Angeles, CA, USA. ✉e-mail: sbensinger@mednet.ucla.edu

amount of preexisting cellular cholesterol. IFN-mediated changes in cholesterol homeostasis were also dependent on the endogenous production of 25HC, and we found that loss of the enzyme cholesterol 25-hydroxylase (CH25H) resulted in increased binding of CDC proteins at the plasma membrane. Accordingly, perturbations in sterol metabolic pathways abrogated the protective effects of IFNs for phagocytes and rendered mice more susceptible to CDC-induced tissue damage. Together, these findings indicate that IFN-mediated changes to sterol metabolism convey resistance to CDCs by decreasing a small pool of cholesterol in the plasma membrane and suggest that specifically targeting this pool of cholesterol could facilitate host defense to CDC-producing pathogenic bacteria.

Results

IFNs mediate resistance to CDCs. Activation of macrophages through TLR and cytokine signals reprograms their lipid metabolism[5–8,10,27], leading us to ask whether these changes in lipid metabolism alter sensitivity to CDCs. To address this question, mouse bone marrow-derived macrophages (BMDMs) were stimulated with TLR1/TLR2, TLR3, TLR4, TLR7 or TLR9 agonist for 24 h and then challenged with the CDC perfringolysin O (PFO) for up to 60 min. The membrane-impermeable dye propidium iodide (PI) was added to the medium just before PFO treatment to assess pore formation and loss of membrane integrity but not cell death in macrophages. As expected, PFO increased the percentage of PI-positive (PI^+) cells over time in unstimulated macrophages (Fig. 1a and Extended Data Fig. 1a). Activation of macrophages with TLR1/TLR2, TLR4, TLR7 or TLR9 agonist resulted in little or no change in sensitivity to PFO treatment (Fig. 1a and Extended Data Fig. 1a,b), whereas TLR3-mediated activation markedly decreased macrophage sensitivity to PFO treatment (Fig. 1a and Extended Data Fig. 1a).

Unexpectedly, TLR3 activation, which is associated with antiviral responses, provided a substantial measure of protection to PFO-induced pore formation. Because a primary inflammatory outcome of TLR3 signaling is the generation of type I IFNs[28,29], we tested whether type I IFN stimulation alone would convey resistance to PFO. We observed that treatment of macrophages with IFN-β overnight also conveyed resistance to PFO (Fig. 1b and Extended Data Fig. 1c). IFN-γ treatment of macrophage cultures also induced resistance when cells were challenged with PFO (Fig. 1b and Extended Data Fig. 1c), indicating that protection is mediated by both type I and type II IFNs. We also tested whether activation of other PRRs that generate type I IFN responses[30] would also protect macrophages when challenged with CDCs. The stimulator of IFN genes (STING; TMEM173) is activated by cyclic dinucleotides generated by intracellular microorganisms (for example, *Listeria monocytogenes*)[31]. We found that treatment of BMDM cultures with STING ligands (2′,3′-cGAMP or c-di-GMP) for 24 h also resulted in protection from the PFO challenge (Fig. 1c and Extended Data Fig. 1d). Nucleotide-binding oligomerization domain-containing protein 2 (NOD2), an intracellular receptor stimulated by peptidoglycans produced by Gram-positive microorganisms, has also been shown to induce low levels of type I IFN during bacterial infections[32]. Consistent with this, activation of NOD2 with *N*-glycolyl-MDP resulted in modest protection against the PFO challenge (Fig. 1c and Extended Data Fig. 1d). Importantly, we observed a similar pattern of IFN-mediated resistance for macrophages challenged with the CDCs streptolysin O (SLO) or anthrolysin O (ALO; Fig. 1d,e and Extended Data Fig. 1e–g), indicating that the protection conveyed by IFNs may be a general strategy for resistance to the larger group of pore-forming CDCs.

We were surprised that TLR1/TLR2 activation did not induce resistance to CDCs given the important role of this TLR signaling module in mediating immune responses to Gram-positive bacteria. However, we found that macrophages co-stimulated with the TLR1/TLR2 agonist and IFN-β acquired some measure of resistance to PFO and SLO (Fig. 1f,g and Extended Data Fig. 1h,i), indicating that IFN signals can induce a 'resistant' phenotype regardless of the PRR engaged. We also found that IFN stimulation (IFN-γ or IFN-β; 4 h) of purified neutrophils from mouse bone marrow resulted in resistance to CDC-mediated loss of membrane integrity (Fig. 1h), demonstrating the ability of IFN to induce protection in other phagocytic, innate immune cells. Importantly, IFN stimulation largely preserved the ability of macrophages to phagocytose extracellular bacteria (that is, *Staphylococcus aureus*) when cells were challenged with PFO (Fig. 1i). Together, these data demonstrate that autocrine or paracrine IFN signals induce resistance to CDC-mediated pore formation, resulting in preservation of macrophage membrane integrity and phagocytic function.

IFNs decrease binding of CDCs to the plasma membrane. To understand whether the observed changes in CDC sensitivity could be due to altered binding of CDCs to the plasma membrane, we performed studies on IFN-stimulated macrophages with fluorescently labeled ALO domain 4 (ALO-D4), a modified CDC toxin that has markedly reduced pore-forming capacity but retains near-normal binding characteristics to the plasma membrane[33–36]. We found that the binding of ALO-D4 to IFN-β- or IFN-γ-stimulated macrophages was substantially decreased when compared to control macrophages (Fig. 2a). High-throughput imaging analysis of macrophage cultures (>3,000 macrophages for each condition) stimulated with IFN-β, IFN-γ, STING or TLR3 ligand showed a marked reduction in the average intensity of ALO-D4 binding (Fig. 2b–e). By contrast, ALO-D4 binding was maintained or modestly increased in TLR1/TLR2-stimulated macrophages (Fig. 2f,g), consistent with our data indicating that TLR1/TLR2-stimulated macrophages maintained sensitivity to CDC-induced loss of membrane integrity. A similar decrease in ALO-D4 binding in response to either IFN-α or IFN-β was observed in macrophages derived from human peripheral blood mononuclear cells (hPBMCs; Fig. 2h,i). Likewise, stimulation (6 h) of purified neutrophils from mouse bone marrow with IFNs also decreased ALO-D4 binding (Extended Data Fig. 2a,b). Time-course studies showed that a decrease in ALO-D4 binding could be observed within 2 h of IFN stimulation of BMDMs (Fig. 2j,k). As expected, the decrease in ALO-D4 signal induced by IFN-β (or PRR-induced type I IFNs) was abrogated in type I IFN receptor (IFNAR)-deficient macrophages (Extended Data Fig. 2c,d). However, overnight IFN-γ treatment of IFNAR-deficient macrophages decreased ALO-D4 binding (Fig. 2l,m), demonstrating that resistance induced by type I and type II IFN cytokines are not interdependent. In combination, these data indicate that protection from CDCs is induced quickly in response to IFNs and is mediated by reduced binding of CDCs to the plasma membrane.

IFNs decrease a small pool of membrane cholesterol targeted by CDCs. Next, we asked whether IFN signals altered the binding of CDCs to the plasma membrane by decreasing macrophage cholesterol content. To address this, we performed gas chromatography–mass spectrometry (GC–MS) to quantify total cellular cholesterol levels in IFN-stimulated BMDMs. We observed that IFNs modestly increased total cholesterol in macrophages (Fig. 3a). Likewise, we observed that STING or TLR3 activation, which induces robust type I IFN responses, also increased total cholesterol (Extended Data Fig. 3a). Thus, the protection mediated by IFNs could not be attributed to a global decrease in cholesterol content. We also performed GC–MS on purified plasma membranes from quiescent and IFN-γ-stimulated macrophages; however, no difference in cholesterol pool size was observed (Fig. 3b and Extended Data Fig. 3b). We also stained BMDMs with filipin III, a bacterial product that binds to unesterified cholesterol in membranes and forms a fluorescent complex[37]. Consistent with our mass spectrometry studies, no change in filipin III staining was observed in response

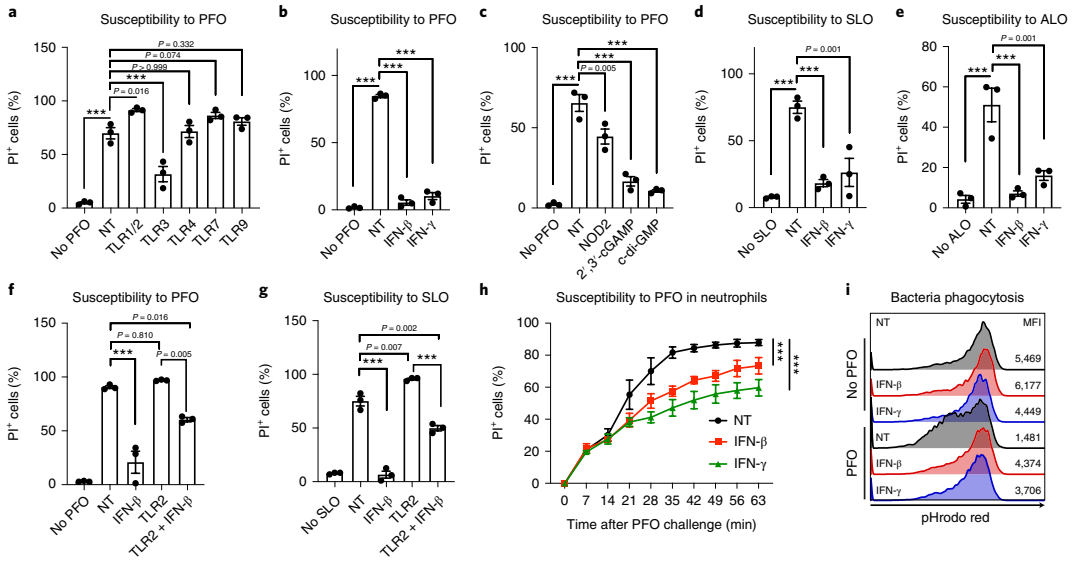

Fig. 1 | IFN signaling mediates resistance to CDCs. a, Percentage of PI+ BMDMs treated with the TLR1/TLR2 agonist (Pam3CSK4; 50 ng ml^{-1}), TLR3 agonist (poly(I:C); 1 μg ml^{-1}), TLR4 agonist (LPS; 50 ng ml^{-1}), TLR7 agonist (CL307; 100 nM), TLR9 agonist (ODN1668; 100 nM) or unstimulated (NT) for 24 h and then challenged with PFO for 60 min in the presence of PI. **b**, Percentage of PI+ BMDMs treated with IFN-β (20 ng ml^{-1}) and IFN-γ (20 ng ml^{-1}) for 24 h and then challenged with PFO for 60 min in the presence of PI. **c**, Percentage of PI+ BMDMs treated with NOD2 agonist (*N*-glycolyl-MDP; 20 μg ml^{-1}) or STING agonists (2′,3′-cGAMP and c-di-GMP; 2 μg ml^{-1}) for 24 h and then challenged with PFO for 60 min in the presence of PI. **d**, Percentage of PI+ BMDMs treated with the indicated IFNs (20 ng ml^{-1}) for 24 h and then challenged with SLO for 2 h in the presence of PI. **e**, Percentage of PI+ BMDMs treated with the indicated IFNs (20 ng ml^{-1}) for 24 h and then challenged with ALO for 2 h in the presence of PI. **f**, Percentage of PI+ BMDMs treated with TLR1/TLR2 agonist (50 ng ml^{-1}) together with IFNs (100 ng ml^{-1}) for 24 h and then challenged with PFO for 60 min in the presence of PI. **g**, Percentage of PI+ BMDMs treated with TLR1/TLR2 agonist (50 ng ml^{-1}) together with IFNs (100 ng ml^{-1}) for 24 h and then challenged with SLO for 2 h in the presence of PI. **h**, Percentage of PI+ neutrophils treated with IFN-β or IFN-γ (both 20 ng ml^{-1}) for 4 h and then challenged with PFO for 60 min in the presence of PI ($n = 3$). **i**, Flow cytometry plots of *S. aureus* phagocytosed by control or IFN-stimulated BMDMs. Macrophage cultures were stimulated with IFNs (100 ng ml^{-1}) for 24 h. BMDMs were then washed and incubated with PFO for 15 min. PFO-containing medium was then replaced with fresh medium containing pHrodo (red)-labeled *S. aureus*. Median fluorescence intensity (MFI) is indicated on the right. Data are representative of three independent experiments. Data in **a**–**h** are shown as the mean ± s.e.m. ($n = 3$). Statistical significance was determined using one-way ANOVA with Dunnett's correction (**a**–**e**), two-way ANOVA with Tukey's correction (**f** and **g**) or one-way repeated-measures ANOVA with Dunnett's correction (**h**). ***$P < 0.001$.

to IFN stimulation (Extended Data Fig. 3c). We also investigated whether IFN stimulation disrupted sphingomyelin-associated cholesterol in the plasma membrane. Ostreolysin A (OlyA) is a protein that specifically binds to cholesterol when associated with sphingomyelin[38]. To assess whether IFNs altered this pool of cholesterol in the plasma membrane of macrophages, we applied nanoscale secondary ion mass spectrometry (NanoSIMS)[39,40] using stable-isotope-labeled ALO-D4 and OlyA proteins. Consistent with the fluorescent ALO-D4 imaging studies, we observed a decrease in ^{15}N-labeled ALO-D4 binding in response to IFN-β stimulation (Fig. 3c). In contrast, [^{15}N]OlyA binding remained unchanged (Fig. 3c). High-throughput imaging studies with fluorescence-labeled OlyA showed a similar binding pattern for unstimulated and IFN-treated macrophage cultures (Extended Data Fig. 3d,e). Cholera toxin B (CTB) staining also showed no change, indicating that IFN signaling does not disrupt GM1 ganglioside-containing microdomains of the plasma membrane (Extended Data Fig. 3f). Together, these data support the conclusion that substantial amounts of cholesterol remain in the plasma membrane in association with sphingolipids after IFN stimulation[38]. Consistent with this concept, brief treatment of IFN-stimulated macrophages with sphingomyelinase[39] restored ALO-D4 binding (Fig. 3d,e). Thus, we conclude that CDCs are targeting a small fraction of non-sphingomyelin-associated cholesterol within the plasma membrane and that IFN signaling alters the availability of this pool of cholesterol to reduce CDC binding to phagocytes.

Cholesterol synthesis is linked to CDC susceptibility. We and others have previously reported that IFN signaling can reduce de novo cholesterol synthesis in macrophages[7,9,10]. Thus, we considered the possibility that changes in CDC sensitivity were linked to the cholesterol biosynthetic capacity of activated macrophages. To address this, we performed studies of [^{13}C] glucose tracer enrichment on PRR- and IFN-stimulated macrophages. IFN-β and IFN-γ stimulation markedly decreased macrophage cholesterol synthesis (Fig. 4a). Likewise, activation of STING or TLR3 also decreased cholesterol biosynthesis (Extended Data Fig. 4a,b). In contrast, activation of TLR1/TLR2, TLR7 and TLR9 increased the amounts of synthesized cholesterol accumulated (Extended Data Fig. 4b). These data largely mirror the differential sensitivity to CDCs that we observed in PRR- and IFN-stimulated macrophages, leading us to hypothesize that cholesterol biosynthetic flux determines susceptibility to CDC-induced plasma membrane damage. Consistent with this, pharmacologic inhibition of cholesterol synthesis using simvastatin reduced ALO-D4 binding to otherwise unstimulated macrophages and protected against CDC-mediated membrane damage (Fig. 4b,c

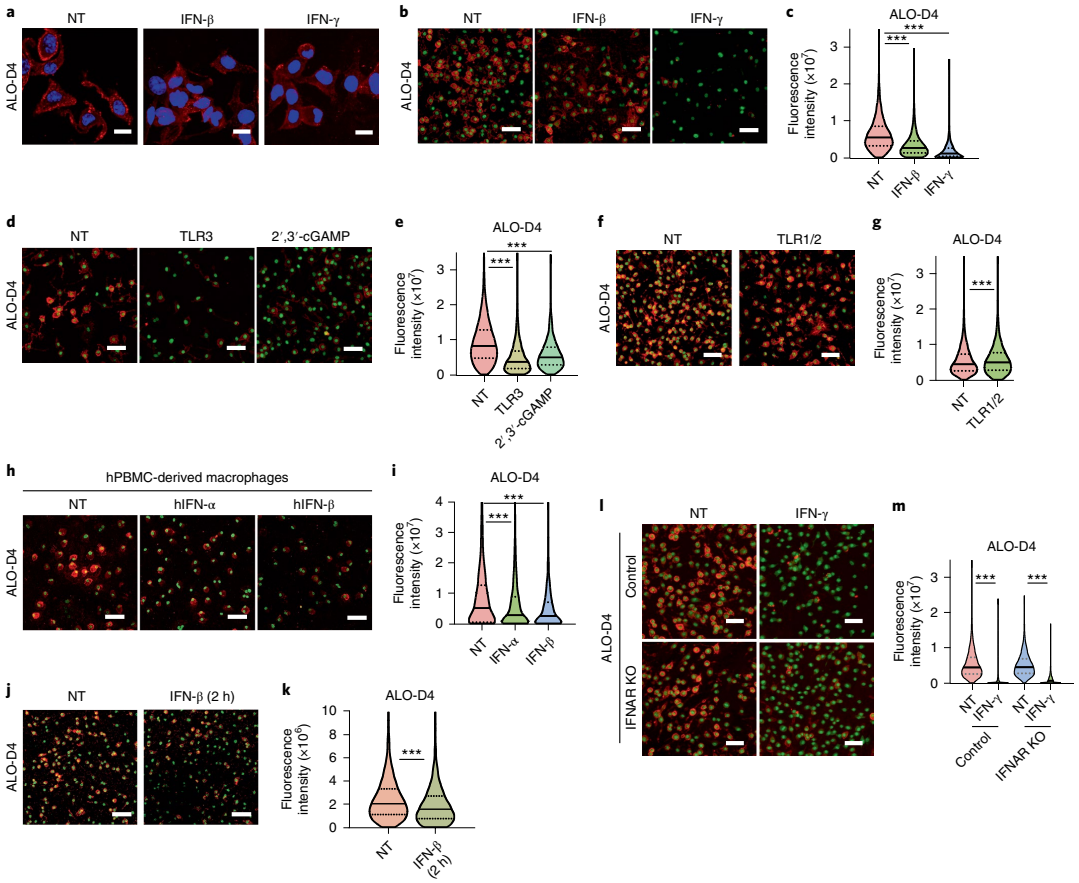

Fig. 2 | IFN signals decrease ALO-D4 binding to the plasma membrane. a, Super-resolution confocal images of macrophage cultures stimulated with the indicated IFNs (20 ng ml^{-1}) for 24 h and then stained with fluorescent ALO-D4 and DAPI. **b**, Confocal images of macrophage cultures stimulated with the indicated IFNs (20 ng ml^{-1}) for 24 h and then stained with fluorescent ALO-D4 and DAPI. **c**, Violin plots of cellular fluorescence intensity quantified from **b** (from left to right, $n = 6{,}539$, 4,561 and 5,367). **d**, Confocal images of macrophage cultures stimulated with the indicated PRR ligands for 24 h and then stained with fluorescent ALO-D4 and DAPI. **e**, Violin plots of cellular fluorescence intensity quantified from **d** ($n = 5{,}931$, 4,766 and 5,660). **f**, Confocal images of macrophage cultures stimulated with the indicated TLR agonists for 24 h and then stained with fluorescent ALO-D4 and DAPI. **g**, Violin plots of cellular fluorescence intensity quantified from **f** ($n = 4{,}358$ and 3,270). **h**, Confocal images of hPBMC-derived macrophages stimulated with human IFN-α or IFN-β (10 ng ml^{-1}) for 24 h and then stained with fluorescent ALO-D4 and DAPI. **i**, Violin plots of cellular fluorescence intensity quantified from **h** ($n = 2{,}084$, 1,818 and 1,728). **j**, Confocal images of macrophage cultures stimulated with IFN-β (20 ng ml^{-1}) for 2 h and then stained with fluorescent ALO-D4 and DAPI. **k**, Violin plots of cellular fluorescence intensity quantified from **j** ($n = 6{,}550$ and 7,012). **l**, Confocal images of control or IFNAR-deficient (IFNAR KO) mouse BMDMs stimulated with IFN-γ (20 ng ml^{-1}) for 24 h and then stained with fluorescent ALO-D4 and DAPI. **m**, Violin plots of cellular fluorescence intensity quantified from **l** ($n = 4{,}358$, 2,853, 7,089 and 5,458). Data in **a** are representative of three independent samples. Data in **b**–**m** are representative of three (**b**–**k**) or two (**l** and **m**) independent experiments. Violin plots in **c**, **e**, **g**, **i**, **k** and **m** are shown with the median (solid line) and 25th and 75th percentiles (dashed lines). Statistical significance was determined using a Kruskal–Wallis test with Dunn's correction (**c, e** and **i**) or a two-tailed Mann–Whitney test (**g**, **k** and **m**). ***$P < 0.001$. Scale bars represent 10 μm (**a**) or 50 μm (**b**, **d**, **f**, **h**, **j** and **l**).

and Extended Data Fig. 4c). In addition, we asked whether genetic attenuation of cholesterol synthesis would intrinsically convey resistance to CDC recognition. Loss of the cleavage-activating protein SCAP, which is required to chaperone the sterol regulatory element binding protein (SREBP), has been shown to attenuate cholesterol synthesis in macrophages[10]. We observed that quiescent SCAP-deficient macrophages exhibited decreased ALO-D4 binding, and, accordingly, these cells were protected from the PFO challenge (Fig. 4d,e). The oxysterol 25HC is an endogenous inhibitor of cholesterol biosynthesis through its ability to induce degradation of 3-hydroxy-3-methylglutaryl-CoA reductase (HMGCR), the rate-limiting enzyme in cholesterol synthesis, and inhibition of the SREBP transcriptional axis[41,42]. Thus, we asked whether treating macrophage cultures with 25HC would also alter ALO-D4 binding. To this end, wild-type quiescent macrophages were treated with 25HC (3 μM) for 4 h. We found that treatment with 25HC

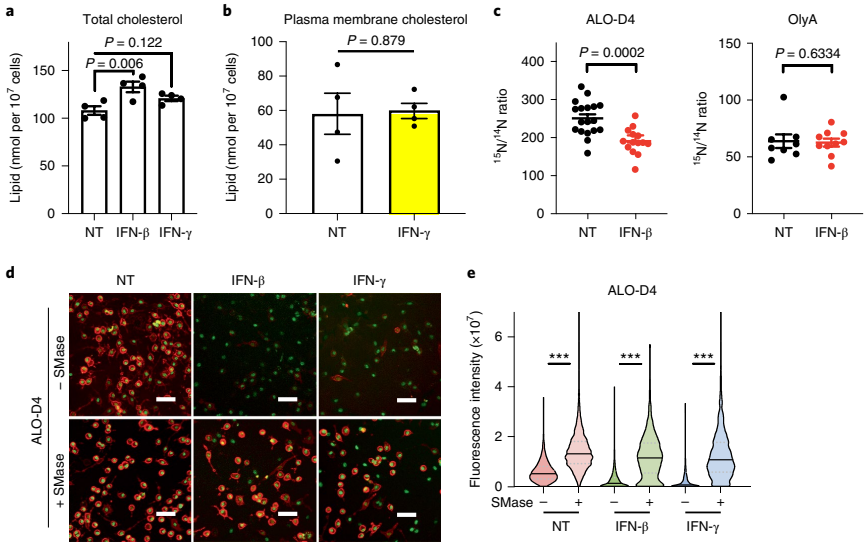

Fig. 3 | IFN signals reprogram cholesterol metabolism to decrease the pool of cholesterol targeted by CDCs. a, Total cholesterol (nmol lipid per 10^7 cells) from C57BL/6 BMDMs stimulated with IFN-β (20 ng ml^{-1}), IFN-γ (20 ng ml^{-1}) or unstimulated (NT) for 48 h ($n = 4$). **b**, Total plasma membrane cholesterol (nmol lipid per 10^7 cells) from C57BL/6 BMDMs stimulated with IFN-γ (40 ng ml^{-1}) or unstimulated (NT) for 24 h ($n = 4$). **c**, Quantification of [^{15}N]ALO-D4 or [^{15}N]OlyA binding on untreated (NT) or IFN-β-stimulated (100 ng ml^{-1}, 16 h) BMDMs determined by NanoSIMS. Quantification is based on the average ^{15}N/^{14}N ratio in cells. Data are the mean ± s.e.m ($n = 18$ and 14 for ALO-D4; $n = 8$ and 10 for OlyA). **d**, Confocal images of WT BMDM cultures stimulated with IFNs (20 ng ml^{-1}) for 24 h, treated with sphingomyelinase (SMase; 200 mU ml^{-1}) for 30 min at 37 °C and then stained with fluorescent ALO-D4 and DAPI. Scale bars represent 50 μm. **e**, Violin plots of cellular fluorescence intensity quantified from **d** ($n = 6{,}868$, 6,811, 3,404, 3,838, 2,930 and 2,642). Data are representative of three independent experiments (**a**, **d** and **e**), three independent samples (**c**) or from four biological replicates (**b**). Data in **a**–**c** are shown as the mean ± s.e.m. The violin plot in **e** is shown with the median (solid lines) and 25th and 75th percentiles (dashed lines). Statistical significance was determined using one-way ANOVA with Dunn's correction (**a**), an unpaired two-tailed Student's *t*-test (**b**) or a two-tailed Mann–Whitney test (**c** and **e**). ***$P < 0.001$.

markedly reduced ALO-D4 binding (Fig. 4f,g). Together, these data support the concept that the pool of newly synthesized cholesterol, rather than the total cholesterol available in the plasma membrane, is linked to the sensitivity or resistance of macrophages to CDC-mediated toxicity.

Production of 25HC is required for resistance to CDCs. IFNs have a well-defined role in inducing the conversion of cholesterol into 25HC via the enzyme CH25H in macrophages[5,13,14]. Thus, we next asked whether the endogenous production of 25HC is required for IFN-mediated protection against CDCs. To address this, control and CH25H-deficient macrophages were stimulated with IFNs and ALO-D4 binding was assessed. We observed that neither IFN-β nor IFN-γ treatment of CH25H-deficient macrophage cultures reduced ALO-D4 binding (Fig. 5a,b). Correspondingly, we found that stimulating CH25H-deficient macrophages with IFN-β or IFN-γ was unable to induce protection against either PFO or SLO challenge (Fig. 5c,d and Extended Data Fig. 5a,b). We also observed that, in contrast to control macrophages, IFN treatment of CH25H-deficient macrophages reduced their ability to maintain efficient phagocytosis of bacteria when challenged with PFO (Fig. 5e). Importantly, provisioning of 25HC to cultures of CH25H-deficient or control macrophages protected them from CDC-induced pore formation (Fig. 5f) and largely restored their ability to phagocytose bacteria (Fig. 5e). Thus, endogenous production of 25HC appears to be critical for macrophage protection to CDCs.

Next, we sought to better define the mechanism by which IFN signaling and the production of 25HC mediate protection against CDCs. Our studies to this point correlated a decrease in cholesterol biosynthesis with protection against challenge by CDCs, leading us to ask whether the loss of CH25H altered IFN-mediated reduction in the cholesterol synthesis. [^{13}C] glucose tracer enrichment studies showed that loss of CH25H in macrophages resulted in basally higher production of cholesterol as compared to control macrophages but did not alter total cholesterol content (Fig. 5g). IFN-β stimulation was able to reduce cholesterol synthesis in both control and CH25H-deficient macrophages, but the reduction was attenuated in the absence of CH25H, resulting in a synthetic profile that more closely resembled that observed in unstimulated control macrophages (Fig. 5g). Treatment of CH25H-deficient macrophages with simvastatin was sufficient to reduce ALO-D4 binding, supporting the concept that the ability of 25HC to regulate cholesterol synthetic flux is an important mechanism by which IFNs mediate protection from CDCs (Fig. 5h,i).

Cholesterol esterification contributes to CDC resistance of macrophages. We observed that IFNs induce a number of genes involved in cholesterol esterification and efflux (Fig. 6a), prompting us to ask whether these processes were also necessary for IFN-mediated protection from CDCs. As expected, IFN treatment of macrophages increased cholesterol ester formation[43,44] (Fig. 6b). Unexpectedly, we found that cholesterol in culture medium was not required for accumulation of esterified cholesterol in response to IFNs (Extended Data Fig. 6a), indicating that the source of cholesterol for esterification can be derived from host cell membranes rather than from the extracellular milieu. Pharmacologic inhibition of the cholesterol

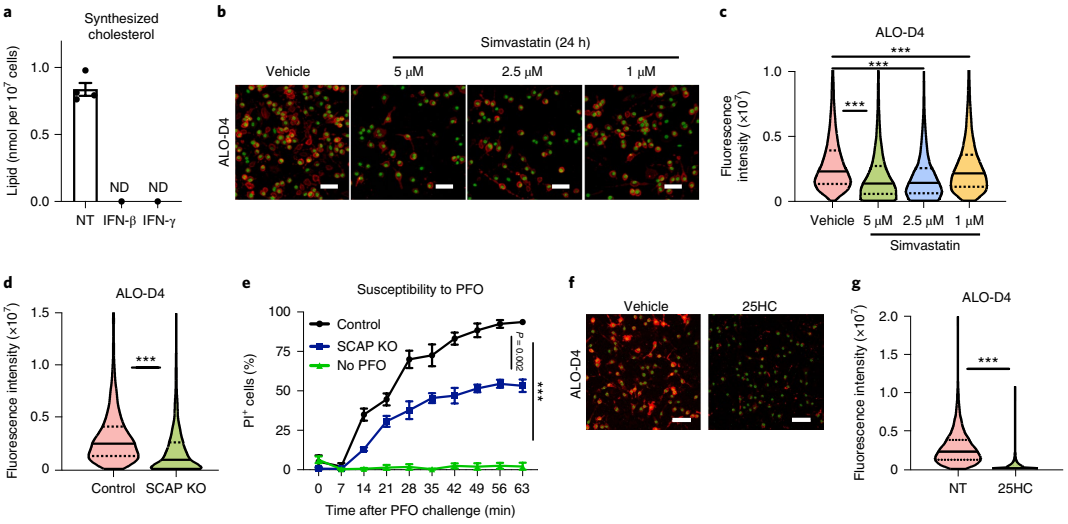

Fig. 4 | Cholesterol synthesis is linked to CDC susceptibility. a, Net synthesized cholesterol (nmol lipid per 10^7 cells) from C57BL/6 BMDMs stimulated with IFN-β (20 ng ml^{-1}), IFN-γ (20 ng ml^{-1}) or unstimulated (NT) for 48 h. Synthesized cholesterol was determined by GC–MS and ISA modeling ($n = 4$). ND, not detectable. **b**, Confocal images of WT BMDMs treated with simvastatin (1–5 μM) for 24 h and then stained with fluorescent ALO-D4 and DAPI. **c**, Violin plots of cellular fluorescence intensity quantified from **b** ($n = 5{,}713$, 2,252, 2,808 and 5,556). **d**, Violin plots of cellular fluorescence intensity quantified from control or SCAP KO BMDMs stained with fluorescent ALO-D4 and DAPI ($n = 3{,}306$ and 2,927). **e**, Percentage of PI$^+$ control or SCAP KO BMDMs challenged with PFO for 60 min in the presence of PI ($n = 3$). **f**, Confocal images of WT BMDM cultures incubated with 25HC (3 μM) for 4 h and then stained with fluorescent ALO-D4 and DAPI. **g**, Violin plots of cellular fluorescence intensity quantified from **f** ($n = 5{,}861$ and 5,769). Data are representative of three independent experiments. Data in **a** and **e** are shown as the mean ± s.e.m. Violin plots in **c**, **d** and **g** are shown with the median (solid lines) and 25th and 75th percentiles (dashed lines). Statistical significance was determined using a Kruskal–Wallis test with Dunn's correction (**c**), a two-tailed Mann–Whitney test (**d** and **g**) or one-way repeated-measures ANOVA (**e**). ***$P < 0.001$. Scale bars in **b** and **f** represent 50 μm.

esterification enzymes acyl-CoA:cholesterol acyltransferase 1 and 2 (ACAT1 and ACAT2) partially attenuated the protection from PFO-mediated pore formation conveyed by IFN signaling (Fig. 6c and Extended Data Fig. 6b). 25HC has also been shown to mediate cholesterol ester formation[45,46]; thus, we asked whether CH25H deficiency influenced cholesterol ester production in response to IFN signals. We found that quiescent CH25H-deficient macrophages had modestly increased levels of cholesterol esters and were able to increase this pool to the levels seen in control macrophages in response to IFN stimulation (Extended Data Fig. 6c). Consistent with this, we observed that treatment of CH25H-deficient macrophages with an ACAT inhibitor further increased ALO-D4 binding and increased their susceptibility to CDC-mediated membrane damage (Fig. 6d and Extended Data Fig. 6d). These data indicate that synthesis of cholesterol esters in macrophages is required, in part, for resistance to CDCs.

To test whether cholesterol efflux was required for IFN-mediated protection from CDCs, we activated macrophages deficient in the key cholesterol efflux transporters ATP-binding cassette sub-family A member 1 (ABCA1) or ATP-binding cassette sub-family G member 1 (ABCG1) with IFN[11,12]. We found that IFN treatment (24 h) reduced ALO-D4 binding in both ABCA1- and ABCG1-deficient macrophages to a level similar to that of control macrophages (Extended Data Fig. 6e). No difference in susceptibility to CDC-mediated pore formation was observed between quiescent control and ABCA1-deficient macrophages (Fig. 6e). Furthermore, IFN treatment conveyed resistance to PFO challenge for ABCA1-deficient macrophages, indicating that efflux was unlikely to be an important component of the IFN-mediated protection under these conditions. However, we did find that pharmacological enforcement of cholesterol efflux by treating with liver X receptors (LXR) agonist GW3965 (ref. [47]) for 24 h decreased ALO-D4 binding and provided robust protection against CDCs in wild-type macrophages (Fig. 6f,g). We also observed that LXR activation with GW3965 decreased ALO-D4 binding and conveyed protection for CH25H-deficient macrophages when challenged with PFO (Fig. 6f,g), indicating that 25HC mediates protection by regulating synthesis of cholesterol rather than by blocking CDCs at the membrane or inducing esterification. Taken together, these data support a model where IFNs reduce cholesterol synthesis and increase esterification of free cholesterol to reduce the cholesterol pool size in the plasma membrane targeted by CDCs.

25HC mediates protection to CDC-induced tissue damage. Finally, we asked whether reprogramming of cholesterol homeostasis would influence CDC susceptibility in vivo. To this end, SLO was injected into the skin of control and CH25H-deficient mice. Injection sites were visually monitored for up to 48 h for the appearance of erythema and ulceration. The SLO challenge resulted in modest erythema within 24 h and small ulcers at 48 h (Fig. 7a and Extended Data Fig. 7a). In contrast, CH25H-deficient mice developed severe erythema within 24 h, which progressed to ulcerative lesions that had upwards of a six-fold larger area than those of their wild-type counterparts (Fig. 7a and Extended Data Fig. 7a). Histologic examination confirmed greater epidermal ulceration area, along with a greater depth of tissue necrosis into the deep dermis and, in some cases, the adipose tissue, in CH25H-deficient mice (Fig. 7b). We also asked whether injecting 25HC into the dermis would protect mice from CDC-induced tissue damage. For these studies, we used the ALO challenge,

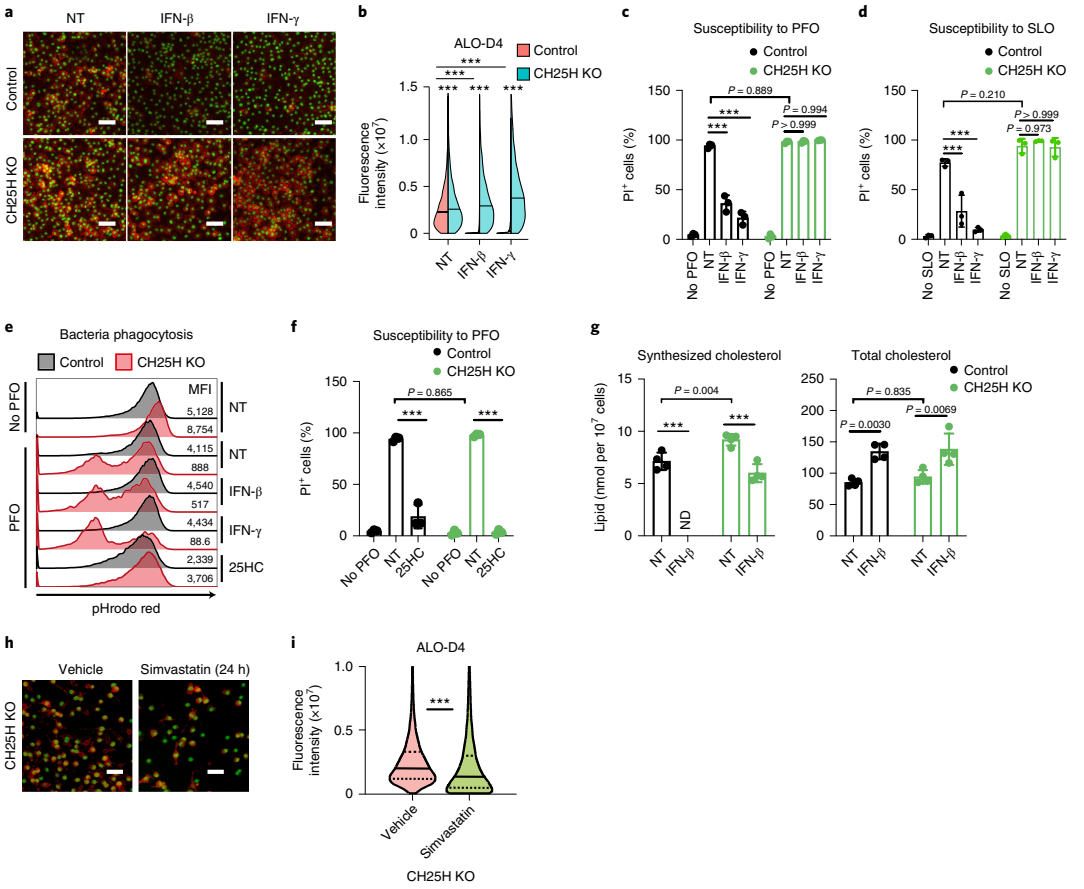

Fig. 5 | Production of 25HC is required to maintain changes in plasma membrane cholesterol and mediates resistance to CDCs. a, Confocal images of control or CH25H-deficient (CH25H KO) BMDM cultures stimulated with IFN-β or IFN-γ (20 ng ml^{-1}) for 24 h and then stained with fluorescent ALO-D4 and DAPI. **b**, Violin plots of cellular fluorescence intensity quantified from **a** (n = 5,294, 5,505, 4,564, 4,066, 5,370 and 4,962). **c**, Percentage of PI$^+$ control or CH25H KO BMDMs stimulated with IFNs (20 ng ml^{-1}) for 24 h and then challenged with PFO for 60 min in the presence of PI. **d**, Percentage of PI$^+$ control or CH25H KO BMDMs stimulated with IFNs (20 ng ml^{-1}) for 24 h and then challenged with SLO for 2 h in the presence of PI. **e**, Flow cytometry plots of *S. aureus* phagocytosed by control or CH25H KO BMDMs. Macrophage cultures were treated with IFNs (100 ng ml^{-1}) or 25HC (3 μM). After 24 h, BMDMs were washed and then incubated with PFO for 15 min. PFO-containing medium was then replaced with fresh medium containing pHrodo (red)-labeled *S. aureus*. MFI is indicated on the right. **f**, Percentage of PI$^+$ control or CH25H KO BMDMs incubated with 25HC (1 μM) overnight and then challenged with PFO for 60 min in the presence of PI. **g**, Net synthesized and total cholesterol (nmol per 10^7 cells) from CH25H KO or control BMDMs stimulated with IFN-β (20 ng ml^{-1}) or unstimulated (NT) for 48 h. Total and synthesized cholesterol was determined by GC–MS and ISA modeling. ND, not detectable. **h**, Confocal images of CH25H KO BMDMs treated with simvastatin (5 μM) for 24 h and then stained with fluorescent ALO-D4 and DAPI. **i**, Violin plots of cellular fluorescence intensity quantified from **h** (n = 6,666 and 2,867). Data are representative of three independent experiments. Data in **c**, **d**, **f** and **g** are shown as the mean ± s.e.m. (n = 3 in **c**, **d** and **f**; n = 4 in **g**). Violin plots in **b** and **i** are shown with the median (solid lines) and 25th and 75th percentiles (dashed lines in **i**). Statistical significance was determined using a Kruskal–Wallis test with Dunn's correction (**b**), two-way ANOVA with Tukey's correction (**c**, **d**, **f** and **g**) or a two-tailed Mann–Whitney test (**i**). ***P < 0.001. Scale bars in **a** and **h** represent 50 μm.

because we found that ALO reliably induces larger skin lesions in control mice compared to SLO. We found that preinjection of 25HC into the dermis of mice for 6 h markedly reduced ALO-induced tissue damage (Fig. 7c and Extended Data Fig. 7b). Histologic examination revealed that, in general, 25HC pretreatment completely prevented tissue damage, or, in cases with damage, 25HC pretreatment reduced both ulcer area and depth (Fig. 7d). Thus, we conclude that generation of 25HC and the consequent ability to reprogram cholesterol metabolism protect mice from CDC-mediated tissue damage.

Discussion

Immune cells have presumably evolved strategies to evade the deleterious effects of virulence factors to efficiently combat pathogens and protect the host from damage. In this study, we delineate a mechanism by which IFN signals alter the abundance of a small

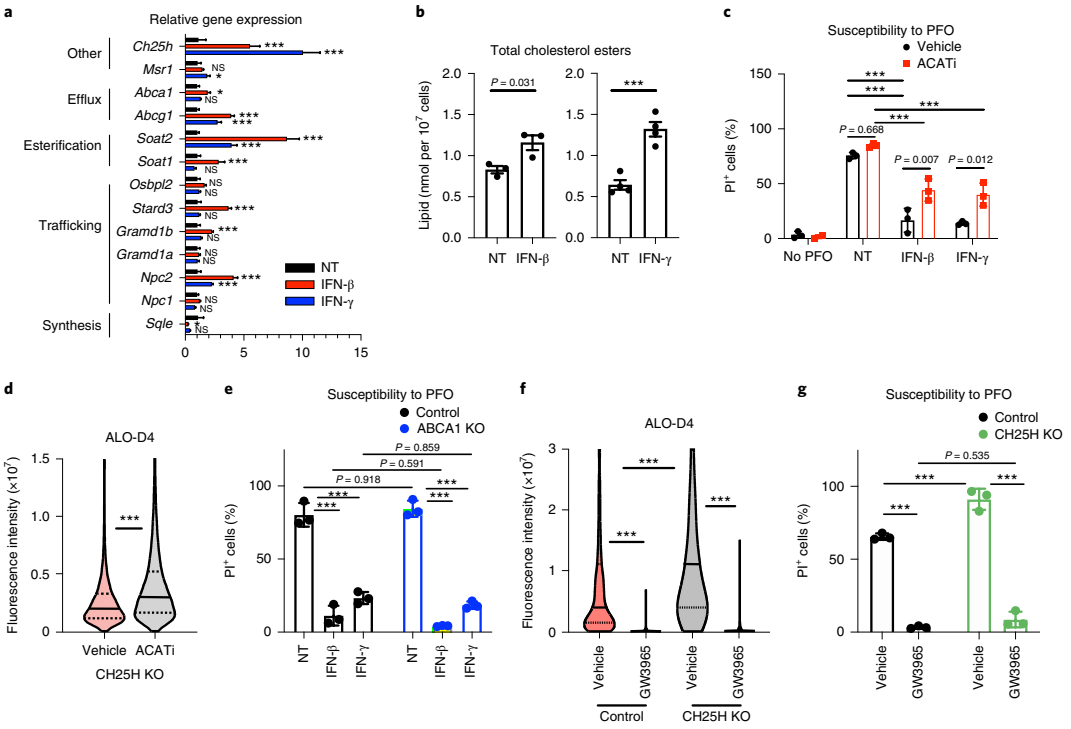

Fig. 6 | Cholesterol esterification contributes to CDC resistance of macrophages. a, Quantitative PCR (qPCR) analysis of genes that regulate cholesterol homeostasis in WT BMDMs treated with IFNs (20 ng ml^{-1}) for 24 h. **b**, Quantification (nmol lipid per 10^7 cells) of total cholesterol ester in WT BMDMs stimulated with IFN-β (20 ng ml^{-1}) or IFN-γ (20 ng ml^{-1}) for 48 h. Cholesterol ester pool sizes were determined by direct infusion mass spectrometry (left, $n = 3$; right, $n = 4$). **c**, Percentage of PI$^+$ BMDMs treated with IFN-β or IFN-γ (20 ng ml^{-1}) for 24 h in the presence of the ACAT inhibitor (ACATi) 58-035 (4.3 μM) and then challenged with PFO for 60 min in the presence of PI. **d**, Violin plots of cellular fluorescence intensity quantified from control or CH25H KO BMDMs treated with ACAT inhibitor 58-035 (4.3 μM) for 24 h and then stained with fluorescent ALO-D4 and DAPI ($n = 6{,}666$ and 9,997). **e**, Percentage of PI$^+$ control or ABCA1 KO BMDMs stimulated with IFNs (20 ng ml^{-1}) for 24 h and then challenged with PFO for 60 min in the presence of PI. **f**, Violin plots of cellular fluorescence intensity quantified from control or CH25H KO BMDMs treated with LXR agonist GW3965 (1 μM) for 24 h and then stained with fluorescent ALO-D4 and DAPI ($n = 2{,}304$, 3,954, 2,712 and 2,322). **g**, Percentage of PI$^+$ control or CH25H KO BMDMs treated with LXR agonist GW3965 (1 μM) for 24 h and then challenged with PFO for 60 min in the presence of PI. Data are representative of three independent experiments. Data in **a**–**c**, **e** and **g** are shown as the mean ± s.e.m. ($n = 3$) unless otherwise specified. Violin plots in **d** and **f** are shown with the median (solid lines) and 25th and 75th percentiles (dashed lines). Statistical significance was determined using one-way ANOVA with Dunnett's correction (**a**), an unpaired two-tailed Student's *t*-test (**b**), two-way ANOVA with Tukey's correction (**c**, **e** and **g**), a two-tailed Mann–Whitney test (**d**) or a Kruskal–Wallis test with Dunn's correction (**f**). ***$P < 0.001$; NS, not significant.

pool of cholesterol in the plasma membrane to protect macrophages and neutrophils from pathogen-produced toxins. It is likely that IFN-mediated reprogramming of cholesterol homeostasis will extend into other cell types, such as endothelium, adipocytes and epithelium, given the extent of tissue damage observed in the skin of CH25H-deficient mice in response to CDC challenge. Mechanistically, we find that inhibition of new cholesterol synthesis through the actions of CH25H is required to induce this protection mechanism. We also find that the IFN-mediated conversion of cholesterol into cholesterol esters is required for maximal protection. In combination, IFN regulation of these distinct but interrelated cholesterol metabolic pathways ensures that the cholesterol pool targeted by CDCs remains small, and consequently macrophages and neutrophils retain their function. These data also imply that pharmacologic manipulation of the cholesterol homeostatic machinery in the skin might decrease tissue damage associated with the deleterious effects of Gram-positive infections observed in necrotizing fasciitis or similar soft tissue infections. However, it will be necessary to determine whether manipulating cholesterol homeostasis in infected tissues interferes with other host defense pathways and clearance of microorganisms.

One unexpected finding of our studies is that the IFN-induced changes in plasma membrane cholesterol are restricted to a very small fraction of the total membrane cholesterol. The exact pool of cholesterol in the plasma membrane targeted by CDCs remains poorly characterized[19,20], and our data suggest that a minor fraction of cholesterol in the plasma membrane is required for CDC binding and pore formation. The majority of cholesterol is not evenly distributed across the plasma membrane[2,48], but rather is tightly associated with sphingomyelins or other phospholipids in microdomains[38,49]. Recent studies provide evidence for distinct pools of cholesterol within the plasma membrane. These studies describe a

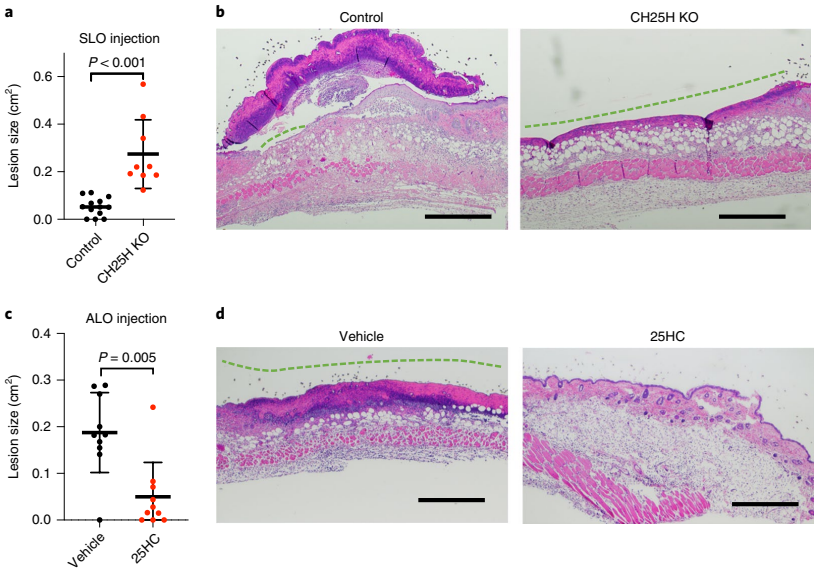

Fig. 7 | 25HC mediates protection against CDC-induced tissue damage. a, Quantification of lesion size from WT ($n = 13$) and CH25H KO ($n = 9$) mice challenged with SLO for 48 h. **b**, Representative histology from mice demonstrates serum crust overlying partial thickness erosion with a small full-thickness ulceration (green dashed line) of the epidermis and a robust inflammatory response in the dermis and adipose tissue in control (C57BL/6) mice (left). Wound areas in CH25H-deficient mice demonstrate a large ulceration (green dashed line) with necrosis of the papillary and much of the reticular dermis, with a less pronounced inflammatory response (right). **c**, Quantification of lesion size from WT mice ($n = 10$ each) pretreated with vehicle or 25HC for 6 h and challenged with ALO for 48 h. **d**, Representative histology of wounds demonstrates full-thickness ulceration (green dashed line) with overlying neutrophilic/serum crust by ALO in wounds pretreated with ethanol vehicle (left). Edema and a mixed mononuclear and neutrophilic inflammatory host response without ulceration are present in the dermis and adipose tissue of mice pretreated with 25HC (right). Data in **a** and **c** are shown as the mean ± s.e.m. Statistical significance was determined using a two-tailed Mann–Whitney test. Scale bars represent 500 μm (**b** and **d**).

small pool of cholesterol, termed 'accessible' cholesterol, that is in rapid equilibrium with the endoplasmic reticulum cholesterol pool and, consequently, the cholesterol biosynthetic machinery[48]. We suspect that this is the cholesterol pool that is targeted by CDCs and rapidly reduced upon IFN signaling. Our data indicate that this IFN-dependent reduction of the accessible cholesterol pool occurs through the combined actions of the ACAT enzymes and inhibition of cholesterol biosynthesis. We cannot rule out the possibility that IFN signals also move cholesterol laterally or vertically from the accessible pool into other domains in the plasma membrane. It will be of considerable interest to determine the spatial distribution of the accessible cholesterol pool within the plasma membrane and how this specific cholesterol pool relates to canonical domains in the plasma membrane as described previously.

We also believe that other cholesterol metabolic pathways will be involved in this protective mechanism. We found that IFNs induce changes in ALO-D4 binding within 2 h; thus, it seems likely that direct signaling events downstream of the IFN receptors initiate this process, and it will be of interest to define the cholesterol transport machinery involved in the rapid removal of this small cholesterol pool from the plasma membrane. The observation that both type I and type II IFNs regulate a broad cassette of genes involved in cellular cholesterol homeostasis (for example, efflux, esterification, synthesis and intracellular trafficking) leads us to surmise that considerable pressure exists to sequester or limit accessible or free cholesterol from pathogens, and it will be of interest to determine the pathophysiologic context where this reshaping of membrane cholesterol homeostasis contributes to host defense. These observations also imply that other mechanisms that can influence the pool size of accessible cholesterol, such as metabolic dysfunction, could influence the susceptibility of cells to these pore-forming toxins. Consistent with this notion, it has been shown that diabetes and obesity are independent risk factors for necrotizing fasciitis[50,51], and we posit that restoring cellular cholesterol homeostasis with drugs that target cholesterol metabolic machinery might serve to decrease the severity of disease in these patients. In support of this idea, we find that enforced cholesterol efflux through the activation of LXR can induce protection independently of IFN signaling. Likewise, injecting 25HC into the skin protected the dermis from ALO-induced damage, providing initial proof of concept that metabolic manipulation could be an adjunctive approach to conventional antimicrobials.

In conclusion, these studies provide evidence that rapid remodeling of the lipid content of membranes is used as a host defense strategy by macrophages and neutrophils. Given the breadth of microbial and viral proteins that target host lipids, we propose that signal-specific reprogramming of the lipidome of cells will be a fundamentally important strategy for host cells to evade different pathogens.

Online content

Any methods, additional references, Nature Research reporting summaries, source data, extended data, supplementary information, acknowledgements, peer review information; details of author contributions and competing interests; and statements of

data and code availability are available at https://doi.org/10.1038/s41590-020-0695-4.

Received: 11 March 2020; Accepted: 28 April 2020;
Published online: 8 June 2020

References

1. Lange, Y., Swaisgood, M. H., Ramos, B. V. & Steck, T. L. Plasma membranes contain half the phospholipid and 90% of the cholesterol and sphingomyelin in cultured human fibroblasts. *J. Biol. Chem.* **264**, 3786–3793 (1989).
2. Ikonen, E. Cellular cholesterol trafficking and compartmentalization. *Nat. Rev. Mol. Cell Biol.* **9**, 125–138 (2008).
3. van Meer, G., Voelker, D. R. & Feigenson, G. W. Membrane lipids: where they are and how they behave. *Nat. Rev. Mol. Cell Biol.* **9**, 112–124 (2008).
4. Luo, J., Yang, H. & Song, B. L. Mechanisms and regulation of cholesterol homeostasis. *Nat. Rev. Mol. Cell Biol.* **21**, 225–245 (2020).
5. Blanc, M. et al. The transcription factor STAT-1 couples macrophage synthesis of 25-hydroxycholesterol to the interferon antiviral response. *Immunity* **38**, 106–118 (2013).
6. Reboldi, A. et al. 25-hydroxycholesterol suppresses interleukin-1-driven inflammation downstream of type I interferon. *Science* **345**, 679–684 (2014).
7. Dang, E. V., McDonald, J. G., Russell, D. W. & Cyster, J. G. Oxysterol restraint of cholesterol synthesis prevents AIM2 inflammasome activation. *Cell* **171**, 1057–1071 (2017).
8. Araldi, E. et al. Lanosterol modulates TLR4-mediated innate immune responses in macrophages. *Cell Rep.* **19**, 2743–2755 (2017).
9. Blanc, M. et al. Host defense against viral infection involves interferon-mediated down-regulation of sterol biosynthesis. *PLoS Biol.* **9**, e1000598 (2011).
10. York, A. G. et al. Limiting cholesterol biosynthetic flux spontaneously engages type I IFN signaling. *Cell* **163**, 1716–1729 (2015).
11. Shibata, N. & Glass, C. K. Regulation of macrophage function in inflammation and atherosclerosis. *J. Lipid Res.* **50** (Suppl.), S277–S281 (2009).
12. Tall, A. R. & Yvan-Charvet, L. Cholesterol, inflammation and innate immunity. *Nat. Rev. Immunol.* **15**, 104–116 (2015).
13. Bauman, D. R. et al. 25-hydroxycholesterol secreted by macrophages in response to Toll-like receptor activation suppresses immunoglobulin A production. *Proc. Natl Acad. Sci. USA* **106**, 16764–16769 (2009).
14. Liu, S.-Y. et al. Interferon-inducible cholesterol-25-hydroxylase broadly inhibits viral entry by production of 25-hydroxycholesterol. *Immunity* **38**, 92–105 (2013).
15. Viard, M. et al. Role of cholesterol in human immunodeficiency virus type 1 envelope protein-mediated fusion with host cells. *J. Virol.* **76**, 11584–11595 (2002).
16. Goluszko, P. & Nowicki, B. Membrane cholesterol: a crucial molecule affecting interactions of microbial pathogens with mammalian cells. *Infect. Immun.* **73**, 7791–7796 (2005).
17. Rawat, S. S. et al. Modulation of entry of enveloped viruses by cholesterol and sphingolipids. *Mol. Membr. Biol.* **20**, 243–254 (2003).
18. Mazzon, M. & Mercer, J. Lipid interactions during virus entry and infection. *Cell. Microbiol.* **16**, 1493–1502 (2014).
19. Tweten, R. K. Cholesterol-dependent cytolysins, a family of versatile pore-forming toxins. *Infect. Immun.* **73**, 6199–6209 (2005).
20. Tweten, R. K., Hotze, E. M. & Wade, K. R. The unique molecular choreography of giant pore formation by the cholesterol-dependent cytolysins of Gram-positive bacteria. *Annu. Rev. Microbiol.* **69**, 323–340 (2015).
21. Gilbert, R. J. Inactivation and activity of cholesterol-dependent cytolysins: what structural studies tell us. *Structure* **13**, 1097–1106 (2005).
22. Timmer, A. M. et al. Streptolysin O promotes group A *Streptococcus* immune evasion by accelerated macrophage apoptosis. *J. Biol. Chem.* **284**, 862–871 (2009).
23. Bhattacharjee, P. & Keyel, P. A. Cholesterol-dependent cytolysins impair pro-inflammatory macrophage responses. *Sci. Rep.* **8**, 6458 (2018).
24. Corrotte, M., Fernandes, M. C., Tam, C. & Andrews, N. W. Toxin pores endocytosed during plasma membrane repair traffic into the lumen of MVBs for degradation. *Traffic* **13**, 483–494 (2012).
25. McNeil, P. L. & Kirchhausen, T. An emergency response team for membrane repair. *Nat. Rev. Mol. Cell Biol.* **6**, 499–505 (2005).
26. Romero, M. et al. Intrinsic repair protects cells from pore-forming toxins by microvesicle shedding. *Cell Death Differ.* **24**, 798–808 (2017).
27. Oishi, Y. et al. SREBP1 contributes to resolution of pro-inflammatory TLR4 signaling by reprogramming fatty acid metabolism. *Cell Metab.* **25**, 412–427 (2017).
28. Stetson, D. B. & Medzhitov, R. Type I interferons in host defense. *Immunity* **25**, 373–381 (2006).
29. McNab, F., Mayer-Barber, K., Sher, A., Wack, A. & O'Garra, A. Type I interferons in infectious disease. *Nat. Rev. Immunol.* **15**, 87–103 (2015).
30. Takeuchi, O. & Akira, S. Pattern recognition receptors and inflammation. *Cell* **140**, 805–820 (2010).
31. Woodward, J. J., Iavarone, A. T. & Portnoy, D. A. c-di-AMP secreted by intracellular *Listeria monocytogenes* activates a host type I interferon response. *Science* **328**, 1703–1705 (2010).
32. Pandey, A. K. et al. NOD2, RIP2 and IRF5 play a critical role in the type I interferon response to *Mycobacterium tuberculosis*. *PLoS Pathog.* **5**, e1000500 (2009).
33. Gay, A., Rye, D. & Radhakrishnan, A. Switch-like responses of two cholesterol sensors do not require protein oligomerization in membranes. *Biophys. J.* **108**, 1459–1469 (2015).
34. Chakrabarti, R. S. et al. Variability of cholesterol accessibility in human red blood cells measured using a bacterial cholesterol-binding toxin. *Elife* **6**, e23355 (2017).
35. Infante, R. E. & Radhakrishnan, A. Continuous transport of a small fraction of plasma membrane cholesterol to endoplasmic reticulum regulates total cellular cholesterol. *Elife* **6**, e25466 (2017).
36. Endapally, S., Infante, R. E. & Radhakrishnan, A. Monitoring and modulating intracellular cholesterol trafficking using ALOD4, a cholesterol-binding protein. *Methods Mol. Biol.* **1949**, 153–163 (2019).
37. Maxfield, F. R. & Wustner, D. Analysis of cholesterol trafficking with fluorescent probes. *Methods Cell Biol.* **108**, 367–393 (2012).
38. Endapally, S. et al. Molecular discrimination between two conformations of sphingomyelin in plasma membranes. *Cell* **176**, 1040–1053 (2019).
39. He, C. et al. High-resolution imaging and quantification of plasma membrane cholesterol by NanoSIMS. *Proc. Natl Acad. Sci. USA* **114**, 2000–2005 (2017).
40. He, C. et al. Macrophages release plasma membrane-derived particles rich in accessible cholesterol. *Proc. Natl Acad. Sci. USA* **115**, E8499–E8508 (2018).
41. Kandutsch, A. A. & Chen, H. W. Regulation of sterol synthesis in cultured cells by oxygenated derivatives of cholesterol. *J. Cell Physiol.* **85**, 415–424 (1975).
42. Goldstein, J. L., DeBose-Boyd, R. A. & Brown, M. S. Protein sensors for membrane sterols. *Cell* **124**, 35–46 (2006).
43. Panousis, C. G. & Zuckerman, S. H. Regulation of cholesterol distribution in macrophage-derived foam cells by interferon-γ. *J. Lipid Res.* **41**, 75–83 (2000).
44. Keyel, P. A., Tkacheva, O. A., Larregina, A. T. & Salter, R. D. Coordinate stimulation of macrophages by microparticles and TLR ligands induces foam cell formation. *J. Immunol.* **189**, 4621–4629 (2012).
45. Collins, J. L. et al. Identification of a nonsteroidal liver X receptor agonist through parallel array synthesis of tertiary amines. *J. Med. Chem.* **45**, 1963–1966 (2002).
46. Das, A., Brown, M. S., Anderson, D. D., Goldstein, J. L. & Radhakrishnan, A. Three pools of plasma membrane cholesterol and their relation to cholesterol homeostasis. *Elife* **3**, e02882 (2014).
47. Pike, L. J. Lipid rafts: bringing order to chaos. *J. Lipid Res.* **44**, 655–667 (2003).
48. Das, D. K., Baker, M. G. & Venugopal, K. Risk factors, microbiological findings and outcomes of necrotizing fasciitis in New Zealand: a retrospective chart review. *BMC Infect. Dis.* **12**, 348 (2012).
49. Arif, N., Yousfi, S. & Vinnard, C. Deaths from necrotizing fasciitis in the United States, 2003–2013. *Epidemiol. Infect.* **144**, 1338–1344 (2016).
50. Timmins, J. M. et al. Targeted inactivation of hepatic *Abca1* causes profound hypoalphalipoproteinemia and kidney hypercatabolism of apoA-I. *J. Clin. Invest.* **115**, 1333–1342 (2005).
51. Sag, D., Cekic, C., Wu, R., Linden, J. & Hedrick, C. C. The cholesterol transporter ABCG1 links cholesterol homeostasis and tumour immunity. *Nat. Commun.* **6**, 6354 (2015).

Methods

Mouse strains. Wild-type and gene-targeted mice were purchased from The Jackson Laboratory: WT C57BL/6J (JAX 000664), B6.129S6-*Ch25h*^{tm1Rus}/J (*Ch25h*$^{-/-}$, JAX 016263) and B6(Cg)-*Ifnar1*$^{tm1.2Es}$/J (*Ifnar1*$^{-/-}$, JAX 028288). SCAP-deficient macrophages were generated from a *Lzy2*-Cre × *Scap*$^{fl/fl}$ cross as previously described[10]. ABCA1- and ABCG1-deficient macrophages were generated from *Lzy2*-Cre × *Abca1*$^{fl/fl}$ or *Lyz2*-Cre × *Abcg1*$^{fl/fl}$ animals as previously described[50,51]. All mice used for BMDMs were males aged 8–16 weeks. For in vivo CDC injections, mice were female and aged 8–12 weeks. All mice were maintained in pathogen-free facilities of the University of California, Los Angeles. All experiments on mice and tissues collected from mice were performed in strict accordance with the University of California policy on the humane and ethical treatment of animals.

PBMC-derived macrophages. Human monocyte-derived monocytes were isolated from leukopacks using standard Ficoll isolation procedures and plastic adherence. Isolation of monocytes was conducted by the UCLA Center for AIDS Research Virology Core laboratory. Monocytes were differentiated into macrophages with 50 ng ml^{-1} human GM-CSF (Peprotech, 300-03) in IMDM medium (HyClone) with 10% FBS and 1% (vol/vol) penicillin–streptomycin for 7 d before experimental use.

Mouse cells. Bone marrow cells were differentiated into macrophages in DMEM containing 10% (vol/vol) FBS (HyClone, GE SH3007103), 5% (vol/vol) M-CSF conditioned medium, 1% (vol/vol) penicillin–streptomycin, 1% (vol/vol) glutamine (Invitrogen) and 0.5% (vol/vol) sodium pyruvate (Invitrogen) for 7–9 d before experimental use. Cells were changed to medium with 5% FBS at the time of stimulation. Mouse neutrophils were isolated from the bone marrow using the EasySep Mouse Neutrophil Enrichment Kit following the manufacturer's protocol (StemCell, 19762).

Reagents. PRR ligands used were LPS (Invivogen, tlrl-smlps), poly(I:C) (Invivogen, tlrl-pic (HMW)), Pam3CSK4 (Invivogen, tlrl-pms), CL307 (Invivogen, tlrl-c307), ODN1668 (Invivogen, tlrl-1668), 2′,3′-cGAMP (Invivogen, tlrl-nacga23), c-di-GMP (Invivogen, tlrl-cdg), 5′-ppp-dsRNA (Invivogen, tlrl-3prn), iE-DAP (Invivogen, tlrl-dap) and *N*-glycolyl-MDP (Invivogen, tlrl-gmdp). Cytokines used were recombinant murine IFN-γ (Peprotech, 315-05), recombinant mouse IFN-β1 (carrier-free; BioLegend, 581302), recombinant human IFN-β (Peprotech, 300-02BC) and IFN-α was a kind gift from the laboratory of R. Modlin (UCLA). HyClone IMDM medium (16750-088) and FBS (SH3007103) were purchased from VWR. PFO was a kind gift from the laboratory of A.S. Divakaruni[52] (Agilent, 102504-100). SLO from *Streptococcus pyogenes* (gamma irradiated; S0149-25KU), 58-035 (S9318), simvastatin (S6196-5MG) and LXR agonist GW3965 (G6295-5MG) were purchased from Sigma-Aldrich.

Cholesterol ester analysis. Macrophages were cultured in six-well dishes (Fisher, 08-772-1B) and stimulated with TLR ligands as described above. At 48 h after stimulation, cells were imaged for cell counting as previously described[10], scraped and spun down in PBS and snap frozen as cell pellets. A modified Bligh and Dyer extraction[53] was carried out on samples. Before biphasic extraction, a 13-lipid class Lipidyzer Internal Standard Mix was added to each sample (AB SCIEX, 5040156). Following two successive extractions, pooled organic layers were dried down in a Genevac EZ-2 Elite. Lipid samples were resuspended in 1:1 methanol/dichloromethane with 10 mM ammonium acetate and transferred to robovials (Thermo Fisher, 10800107) for analysis. Samples were analyzed on the Lipidyzer Platform for targeted quantitative measurement of 1,100 lipid species across 13 classes. The Differential Mobility device on the Lipidyzer was tuned with a SelexION tuning kit (SCIEX, 5040141). Instrument settings, tuning settings and the MRM list are available upon request. Data analysis was performed on Lipidyzer software. Quantitative values were normalized to cell counts.

Isotope-enrichment experiments. BMDMs differentiated for 8 d were transferred to complete medium containing 50% [^{13}C] glucose (Cambridge Isotope Laboratories, CLM-1396-MPT-PK) with or without TLR stimulation for 48 h before collection. Analysis of labeled fatty acids and cholesterol was performed as described previously[10,54,55]. The relative contributions of synthesis to the total cholesterol pool over the 48-h labeling period were determined by fitting the isotopolog distributions for cholesterol in a model similar to isotopomer spectral analysis (ISA) as described previously[10,54,55].

Gene expression analysis. RNA was extracted from all cells with TRIzol (Thermo Fisher, 15596-018) using the manufacturer's protocols. cDNA was synthesized with a high-capacity cDNA reverse transcription kit (Applied Biosystems, 4368814) according to the manufacturer's instructions (700 ng µl^{-1} RNA per cDNA synthesis reaction). qPCR was conducted on the Roche LightCycler 480 using SYBR green master mix (Kapa Biosciences) or PowerUp SYBR green master mix (Thermo Fisher, A25778) and 0.5 µmol l^{-1} primers. Relative expression values were normalized to a control gene (*Rplp0*) and expressed in terms of linear relative mRNA values.

CDC permeabilization live-cell imaging. BMDMs and neutrophils were seeded at 5 × 10^4 cells per well on 96-well plates (E&K Scientific, EK-25090, Greiner) and BMDMs were left for 2 d before stimulation. Cells were pretreated with TLR ligands for 2–24 h depending on the experiment. For live-cell imaging, culture media were replaced by 37 °C PBS with 0.05% BSA, 1 µg ml^{-1} PI (VWR, 80057-368) and 5 µg ml^{-1} Hoechst 33342 (Thermo Fisher, H3570). Next, cells were challenged by spiking recombinant PFO (final concentration of 1 nM), gamma-irradiated SLO (final concentration of 22 nM) or recombinant ALO (final concentration of 1.5 nM), and plates were imaged every 10 min on a Molecular Devices ImageXpress XL using a ×20 objective (Nikon Plan Fluor; NA = 0.3). SLO was activated with the addition of 10 mM dithiothreitol (DTT) at 22 °C for 10 min. Total (Hoechst 33342$^+$) and permeabilized (PI$^+$) cell numbers were assessed using MetaXpress Software with Powercore using the multi-wavelength cell scoring module.

Macrophage phagocytosis assay. BMDMs were seeded at 1.5 × 10^5 cells per well on 24-well plates and left for 1–3 d before stimulation. Cells were pretreated with TLR ligands for 24 h. PFO was diluted in PBS to a final concentration of 2 nM, and cells were left to incubate for 15 min at 37 °C, after which cells were washed with PBS twice and the medium was replaced with fresh BMDM medium with 5% FBS. pHrodo red *S. aureus* Bioparticles Conjugate (0.4 mg ml^{-1}; Thermo Fisher, A10010) was added on top of the macrophages, and the plates were incubated for 1 h at 37 °C. To remove the non-phagocytosed apoptotic thymocytes or pHrodo red bioparticle conjugate, cells were washed once with PBS and then subjected to flow cytometry analysis.

Flow cytometry analysis. BMDMs were lifted off the plates by scraping with the plunger of a 1-ml syringe and transferred to a 96-well round-bottom plate. After pelleting, cells were first incubated with TruStain FcX (anti-mouse CD16/32) antibody (BioLegend, 101319; 1:500) in FACS buffer (PBS with 2% FBS and 1 mM EDTA) for 10 min on ice. Cells were then stained with antibodies for surface marker CD11b (BioLegend, 101207; 1:400) for 20 min on ice. After one wash, cells were resuspended in FACS buffer with 1 µg ml^{-1} DAPI (Thermo Fisher, D1306) and analyzed on a flow cytometer (Attune NxT). Data were analyzed by FlowJo V10.

Plasma membrane purification. BMDMs were seeded at 8 × 10^6 cells per plate on 10-cm tissue-culture-treated dishes. Cells were left for 2 d before stimulation. Cells were then treated with IFNs for 24 h. Plasma membrane purification was carried out by cell surface biotinylation followed by streptavidin affinity chromatography as previously described[36,46].

Filipin III staining. BMDMs were seeded at 1.5 × 10^5 cells per well on 24-well plates. Cells were left for 1–3 d before stimulation. Cells were pretreated with TLR ligands for 24 h. Filipin III was purchased from Sigma-Aldrich (F4767) and resuspended in ethanol to 2 mg ml^{-1}. BMDMs were washed once with PBS and fixed with 3% paraformaldehyde for 15 min at 22 °C. Cells were then washed twice and stained with 100 µg ml^{-1} filipin III for 30 min at 22 °C in darkness. After staining, cells were washed once with PBS and visualized using a Zeiss Axio Observer Z1.

CTB staining. BMDMs were seeded at 1.5 × 10^5 cells per well on 24-well plates and left for 1–3 d before stimulation. Cells were pretreated with IFNs for 24 h. BMDMs were lifted off the plates by scraping with the plunger of a 1-ml syringe and transferred to a 96-well round-bottom plate. CTB was purchased from Thermo Fisher Scientific (C34777). Cells were stained with 1 µg ml^{-1} CTB for 10 min on ice. Cells were then resuspended in FACS buffer and analyzed with a flow cytometer (Attune NxT). Data were analyzed by FlowJo V10.

Preparation of ^{15}N- or ^{13}C-labeled His-tagged ALO-D4. A plasmid for ALO-D4 (ALO amino acids 404–512 with C472A and S404C substitutions) was originally obtained from A. Radhakrishnan[36,38] (University of Texas Southwestern Medical Center, Dallas), and ^{15}N-labeled ALO-D4 was prepared as described before[56]. Briefly, ALO-D4 was expressed in BL21(DE3)pLysS *Escherichia coli* (Invitrogen) induced with 1 mM isopropyl β-D-1-thiogalactopyranoside (IPTG) in 1 liter of minimal medium containing 20.2 mM NH_4Cl and 2 g of glucose at 18 °C for 16 h. [^{15}N]NH_4Cl or [^{13}C]glucose was used for preparation of [^{15}N]ALO-D4- or [^{13}C]-ALO-D4, respectively. Cells were pelleted and lysed by sonication, and the lysate was centrifuged at 4 °C. The supernatant was mixed with 4 ml of HisPur Cobalt resin (50% bed volume; Thermo Fisher Scientific). The mixture was loaded into a column and allowed to flow through by gravity. The column was washed, and [^{15}N]ALO-D4 was eluted with a buffer containing 300 mM imidazole. The eluates were pooled and concentrated to 1 ml with an Amicon 10-kDa-cutoff concentrator (Millipore). The purified [^{15}N]ALO-D4 was stored at 4 °C.

Preparation of His-tagged OlyA and full-length ALO. Plasmids for OlyA (with C62S, C94S and S151C substitution) and ALO were kind gifts from A. Radhakrishnan[38] (University of Texas Southwestern Medical Center, Dallas).

Preparation of fluorescent ALO-D4 and OlyA. Purified protein was conjugated as described previously, with slight modifications[10]. Briefly, cysteine-substituted

ALO-D4 or OlyA was incubated with AlexaFluor-488 or AlexaFluor-594 (Life Technologies) at 4 °C overnight in 50 mM Tris-HCl (pH 7.5) and 150 mM NaCl (1× TBS) containing 1 mM Tris(2-carboxyethyl)phosphine hydrochloride (TCEP). Free dye was separated by extensive buffer exchange with 1× TBS in Amicon 10-kDa-cutoff concentrator (Millipore) and stored at 4 °C.

Binding of ALO-D4 and OlyA to cells. Cells were seeded at 1.5×10^5 cells per well on poly(D-lysine)-coated coverslips (Neuvitro, Fisher Scientific, NC0672873) on a 24-well plate. After stimulation, cells were incubated with ALO-D4 or OlyA as described previously[40]. Briefly, macrophages were washed three times for 10 min in PBS with Ca^{2+} and Mg^{2+} containing 0.2% (wt/vol) BSA. Cells were then incubated with ALO-D4 or OlyA (all 20 μg ml^{-1}) in PBS with Ca^{2+} and Mg^{2+} containing 0.2% (wt/vol) BSA for 2 h at 4 °C. The unbound proteins were removed by washing three times with PBS with Ca^{2+} andMg^{2+} for 2 min each.

Confocal microscopy analysis. After fluorescently labeled ALO-D4 or OlyA binding, cells were fixed with 3% paraformaldehyde for 15 min and stained with 5 μg ml^{-1} DAPI, and cells were washed twice with PBS with Ca^{2+} and Mg^{2+}. Images were taken using an Axiovert 200 M microscope and processed with Zen 2010 software (Zeiss). High-resolution images were captured using a Zeiss LSM880.

Quantification of fluorescence intensity. For signal quantification, cells were plated on 24-well plates (Cellvis, P24-0-N) and treated and stained as above, and fixed cells in DPBS with Ca^{2+} and Mg^{2+} were imaged within 24 h. Images were taken at the UCLA Molecular Screening Shared Resource core facility on a Molecular Devices ImageXpress confocal using a ×20 objective (Nikon Plan Fluor; NA = 0.3) on a Molecular Devices ImageXpress XL imaging system. Maximum projected cellular fluorescence intensity was assessed by MetaXpress software with Powercore using the multi-wavelength cell scoring module. Integrated fluorescence intensity profiles were exported and analyzed in R with the ggplot2 package or in GraphPad Prism 8. Filipin III staining was quantified with FIJI by measuring fluorescent signals on plasma membranes.

NanoSIMS sample preparation. As described previously[56], after ALO-D4 or OlyA binding, cells were fixed with 4% paraformaldehyde (Electron Microscopy Sciences) and 2.5% glutaraldehyde (Electron Microscopy Sciences) in 0.1 M phosphate buffer (1.14 g NaH_2PO_4 and 1.69 g Na_2HPO_4 in a 100-ml final volume of ddH_2O, pH 7.4) for 20 min at 4 °C followed by 1 h at 22 °C. The samples were washed three times for 7 min each in 0.1 M phosphate buffer, postfixed with 1% osmium tetroxide (Electron Microscopy Sciences) in 0.1 M phosphate buffer for 45 min and washed three times for 7 min each in ice-cold ddH_2O. After washing, cells were air-dried.

NanoSIMS analyses. As described before[40,56], platinum-coated (5-nm) cells were analyzed with a NanoSIMS 50l instrument (CAMECA) with some modifications. Briefly, samples were bombarded with a focused $^{133}Cs^+$ primary beam, and secondary ions (for example, $^{12}C^-$, $^{13}C^-$, $^{16}O^-$, $^{12}C^{14}N^-$ and $^{12}C^{15}N^-$) and secondary electrons were collected. Before imaging, a high $^{133}Cs^+$ primary beam (current of 1 nA; primary aperture D1 = 1) was used to presputter an area of 50 × 50 μm^2 for 25 s to remove the platinum coating and implant $^{133}Cs^+$. In the same region, low-magnification images (~ 40 × 40 μm^2) were obtained with a ~2.5-pA beam current (primary aperture D1 = 2), a dwell time of 2.5 ms per pixel and scans of 512 × 512 pixels. High-magnification images (~10 × 10 μm^2) were obtained with a ~0.8-pA beam current (primary aperture D1 = 3), a dwell time of ~10 ms per pixel and scans of 512 × 512 pixels.

NanoSIMS quantification. To quantify $^{13}C/^{12}C$ and $^{15}N/^{14}N$ ratios in cells, we identified particles by SEM and/or $^{12}C^-$, $^{12}C^{14}N^-$, $^{16}O^-$ or secondary electron nanoSIMS images, and regions of interest in the middle of the particles were defined with the OpenMIMS plugin in ImageJ (NIH). For each image, the mean $^{15}N/^{14}N$ and $^{13}C/^{12}C$ ratios of the regions of interest were measured by ImageJ and processed by Prism 7.0.

In vivo CDC injection. For SLO challenge studies, litter-matched control and *Ch25h*$^{-/-}$ C57BL/6J mice were shaved on the lower back and recovered overnight. On the next day, mice were intradermally injected with either PBS or SLO (8 kU per mouse). SLO was activated with 10 mM DTT at 22 °C. Photographs of the skin lesions were taken 48 h later, and the lesion area (in cm^2) was measured using ImageJ software, followed by an unequal *t*-test. For ALO challenge studies, wild-type C57BL/6 mice were shaved on the lower back and preinjected intradermally with 25HC (10 mg kg^{-1}) or ethanol vehicle control for 6 h, followed by ALO injection (20 nM). Lesion sizes were quantified as above 48 h after ALO injection. Photographs of the skin lesions were taken 48 h after the ALO challenge, and the lesion area was measured using ImageJ software, followed by an unequal *t*-test. Samples were collected for histologic analysis in the UCLA Translational and Pathology Core Laboratory.

Statistical analysis. Experiments were conducted as three biologically distinct independent replicates unless otherwise stated. Statistical significance was determined using GraphPad Prism software. For bar graphs, line graphs and scatterplots, data are shown as the mean and the error bars depict the s.e.m. unless otherwise indicated. For all CDC-permeabilization assays, an average of 800 cells were imaged per well and used for calculations. Statistical analysis and assessment of CDC-permeabilization curves began when the first images were taken after CDCs were added to cultures until the end of the assay at 60 min. Statistical tests used for each graph are specified in the figure legend.

Reporting Summary. Further information on research design is available in the Nature Research Reporting Summary linked to this article.

Data availability

All original data are available from the corresponding author upon request.

References

52. Divakaruni, A. S. et al. Thiazolidinediones are acute, specific inhibitors of the mitochondrial pyruvate carrier. *Proc. Natl Acad. Sci. USA* **110**, 5422–5427 (2013).
53. Bligh, E. G. & Dyer, W. J. A rapid method of total lipid extraction and purification. *Can. J. Biochem. Physiol.* **37**, 911–917 (1959).
54. Williams, K. J. et al. An essential requirement for the SCAP/SREBP signaling axis to protect cancer cells from lipotoxicity. *Cancer Res.* **73**, 2850–2862 (2013).
55. Argus, J. P. et al. Development and application of FASA, a model for quantifying fatty acid metabolism using stable isotope labeling. *Cell Rep.* **25**, 2919–2934 (2018).
56. He, C., Fong, L. G., Young, S. G. & Jiang, H. NanoSIMS imaging: an approach for visualizing and quantifying lipids in cells and tissues. *J. Investig. Med.* **65**, 669–672 (2017).

Acknowledgements

This research was supported by NIH grants AI093768 (to S.J.B.), HL146358 (to S.J.B. and P.T.), AR073940 (to P.O.S), and HL136543 (to E.J.T.). M.S.L. is supported by Ruth L. Kirschstein National Research Service Award AI007323. The research described was also supported by an NIH/National Center for Advancing Translational Science (NCATS) UCLA CTSI grant (UL1TR001881). We thank S. Young, T. Weston and R.S. Jung for help with protein purification. We thank T. Weston for NanoSIMS sample preparation and SEM imaging. We thank A. Divakaruni for guidance with PFO permeabilization assays. We thank A. Radhakrishnan for ALO-D4 and full-length ALO plasmids. We thank S. Young, A. Hoffmann, Y. Du, R. Sun, T.-T. Wu, J. F. Miller and M. Li for thoughtful discussions.

Author contributions

S.J.B. conceived the study. Q.D.Z. led the design and execution of experiments. X.C. codesigned and performed all flow cytometry experiments and data analysis. V.L.B., W.Y.H. and J.J.M. contributed to flow cytometry experiments. J.J.M. and M.S.L. contributed to protein purification and staining experiments. Q.D.Z., M.S.L. and R.D. developed and performed live-cell imaging assays. C.H. performed NanoSIMS analysis and contributed to protein purification. J.J.M. and E.B.K. contributed to RNA analysis. W.Y.H. and A.G.Y. performed GC–MS analysis with help from Q.D.Z. and E.B.K. K.J.W. conducted lipidomic studies. X.X., A.F., P.T. and E.J.T. contributed to *Abcg1*, *Abca1* and SCAP KO studies. A.E.D. analyzed gene expression data. A.-C.F., P.O.S., M.S.L. and S.T.S. conceptualized and developed the in vivo SLO challenge assay. W.Y.H. contributed to data visualization. S.J.B., Q.D.Z., W.Y.H., X.C. and P.T. contributed to construction of the manuscript.

Competing interests

The authors declare no competing interests.

Additional information

Extended data is available for this paper at https://doi.org/10.1038/s41590-020-0695-4.

Supplementary information is available for this paper at https://doi.org/10.1038/s41590-020-0695-4.

Correspondence and requests for materials should be addressed to S.J.B.

Editor recognition statement L. A. Dempsey was the primary editor on this article and managed its editorial process and peer review in collaboration with the rest of the editorial team.

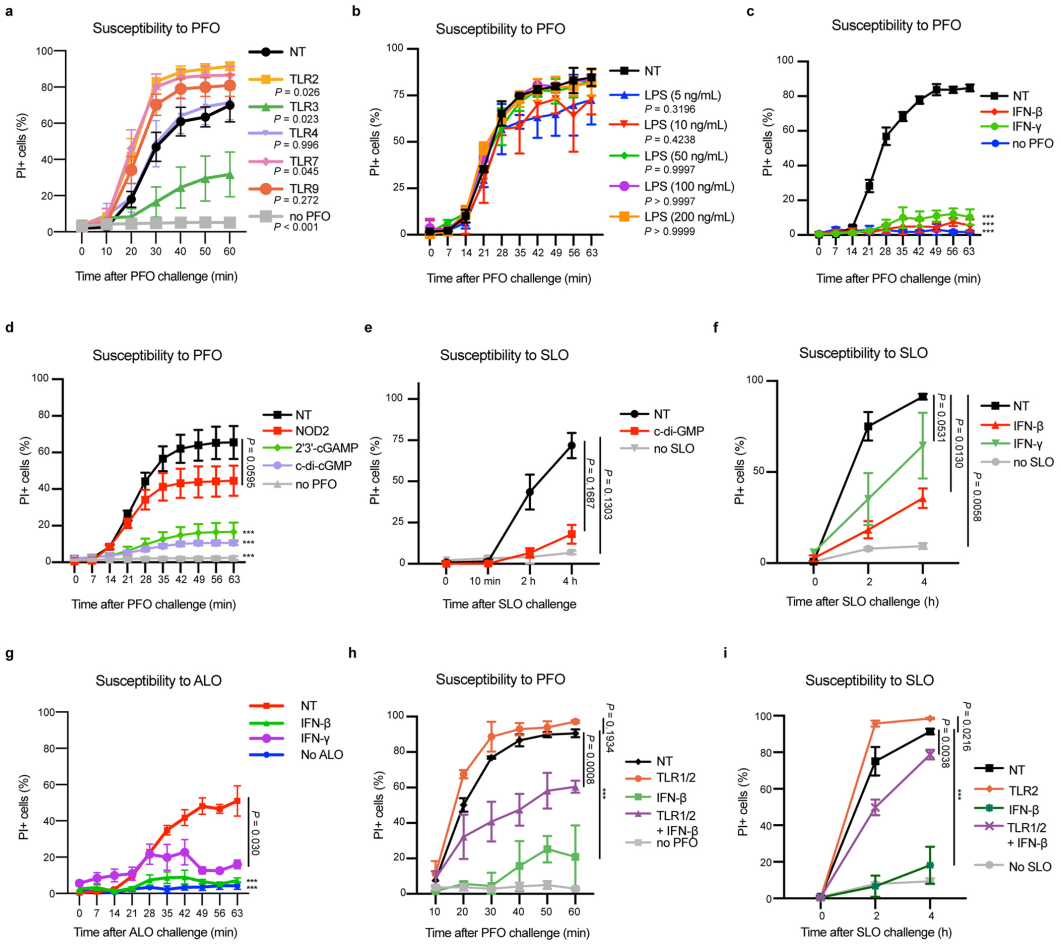

Extended Data Fig. 1 | Interferon signaling mediates resistance to cholesterol-dependent cytolysins. a, Percentage of PI-positive BMDMs treated with TLR1/2 agonist (Pam3CSK4; 50 ng/mL), TLR3 agonist (Poly(I:C); 1 μg/mL), TLR4 agonist (LPS; 50 ng/mL), TLR7 agonist (CL307; 100 nM), TLR9 (ODN1668; 100 nM) agonist, or unstimulated (NT) for 24 h and then challenged with PFO for up to 60 min in the presence of PI. Cells were imaged every 10 min to assess changes in PI incorporation. **b**, Percentage of PI-positive BMDMs treated with the various concentrations of TLR4 agonist for 24 h and then challenged with PFO for up to 60 min in the presence of PI. Cells were imaged every 7 min to assess changes in PI incorporation. **c**, Percentage of PI-positive BMDMs treated with IFN-β or IFN-γ (20 ng/mL) for 24 h and then challenged with PFO for 60 min in the presence of PI. **d**, Percentage of PI-positive BMDMs treated with NOD2 agonist (N-Glycolyl-MDP; 20 μg/ml), STING agonist (2',3'cGAMP and c-di-GMP; both 2 μg/mL) for 24 h and then challenged with PFO for 60 min in the presence of PI. **e**, Percentage of PI-positive BMDMs treated with STING ligand for 24 h and then challenged with Streptolysin O (SLO) for 4 h in the presence of PI. **f**, Percentage of PI-positive BMDMs treated with IFN-β or IFN-γ (20 ng/mL) for 24 h and then challenged with SLO for 4 h in the presence of PI. **g**, Percentage of PI-positive BMDMs treated with IFN-β or IFN-γ (20 ng/mL) for 24 h and then challenged with ALO for 60 min in the presence of PI. **h**, Percentage of PI-positive BMDMs treated with IFN-β (100 ng/mL) or TLR1/2 agonist, or IFN-β (100 ng/mL) together with TLR1/2 agonist for 24 h and then challenged with PFO for 60 min in the presence of PI. **i**, Percentage of PI-positive BMDMs treated with IFN-β (100 ng/mL) or TLR1/2 agonist, or IFN-β (100 ng/mL) together with TLR1/2 agonist for 24 h and then challenged with SLO for 4 h in the presence of PI. Data are representatives of three independent experiments, and are shown as mean ± s.e.m. (n = 3). Statistical significance was determined using an RM one-way ANOVA with Dunnett's correction (**a**-**g**) or a two-way ANOVA with Dunnett's correction (**h**, **i**). ***P<0.001.

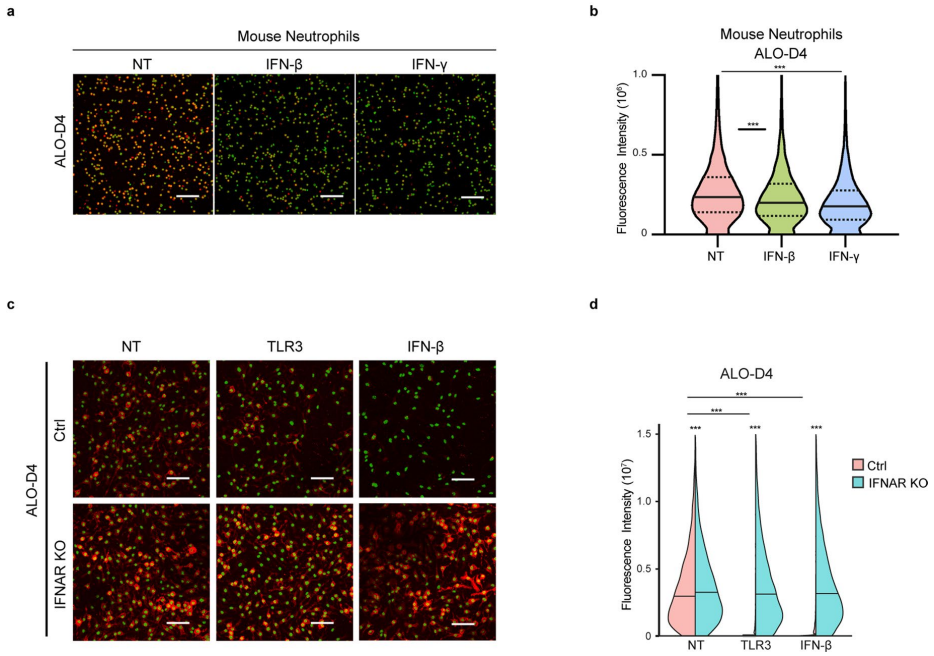

Extended Data Fig. 2 | IFN signals decrease plasma membrane binding to ALO-D4 protein. a, Confocal images of neutrophils stimulated with IFN-β or IFN-γ (20 ng/mL) for 6 h, and then stained with fluorescent ALO-D4 and DAPI. **b**, Violin plots of cellular fluorescent intensity quantified from **a** (n = 20334, 18546, 16290). **c**, Confocal images of WT or type I interferon receptor–deficient (IFNAR KO) BMDMs stimulated with TLR3 agonist (1 μg/mL) or IFN-β (20 ng/mL) for 24 h, and then stained with fluorescent ALO-D4 and DAPI. **d**, Violin plots of cellular fluorescent intensity quantified from **c** (n = 5543, 6682, 4673, 8231, 5201, 7906). Data are representatives of three independent experiments. Violin plots are shown with median (solid lines in **b**, **d**) and 25% and 75% percentiles (dashed lines in **b**), and statistical significance was determined using a Kruskal-Wallis test with Dunn's correction. ***P<0.001. Scale bars in **a**, **c** represent 50 μm.

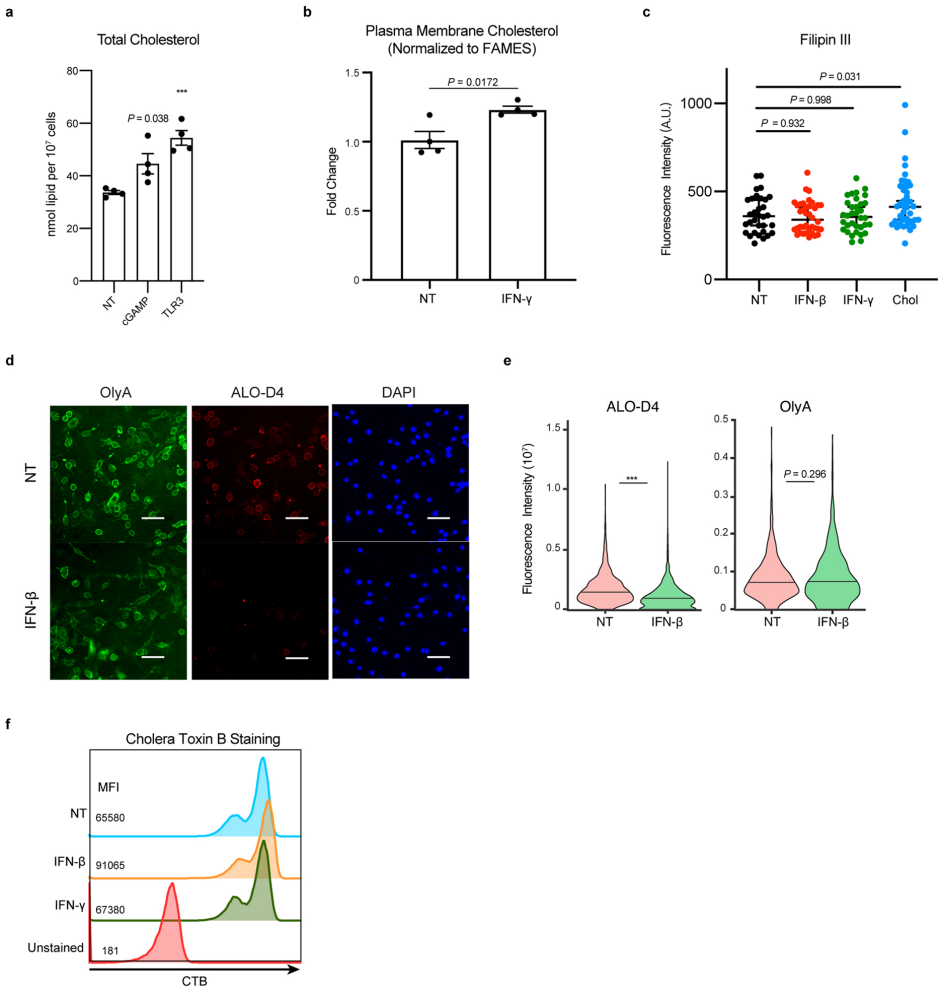

Extended Data Fig. 3 | IFN signals reprogram cholesterol metabolism to decrease the pool of cholesterol targeted by CDCs. a, Total cholesterol (nmol/10^7 cells) from C57BL/6 bone marrow-derived macrophages (BMDMs) stimulated with cGAMP (2 μg/mL), TLR3 agonist (Poly(I:C); 1 μg/mL), or unstimulated (NT) for 48 h. Total cholesterol was determined by GC-MS (n = 4). **b**, Total plasma membrane cholesterol (normalized to total FAMEs) from C57BL/6 bone marrow-derived macrophages (BMDMs) stimulated with IFN-γ (40 ng/mL) or unstimulated (NT) for 24 h (n = 4). **c**, Relative Fillipin III fluorescence intensity of plasma membranes of untreated macrophages or macrophages stimulated with IFN-β (20 ng/mL) or IFN-γ (20 ng/mL) for 24 h (n = 32, 38, 34, 42). MβCD-Cholesterol loaded macrophages indicate dynamic range of Fillipin III fluorescence and are included as a positive control. **d**, Confocal images of BMDM stimulated with IFN-β (20 ng/mL) for 24 h, and then stained with fluorescent ALO-D4 or OlyA and DAPI. Scale bar, 50 μm. **e**, Violin plots of cellular fluorescent intensity quantified from **d** (n = 2225, 2021, 2225, 2021). **f**, Cholera Toxin B staining of BMDM stimulated with IFN-β or IFN-γ (20 ng/mL) for 24 h. Median fluorescence intensity (MFI) are indicated on the left. Data are representative of three (**a**, **d**, **e**, **f**) independent experiments, three independent samples (**c**) or from 4 biological replicates (**b**). Data in **a**-**c** are shown as mean ± s.e.m., violin plots in **e** are shown with median (solid lines). Statistical significance was determined using an unpaired two-tailed Student's *t*-test (**a**, **b**), a one-way ANOVA with Dunnett's correction (**c**), or a two-tailed Mann–Whitney test (**e**) ***$P<0.001$.

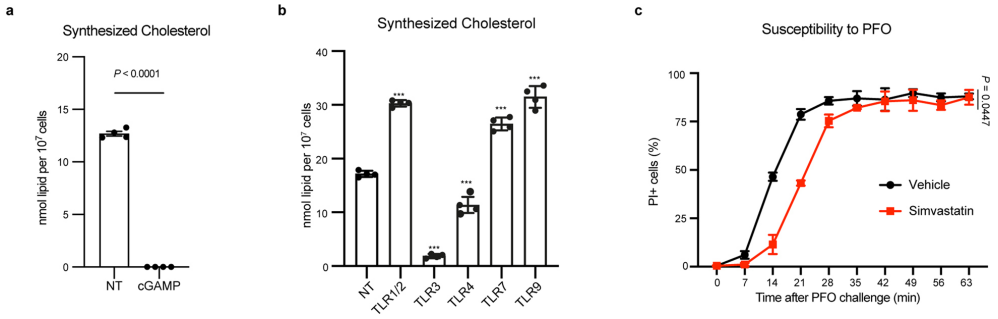

Extended Data Fig. 4 | Cholesterol synthesis is linked to CDC susceptibility. a, Net synthesized cholesterol (nmol/10^7 cells) from C57BL/6 bone marrow-derived macrophages (BMDMs) stimulated with cGAMP (2 μg/mL), or unstimulated (NT) for 48 h. Synthesized cholesterol was determined by GC-MS and isotopomer spectral analysis modeling (n = 4). **b**, Net synthesized cholesterol (nmol/10^7 cells) from C57BL/6 bone marrow-derived macrophages (BMDMs) stimulated with TLR1/2 agonist (Pam3CSK4; 50 ng/mL), TLR3 agonist (Poly(I:C); 1 μg/mL), TLR4 agonist (LPS; 50 ng/mL), TLR7 agonist (CL307; 100 nM), TLR9 (ODN1668; 100 nM) agonist, or unstimulated (NT) for 48 h. Synthesized cholesterol was determined by GC-MS and isotopomer spectral analysis modeling (n = 4). **c**, Percentage of PI-positive WT BMDMs treated with Simvastatin (1 μM) for 4 h and then challenged with PFO for 60 min in the presence of PI (n = 3). Data are representative of three independent experiments and are shown as mean + s.e.m. Statistical significance was determined using an unpaired two-tailed Student's *t*-test (**a**), a one-way ANOVA with Dunnett's correction (**b**), or a paired two-tailed Student's *t*-test (**c**). ***P<0.001.

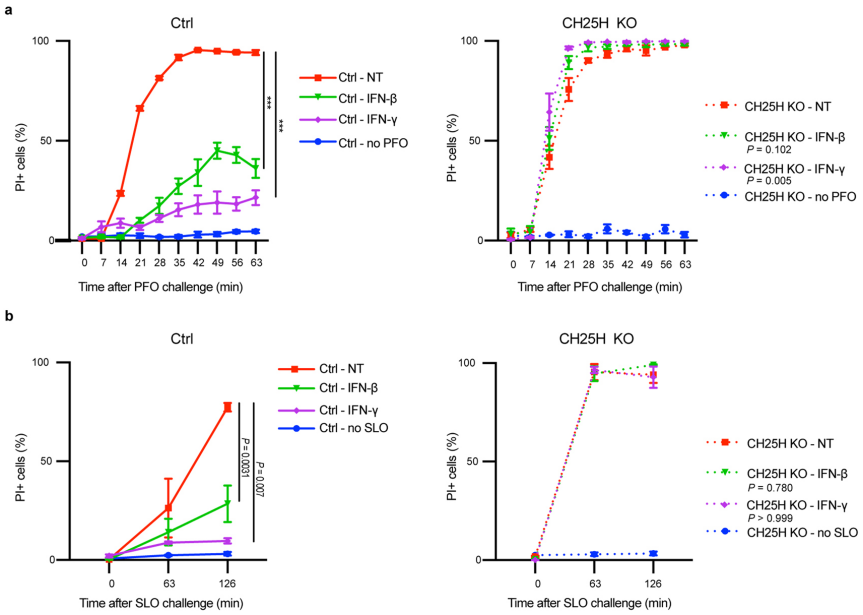

Extended Data Fig. 5 | Production of 25-hydroxycholesterol is required to maintain changes in plasma membrane cholesterol and mediates resistance to CDCs. a, Percentage of PI–positive control or CH25H KO BMDMs stimulated with IFNs (20 ng/mL) for 24 h and then challenged with PFO for 60 minutes in the presence of PI. **b**, Percentage of PI–positive control or CH25H KO BMDMs stimulated with IFNs (20 ng/mL) for 24 h and then challenged with SLO for 2 h in the presence of PI. Data are representative of three independent experiments and are shown as mean + s.e.m. (n = 3) and statistical significance was determined using a two-way ANOVA with Dunnett's correction. ***P<0.001.

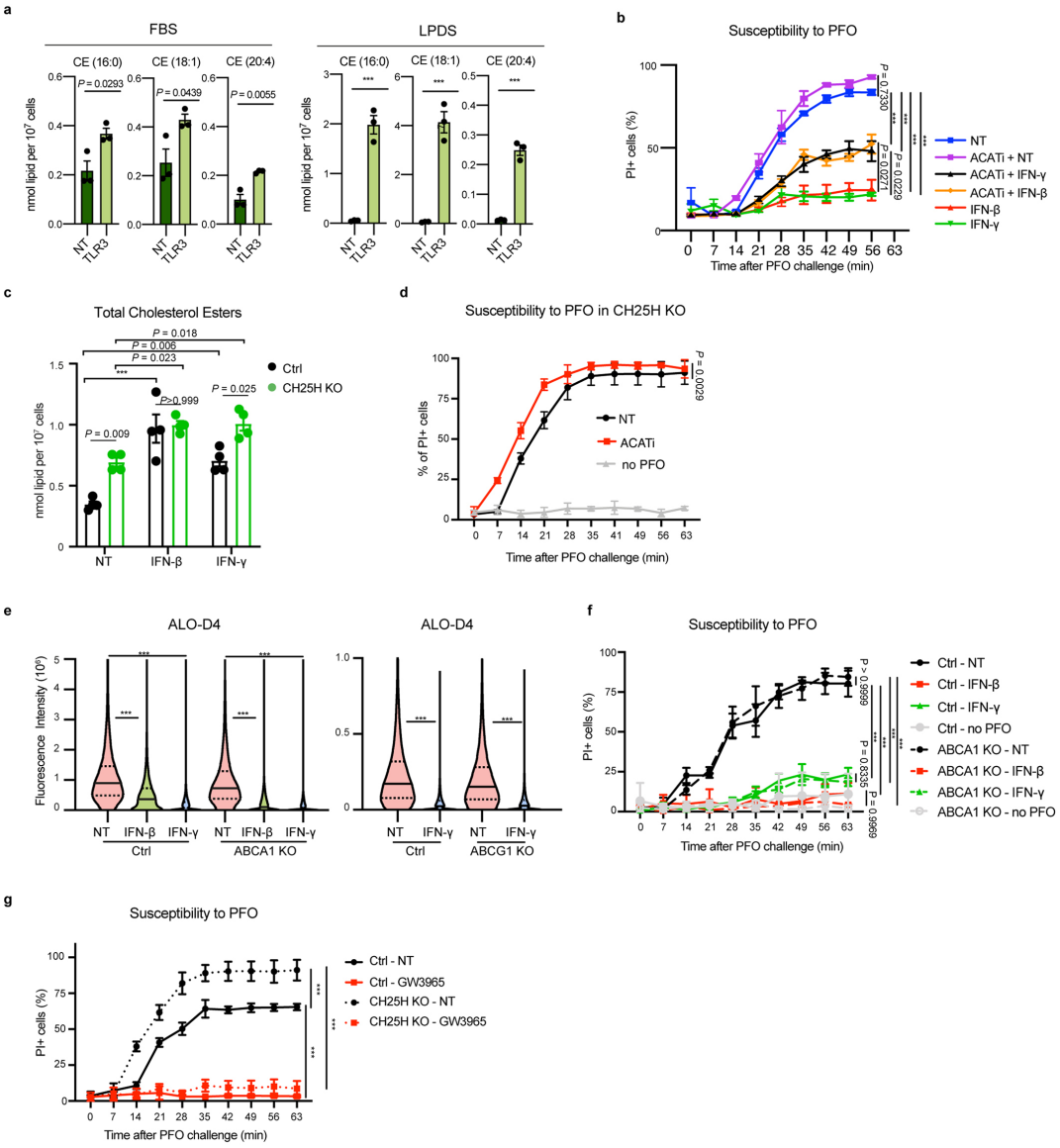

Extended Data Fig. 6 | Cholesterol esterification contributes to CDC resistance of macrophages. a, Quantification (nmol/10^7 cells) of cholesterol ester species (16:0. 18:1, 20:4) in BMDMs stimulated with TLR3 agonist (1 μg/mL) in FBS or LPDS for 48 h. CE species pool sizes were determined by direct infusion MS. **b**, Percentage of PI-positive WT BMDMs treated with IFN-β, or IFN-γ (20 ng/mL), or in combination with ACATi 58-035 (4.3 μM) for 24 h and then challenged with PFO for 60 min in the presence of PI. **c**, Quantification (nmol/10^7 cells) of total cholesterol ester (CE) in control or CH25H KO BMDMs stimulated with IFN-β (20 ng/mL) or IFN-γ (20 ng/mL) for 48 h. CE pool sizes were determined by direct infusion mass spectrometry. **d**, Percentage of PI-positive CH25H KO BMDMs treated with ACATi 58-035 (4.3 μM) for 24 h and then challenged PFO for 60 min in the presence of PI. **e**, Violin plots of cellular fluorescent intensity quantified from control or ABCA1 KO or ABCG1 KO BMDMs stimulated with IFNs (20 ng/mL) for 24 h and then stained with fluorescent ALO-D4 and DAPI (n = 5943, 4126, 5727, 6914, 5740, 7898; n=7201, 7532, 7563, 7417). **f**, Percentage of PI-positive control or ABCA1 KO BMDMs treated with IFNs (20 ng/mL) for 24 h and then challenged PFO for 60 min in the presence of PI. **g**, Percentage of PI-positive control or CH25H KO BMDMs treated with LXR agonist GW3965 (1 μM) for 24 h and then challenged PFO for 60 min in the presence of PI. Data are representatives of two (**a**, **c**) or three (**b**, **d**, **e**, **f**, **g**) independent experiments. Data in **a**, **b**, **c**, **d**, **f** and **g** are shown as mean + s.e.m. (n = 3 in **a**, **b**, **d**, **g**; n = 4 in **c**). Violin plots in **e** are shown with median (solid lines) and 25% and 75% percentiles (dashed lines). Statistical significance was determined using an unpaired two-tailed Student's *t*-test (**a**), a two-way ANOVA with Tukey's correction (**b**, **c**, **f**, **g**), a paired two-tailed Student's *t*-test (**d**), or a Kruskal–Wallis test with Dunn's correction (**e**). ***$P<0.001$.

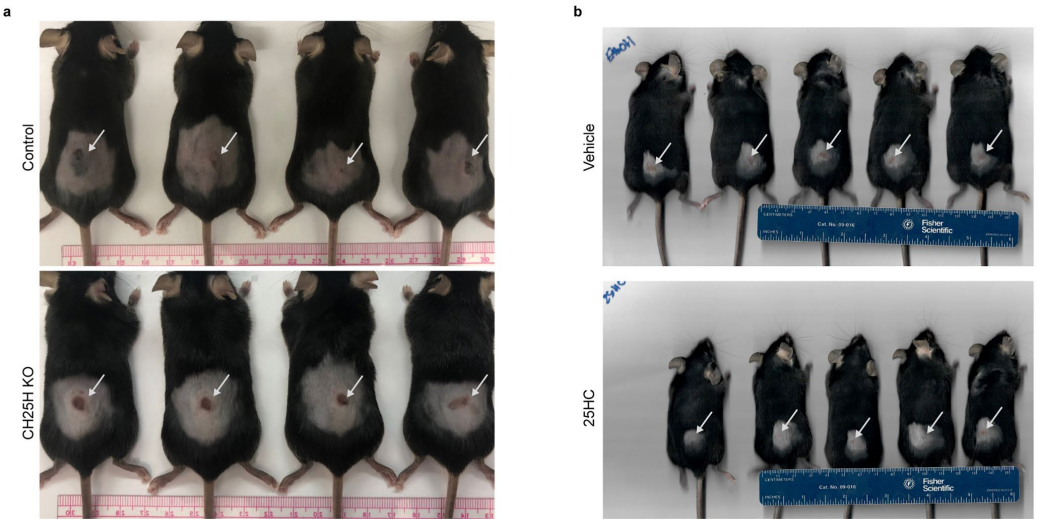

Extended Data Fig. 7 | 25HC mediates protection to CDC induced tissue damage. a, Lesion images of control or CH25H KO mice challenged intradermally with SLO (8 kU/mouse) for 48 h. **b**, Lesion images of vehicle or 25HC pretreated mice challenged intradermally with ALO (20 nM) for 48 h.

APPENDIX C

Collaborative Interactions of Heterogenous Ribonucleoproteins Contribute to Transcriptional Regulation of Sterol Metabolism in Mice

nature COMMUNICATIONS

ARTICLE

https://doi.org/10.1038/s41467-020-14711-4 OPEN

Collaborative interactions of heterogenous ribonucleoproteins contribute to transcriptional regulation of sterol metabolism in mice

Zhengyi Zhang[1,2], An-Chieh Feng[3,4,5], David Salisbury[1,3], Xin Liu[3], Xiaohui Wu[1,2], Jason Kim[1,2], Irina Lapina[1,2], Dan Wang[1,2], Brennan Lee[1,2], Josue Fraga[1], Calvin Pan[1,6], Kevin J. Williams[7], Aldons J. Lusis[1,6], Phil Scumpia[4] & Tamer Sallam[1,2,8]✉

Heterogeneous nuclear ribonucleoproteins (hnRNPs) are a group of functionally versatile proteins that play critical roles in the biogenesis, cellular localization and transport of RNA. Here, we outline a role for hnRNPs in gene regulatory circuits controlling sterol homeostasis. Specifically, we find that tissue-selective loss of the conserved hnRNP RALY enriches for metabolic pathways. Liver-specific deletion of RALY alters hepatic lipid content and serum cholesterol level. In vivo interrogation of chromatin architecture and genome-wide RALY-binding pattern reveal insights into its cooperative interactions and mode of action in regulating cholesterogenesis. Interestingly, we find that RALY binds the promoter region of the master metabolic regulator *Srebp2* and show that it directly interacts with coactivator Nuclear Transcription Factor Y (NFY) to influence cholesterogenic gene expression. Our work offers insights into mechanisms orchestrating selective promoter activation in metabolic control and a model by which hnRNPs can impact health and disease states.

[1] Division of Cardiology, Department of Medicine, University of California, Los Angeles, CA 90095, USA. [2] Molecular Biology Institute, University of California, Los Angeles, CA 90095, USA. [3] Molecular Biology Interdepartmental Doctoral Program, University of California, Los Angeles, CA 90095, USA. [4] Division of Dermatology, Department of Medicine, University of California, Los Angeles, CA 90095, USA. [5] Department of Microbiology, Immunology and Molecular Genetics, University of California, Los Angeles 90095, USA. [6] Department of Human Genetics, University of California, Los Angeles, CA 90095, USA. [7] Department of Biological Chemistry, University of California, Los Angeles, CA 90095, USA. [8] Molecular, Cellular and Integrative Physiology Program, University of California, Los Angeles, CA 90095, USA. ✉email: tsallam@mednet.ucla.edu

Heterogeneous nuclear ribonucleoproteins (hnRNPs) are a family of multifunctional RNA-binding proteins with critical roles in gene regulation. Cooperative activities of hnRNPs have been shown to impact various aspects of RNA metabolism[1]. Although much of the focus on hnRNPs has been geared to their role in splicing and transcript processing, their direct effects on mRNA biogenesis are far less understood with limited compelling roles for transcriptional contributions of hnRNPs. In addition, several lines of evidence link hnRNP abnormalities to neurodegenerative diseases and cancer, but their impact in metabolic control remains unexplored[2,3].

A number of genome-wide association studies have linked variants at the hnRNP *RALY* (also known as heterogeneous nuclear ribonucleoprotein C-like 2) with cardiometabolic traits, including total cholesterol and coronary artery disease, yet little is known about the function and mechanisms of actions of RALY[4–6]. Our previous studies have shown that RALY interacts with *LeXis*, a noncoding RNA mediating crosstalk between the cholesterol biosynthesis and efflux pathways[7]. *LeXis* is a direct transcriptional target of LXR, a sterol-sensing nuclear receptor that triggers an "emergency response" to a lipid overload state. Activation of LXR induces the expression of genes involved in cholesterol efflux (*ABCA1* and *ABCG1*), limiting lipid uptake (*IDOL*), and promoting triglyceride-rich lipoprotein formation (*SREBP1C* and *SCD1*)[8]. On the other hand, the sterol regulatory element-binding proteins (SREBPs) are master regulators of sterol metabolism, directly activating the expression of genes involved in cholesterol and fatty acid biosynthesis[9]. Although all SREBP isoforms can influence a large repertoire of genes at extreme perturbations, it is well established that SREBP1c preferentially activates genes involved in fatty acid biosynthesis, whereas SREBP2 influences cholesterol biosynthetic machinery[10]. Consistent with unique epistatic relationship between various SREBPs, loss of SREBP2 in mouse liver reduces SREBP1c and triglyceride levels in addition to impacting cholesterol stores[11]. Despite their unique activation signature both isoforms appear to bind similar DNA response elements and to partner with common transcriptional coactivators, including Nuclear Transcription Factor Y (NFY) and SP1 (ref. [12,13]).

In this work, we outline a role for hnRNPs in regulatory circuits controlling sterol homeostasis. Liver-specific deletion of the hnRNP *Raly* lowers serum cholesterol and hepatic lipid content. By mapping RALY-binding sites and utilizing unbiased chromatin interrogation techniques, we show preferential binding patterns of RALY at gene promoter regions and decipher its cooperative interactions. Intriguingly, we find that RALY binds at the *Srebp2* but not *Srebp1* promoter region, and show that it interacts directly with NFY to influence transcription of cholesterogenic genes. Our work offers insights into mechanisms orchestrating selective promoter activation and a model by which hnRNPs can impact metabolic disease states.

Results

Ablation of Raly impacts cholesterol biosynthetic genes. To gain insights into the contribution of hnRNPs in metabolic disease, we generated mice with LoxP sites flanking exons 3 and 4 of *Raly* (Fig. 1a, Supplementary Fig. 1). Administration of a Cre or control adenovirus to $Raly^{flox/flox}$ primary murine hepatocytes resulted in the ablation of RALY transcript and protein levels (Supplementary Fig. 2a, b). Since RALY is one of the few hnRNPs linked to human lipid traits, and since our previous studies have shown that disruption of the *LeXis*-RALY axis perturbs cholesterogenic gene expression, we sought to determine the effect of genetic deletion of *Raly* on *Srebp2* (official gene symbol Srebf2) gene expression. Deletion of *Raly* from primary murine hepatocytes led to a significant reduction of Srebp2 and its target genes involved in cholesterol biosynthesis, including Hmgcr (Supplementary Fig. 2c). Surprisingly, the deletion of *Raly* from mouse hepatocytes also led to a significant reduction in Srebp1c, the isoform responsible for triglyceride biosynthesis (Supplementary Fig. 2c). We confirmed reduced protein levels of a nuclear SREBP2 and a number of targets, including 3-Hydroxy-3-Methylglutaryl-CoA Synthase (HMGCS) and Farnesyl Diphosphate Synthase (FDPS) (Supplementary Fig. 2d, e). To explore the contributions of *Raly* in liver metabolism, we generated liver-specific *Raly* knockout mice (referred to as L-*Raly*KO while $Raly^{flox/flox}$ Cre-negative littermates are controls). Quantitative PCR (qPCR) analysis and western blotting confirmed significant and robust decrease in RALY in liver following Cre recombination (Fig. 1b, c). Previous studies have shown that at least a subset of hnRNP complexes influence gene expression in a non-discriminate fashion[14]. To better define the range of RALY activities in liver, we performed unbiased transcriptional profiling of livers from L-*Raly*KO and control mice on chow diet (Fig. 1d). Analysis of differentially regulated genes showed a significant and strong enrichment of lipid metabolic and related pathways (Fig. 1e), as well as substantial overlap with pathways known to be modulated by SREBP2 (Fig. 1e)[15]. qPCR showed a significant reduction in expression of Srebp2 and its target genes in L-RalyKO mice (Fig. 1f). There was also a trend to reduced Srebp1c expression although did not reach significance (fasting mice). Consistent with gene expressing results loss of RALY was associated with a reduction in serum cholesterol level (Fig. 1g). Lipid fractionation analysis revealed a reduction in low-density lipoprotein (LDL) and high-density lipoprotein fractions the predominant circulating pool in chow-few mice (Fig. 1h). Taken together, these results suggest that hnRNPs can regulate the activity of specific gene expression programs and that the effects of RALY on cholesterogenesis are non-redundant.

Liver-specific deletion of Raly reduces hepatic sterol content. We noted that loss of *Raly* from hepatocytes was associated with a decrease in cellular cholesterol and triglyceride content (Fig. 2a, b). To better define the contributions of RALY on hepatic lipid composition, we performed unbiased shotgun lipidomics on mouse liver comparing L-*Raly*KO and controls. We observed that vast majority of lipid species were unchanged with the exception of hepatic cholesterol and triglyceride content (Fig. 2, Supplementary Fig. 3). Examination of cholesterol esters showed a reduction in most species in L-*Raly*KO although only a subset reached statistical significance (Fig. 2c, d). Similarly triglyceride content was significantly reduced in L-*Raly*KO livers (Fig. 2e, f). We observed no changes in the expression of genes involved in lipolysis (Supplementary Fig. 4). Intriguingly, these results partially phenocopy the chow-fed *Srebp2* liver-specific knockout mice, that exhibit mildly reduced liver cholesterol content as well altered SREBP1c and triglycerides levels[11]. These results are also consistent with unique epistatic relationship between various SREBPs. Taken together, the lipidomics findings reinforce the gene expression results and support the notion that RALY may be affecting sterol metabolism through interaction with the *Srebp2* pathway. To more thoroughly investigate the contributions of RALY in chronic lipid abundance states, we fed L-*Raly*KO mice and controls a diet known to induce sterol accumulation and Non-Alcoholic Steatohepatitis (NASH). After 9 weeks of feeding, L-*Raly*KO showed significant reduction in Oil Red O staining (Fig. 2g, h). These results demonstrate that in a preclinical disease model the hepatic loss of RALY partially protects against lipid overload.

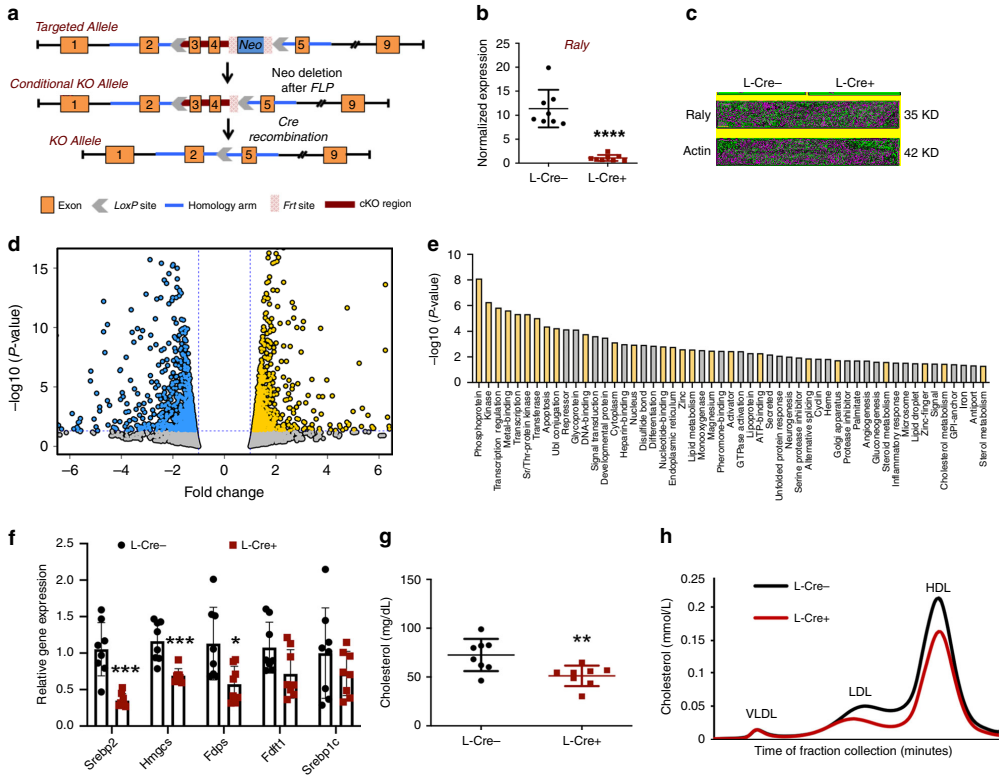

Fig. 1 Loss of RALY reduces Srebp2 and specifically enriches for metabolic pathways. a Schematic of Raly conditional knockout strategy. **b** Gene expression of RALY in liver from chow-fed mice ($n = 8$ per group). **c** Protein level of RALY in liver from chow-fed mice ($n = 8$ per group). **d** Volcano plot of RNA-seq results from liver with and without RALY ($n = 4$ per group). **e** Enriched functional terms from RNA-seq of differentially regulated genes from mouse liver. Yellow bar indicates functional keyword is also enriched in liver SREBP2 ChIP. **f** Gene expression in mice liver on chow diet ($n = 8$ per group). **g** Total serum cholesterol levels isolated from chow-fed mice ($n = 8$ per group). **h** Cholesterol levels in pooled fractionated serum from mice in **g**. All data are mean ± SD. $^*P < 0.05$; $^{**}P < 0.01$, and $^{***}P < 0.001$, using two-tailed Student's *t*-test.

DNA binding of RALY enriches for metabolic regulators. Our previous studies have shown that *LeXis* and RALY are almost exclusively present in the cell nucleus in association with chromatin and that *LeXis* may be impacting cholesterogenic gene expression through transcriptional mechanisms[7]. Thus, we hypothesized that RALY may also be impacting *Srebp2* levels through nascent transcript production. To gain better insight as to how RALY may regulate gene expression, we mapped genome-wide RALY-binding sites. We performed chromatin immunoprecipitation sequencing (ChIP-seq) to assess RALY DNA binding in murine hepatocytes and identified a total of 2950 RALY peaks that were independent identified by the same peak calling algorithm in at least two independent samples (Fig. 3a). Global analysis of fragment distribution around the peak summit showed overall agreement between samples and a broad peak contour profile spanning ~500 bps, a feature often associated with co-regulators (Fig. 3b). Interestingly, RALY showed strong enrichment for promoter binding but was also in enriched in other parts of the genome, including intronic and intergenic regions (Fig. 3c, d). Furthermore, unbiased peaking calling showed that RALY bound the *Srebp2* promoter region but not the *Srebp1* promoter (Fig. 3d, Supplementary Fig. 5). These results reinforce the notion that RALY primarily affects Srebp2 and that perturbations in hepatic triglycerides content are likely a downstream consequence of reduced SREBP2 activity. In addition, motif discovery analysis of RALY-bound peaks identified the transcription factor NFY as a highly enriched motif (Fig. 3e). NFY is a promoter-binding transcription factor (formed with trimeric complex of NFYA, NFYB, and NFYC with all subunits required for proper function) with an established role in mediating SREBP responses[16]. Taken together, these results hint that RALY may be influencing cholesterogenesis by modulating collaborative interactions with transcriptional coactivators at the *Srebp2* promoter.

A number of studies have shown that noncoding RNA–protein interactions can regulate gene activities by modulating a number of histone modifications at target genes[17,18]. To explore the possibility that RALY may influence gene expression by altering epigenetic states, we performed Assay for Transposase-Accessible Chromatin using sequencing (ATAC-seq)[19], a method that allows unbiased interrogation of chromatin architecture, on livers from L-*Raly*KO and controls (Fig. 3f). Loss of RALY in mouse liver did not globally alter chromatin accessibility (Fig. 3g) arguing against the idea that RALY may be impacting gene expression by impacting histone modifiers, such as polycomb repressive

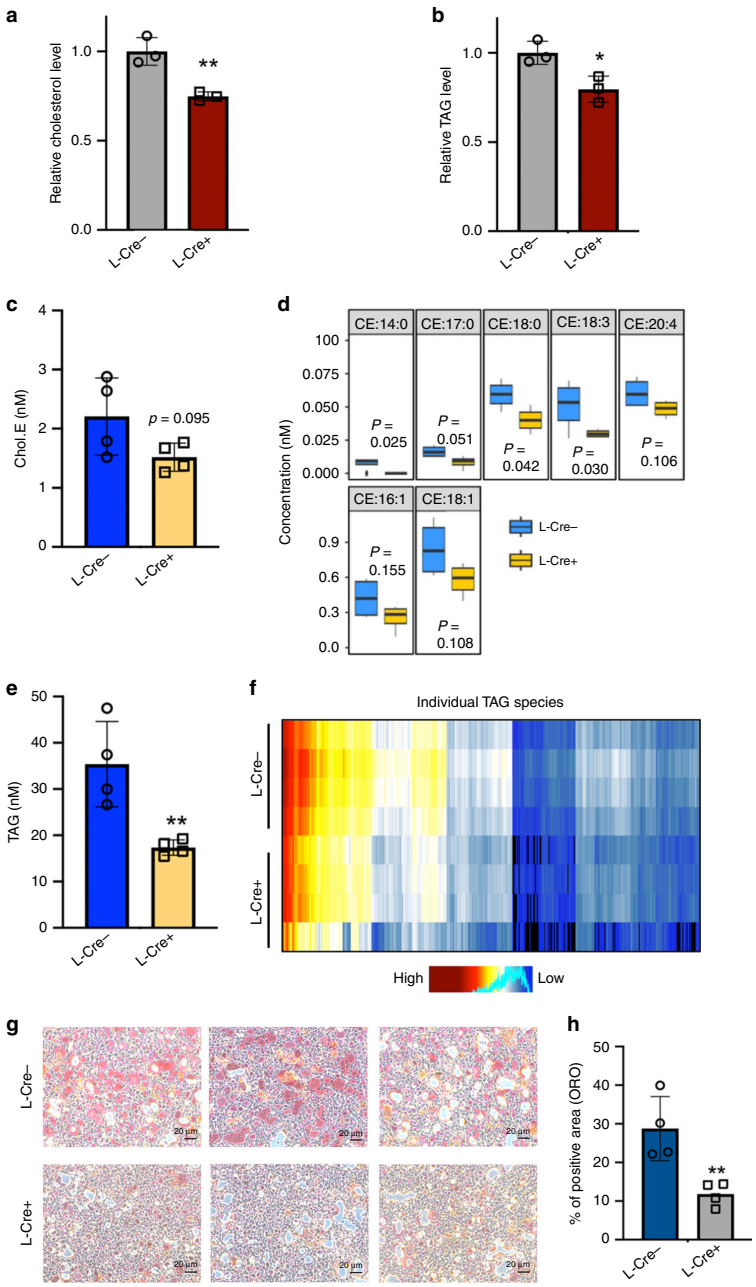

Fig. 2 Liver-specific deletion of RALY alters hepatic lipid content. a, **b** Cholesterol level **a** and triglycerides level **b** from primary hepatocytes relative to baseline levels (normalized to cell number). **c**, **d** Lipidomics investigation of cholesterol ester (CE) species from liver from L-Raly knockout mice and controls ($n = 4$ per group). **e**, **f** Lipidomics investigation of triglycerides species from liver from L-Raly knockout mice and controls ($n = 4$ per group). Each line on heat map represents an individual triglyceride species of 411 different triglycerides detected (four mice per group). **g** Oil Red O (ORO) staining of liver from NASH diet-fed mice (scale bar, 20 µm). **h** Quantification of positive ORO staining area from done with automated image j detection. Values are shown as means ± SD. $^*P < 0.05$ and $^{**}P < 0.01$, using two-tailed Student's *t*-test.

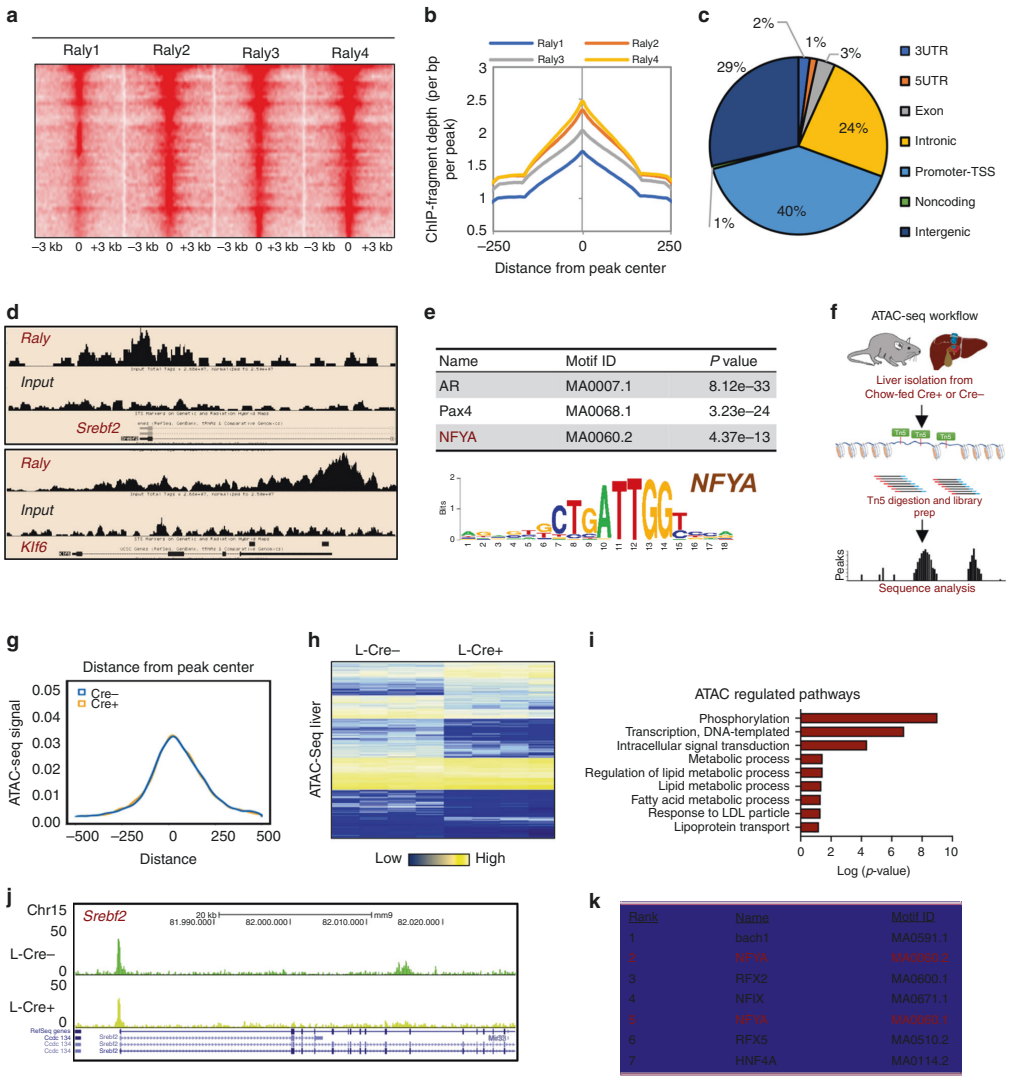

Fig. 3 Interrogation of the RALY cistrome and chromatin dynamics enriches for promoter binding and metabolic coregulators. a Heat map of reproducible counts centered around a gene transcription start site for RALY ChIP-seq samples in hepa1-6 cells ($n = 4$ per group). **b** ChIP fragment depth enrichment for RALY across samples. **c** Pi chart showing the binding pattern of RALY according to the location of a given peak. **d** Representative RALY ChIP-seq profiles at *Srebf2* and *Klf6* loci. **e** Motif analysis surrounding called peaks from RALY ChIP-seq in hepa1-6 cells. **f** Schematic of ATAC-seq workflow. **g** Metagene representation of the mean ATAC-seq signal. ATAC-seq was performed from mice liver with Raly f/f L-Cre+ or Cre− ($n = 4$ per group). **h**, **i** Heat map shows the differential enrichment of ATAC peaks of Cre− or Cre+ livers and Gene ontology analysis. **j** Representative ATAC-seq heat map in liver with Raly f/f L-Cre+ or Cre− at the *Srebf2* locus. **k** Motif analysis showing top enriched factors at differentially regulated sites from Raly f/f L-Cre+ or L-Cre− liver.

complex proteins or histone deacetylase[20]. In addition to directly interrogating changes in nucleosome rearrangements, ATAC-seq allowed us to infer transcriptional activity by examining changes in enhancer landscapes with targeted perturbations. Although globally most ATAC peaks did not change between controls and L-*Raly*KO samples, a number of peaks were differentially regulated (Fig. 3h). Intriguingly, many of these peaks clustered near genes involved in lipid metabolism (Fig. 3i, j, Supplementary Fig. 6). Furthermore, motif analysis of these differentially altered peaks showed specific enrichment for number of transcription factors known to impact metabolic regulation, including NFY (Fig. 3k). Taken together, the above results suggest that RALY may be regulating cholesterol metabolism by impacting the coactivator NFY at the *Srebp2* gene.

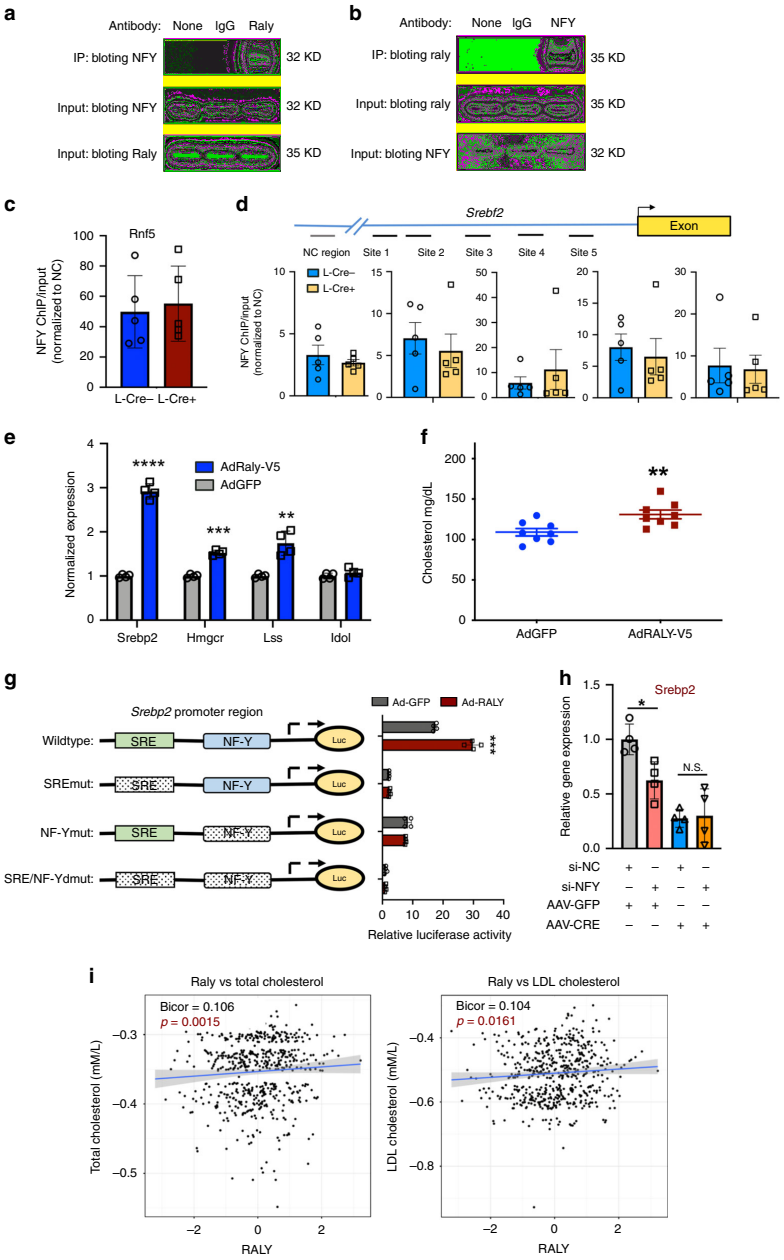

Fig. 4 The coactivator NFY is required for the transcriptional effects of RALY on cholesterogenesis. a, **b** Western blot from Co-IP studies performed in hepa1-6 cells. **c** NFY ChIP-qPCR of the positive control NFY gene done from Raly f/f L-Cre+ or L-Cre− livers ($n = 5$ per group). **d** ChIP-qPCR on Srebf2 promoter using various primers around NFY sites from ChIP in **c**. Data were normalized to negative control region; ($n = 5$ per group). Data are mean± SEM. **e** Gene expression results from hepa1-6 cells treated with adenovirus GFP or RALY ($n = 4$ per group). **f** Serum cholesterol levels from chow-fed mice treated with adenovirus GFP or RALY harvested after 6 days of injection. Data mean± SEM; ($n = 8$ per group). **g** Luciferase promoter assays of Srebp2 promoter region performed in hepa1-6 cells and with GFP or RALY overexpression. **h** Srebp2 gene expression after NFY knockdown in control or RALY-deficient primary hepatocytes ($n = 4$ per group); values are mean±SD. **i** Gene expression results from METISM study showing correlation of metabolic traits with RALY. Values are inverse normal transformed. $^*P < 0.05$; $^{**}P < 0.01$, $^{***}P < 0.001$, and $^{****}P < 0.0001$.

RALY is required for NFY-dependent activation of Srebp2. To clarify whether RALY directly interacts with transcriptional machinery at SREBP2, we performed co-immunoprecipitation (Co-IP) studies in murine hepatocytes. Pulldown of RALY enriches for NFY and vice versa confirming a robust interaction between the two factors (Fig. 4a, b). To clarify whether RALY is required for NFY binding at promoter regions, we performed ChIP of NFY in L-*Raly*KO or control livers. We confirmed NFY enrichment at its known target gene Rnf5 (Fig. 4c), as well as the SREBP2 promoter region (Fig. 4d). Our results suggest that NFY binding is minimally rearranged by the loss of RALY consistent with the idea that RALY does not act as a guide to facilitate NFY complex DNA binding, rather it works cooperatively with NFY at select sites to influence its transcriptional activity. To determine if RALY was sufficient to induce the expression of cholesterogenic genes, we overexpressed RALY using an adenoviral vector in a murine hepatocyte cell line (Supplementary Fig. 7). We found that cholesterogenic gene expression was increased in response to RALY expression (Fig. 4e). In addition, hepatic RALY overexpression increased serum cholesterol in chow-fed mice (Fig. 4f). To more thoroughly investigate the cooperative relationship between RALY and cis/trans promoter factors, we performed luciferase reporter assays with an *Srebp2* promoter construct (Fig. 4g). Adenoviral expression of RALY in hepatocytes enhanced wild-type *Srebp2* promoter-driven luciferase activity, but failed to increase luciferase activity when either NFY or SRE sites were mutated (Fig. 4d). These results reinforce the idea that RALY is a coactivator that requires the binding of canonical transcriptional factors at the *Srebp2* promoter including SREBP itself. To better clarify the epistatic relationship between NFY and RALY, we performed a knockdown of NFY in RALY-deficient cells. Our results show that reduction of NFY on a *Raly*-deficient background no longer alters Srebp2 expression (Fig. 4h, Supplementary Fig. 8). These results suggest that RALY is required for NFY-dependent transcription of SREBP2 and is consistent with notion, and RALY and NFY work cooperatively to influence gene expression.

To better explore the relationship between hnRNPs and human lipid traits, we analyzed expression data from the *METISM* cohort[21]. Interestingly, expression of RALY was positively associated with a number of metabolic, traits including total and LDL serum cholesterol levels though the strength of association was modest (Fig. 4i). Importantly, other hnRNPs, including ones that contribute to transcriptional control mechanisms (hnRNP K), were not significantly associated with total cholesterol or LDL cholesterol in this cohort (Supplementary Fig. 9). Although hnRNPs are known to form complexes with one another, these observations are consistent with the idea that individual hnRNPs may play functional roles favoring specific pathways

Discussion

Previous work has identified important roles for hnRNPs in neurodegenerative disease, most prominently amyotrophic lateral sclerosis and frontotemporal lobar degeneration[1,2]. Our work expands the contributions of hnRNPs in health and disease by showing that a conserved hnRNP can help direct the fundamental metabolic regulatory circuits. In addition, our work offers insights into the precise molecular mechanisms that link hnRNP abnormalities with pathologic states. The functional versatility of hnRNPs is thought to stem from their ability to "dance with different partners" to impact diverse biologic process, such as RNA splicing, polyadenylation, export, and translation. Thus, there are potentially multiple ways by which hnRNPs abnormalities can lead to disease states. Defects in hnRNPs leading to stress granule changes and the accumulation of pathological inclusions are thought to be important in neurodegenerative states[22,23]. Our work shows that hnRNPs proactively participate in transcriptional control mechanisms regulating cholesterol homeostasis and that loss of a single hnRNP (RALY) influences hepatic lipid stores. It should be noted that our work does not exclude the possibility that RALY may play other functional roles or influence gene regulation though multiple mechanisms. In addition, RALY may be impacting transcript splicing or other redundant functions that may be masked in our knockout model or perhaps more critical in other tissues or cell types. Intriguingly, we find that RALY has multiple isoforms and it is unclear whether different isoforms perform different functions.

It is well established that the predominantly cholesterogenic SREBP2 and lipogenic SREBP1 transcription factors may be differentially processed depending on the environment cues. However, both isoforms are capable of binding diverse SREs and collaborate with common coactivators despite possessing distinct transcriptional effects once in the nucleus. In addition, it is unclear how generic collaborative partners, such as NFY and SP1 are capable of turning on some but not all their target genes in response to specific environmental cues. The characterization of RALY offers some important clues into the selective promoter activities of different SREBPs. The fact that RALY binds the promoter of one isoform (*Srebp2*) and not the other hints that spatial collaborative interactions may favor a specific gene activation signature. The finding that RALY interacts with the SREBP coactivator NFY also raises a number of intriguing questions. How do hnRNPs influence some genes but not others? and what is the biochemical basis for their interactions? can RALY directly collaborate with other transcriptional regulators besides NFY? Future studies will provide more insights into these questions.

Methods

Study approval. All experiments were approved by the UCLA Institutional Animal Care and Research Advisory Committee and performed in strict accordance with the recommendations in the Guide for the Care and Use of Laboratory Animals of the National Institutes of Health. Please see supplemental materials for detailed methods.

Animals. All animals used in the study were in C57BL/6 background. Our study used male mice unless otherwise specified. Mice were fed chow diet (Research Diet) and housed temperature-controlled room under a 12-h light/12-h dark cycle and pathogen-free conditions. $Raly^{flox/flox}$ mice were generated by Cyagen using the strategy outlined in Fig. 1a. To the generated RALY liver-specific knockout mice and littermate controls, we treated $Raly^{flox/flox}$ with adeno-associated virus (AAV) with TBG promoter (AAV8.TBG.Cre) or (AAV8.TBG.GFP; green fluorescent protein) purchased from Penn Vector Core. AAV administered intraperitoneal injection at dose of 5×10^{11} GC per mice. Mice were euthanized 4 weeks after AAV injection. Liver tissues were frozen in liquid nitrogen and stored at −80 °C or fixed in 10% formalin. Blood was collected by retro-orbital bleeding, and the plasma was separated by centrifugation. Plasma lipids were measured with the Wako L-Type TG M kit, the Wako Cholesterol E kit. All animal experiments were approved by the UCLA Institutional Animal Care and Research Advisory Committee.

Cells culture. Mouse primary hepatocytes were isolated as previously described and cultured in William's E medium with 5% bovine serum albumin (BSA)[24]. Hepa1-6 cells were originally obtained from ATCC and cultured in Dulbecco's Modified Eagle Medium (DMEM) medium with 10% fetal bovine serum (FBS). Adenovirus studies were performed as previously described[7]. RALY was cloned from mouse cDNA using a gateway cloning system and into the pAd/CMV/V5-DEST Gateway vector by LR recombination according to the manufactures guidelines. NFY knockdown was done in primary hepatocytes using short interfering RNA against nfya (Dharmacon™ catalog number LQ-065522-00-0005). Transfection was proceed using DharmaFECT™ 4 transfection reagent (Dharmacon™) according to the manufacturers recommendation. Cells were collected for RNA isolation or protein extraction 48 h after transfection.

Gene expression analysis and immunoblot analysis. Total RNA was isolated using TRIzol reagent (Invitrogen) and reverse transcribed using a homemade RT, as we previously described[25]. cDNA was quantified by real-time PCR using SYBR Green Master Mix (Diagenode) on BioRad Real-time PCR instrument. Gene expression levels were determined by using a standard curve. Each gene was normalized to the

housekeeping gene 36B4. For immunoblot analysis, whole cell lysate or tissue lysate was extracted using RIPA lysis buffer (Boston Bioproducts) supplemented with complete protease inhibitor cocktail (Roche). For SREBP2 proteins immunoblot analysis, nuclei from primary hepatocytes were prepared using Subcellular Protein Fractionation Kit for Cultured Cells (78840, Thermo Scientific). Proteins were diluted in Nupage loading dye (Invitrogen), heated at 95 °C for 5 min, and run on 4–12% NuPAGE Bis-Tris Gel (Invitrogen). Proteins were transferred to hybond ECL membrane (GE Healthcare) blocked with 5% milk (or 5% BSA for anti-SREBP2) to quench nonspecific protein binding and blotted with the indicated primary antibody. For complete listing of antibodies and primers please see Supplementary Table 1. Uncropped blots are provided in Supplementary Fig. 10.

Dual luciferase assay. DNA transfection of Hepa1-6 cells was performed with LipofectamineTM 3000 (Invitrogen) according to user's manuscript on 24-well plates with a cell density of 1.5×10^5 cells/well. The cells were transfected with 200 ng of the *Srebp2* promoter firefly reporter plasmid, 50 ng of *Renilla* reporter plasmid (Promega), and 200 ng of nSREBP2 expression vector. At 12 h after transfection, the cells were cultured in DMEM supplemented with 1% (v/v) FBS and adenovirus was administered. After 24 h, assays for both luciferase and Renilla activities were performed. The reporter activities were expressed as the relative firefly luciferase activity/Renilla luciferase activity.

RNA-seq. Libraries for RNA-Seq were prepared with KAPA Stranded RNA-Seq Kit on RNA isolated from livers of chow diet feeding mice with AAV-GFP or AAV-Cre transduction. The data were sequenced on Illumina HiSeq 3000 for a pair-end 150 bp read run. Data quality check were done on Illumina SAV. Demultiplexing was performed with Illumina Bcl2fastq2 v 2.17 program. RNA-seq reads were aligned with TopHatv2.0.2 to the mouse genome, version mm9 25. Transcripts were assessed and quantities were determined by Cufflinks v2.0.2, using a GTF file based on Ensembl mouse NCBI37. Comparison expression levels were made using Fragments Per Kilobase of transcript per Million (FPKM) values using Cuffdiff from the Cufflinks package 26.

NASH diet feeding and Oil Red O staining. Twelve-week-old male mice were fed with diet composition of 60 kcal% fat with 0.1% methionine and no added choline (A06071302, Research Diets) for 9 weeks. Oil Red O histochemistry staining were performed using frozen sections from mouse liver. Briefly, frozen sections were fixed in 10% neutral formalin for 10 min, followed by treatment in 60% isopropanol for 5 s and then staining in Oil Red O working solution (O-0625, Sigma Aldrich) for 15 min. This procedure was followed by washing with 60% isopropanol for 5 s and then water 1 min. Finally, sections were contained with Mayer's Hematoxylin for 3 min.

Lipidomics. A total of 50–100 mg of frozen liver are homogenized in the Omni Bead Ruptor Elite with 2 mL homogenizer tube system (Omni, 19-628D). Samples are homogenized in cold phosphate-buffered saline (PBS) for 3 cycles of 10 s each at 5 m/s with a 10 s dwell time between cycles. A total of 3–6 mg of homogenized material are applied to a modified Bligh and Dyer extraction[26]. Prior to biphasic extraction, a 13 lipid class Lipidyzer Internal Standard Mix is added to each sample (AB Sciex, 5040156). Following two successive extractions, pooled organic layers are dried down in a Genevac EZ-2 Elite. Lipid samples are resuspended in 1:1 methanol/dichloromethane with 10 mM ammonium acetate and transferred to robovials (Thermo 10800107) for analysis.

Samples are analyzed on the Sciex Lipidyzer Platform for targeted quantitative measurement of 1100 lipid species across 13 lipid sub-classes. Differential Mobility Device on Lipidyzer is tuned with SelexION tuning kit (Sciex 5040141). Instrument settings, tuning settings, and MRM list available upon request. Data analysis performed on Lipidyzer software. Quantitative values are normalized to milligrams of material used.

Chromatin immunoprecipitation. ChIP experiments were performed as we previously described with exception of a few changes[25]. For RALY ChIP, 20 million cells were used for each sample and four replicates were performed for each group. Sonication was performed using a M220 Focused-ultrasonicator (Covaris) according to the manufacturer's protocol (10 min for cells), and chromatin was immunoprecipitated with 4 µg antibodies against RALY (Ab170105, Abcam) overnight at 4 °C. ChIP-Seq libraries were prepared using the Kapa LTP Library Preparation Kit (Kapa Biosystems). ChIP-Seq was performed as described[27]. Bowtie2 was used for alignment and we identified Raly enriched peaks in using by Homer findPeaks[28] with FDR < 0.01. The called peaks were subsequently used for identifying the motifs enrichment by PscanChIP[29]. For NFY ChIP, chromatin samples from mice livers were prepared using truChIP Chromatin Shearing Tissue Kit (Covaris) according to manufacturer's recommendation. Sonication was performed using a M220 Focused-ultrasonicator (Covaris) according to the manufacturer's protocol for 12 min, and chromatin was immunoprecipitated with 6 µg antibodies against NFYA subunit (sc-17753×, Santa Cruz Biotechnology) overnight at 4 °C. The ChIP samples were analyzed by real-time PCR using primers listed in Supplementary Table 1. All values obtained were normalized to the primers of negative control region.

ATAC-seq. ATAC-seq was optimized in liver after several modifications from original Buenstero protocol[19]. A total of 100 mg of frozen liver were grinded to fine powder using cellcrusher and 1 mL of ice cold nuclei isolation buffer was added (20 mM Tris-HCl, 50 mM EDTA, 5 mM spermidine, 0.15 mM spermine, 0.1% mercaptoethanol, 40% glycerol, pH 7.5, mM EGTA, and 60 mM KCl). After 5 min of cooling on ice, cell suspension was filtered through Miracloth (Calbiochem) followed by centrifugation at $1100 \times g$ for 10 min at 4 °C. Pellet was resuspended with 50 µL RSB buffer (10 mM Tris-HCl, 10 mM NaCl, 3 mM MgCl2, and pH 7.4) followed by centrifugation at $500 \times g$ for 5 min at 4 °C and resuspension in PBS. A total of 75,000 nuclei pellet were used for transposase reaction. The rest of the protocol followed that described by Buenstero. ATAC-Seq libraries were prepared using the Nextera Tn5 Transposase and DNA library preparation kit (Illumina) as described[19]. Libraries were single-end sequenced (50 bp) on an Illumina HiSeq 2000. Reads were mapped to the mouse genome (NCBI37/mm9) using Bowtie2 and were removed from the subsequent analysis if they were duplicated, mapped to mitochondrial genome, or aligned to unmapped contiguous sequences. Peak calling was performed using MACS2. The reads were converted to reads per thousand base pairs peak per million mapped reads (RPKM) by dividing by the total number of reads per sample. The average RPKM from four replicates was used to quantify the accessibility across all called peaks.

Statistical analysis. A non-paired Student's *t*-test was used to determine statistical significance, defined at $P < 0.05$. For multiple group experiments analysis of variance was used followed by multiple group analysis. Unless otherwise noted, error bars represent standard deviations. Experiments were independently performed at least twice. Sample size is based on statistical analysis of variance and prior experience with similar in vivo studies.

Reporting summary. Further information on research design is available in the Nature Research Reporting Summary linked to this article.

Data availability

Data that support the findings of this study have been deposited in GEO with the following accession number GSE133166. All other relevant data supporting the key findings of this study are available within the article and its Supplementary Information files or from the corresponding author upon reasonable request. The source data underlying Figs. 1b, f–h, 2a–e, h, and 4c–h, and Supplementary Figs. 2a, c, 3 and 4 are provided as a source data file. A reporting summary for this article is available as a Supplementary Information file.

Received: 10 June 2019; Accepted: 29 January 2020;
Published online: 20 February 2020

References

1. Geuens, T., Bouhy, D. & Timmerman, V. The hnRNP family: insights into their role in health and disease. *Hum. Genet* **135**, 851–867 (2016).
2. Purice, M. D. & Taylor, J. P. Linking hnRNP function to ALS and FTD pathology. *Front. Neurosci.* **12**, 326 (2018).
3. Cooper, T. A., Wan, L. & Dreyfuss, G. RNA and disease. *Cell* **136**, 777–793 (2009).
4. Howson, J. M. M. et al. Fifteen new risk loci for coronary artery disease highlight arterial-wall-specific mechanisms. *Nat. Genet.* **49**, 1113–1119 (2017).
5. Nelson, C. P. et al. Association analyses based on false discovery rate implicate new loci for coronary artery disease. *Nat. Genet.* **49**, 1385–1391 (2017).
6. Strachan, D. P. et al. Lifecourse influences on health among British adults: effects of region of residence in childhood and adulthood. *Int. J. Epidemiol.* **36**, 522–531 (2007).
7. Sallam, T. et al. Feedback modulation of cholesterol metabolism by the lipid-responsive non-coding RNA LeXis. *Nature* **534**, 124–128 (2016).
8. Calkin, A. C. & Tontonoz, P. Transcriptional integration of metabolism by the nuclear sterol-activated receptors LXR and FXR. *Nat. Rev. Mol. Cell Biol.* **13**, 213–224 (2012).
9. Horton, J. D., Goldstein, J. L. & Brown, M. S. SREBPs: activators of the complete program of cholesterol and fatty acid synthesis in the liver. *J. Clin. Invest.* **109**, 1125–1131 (2002).
10. Jeon, T. I. & Osborne, T. F. SREBPs: metabolic integrators in physiology and metabolism. *Trends Endocrinol. Metab.* **23**, 65–72 (2012).
11. Rong, S. et al. Expression of SREBP-1c requires SREBP-2-mediated generation of a sterol ligand for LXR in livers of mice. *Elife* **6**, e25015 (2017).
12. Ishimoto, K. et al. Sterol-regulatory-element-binding protein 2 and nuclear factor Y control human farnesyl diphosphate synthase expression and affect cell proliferation in hepatoblastoma cells. *Biochem. J.* **429**, 347–357 (2010).
13. Ericsson, J., Jackson, S. M. & Edwards, P. A. Synergistic binding of sterol regulatory element-binding protein and NF-Y to the farnesyl diphosphate

synthase promoter is critical for sterol-regulated expression of the gene. *J. Biol. Chem.* **271**, 24359–24364 (1996).
14. Chaudhury, A., Chander, P. & Howe, P. H. Heterogeneous nuclear ribonucleoproteins (hnRNPs) in cellular processes: focus on hnRNP E1's multifunctional regulatory roles. *RNA* **16**, 1449–1462 (2010).
15. Seo, Y. K. et al. Genome-wide localization of SREBP-2 in hepatic chromatin predicts a role in autophagy. *Cell Metab.* **13**, 367–375 (2011).
16. Reed, B. D., Charos, A. E., Szekely, A. M., Weissman, S. M. & Snyder, M. Genome-wide occupancy of SREBP1 and its partners NFY and SP1 reveals novel functional roles and combinatorial regulation of distinct classes of genes. *PLoS Genet.* **4**, e1000133 (2008).
17. Davidovich, C. & Cech, T. R. The recruitment of chromatin modifiers by long noncoding RNAs: lessons from PRC2. *RNA* **21**, 2007–2022 (2015).
18. Wang, K. C. & Chang, H. Y. Molecular mechanisms of long noncoding RNAs. *Mol. Cell* **43**, 904–914 (2011).
19. Buenrostro, J. D., Wu, B., Chang, H. Y. & Greenleaf, W. J. ATAC-seq: a method for assaying chromatin accessibility genome-wide. *Curr. Protoc. Mol. Biol.* **109**, 21–29 (2015). 21 29.
20. Margueron, R. & Reinberg, D. The polycomb complex PRC2 and its mark in life. *Nature* **469**, 343–349 (2011).
21. Orozco, L. D. et al. Epigenome-wide association in adipose tissue from the METSIM cohort. *Hum. Mol. Genet.* **27**, 1830–1846 (2018).
22. Boeynaems, S. et al. Phase separation of C9orf72 dipeptide repeats perturbs stress granule dynamics. *Mol. Cell* **65**, 1044–1055 e1045 (2017).
23. Alami, N. H. et al. Axonal transport of TDP-43 mRNA granules is impaired by ALS-causing mutations. *Neuron* **81**, 536–543 (2014).
24. Rong, X. et al. LXRs regulate ER stress and inflammation through dynamic modulation of membrane phospholipid composition. *Cell Metab.* **18**, 685–697 (2013).
25. Sallam, T. et al. Transcriptional regulation of macrophage cholesterol efflux and atherogenesis by a long noncoding RNA. *Nat. Med.* **24**, 304–312 (2018).
26. Bligh, E. G. & Dyer, W. J. A rapid method of total lipid extraction and purification. *Can. J. Biochem. Physiol.* **37**, 911–917 (1959).
27. Tong, A. J. et al. A stringent systems approach uncovers gene-specific mechanisms regulating inflammation. *Cell* **165**, 165–179 (2016).
28. Heinz, S. et al. Simple combinations of lineage-determining transcription factors prime cis-regulatory elements required for macrophage and B cell identities. *Mol. Cell* **38**, 576–589 (2010).
29. Zambelli, F., Pesole, G. & Pavesi, G. PscanChIP: finding over-represented transcription factor-binding site motifs and their correlations in sequences from ChIP-Seq experiments. *Nucleic Acids Res.* **41**, W535–W543 (2013).

Acknowledgements

This work was supported by NIH grants HL128822 (TS), HL139549(TS), DK118086(TS) and Burroughs Wellcome Fund 469LRRLBWF(TS).

Author contributions

T.S. supervised and conceived the study, guided the interpretation of results, and the preparation of the manuscript. Z.Z. and T.S. designed the studies and wrote the manuscript. Z.Z. performed the majority of experiments and data analysis. X.W., J.K., and J.F. assisted with mouse experiments. D.S., B.L., and I.L. assisted with molecular in vitro studies. A.F., X.L., D.W., and P.S. assisted with ChIP and ATAC studies, including data analysis and results interpretation. K.J.W. performed lipidomics and data analysis. C.P. and A.J.L. assisted with gene expression data of RALY from human tissues. All authors listed have made a substantial, direct, and intellectual contribution to the work, and approved it for publication.

Competing interests

T.S. is an inventor on a patent (US62/954,993) pertaining to aspects of the RALY work. All other authors declare no competing interests.

Additional information

Supplementary information is available for this paper at https://doi.org/10.1038/s41467-020-14711-4.

Correspondence and requests for materials should be addressed to T.S.

Peer review information *Nature Communications* thanks Francisco Verdeguer and the other, anonymous, reviewer(s) for their contribution to the peer review of this work.

Reprints and permission information is available at http://www.nature.com/reprints

Publisher's note Springer Nature remains neutral with regard to jurisdictional claims in published maps and institutional affiliations.

APPENDIX D

Single Sell Analysis Reveals Immune Cell-adipocyte Crosstalk Regulating the Transcription of Thermogenic Adipocytes

eLIFE elifesciences.org

RESEARCH ARTICLE

Single cell analysis reveals immune cell–adipocyte crosstalk regulating the transcription of thermogenic adipocytes

Prashant Rajbhandari[1,2†*], Douglas Arneson[3,4†], Sydney K Hart[2], In Sook Ahn[3], Graciel Diamante[3,4], Luis C Santos[2], Nima Zaghari[4], An-Chieh Feng[5], Brandon J Thomas[5], Laurent Vergnes[6], Stephen D Lee[1], Abha K Rajbhandari[7], Karen Reue[6,8], Stephen T Smale[5,8], Xia Yang[3,4,8], Peter Tontonoz[1,8,9*]

[1]Department of Pathology and Laboratory Medicine, University of California, Los Angeles, Los Angeles, United States; [2]Diabetes, Obesity, and Metabolism Institute, Icahn School of Medicine at Mount Sinai, New York, United States; [3]Department of Integrative Biology and Physiology, University of California, Los Angeles, Los Angeles, United States; [4]Bioinformatics Interdepartmental Program, University of California, Los Angeles, Los Angeles, United States; [5]Department of Microbiology, Immunology, and Molecular Genetics, University of California, Los Angeles, Los Angeles, United States; [6]Department of Human Genetics, David Geffen School of Medicine, University of California, Los Angeles, Los Angeles, United States; [7]Department of Psychiatry and Neuroscience, Icahn School of Medicine at Mount Sinai, New York, United States; [8]Molecular Biology Institute, University of California, Los Angeles, Los Angeles, United States; [9]Department of Biological Chemistry, University of California, Los Angeles, Los Angeles, United States

***For correspondence:** prashant.rajbhandari@mssm.edu (PR); ptontonoz@mednet.ucla.edu (PT)

[†]These authors contributed equally to this work

Competing interest: See page 22

Funding: See page 22

Received: 19 June 2019
Accepted: 22 October 2019
Published: 23 October 2019

Reviewing editor: Michael Czech, University of Massachusetts Medical School, United States

Abstract Immune cells are vital constituents of the adipose microenvironment that influence both local and systemic lipid metabolism. Mice lacking IL10 have enhanced thermogenesis, but the roles of specific cell types in the metabolic response to IL10 remain to be defined. We demonstrate here that selective loss of IL10 receptor α in adipocytes recapitulates the beneficial effects of global IL10 deletion, and that local crosstalk between IL10-producing immune cells and adipocytes is a determinant of thermogenesis and systemic energy balance. Single Nuclei Adipocyte RNA-sequencing (SNAP-seq) of subcutaneous adipose tissue defined a metabolically-active mature adipocyte subtype characterized by robust expression of genes involved in thermogenesis whose transcriptome was selectively responsive to IL10Rα deletion. Furthermore, single-cell transcriptomic analysis of adipose stromal populations identified lymphocytes as a key source of IL10 production in response to thermogenic stimuli. These findings implicate adaptive immune cell-adipocyte communication in the maintenance of adipose subtype identity and function.
DOI: https://doi.org/10.7554/eLife.49501.001

Introduction

Adipose tissue plays an important role in the maintenance of energy balance in mammals. A chronic imbalance between energy intake and expenditure increases adiposity and leads to obesity and predisposes to the development of metabolic disease (***Rosen and Spiegelman, 2014***; ***Wajchenberg, 2000***). White adipose tissue (WAT) is essential for triglyceride (TG) storage, whereas thermogenic brown adipose tissue (BAT) dissipates energy as heat through mitochondrial uncoupling mechanisms including uncoupling protein 1 (UCP1) (***Cannon and Nedergaard, 2004***;

Chechi et al., 2013; *Saely et al., 2012*). A subpopulation of mature adipocytes in certain WAT depots, known as beige adipocytes, also acquires thermogenic capacity in response to cold or hormonal stimuli. Increasing the activity of thermogenic adipocytes in animal models counteracts the development of obesity and diabetes (*Cohen et al., 2014*; *Harms and Seale, 2013*; *Song et al., 2016*; *Villanueva et al., 2013*). Therefore, a better understanding of the mechanisms controlling adipose thermogenesis could inform the development of new therapies for metabolic diseases.

In times of metabolic need, white adipocytes mobilize stored lipids through hydrolysis of triglycerides and release of free fatty acid (*Zechner et al., 2009*). Activation of β-adrenergic receptors (β-ARs) by catecholamines released by the sympathetic nervous system (SNS) is a major physiological inducer of lipolysis and adipose thermogenesis (*Bartness et al., 2014*; *Harms and Seale, 2013*; *Vitali et al., 2012*; *Wang et al., 2013*). Cold sensation triggers β-AR activation in adipose tissue, resulting in cAMP production and the activation of protein kinase A (PKA) and p38 kinase. These kinases initiate phosphorylation cascades that impinge on C/EBP, ATF, and CREB transcription factors that regulate the expression of gene involved in mitochondrial biogenesis (such as *Ppargc1*) and thermogenesis (such as *Ucp1*) (*Harms and Seale, 2013*). Adrenergic stimuli induce lipolysis in adipocytes through PKA-dependent phosphorylation of lipases including hormone-sensitive lipase (HSL) and adipose triglyceride lipase (ATGL) (*Duncan et al., 2007*; *Jaworski et al., 2007*; *Zechner et al., 2009*). Free fatty acid (FA) released from adipocytes can be used by peripheral tissues for mitochondrial respiration. The importance of β-AR-dependent lipid mobilization and thermogenesis is underscored by the observations that genetic deletion of β-ARs or adipocyte-specific loss of ATGL causes a drastic reduction in energy expenditure that predisposes mice to obesity (*Bachman et al., 2002*; *Schreiber et al., 2017*).

Clearance of catecholamine is critical in terminating β-adrenergic signals, and local catabolism of catecholamine is an established mechanism for negative regulation of adrenergic signaling in adipose tissue (*Camell et al., 2017*; *Pirzgalska et al., 2017*; *Song et al., 2019*). However, our prior studies revealed an unexpected role for IL10 signaling in the inhibition of β-adrenergic signaling and adipose thermogenesis (*Rajbhandari et al., 2018*). Mice globally-deficient in IL10 expression have enhanced energy expenditure and are protected from diet-induced obesity. We showed that chromatin accessibility at thermogenic genes in subcutaneous adipose tissue was linked to IL10 signaling; however, whether adipocytes themselves are the primary target for the metabolic effects of IL10 in vivo remains to be established. Here, we show that adipocyte-specific deletion of IL10Rα increases adipose adrenergic signaling, recapitulating the effects of whole-body IL10 deletion. Single nuclei transcriptomics of mature subcutaneous adipocytes identified a thermogenic adipocyte subtype that was enriched in IL10Rα-deficient mice. Additionally, single-cell RNA-sequencing (scRNA-Seq) of adipose stromal populations revealed an increase in IL10-producing adaptive immune cells under adrenergic stimulation. These results define an immune-adipocyte axis that plays an important role in the modulation of the adipose adrenergic response.

Results

Loss of AdIL10Rα in adipocytes promotes thermogenesis and confers obesity resistance

We previously reported that global IL10-deficient mice have increased energy expenditure and browning of white adipose tissue (*Rajbhandari et al., 2018*). To definitively determine whether mature adipocytes are the major cellular targets for these metabolic effects of IL10 we generated adipocyte-specific IL10 receptor α-deficient mice (AdIL10Rα KO) by crossing *Il10ra*$^{FL/FL}$ mice to *Adiponectin-Cre* transgenics. Prior published studies have reported that *Adiponectin-Cre* transgenic mice do not present an obvious metabolic phenotype and therefore we chose to use *Cre*-negative floxed mice as the controls for our studies (*Kong et al., 2014*; *Villanueva et al., 2013*).

We confirmed loss of IL10Rα in adipocytes from AdIL10Rα KO mice by western blotting (*Figure 1A*). There was no difference in body weight or food intake between 10 week-old chow-fed AdIL10Rα KO mice and floxed littermate controls (*Figure 1—figure supplement 1A and B*). However, metabolic cage analysis revealed increased oxygen consumption and energy expenditure in AdIL10Rα KO mice, without changes in locomotion and body mass (*Figure 1B* and *Figure 1—figure supplement 1C*). To determine if this difference in energy expenditure was associated with

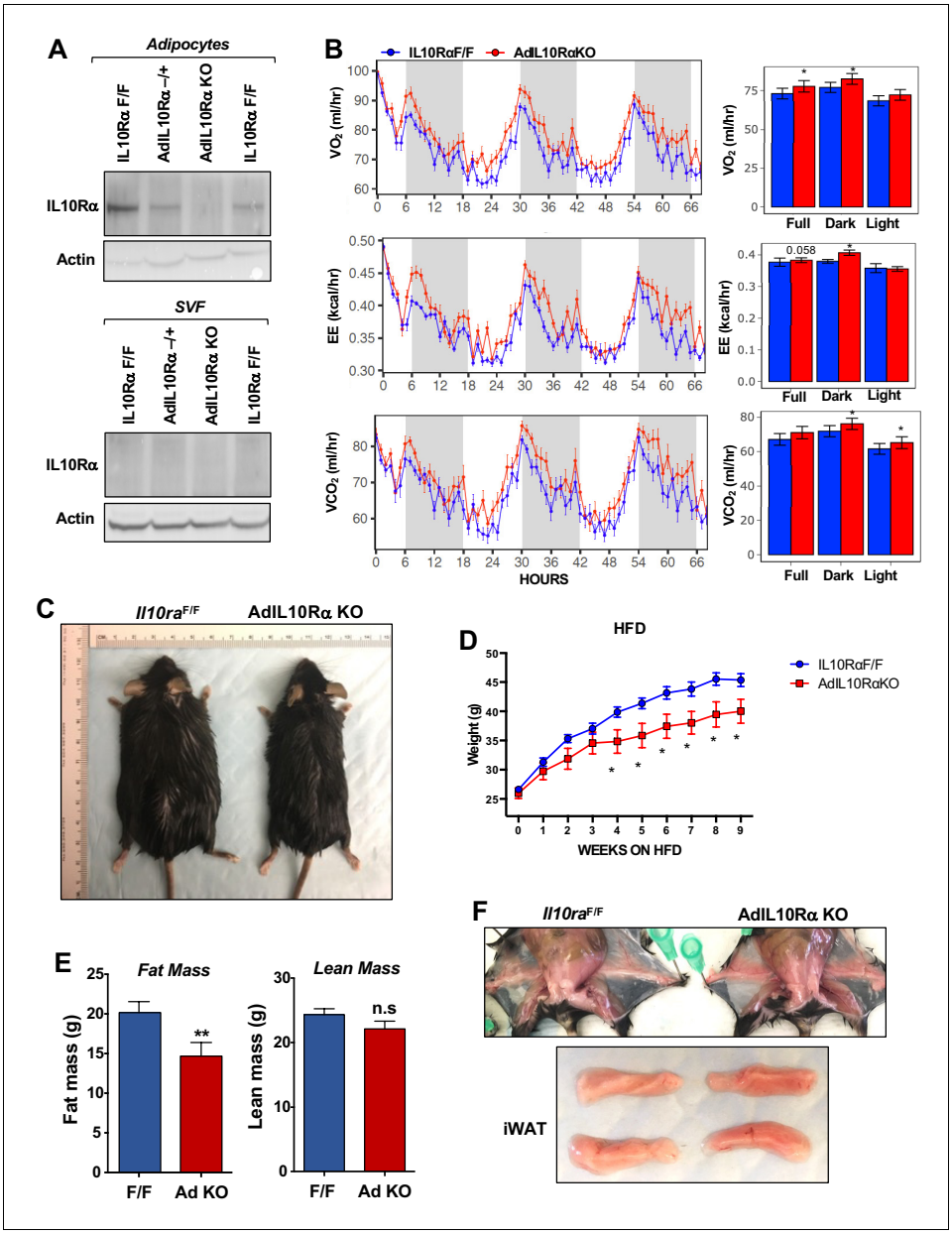

Figure 1. Ablation of IL10Rα in adipocytes increases energy expenditure and protects mice from diet-induced obesity. (**A**) Immunoblot analysis of IL10Rα expression in SVF and adipocyte fractions of iWAT from chow-fed 10 week-old mice. (**B**) Oxygen consumption (VO_2, ml/hr), energy expenditure (EE, kCal/hr), and carbon dioxide production (VCO2, ml/hr) of chow-fed 10-week-old IL10RαF/F and AdIL10Rα KO mice were analyzed in Columbus Oxymax metabolic chambers (12 hr light/dark cycles, 72 hr total duration, each light/dark bar represents 12 hr duration). N = 9,7. Statistical analysis was

Figure 1 continued on next page

Figure 1 continued

performed using ANCOVA. (**C**) External appearance of representative 9 week HFD-fed mice. (**D**) Body weight of mice fed chow diet for 10 weeks and then 60% high-fat diet (HFD) for 9 weeks. N = 13, 7. (**E**) Fat and lean mass of mice in D fed HFD for 6 weeks. (**F**) Internal and gross appearance of iWAT from representative IL10RαF/F and AdIL10RαKO mice. *, p<0.05.

DOI: https://doi.org/10.7554/eLife.49501.002

The following figure supplement is available for figure 1:

Figure supplement 1. AdIL10Rα KO mice are protected against diet-induced obesity.

DOI: https://doi.org/10.7554/eLife.49501.003

protection against diet-induced obesity, we challenged AdIL10Rα KO with high-fat diet (60% calories from fat). After 8–9 weeks of HFD feeding, both male and female AdIL10Rα KO mice were protected against weight gain compared to floxed littermate controls (***Figure 1C,D*** and ***Figure 1—figure supplement 1D***). MRI analysis of body composition showed that the difference in body weight was entirely due to a change in fat mass (***Figure 1E***). Consistent with these findings, the inguinal WAT (iWAT) of AdIL10Rα KO mice was visibly redder than that of controls, suggesting increased tissue 'browning' (***Figure 1F***).

To test the influence of the IL10-IL10R axis on adipose adrenergic responses, we exposed AdIL10RαKO and floxed control mice to cold stress (4˚C) for 24 hr. Analysis of iWAT gene expression by real-time PCR showed increased expression of *Ucp1*, *Elovl3*, *Ppargc1* and other thermogenic genes, but no change in general adipose markers such as *Fabp4* and *Pparg* in AdIL10Rα KO mice (***Figure 2A***). Similar results were observed in AdIL10Rα KO mice treated with β3-adrenergic agonist (CL 316,243; CL, 1 mg/kg/day for 4 days; ***Figure 2B***). To gain insight into the global adipose gene expression changes in AdIL10Rα KO mice, we performed RNA-seq on iWAT. We identified 214 genes that were enriched more than 1.5-fold in AdIL10Rα KO mice compared to control mice (presented as a heatmap as a function of percentile expression in ***Figure 2C***). The data revealed a selective increase in the thermogenic gene program in AdIL10Rα KO mice compared to controls. The gene expression differences between AdIL10Rα KO mice and controls were highly consistent with those observed in global IL10-deficient mice compared to WT controls (***Rajbhandari et al., 2018***), strongly suggesting that the effects of IL10 on adipose tissue gene expression are mediated predominantly through direct action of IL10 on adipose IL10Rα. These data also supporting a specific inhibitory effect of IL10Rα signaling on adrenergic-responsive pathways. We also noted that several genes that were more highly expressed in control mice compared to AdIL10Rα KOs have been linked to negative regulation of thermogenesis. For example, *Cnotl1* and *Brd2* have been reported to negatively regulate the mRNA stability and transcription of UCP1, respectively (***Figure 2C***) (***Takahashi et al., 2015***). In support of the calorimetric findings, we found increased mitochondrial respiration in the iWAT of AdIL10Rα KO mice compared to controls by Seahorse assays (***Figure 2D***).

Identification of thermogenic adipocytes by SNAP-Seq

The data above show that IL10 acts directly on adipocyte AdIL10Rα to regulate the thermogenic gene program in adipocytes. To further dissect the role of the IL10-IL10R axis in regulating the identity and physiology of mature adipocytes, we performed single-cell analyses. As there were no prior reports of single primary adipocyte transcriptomics, we optimized a Single Nuclei Adipocyte RNA sequencing approach (SNAP-seq) for assessing gene expression in mature adipocytes derived from mouse iWAT (***Figure 3A*** and see Materials and methods). The critical step in this procedure is the isolation and purification of adipocyte nuclei which overcomes technical obstacles related to the handling of lipid-laden adipocytes. The single nuclei suspension (n ~ 10,000) was subjected to snRNA-Seq using the 10XGenomics platform, and libraries were sequenced with dedicated 400 million reads per sample (***Figure 3A***).

We chose to analyze mice exposed to a 24 hr cold challenge in these initial studies in order to increase our chance of identifying thermogenic adipocyte populations. We used the 10X genomics data processing and analysis platform to generate cell clusters and identities (see Materials and methods). To classify the adipocyte populations based on gene expression, we performed cluster analysis as represented by t-distributed stochastic neighbor embedding (t-SNE) plots. Remarkably, this analysis revealed that the adipocytes from iWAT of chow-fed C57BL/6 mice were highly

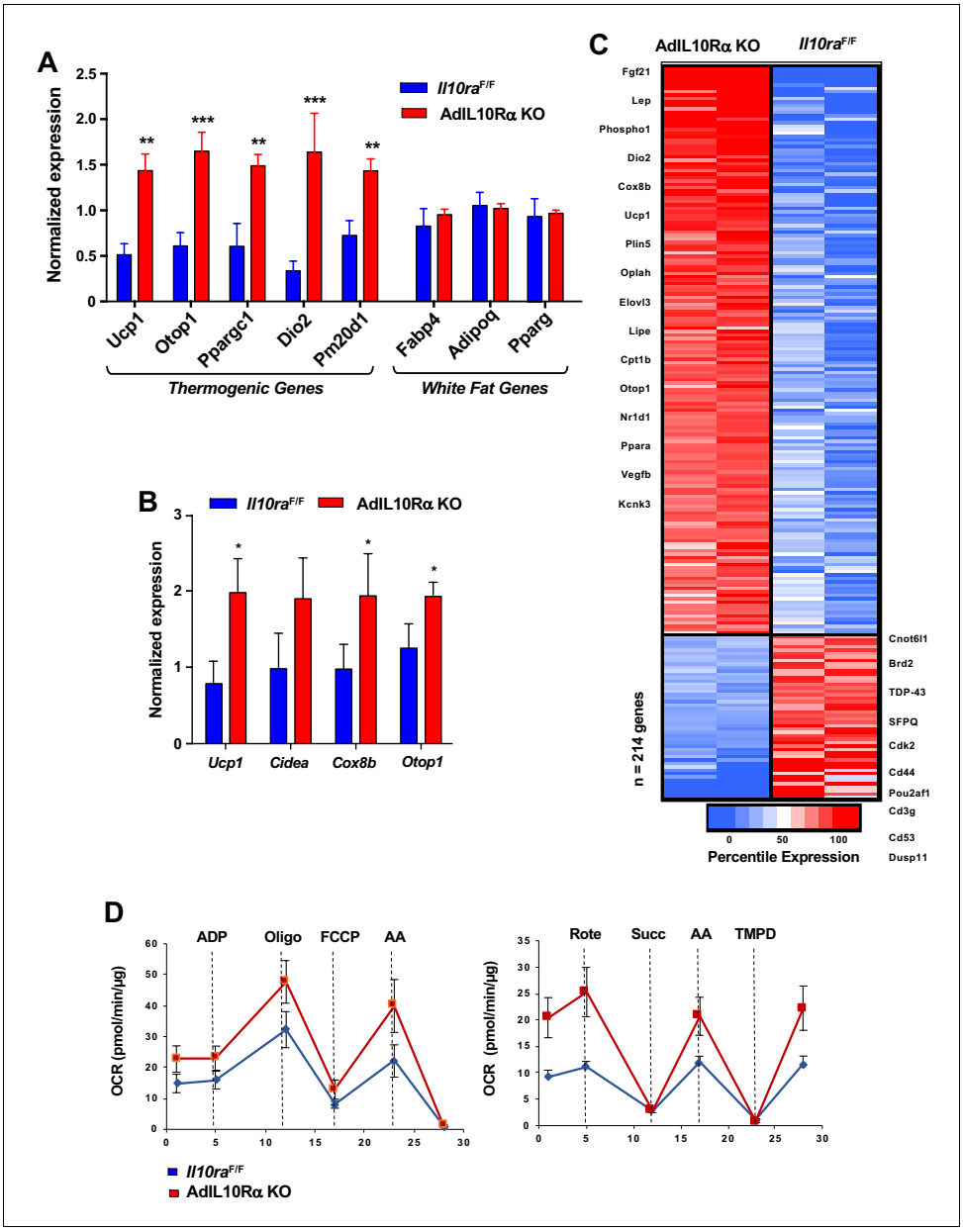

Figure 2. IL10R deficiency promotes adipose tissue browning. (**A and B**) Real-time PCR analysis of gene expression in iWAT from 10 week 24 hr cold-exposed (**A**) or CL 1 mg/kg/day for 4 days; **B**) IL10RαF/F and AdIL10RαKO mice. N = 5,5. *, p<0.05; **, p<0.01; ***, p<0.0001. (**C**) Heatmap representation of genes that changed >1.5 fold (p-value<0.01) as a function of percentile expression by RNA-Seq of iWAT from 10 week-old 24 hr cold-

Figure 2 continued on next page

Figure 2 continued

exposed IL10Rα and AdIL10Rα KO mice. Genes are grouped as upregulated (Red) or downregulated (Blue). (**D**) Average oxygen consumption rate (OCR) in coupling (left) and electron flow (right) assays of mitochondria isolated from iWAT of mice in (**A**).

DOI: https://doi.org/10.7554/eLife.49501.004

heterogeneous. We were able to distinguish 14 distinct clusters (***Figure 3B***). The violin plots in ***Figure 3C*** further revealed that each cluster also uniquely express marker genes that were preferentially expressed in individual cluster. The tSNE-plot in ***Figure 3D*** further show localized expression of genes in particular cluster. Among all the clusters, we noticed a high enrichment of genes involved in fatty acid metabolism such as *Adrb3* and *Acsl1* in cluster 9. Furthermore, genes encoding β3-AR, HSL, and ATGL were highly overrepresented in this cluster, as were a variety of beige/brown adipocyte markers (***Figure 3E***). The gene expression profile of Type nine adipocytes was indicative of a highly metabolically active population whose characteristics were potentially consistent with thermogenic 'beige' adipocytes.

To address the possibility that contaminating stromalvascular cells might have given rise to one or more of these clusters we performed a Fisher's exact test between pairwise sets of cell type marker genes (determined by unadjusted and adjusted p-value<0.05) to find cell types that had substantial overlaps in their marker genes (denoting transcriptional similarity). Cell types from both mature adipocyte nuclei and stromal vascular fraction (SVF) single cells were used in this analysis and they were grouped using hierarchical clustering with tiles colored by -Log10 Bonferroni adjusted p-values. Adjusted p-values were thresholded to aid in visualization with values less than 10^{-5} set to 10^{-5}. As shown in the diagonal correlation in ***Figure 3—figure supplement 1***, we did not find high degree of transcriptional similarity between SVF and adipocyte clusters (top). However, under stringent p-value adjustment, the transcriptomic state of adipocyte clusters 12 and 14 correlated with markers of adaptative immune cells (bottom). Thus, we cannot exclude the possibility that clusters 12 and 14 may be contaminated with immune cells.

Identification of a cold-responsive thermogenic 'beige' adipocyte population by SNAP-seq

To further test the hypothesis that Type nine adipocytes were the thermogenic beige population, we subjected mice to different thermogenic conditions, including cold stress (4˚C) for 24 hr, 48 hr, and 4 days, or treated them with CL for 4 days (1 mg/kg/day). We then performed SNAP-seq on adipocytes derived from iWAT as described above. We performed unbiased aggregated clustering of the processed data for all the conditions as a tSNE-plot (***Figure 4A***). The aggregated cluster represents ~54,000 cell and allows us to confidently assign biological function to each cluster. Hence, to infer the biological properties of the cells in each cluster, we performed cell-type pathway enrichment analysis (Gene ontology (GO), KEGG, Reactome, and BIOCARTA) (***Supplementary file 1***) using enriched genes in each cluster based on false discovery rate (FDR) set at <0.05. This analysis revealed that different adipocyte subtypes express distinct genes with important roles in adipose tissue development, insulin signaling, hypoxia signal, inflammation, lipid synthesis and transport, angiogenesis, myogenesis, hormone responses, mitochondrial respiration, and fatty acid metabolic process (shown in ***Supplementary file 1***). Type one adipocytes appeared to represent classical adipocytes and they expressed genes associated with adipose development, lipid responses, the insulin pathway, and response to corticosteroids (e.g. *Fto, Vldlr, Insr, Apod, Klf9, Sh3pxs2b*); Type three adipocytes were enriched for genes involved in blood vessel morphogenesis and angiogenesis; both Type 3 and 14 adipocytes were enriched for genes involved glycolysis. Type 6 and 7 adipocytes were enriched for genes involved in muscle metabolic process and myogenesis; Type 10 adipocytes were enriched for genes involved in the immune response; Type 11 adipocytes were enriched for cell cycle genes; Type 14 adipocytes were enriched for genes involved in mitochondrial ATP synthesis and respiration. Some adipocyte clusters displayed more commonality in gene expression with others and shared similar biological process, such as the abundant Type 1, 2, 3 and 7, 6 and 17 adipocytes (***Supplementary file 1***).

The top five enriched pathways determined by FDR from each cell type cluster were selected (from ***Supplementary file 1***) and only unique pathways were kept (some top enriched pathways

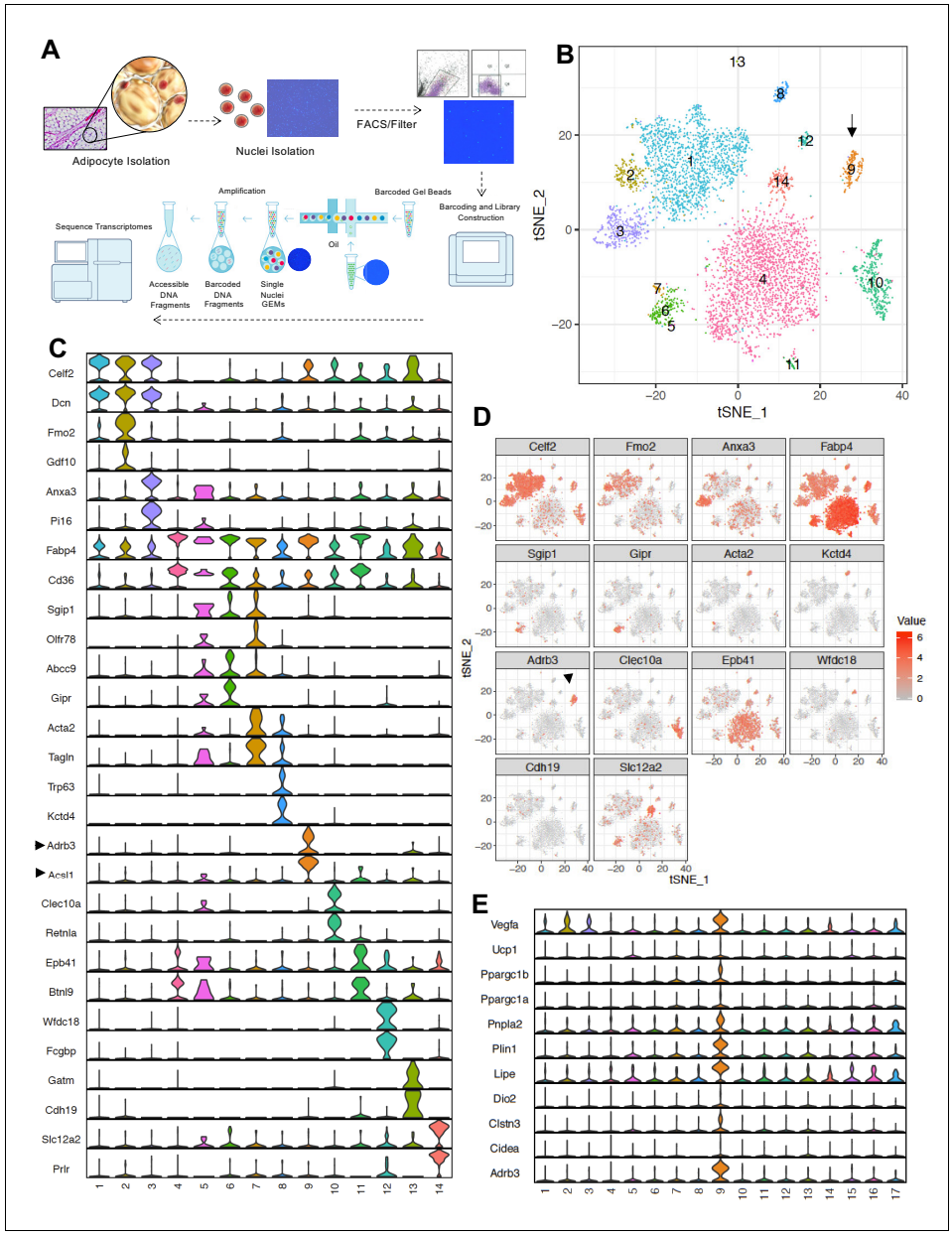

Figure 3. SNAP-seq reveals heterogeneity of tissue adipocytes from iWAT. (**A**) Workflow showing DAPI-stained nuclei pre- and post-FACS/filtration that underwent microfluidic partitioning and library preparation in the 10X genomics platform followed by sequencing using an Illumina HiSeq 4000. (**B**) tSNE-plot showing 14 clusters from ~6000 adipocytes derived from iWAT of mice exposed to cold for 24 hr. Each colored dot is an adipocyte assigned to a cluster based on transcriptomic signature. (**C**) Normalized expression values of the top two adipocyte subtype-specific cluster genes from (**B**)

Figure 3 continued on next page

Figure 3 continued

plotted as violin plots with clusters as rows and genes as columns. (**D**) tSNE-plot showing cluster-specific expression of selected marker genes from (**C**). (**E**) Normalized expression values of indicated genes in subtype-specific clusters plotted as violin plots with clusters as rows and genes as columns. Black arrow is pointing toward metabolically active Type nine adipocyte cluster and enriched gene.

DOI: https://doi.org/10.7554/eLife.49501.005

The following figure supplement is available for figure 3:

Figure supplement 1. Multimodal analysis of SVF and adipocyte single-cell sequencing data.

DOI: https://doi.org/10.7554/eLife.49501.006

were shared across cell type clusters). Enriched pathways (rows) were clustered with hierarchical clustering. The size of each dot represents the -log10 FDR of the pathway enrichment and the color of each dot corresponds to the fold enrichment of each pathway (red- higher enrichment, gray- lower enrichment). In ***Figure 4—figure supplement 1***, we report the top five scoring pathways for each cell type cluster across all pathway sources (***Figure 4—figure supplement 1A***) or from KEGG pathways (***Figure 4—figure supplement 1B***). Overall, the most striking cluster was the Type nine adipocytes. Pathways enriched for triglyceride and neutral lipid catabolism, hormone-sensitive lipase (HSL)-mediated triglyceride hydrolysis and PPARα signaling were particularly enriched in type nine cluster.

Among all clusters (1-17), we noticed a very distinct sub-clustering of Type nine adipocytes, with a gradient of adipocyte subtypes in this population from room-temperature (RT) housed mice (top-RED), to mice exposed to cold for 4 days (Middle-Blue), to mice treated with CL (Bottom-Pink) (***Figure 4B***). Consistent with the data in ***Figure 3***, the genes encoding β3-AR, HSL, ACSL1 were selectively enriched in the Type nine cluster (***Figure 4C*** and ***Figure 4—figure supplement 2A,B***). The tSNE-plot in ***Figure 4D*** reveals localized expression of thermogenic genes in cluster 9. Cluster nine adipocytes from CL- and cold-treated mice showed expression of markers of brown genes such as *Ucp1, Ppargc1a, Cidea, Dio2,* whereas *Adrb3, Lipe, Vegfa, Pnpla2* were expressed by most of the adipocytes in cluster 9 regardless of thermogenic stimuli (***Figure 4D***). Violin plots of thermogenic genes further showed upregulation of genes such as *Ucp1, Ppargc1a, Ppargc1b,* and *Cidea* in Type nine adipocytes in mice treated with thermogenic stimuli, confirming these cells as a bona-fide 'thermogenic adipocyte' cluster (***Figure 4E***). By contrast, genes involved in lipid mobilization such as *Adrb3 and Lipe* were abundant in all Type 9 cells regardless of stimulus, underscoring the relevance of these genes in thermogenic responsiveness and FFA metabolism. *Il10, Il10ra,* and *Il10rb* expression showed a relatively even distribution among mature adipocyte populations (***Figure 4—figure supplement 2C***).

We further confirmed the presence of Type nine adipocytes and validated co-expression of thermogenic genes by using RNAscope fluorescence in situ hybridization (FISH) in iWAT of mice treated with saline or CL (see Materials and method section). As shown in ***Figure 4F***, CL treatment caused a robust increase in the expression of *Ucp1, Pppargc1b,* and *Adrb3* compared to control. Moreover, these transcripts showed a striking co-localization in only a set of adipocytes. We speculate that this population corresponds to Type nine adipocytes.

Increased abundance of metabolically active type nine adipocytes in AdIL10Rα KO mice

To probe if IL10 signaling influenced the percentage of thermogenic adipocytes, we exposed both floxed-control and AdIL10Rα KO mice to either cold stress (4˚C) for 24 hr, 48 hr, or 4 days, or treated them with CL (1 mg/kg/day) for 4 days, and performed SNAP-seq on iWAT of these mice. Cluster nine from the aggregated data showed a progressive increase in the percentage of cells upon exposure to cold for increasing lengths of time (3.4% to 5.7% to 12.1% from 24 hr to 48 hr to 4 days at 4˚C, respectively) as shown both by tSNE- and dot-plots and treatment of mice with CL even more dramatically increased the abundance of Type 9 cells to 23.5% (***Figure 5A***-top and bottom). Dot-plotting further showed that among all clusters, type 1, 4, and nine showed the most changes under the different conditions, and among them only type nine adipocytes showed an adrenergic-dependent positive increase in cell fractions (***Figure 5A***-bottom). We next compared data from control and AdIL10Rα KO mice, and in agreement with the whole tissue RNA-seq data

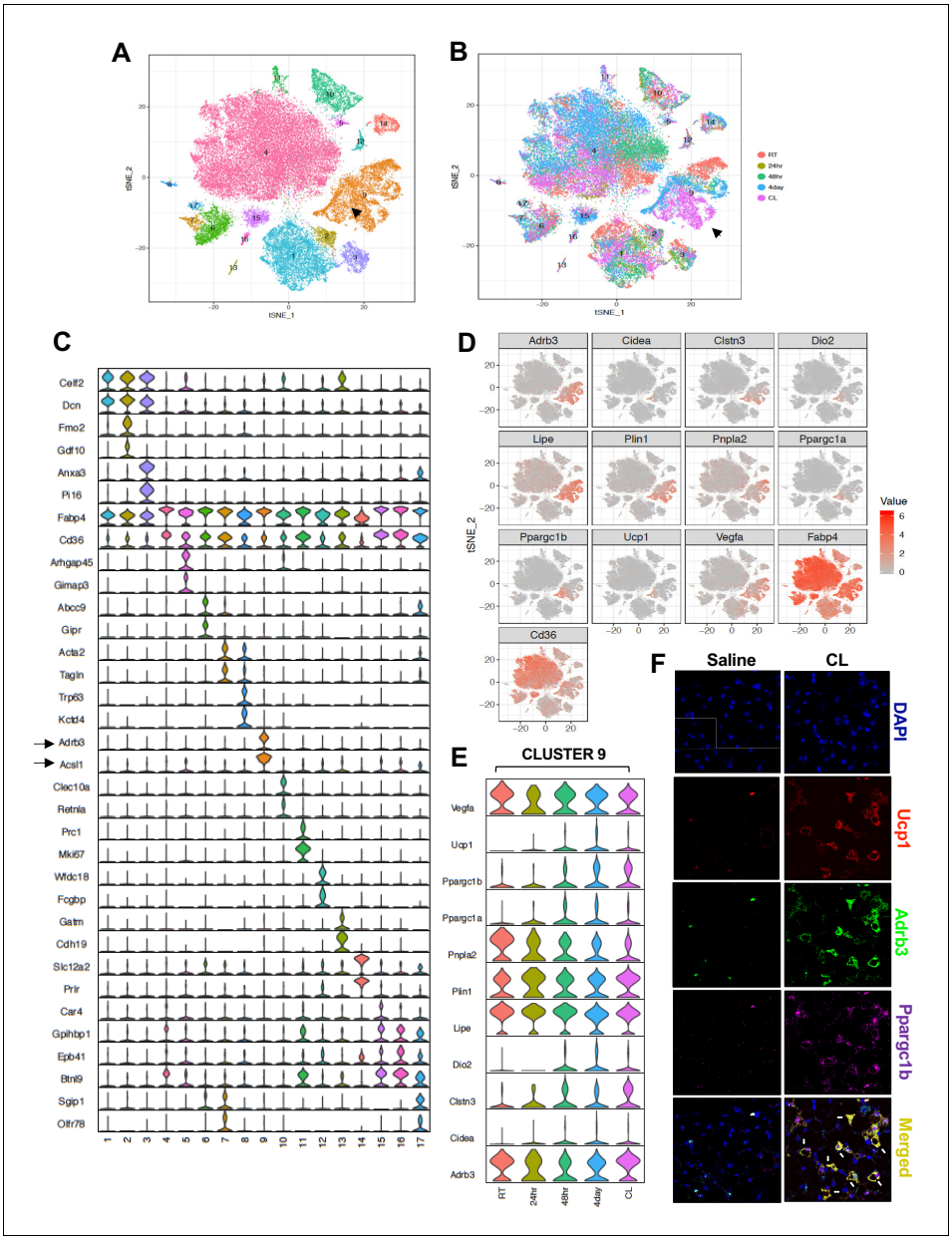

Figure 4. Transcriptomic visualization of thermogenic adipocytes in iWAT. (**A**) Aggregated tSNE-plot showing 17 clusters from ~54,000 adipocytes derived from iWAT of mice at RT, cold-exposed (24 hr, 48 hr, and 4 days), or treated with CL for 4 days at 1 mg/kg/day. Each colored dot is an adipocyte that falls into a cluster based on transcriptomic signature. (**B**) tSNE-plot showing indicated treatment-dependent sub-clustering of aggregated clusters shown in (**A**). Black arrow indicates the Type nine adipocyte cluster. (**C**) Normalized expression values of the top two adipocyte

Figure 4 continued on next page

Figure 4 continued

subtype-specific cluster genes from (**A and B**) plotted as violin plots with clusters as rows and genes as columns. (**D**) tSNE-plot showing distribution of indicated genes from adipocytes from (**A**). (**E**) Normalized expression values of indicated genes in the Type nine adipocyte cluster under different treatment condition plotted as violin plots with treatment conditions as rows and genes as columns. (**F**) RNAScope FISH (see Materials and methods) of indicated probes from iWAT of mice treated with saline or CL for 4 days at 1 mg/kg/day.

DOI: https://doi.org/10.7554/eLife.49501.007

The following figure supplements are available for figure 4:

Figure supplement 1. Enrichment of cells involved in lipid mobilization in Cluster nine adipocytes.

DOI: https://doi.org/10.7554/eLife.49501.008

Figure supplement 2. Type nine cluster constitute of thermogenic adipocytes.

DOI: https://doi.org/10.7554/eLife.49501.009

presented above, adipocytes from AdIL10Rα KO mice showed a specific increase in the population of thermogenic adipocytes (cluster 9) under both basal conditions (RT) and in response to thermogenic stimuli (cold exposure or CL treatment) (***Figure 5B***). The dot-plot in ***Figure 5C*** shows that the overall pattern of adipocyte cluster enrichment was similar to that in ***Figure 5A***-bottom, and only type nine adipocytes showed a positive shift in cell fraction upon IL10R depletion, except for 48 hr cold exposure where we observed unexpected 4% decrease in cell fraction.

Type nine adipocytes from AdIL10RαKO mice were more metabolically active and showed increased expression of genes linked to mitochondrial activity, energy derivation from FFA, and positive regulation of cold-induced thermogenesis (***Figure 5—figure supplement 1A***). A Volcano plot of the data revealed that genes involved in lipid mobilization and adipose thermogenesis (such as *Lipe, Nr1d1, Oplah, Nfkbia, Pck1, Cebpb, Vegfa, Angptl4*) were increased, and genes correlated with obesity and adiposity such as (*Nrip1, Lpl, Zbtb20, Acss2*) were decreased in iWAT adipocytes from AdIL10RαKO mice compared to controls (***Figure 5D***). However, not all adipogenic and thermogenic genes were different between AdIL10Rα KO and control adipocytes. For example, pan-adipocyte genes such as *Cd36, Fabp4*, and *Aqp1* were similarly expressed between cells of both genotypes (***Figure 5—figure supplement 1B***). Overall, our SNAP-seq data reveal previously unappreciated heterogeneity of mature adipocytes in subcutaneous adipose tissue and point to the existence of distinct cell populations with potentially specialized biological functions. These data further show that IL10 signaling in fat tissue targets a distinct, highly metabolically active and thermogenic adipocyte population.

scRNA-Seq of iWAT stromal vascular fraction reveals a role for IL10-expressing adaptive immune cells in regulation of adipose thermogenesis

Prior bone marrow transplantation experiments had shown that IL10 produced by one or more hematopoietic cell types could rescue the thermogenic phenotype of global IL10-deficient mice (***Rajbhandari et al., 2018***). Therefore, we examined changes in non-adipocyte cells types within iWAT in the setting of thermogenic stimuli to evaluate their potential contribution to IL10/IL10R signaling. We treated WT mice with saline or β3-adrenergic agonist (CL; 1 mg/kg/day) for 4 days, separated iWAT stromal cells from adipocytes, and performed scRNA-Seq on ~10,000 isolated stromal vascular cells (SVF) per mouse as described in Materials and methods. t-SNE plotting of the data revealed 12 major cell clusters (***Figure 6A***). Further subclustering analysis based on known cell marker genes identified four clusters of adipocyte precursor cells (APCs), four clusters of B cells, three clusters of macrophages, and four clusters of T cells (***Figure 6A***).

To gain insight into the remodeling of stromal cells under adrenergic stress, we segregated the cumulative tSNE-plot into CL and saline treatment. The tSNE and dot plots in ***Figure 6B and C*** reveal a relative depletion of APCs and a major increase in B-cell populations in iWAT upon CL treatment. Since adaptive immune cells (T- and B-cells) are major potential producers of IL10 (***Saraiva and O'Garra, 2010***), we further examined IL10 transcript levels in our data set. tSNE-plotting showed that total IL10 transcripts increased ~3 fold upon CL treatment in B-cell clusters (***Figure 6D***). To quantitatively determine IL10 transcript levels in saline and CL- treated conditions, we plotted fold change of the ratio of CL and saline as a function of p value. Compared to saline (represented by dotted line) *Il10* was markedly upregulated in T- and B-cell populations (***Figure 6E***).

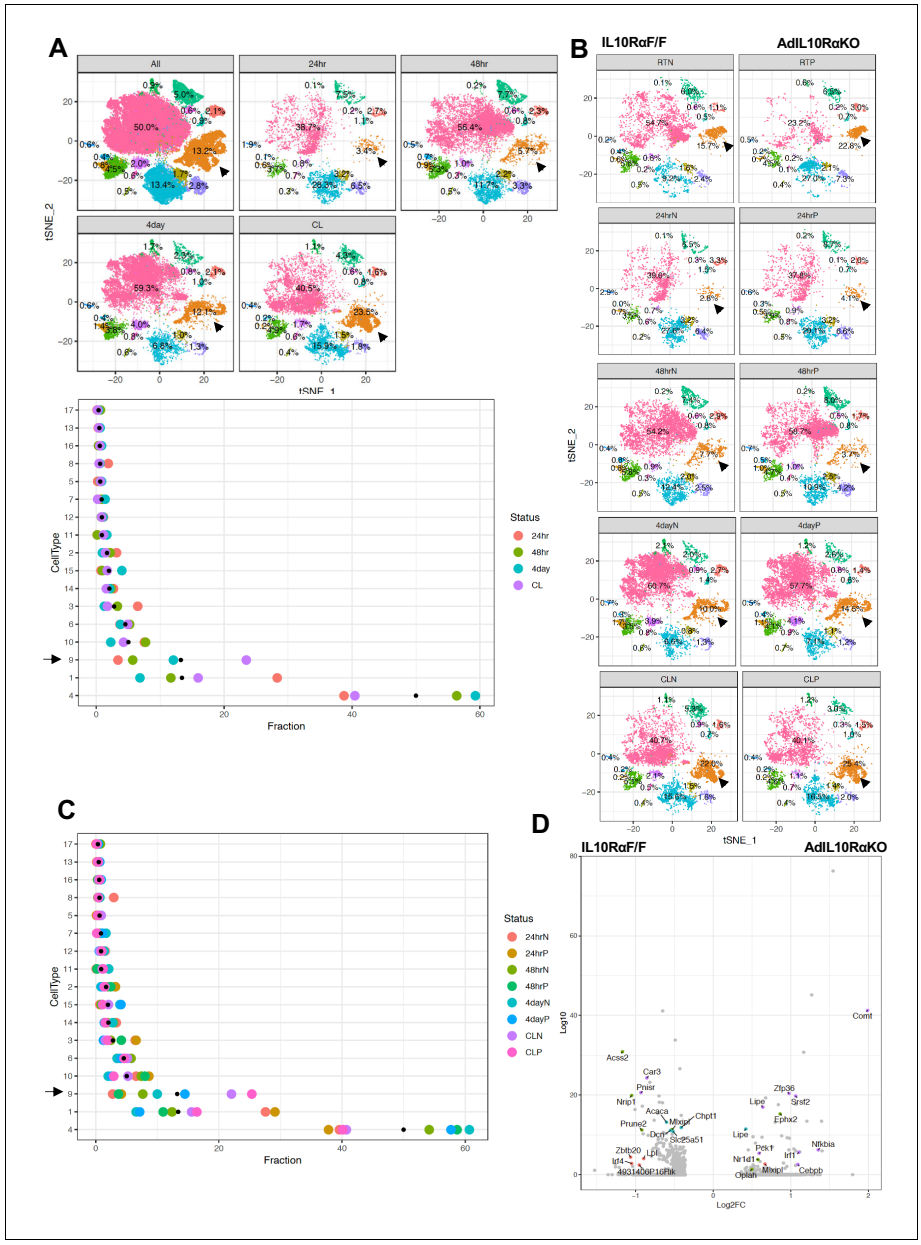

Figure 5. Enrichment of the thermogenic adipocyte cluster in IL10Rα-depleted mice. (**A**) Top: tSNE-plot showing percentage of clusters from aggregated (All) or from indicated treatments. Bottom: Colored dot plot showing percentage of fractions plotted in y-axis and cell types in x-axis under indicated conditions. (**B**) tSNE-plot showing differences in percentage of clusters between adipocytes from iWAT from control and AdIL10Rα KO mice under RT, 24 hr, 48 hr or 4 days cold exposure, or CL treated conditions. (**C**) Colored dot plot showing percentage of fractions plotted in y-axis and cell

Figure 5 continued on next page

Figure 5 continued

types in x-axis under indicated conditions and genotype. N deonotes Adipoq-Cre-Negative IL10RαF/F (IL10RαF/F) and P denotes Adipoq-Cre-Positive (AdIL10Rα KO) mice. (**D**) Volcano plot showing adipocyte gene expression differences between indicated mice from cluster 9. The Log2Fold Change (FC) ratio of floxed control vs. AdIL10Rα KO was plotted as a function of log10 p-value, with select genes indicated with text. Black arrow indicates the Type nine adipocyte cluster.

DOI: https://doi.org/10.7554/eLife.49501.010

The following figure supplement is available for figure 5:

Figure supplement 1. Thermogenic pathway is enriched in the Type 9 cluster of IL10Rα-deficient adipocytes.

DOI: https://doi.org/10.7554/eLife.49501.011

To test the possibility that production of IL10 by iWAT-resident T and B cells might contribute to the regulation of thermogenesis, we treated WT or functional T- and B-cell–deficient SCID mice (***Bosma et al., 1988***) with CL or exposed them to 4˚C for 24 hr. In agreement with our hypothesis, the thermogenic gene program was enhanced in the iWAT of SCID mice compared to controls (***Figure 7A,B***). Accordingly, SCID mice also had higher EE and oxygen consumption and decreased RER, as measured by metabolic chamber studies. (***Figure 7C and D***). Collectively, these results suggest that lymphocytes are an important source of the IL10 acting on adipocyte IL10 receptors during thermogenesis.

Discussion

The influence of inflammation on obesity and adipose insulin resistance has been studied extensively; however, the role of adipose-resident immune cells in regulating the balance between adiposity, lipid mobilization, and thermogenesis is incompletely understood. We previously reported that hematopoietic-secreted IL10 inhibits adrenergic signaling-mediated lipid mobilization and thermogenesis (***Rajbhandari et al., 2018***). Here we provide evidence from scRNA-seq analysis of both adipose stromal-vascular cells and mature adipocytes indicating that adrenergic stimulation causes an increase in the abundance of IL10-secreting adaptive immune cells, and that this cytokine acts directly on the IL10Rα complex in mature adipocytes to antagonize thermogenesis. Genetic ablation of IL10Rα in adipocytes increases the browning of white adipose tissue and selectively enhances thermogenic gene expression, defining mature adipocytes as the primary target of the metabolic actions of IL10. Our SNAP-seq data further revealed that adipose tissue is composed of surprisingly complex subpopulation of adipocytes, including distinct subtypes whose gene expression suggests they are subspecialized for different processes, including lipogenesis and thermogenesis. Deletion of IL10Rα selectively increases the subpopulation of metabolically active, thermogenic adipocytes.

The immune system plays an important role in maintaining adipose homeostasis. Prior studies have shown that signaling from both innate and adaptive immune cells influences lipid handling, adipocyte size and function, and whole body lipid homeostasis (***Bapat et al., 2015***; ***Schäffler and Schölmerich, 2010***; ***Sell et al., 2012***; ***Wernstedt Asterholm et al., 2014***). In a proinflammatory state, as seen in adrenergic stress, cancer cachexia, and burn victims, adipose tissue undergoes remodeling that activates lipid mobilization and thermogenesis which can lead to lipodystrophy (***Patsouris et al., 2015***; ***Petruzzelli et al., 2014***). One established mechanism to block uncontrolled lipolysis is through catabolism of catecholamines. Sympathetic-associated macrophages, NRLP3 inflammasomes, and OCT3 have all been shown to enhance catecholamine clearance in adipose tissue (***Camell et al., 2017***; ***Pirzgalska et al., 2017***; ***Song et al., 2019***). Immune cells also could counteract adrenergic signaling by releasing factors that prevent excessive lipolysis and thermogenesis and thereby direct adipocytes to reserve energy in the setting of starvation or infection. This idea is supported by our scRNA-seq studies on iWAT SVFs of mice under adrenergic stress. Mice treated with β3-adrenergic agonist have expanded adaptive immune cell populations and a 3-fold increase the abundance of IL10 transcript in adipose SVF. Increased production of IL10 in the microenvironment could antagonize adrenergic-mediated thermogenesis, potentially providing a mechanism whereby immune cells help to maintain lipid homeostasis in the setting of energy demand.

A recent study has shown that deletion of Oct coactivator from B-cells (OcaB), which is essential for B-lymphocyte maturation and development, promotes adipose browning and protects mice from age-induced insulin resistance (***Carter et al., 2018***). We showed here that the absence of IL10-

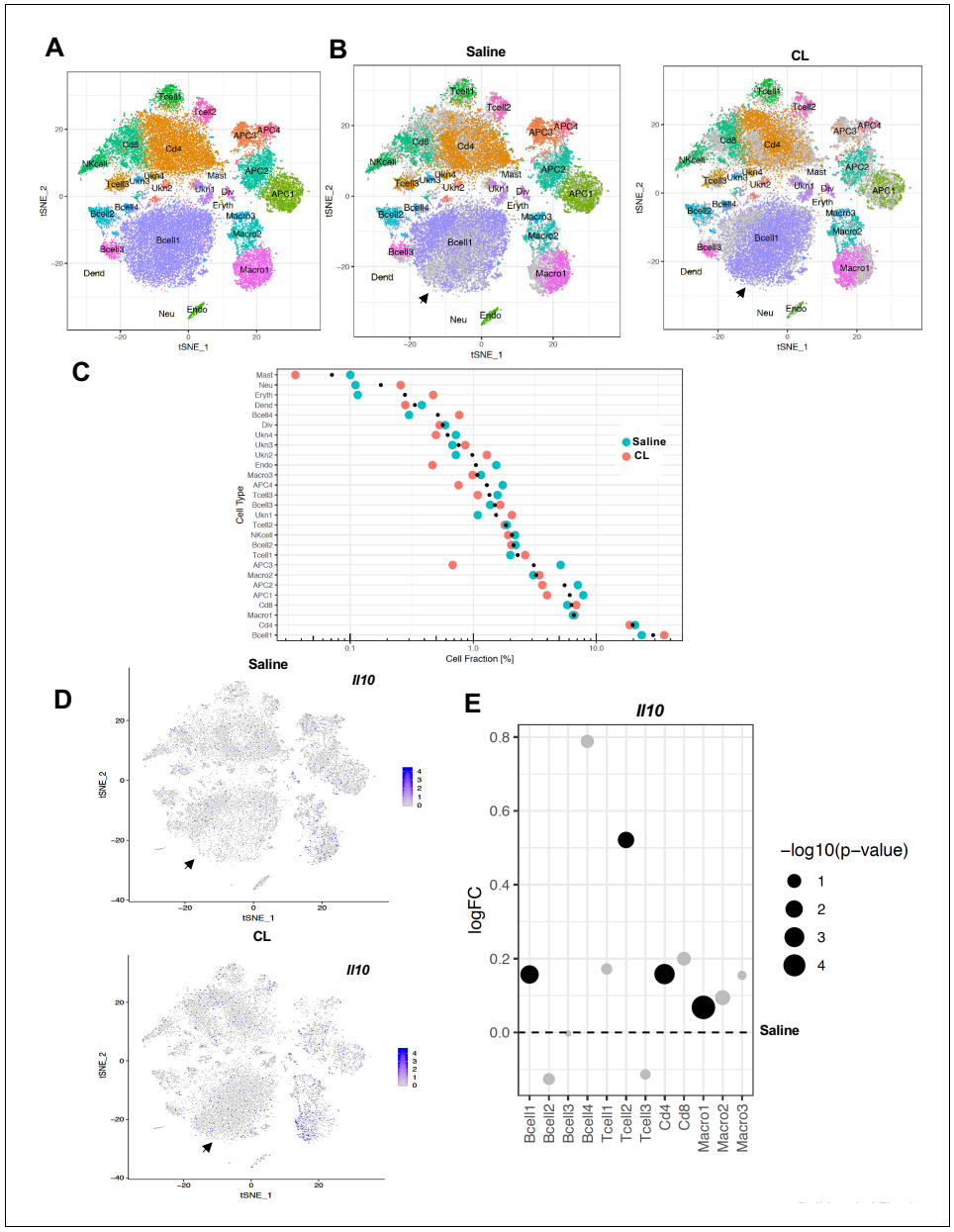

Figure 6. scRNA-Seq reveals an increase in adaptive immune cells under adrenergic stress. (**A**) Aggregated tSNE-plot of combined ~10,000 SVF cells isolated from iWAT of mice treated with CL or saline for 4 days. Colored dots are cells assigned to clusters based on similar transcriptomic signatures and these clusters correspond to specific cell-types. (**B**) Segregated tSNE-plot from (**A**) showing percentage of cell-types between control (Saline) and β3-agonist CL-treated mice. The tSNE-plot also shows differences in percentage of clusters between control and CL-treated mice. Black arrows indicate

Figure 6 continued on next page

Figure 6 continued

major B-cell population. (**C**) Colored dot plot showing percentage of fractions plotted in y-axis and cell types in x-axis under indicated conditions. (**D**) tSNE-plot showing cells expressing *Il10* in control and CL-treated mice. Black arrows indicate major cell clusters with *Il10* expression. (**E**) Dot plot showing expression levels of *Il10* in indicated cells comparing control and CL-treated mice. The Log2Fold Change (FC) ratio of saline vs. CL was plotted as a function of log10 p-value and indicated as different sizes of dots. Fold-change and p-value was compared with saline condition represents as a dotted line.

DOI: https://doi.org/10.7554/eLife.49501.012

secreting adaptive immune cells in mice also leads to enhanced adipose thermogenesis, a finding consistent with the phenotypes of both IL10 KO and AdIL10Rα KO mice.

To more deeply interrogate the effect of IL10 signaling on adipocyte identity and function, we performed SNAP-seq of adipocytes from iWAT. Although prior studies have used FACS and immortalized clonal preadipocytes to assess different types of adipocytes in various adipose tissue depots (***Hagberg et al., 2018***; ***Lee et al., 2019***), to our knowledge, this is the first report of rigorous single nuclei RNA-Seq of adipocytes in the setting of a thermogenic challenge. Our data revealed distinct clusters reflecting subsets of mature adipocytes with differential gene expression. Our data show that the mature tissue adipocyte population is much more heterogeneous than previously appreciated. We categorized by 14 distinct subsets of mature adipocytes that appear to be specialized to participate in at least partially distinct metabolic pathways. These findings suggest that different functions of adipose tissue may be executed by different cell populations, rather than similar cell populations performing diverse functions. Further studies will be needed to test this idea.

Interestingly, Type nine adipocytes were highly metabolically active and thermogenic, and we speculate that this cluster corresponds to the so-called 'beige' adipocyte population. Violin plots of the Type nine cluster showed selective expression of genes involved in lipid mobilization, such as *Adrb3, Acsl2, Lipe, Pnpla2*, and brown/beige-associated genes such as *Ucp1, Cidea, Dio2*, and *Clstn3*. The identity of this cluster was further confirmed by performing snRNA-seq on adipocytes from mice at RT, exposed to cold for various times, or treated with CL. We saw a gradual increase in the percentage of Type nine adipocytes with increasing thermogenic stimulus.

Interestingly, we also noticed distinct sub-clustering of Type nine adipocytes within the cluster. Cells expressing genes involved in lipolysis had an even distribution, whereas cells with higher expression of brown/beige genes were subclustered together after 4 days of cold or CL treatment. This data suggests that *Adrb3*-expressing adipocytes have varying browning capacity. We also noticed that the subclustering patterns of cold-exposed versus CL-treated Type nine adipocytes were also different. This likely reflects different transcriptional responses to cold exposure and pharmacological adrenergic receptor activation. DEG analysis of AdIL10Rα KO and control adipocytes showed that ablation of IL10Rα leads to differential enrichment of adipocyte populations. Type nine adipocytes appear to be enriched in genes that are highly expressed in AdIL10Rα KO compared to control iWAT. Furthermore, AdIL10Rα KO adipocytes are more metabolically active and have heightened response to adrenergic stimulation compared to controls. These data suggest that deletion of IL10Rα from adipocytes leads to the selective enrichment of metabolically active adipocytes that could ultimately lead to increased response to adrenergic signaling and enhanced thermogenesis.

In conclusion, these data provide insight into crosstalk between IL-10-secreting immune cells and adipocytes within adipose tissue, as well as into the complexity of the transcriptional response to adrenergic signaling in mature adipocytes. A better understanding of the pathways influencing the development and phenotypic transformation of Type nine adipocytes could ultimately lead to strategies to increase energy expenditure and protect against diet-induced obesity.

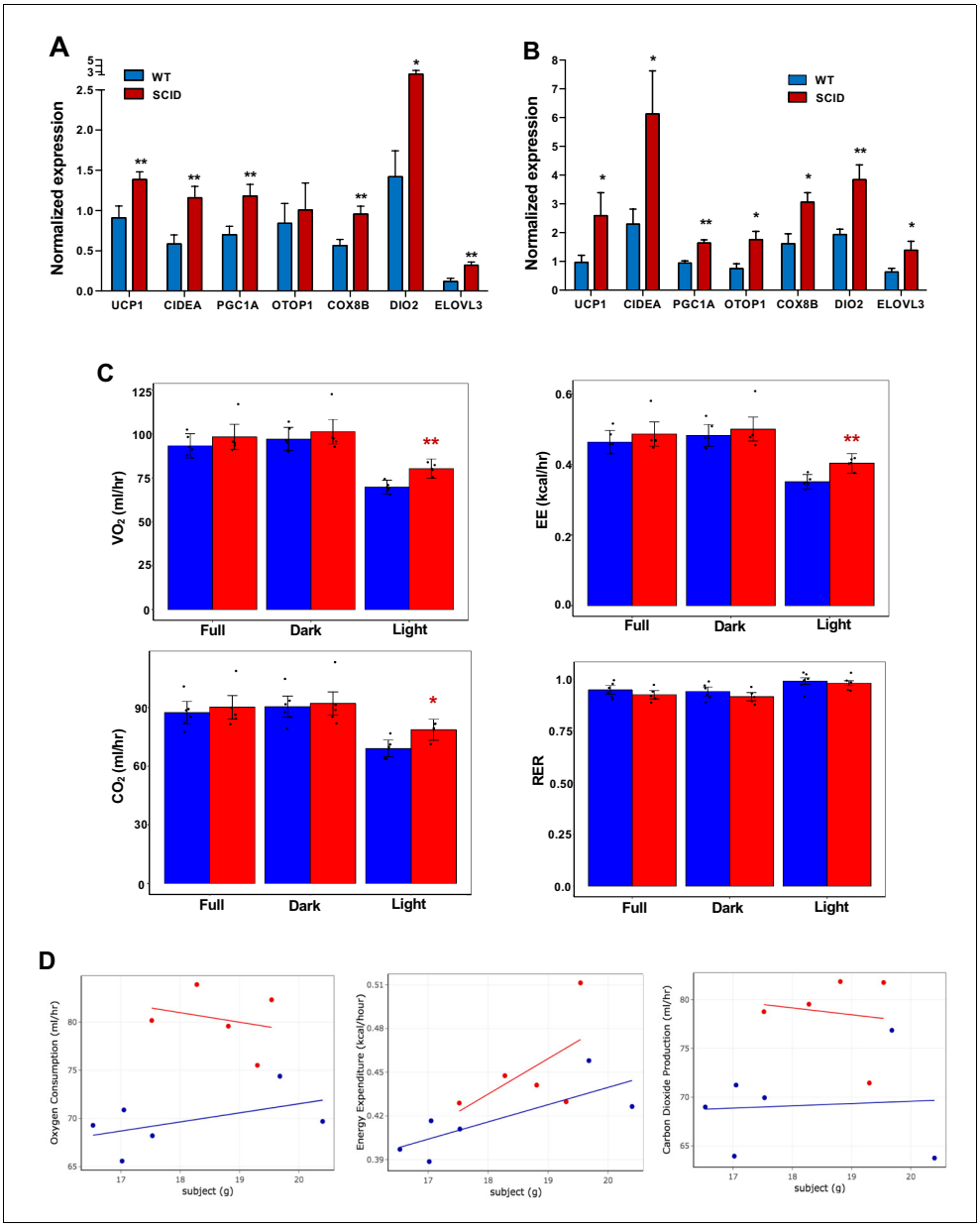

Figure 7. Increased adipose thermogenesis and EE in lymphocyte-deficient mice. (**A and B**) Real-time PCR analysis of gene expression in iWAT from chow-fed 10 week 24 hr cold-exposed (**A**) or CL (1 mg/kg/day for 4 days (**B**) mice. (**C, D**) Bar graphs (C) and scatter plot (D) (Light cycle) showing oxygen consumption, energy expenditure, carbon dioxide production, and RER in CL-treated mice with body mass as covariate. N = 6,5. *, p<0.05, **, p<0.01.
DOI: https://doi.org/10.7554/eLife.49501.013

Materials and methods

Key resources table

Reagent type (species) or resource	Designation	Source or reference	Identifiers	Additional information
Genetic reagent sample (*M. musculus*)	*Il10ra*^{flox}	Jackson Laboratory	Stock No. 028146 RRID:MGI:189797	PMID: 22711892
Genetic reagent sample (*M. musculus*)	C57BL/6J	Jackson Laboratory	Stock No. 000664	
Genetic reagent sample (*M. musculus*)	C57BL/6J SCID	Jackson Laboratory	Stock No. 001913 RRID:MGI:14443	PMID: 8339285
Genetic reagent sample (*M. musculus*)	Adipoq-Cre	Jackson Laboratory	Stock No. 010803 RRID:MGI:168971	PMID: 21356515
Chemical compound	β3-adrenergic receptor agonist (CL 316, 243; CL)	Sigma	C5976	1 mg/kg/day
Chemical compound	Collagenase II	Worthington Biochemical	LS004176	3 mg/ml
Chemical compound	Collagenase D	Sigma	11088882001	9.8 mg/ml
Commercial kit	EvaGreen droplet generation oil	BIO-RAD	1864005	
Commercial kit	ChemGenes barcoded microparticles	ChemGenes	N/A	
Commercial kit	FlowJEM aquapel-treated microfluidic device	FlowJEM	N/A	
Commercial kit	Nextera DNA Library Preparation kit	Illumina	2001874	
Commercial kit	Minute nuclei and cytosol isolation kit for Adipose	Invent Biotech	AN-029	
Commercial kit	40 µm cell strainer	Bel-Art FlowMI	H13680-0040	
Commercial kit	Single Cell 3′ Chip	10X Genomics	1000127	
Commercial kit	Chromium Single Cell 3′ library and Cell Bead kit	10X Genomics	1000128	
Commercial kit	TruSeq Stranded Total RNA Library Prep Kit	Illumina	RS-122–2102	
Commercial kit	RNAscope Multiplex Flurorescent Reagent kit v2	Advanced Cell Diagnostics	323316	
Commercial kit	Opal 520	Akoya Biosciences	FP1487001KT	1:1000
Commercial kit	Opal 570	Akoya Biosciences	FP1488001KT	1:1000
Commercial kit	Opal 620	Akoya Biosciences	FP1495001KT	1:1000
Commercial kit	mm-Adrb3	Advanced Cell Diagnostics	495521	
Commercial kit	mm-UCP1	Advanced Cell Diagnostics	455411	
Commercial kit	mm-Ppargc1b	Advanced Cell Diagnostics	402131	
Commercial kit	TRIzol	Thermo Fischer	15596026	

Continued on next page

Continued

Reagent type (species) or resource	Designation	Source or reference	Identifiers	Additional information
Commercial kit	iScript cDNA synthesis kit	Bio-Rad	1708890	
Commercial kit	SYBER Green Master mix	Diagenode	DMSG-2X-A300	
Commercial kit	RIPA Lysis buffer	Boston Bioproducts	BP-115	
Antibody	IL10Rα	R and D System	AF-474-SP	
Antibody	α-Tubulin	Calbiochem	CP06 RRID:AB_2617116	
Antibody	Actin	Sigma	A2066 RRID:AB_476693	
Software	Drop-seq tools version 1.13	https://github.com/broadinstitute/Drop-seq		
Software	dropSeqPipe	https://github.com/darneson/dropSeqPipeDropEST		
Software	Mouse Genome Allignment mm10	STAR-2.5.0c		https://github.com/alexdobin/STAR
Software	Seurat R package version 3.0.0.9000	https://github.com/satijalab/seurat		
Software	Cell Ranger V3.0.2	10X Genomics		
Other	Prolong Diamond Antifade Mountant with DAPI	Thermo Fischer	P36966	
Other	HFD; 60% kcal fat	Research Diets	D12492	

Animal studies

Breeding pairs of *Il10RaF/F*mice (#028146), Adiponectin CRE (#010803), C57BL/6 SCID (#001913) and C57BL/6 WT controls (#000664) were acquired from Jackson Laboratory and maintained in a pathogen-free barrier-protected environment (12:12 hr light/dark cycle, 22–24˚C) at the UCLA animal facility. Experimental mice were sacrificed at ages mentioned in figure legends for gene expression analysis. For the time course cold exposure experiment, WT mice at 8–10 weeks of age were singly housed at 4˚C room in a non-bedded cage without food and water for first 6 hr; thereafter food, water, and one cotton square were added. For the 24 hr harvest, 3 hr before harvest, food, water, and cotton square were removed and then mice were harvested. For the 48 hr and 4 day cold exposure, cages were changed daily with new cotton squares and 3 hr before the time of harvest, the food, water, and cotton square were removed. For β-adrenergic stimulation experiments, mice were intraperitoneally injected with β3-adrenergic agonist (CL 316,243; CL, at 1 mg/kg/day for 4 days) or saline. For the diet study, 10-week-old *Il10ra*$^{F/F}$ and AdIL10RαKO mice were fed a 60% high-fat diet (Research Diets) for the indicated times. Mouse weights were measured every week and food was replaced weekly. At the end of the experiment, iWATs were resected for gene expression analysis. Indirect calorimetry was performed using a Columbus Instruments Comprehensive Lab Animal Monitoring System (CLAMS, Columbus Instruments). Animals were placed individually in chambers for three consecutive days at ambient temperature (26.5˚C) with 12 hr light/dark cycles. Animals had free access to food and water. Respiratory measurements were made in 20 min intervals after initial 7–9 hr acclimation period. Energy expenditure was calculated from VO2 and RER using the Lusk equation, EE in Kcal/hr = (3.815 + 1.232 X RER) X VO2 in ml/min. CLAMS data were analyzed by CALR web-based software (***Mina et al., 2018***). Animal experiments were conducted in accordance with the UCLA Institutional Animal Care and Research Advisory Committee.

RNA-Seq

Total RNA was prepared as described (*Tong et al., 2016*). Strand-specific libraries were generated from 500 ng total RNA using the TruSeq Stranded Total RNA Library Prep Kit (Illumina). cDNA libraries were single-end sequenced (50 bp) on an Illumina HiSeq 2000 or 4000. Reads were aligned to the mouse genome (NCBI37/mm9) with TopHat v1.3.3 and allowed one alignment with up to two mismatches per read. mRNA RPKM values were calculated using Seqmonk's mRNA quantitation pipeline. A gene was included in the analysis if it met all the following criteria: the maximum RPKM reached four at any time point, the gene length was >200 bp, and for in-vitro studies was induced at least 3-fold from Day 0 samples, and the expression was significantly different from the basal ($p<0.01$) as determined by the DESeq2 package in R Bioconductor. P-values were adjusted using the Benjamini-Hochberg procedure of multiple hypothesis testing (*Benjamini and Hochberg, 1995*).

scRNA-Seq of adipose stromal vascular fraction (SVF) population

Single cell isolation from SVF

Inguinal white adipose tissue (iWAT) from mice treated with saline or CL were dissected and placed on sterile 6-well tissue culture plate with ice-cold 1X DPBS. Fat pads were blotted on a napkin to removed excess liquid. Tissues were cut and minced with scissors and placed in 15 ml conical tubes containing digestion buffer (2 ml DPBS and Collagenase II at 3 mg/ml; Worthington Biochemical, Lakewood, NJ, USA) and incubated at 37˚C for 40 min with gentle shaking at 100 rpm. Following tissue digestion 8 ml of resuspension media (DMEM/F12 with glutamax supplemented with 15%FBS and 1% pen/strep; Thermo Scientific, CA) was added to stop enzyme activity. The digestion mixture was passed through 100 µm cell strainer and centrifuged at 150 x g for 8 min at room temperature. The pellet was resuspended and incubated in RBC lysis buffer (Thermo Scientific, CA) for 3 min at room temperature to remove red blood cells followed by centrifugation at 150 x g for 8 min. The pellet was resuspened in resuspension media and spun down again at 150 x g for 8 min. Finally, the cell pellet was resuspended in 1 ml of 0.01% BSA (in DPBS). This final cell suspension solution was passed through a 40 µm cell strainer (Fisher Scientific, Hampton, NH, USA) to discard debris and cell number was counted for Drop-Seq application.

Drop-seq single cell barcoding and library preparation

The Drop-seq protocol from Macosko et al. and version 3.1 of the online Drop-seq protocol [http://mccarrolllab.com/download/905/] was followed with minor modifications to generate STAMPs (single-cell transcriptomes attached to microparticles) and cDNA libraries (*Macosko et al., 2015*). Briefly, to create oil droplets with barcoded cells, single cell suspensions (100 cells/µl), EvaGreen droplet generation oil (BIO-RAD, Hercules, CA, USA), and ChemGenes barcoded microparticles (ChemGenes, Wilmington, MA, USA) were co-flowed through a FlowJEM aquapel-treated microfluidic device (FlowJEM, Toronto, Canada) at the recommended flow speeds (oil: 15,000 µl/hr, cells: 4000 µl/hr, and beads 4000 µl/hr). After STAMP generation, oil droplets were broken, and cDNA synthesis was performed. To obtain enough cDNA for library preparations the Drop-seq protocol was followed with the following modifications. For the PCR step, 4000 beads were used per tube, the number of cycles was changed to 4 + 11 and multiple PCR tubes were pooled. cDNA library concentration and quality were assessed using the Agilent TapeStation system (Agilent, Santa Clara, CA, USA). The samples were then tagmented using the Nextera DNA Library Preparation kit (Illumina, San Diego, CA, USA) and multiplex indices were added. After another round of PCR, the samples were assessed on a Tapestation high sensitivity DNA screentape (Agilent, Santa Clara, CA, USA) for library quality before sequencing.

Illumina high-throughput sequencing of Drop-seq libraries

Molar concentrations of the Drop-seq libraries were quantified using the Qubit Fluorometric Quantitation system (ThermoFisher, Canoga Park, CA, USA) and library fragment lengths were estimated using a Tapestation high sensitivity DNA screentape (Agilent, Santa Clara, CA, USA). Samples were normalized by concentration and then pooled appropriately. Pooled libraries were then sequenced on an Illumina HiSeq 4000 (Illumina, San Diego, CA, USA) instrument using the Drop-seq custom read 1B primer (GCCTGTCCGCGGAAGCAGTGGTATCAACGCAGAGTAC) (IDT, Coralville, IA, USA)

and PE100 reads were generated. Read 1 consists of the 12 bp cell barcode, followed by the 8 bp UMI, and the last 80 bp on the read are not used. Read two contains the single cell transcripts.

Drop-seq data pre-processing and quality control

Demultiplexed fastq files generated from Drop-seq were processed to digital expression gene matrices (DGEs) using Drop-seq tools version 1.13 (https://github.com/broadinstitute/Drop-seq) and dropEst (***Petukhov et al., 2018***). The workflow is available as modified version of the snakemake-based dropSeqPipe (https://github.com/Hoohm/dropSeqPipe) workflow and is available on github (***Arneson, 2019***; copy archived at https://github.com/elifesciences-publications/dropSeqPipeDropEST). Briefly, fastq files were converted to BAM format and cell and molecular barcodes were tagged. Reads corresponding to low quality barcodes were removed and any occurrence of the SMART adapter sequence or polyA tails found in the reads was trimmed. These cleaned reads were converted back to fastq format to be aligned to the mouse reference genome mm10 using STAR-2.5.0c. After the reads were aligned, the reads which overlapped with exons, introns, and intergenic regions were tagged using a RefFlat annotation file of mm10. To make use of reads aligning to intronic regions, which are not considered in Drop-seq tools v1.13, we used dropEst to construct digital gene expression matrices from the tagged, aligned reads where each row in the matrix is the read count of a gene and each column is a unique single cell. The count values for each cell were normalized by the total number of UMIs in that cell and then multiplied by 10,000 and log transformed. Single cells were identified from background ambient mRNA using thresholds of at least 700 transcripts and a maximum mitochondrial fraction of 10%.

Identification of cell clusters

The Seurat R package version 3.0.0.9000 (https://github.com/satijalab/seurat) was used to project all sequenced cells onto two dimensions using t-SNE and Louvain (***Blondel et al., 2008***; ***van der Maaten and Hinton, 2008***) clustering was used to assign clusters. The optimal number of PCs used for t-SNE/UMAP dimensionality reduction and Louvain clustering was determined using the Jackstraw permutation approach and a grid-search of the parameters. Similarly, the density used to assign clusters was identified using a parameter grid search.

Identification of marker genes of individual cell clusters

We defined cell cluster specific marker genes from our Drop-seq dataset using the FindConservedMarkers function in Seurat across all the samples. Briefly, a Wilcoxon Rank Sum Test is run within each sample and a meta p-value across all samples is computed to assess the significance of each gene as a marker for a cluster. Within each sample, the cells are split into two groups: single cells from the cell type of interest and all other single cells. To be considered in the analysis, the gene had to be expressed in at least 10% of the single cells form one of the groups and there had to be at least a 0.25 log fold change in gene expression between the groups. This process was conducted within each sample separately, and then a meta p-value was assessed from the p-values across all samples. Multiple testing was corrected using the Benjamini-Hochberg method on the meta p-values and genes with an FDR < 0.05 were defined as cell type specific marker genes.

Resolving cell identities of the cell clusters

We used two methods to resolve the identities of the cell clusters. First, we used known cell-type specific markers curated from literature, single cell atlases, previous studies in the SVF and PBMCs, and from Immgen (immgen.org) to find distinct expression patterns in the cell clusters (***Burl et al., 2018***; ***Chen et al., 2018***; ***Han et al., 2018***; ***Hepler et al., 2018***; ***Tabula Muris Consortium et al., 2018***; ***Stoeckius et al., 2017***; ***Zhang et al., 2019***). A cluster showing unique expression of a known marker gene can be used to identify that cell type. To consider more than a single gene, we evaluated the overlap between known cell type marker genes with the marker genes identified in our cell clusters using FindConservedMarkers. Significant overlap was assessed using a Fisher's exact test with Bonferroni correction for multiple testing. The two methods showed consistency in cell identity determination. The GEO accession number for the sequencing data is GSE133486.

Single nuclei adipocyte RNA-Sequencing (SNAP-Seq)

Adipocyte nuclei isolation from iWAT

200–400 mg of inguinal white adipose tissues (iWAT) from mice exposed to conditions mentioned in the text were placed on sterile 6-well tissue culture plate with ice-cold 1XPBS. Fat pads were blotted on a napkin to removed excess liquid. Tissues were cut and minced with scissors and were placed in 15 ml conical tubes containing digestion buffer (DPBS and Collagenase D at 9.8 mg/ml; Sigma, MO) at incubated at 37˚C for 45 mins with gentle shaking at 100 rpm. 10 ml of resuspension media (DMEM/F12 with glutamax supplemented with 15% FBS and 1% pen/strep; Thermo Scientific, CA) was added to digested solution and slowly inverted five times. The digestion mixture was centrifuged at 200 x g for 5 mins at RT. Floating adipocytes were collected using P1000 pipet with half cut P1000 tip. Adipocytes were transferred to a new 15 ml tube and kept on ice for five mins. Excess liquid was aspirated using 1 ml syringe and adipocytes were then washed with 1 ml DPBS and the suspension was spun down at 200 g for 5 mins at RT. Spun down liquid was aspirated using 1 ml syringe and adipocyte nuclei were isolated using Minute nuclei and cytosol isolation kit for adipose tissue using manufacture's instruction (Invent Biotechnologies, MN) with modifications. Briefly, adipocytes were slowly resuspended in 600 µl nuclei lysis buffer (N/C Buffer) and lysate was transferred to a filter cartridge with collection tube and incubated at −20˚C freezer for 20 min with cap open. After incubation, the tube was centrifuged at 2000 rpm for 2 min at 4˚C. The filter cartridge was discarded without agitation and the collection tube was immediately centrifuged at 4000 rpm for 4 min at 4˚C. Supernatant was gently removed using P200 pipet without touching the side walls. Nuclei were resuspended in 30 ul of nuclei resuspension buffer (DPBS+0.1%BSA) per 200–400 mg of iWAT (i.e. one 8–10 week chow fed mouse). For SNAP-seq, 2–3 mice were combined and 60 µl of nuclei suspension was transferred to a new 2 ml tube and resuspended with 500–700 µl of nuclei resuspension buffer and filtered using 40 µm cell strainer (Flowmi Cell Strainer, Belart, NJ) twice to get clean single nuclei suspension. As shown in ***Figure 3A***, for quality control, nuclei were first DAPI stained and then filtered or FACS sorted to get single nuclei suspension. After microfluidic partitioning in 10xGenomics platform (see below), nuclei lysis was checked by observing oil emulsion under fluorescent microscope for DAPI diffusion.

Adipocyte single nuclei barcoding and library preparation

Approximately 10,000 nuclei were loaded onto Single Cell 3' Chip (10xGenomics, CA) per channel with an expected recovery to 4000–7000 nuclei. The Chip was placed on a 10XGenomics Instrument to generate single nuclei gel beads in emulsion (GEMs). For optimal nuclei lysis, GEMs were incubated on ice for 50 mins. After incubation, single nuclei RNA-Seq libraries were prepared using Chromium Single Cell 3' Library and Cell Bead Kit) according to manufacturer's instruction.

Illumina high-throughput sequencing libraries

The 10X genomics library molar concentration was quantified by Qubit Fluorometric Quantitation (ThermoFisher, Canoga Park, CA, USA) and library fragment length was estimated using a TapeStation (Aligent, Santa Clara, CA, USA). Sequencing was performed on an Illumina HiSeq 4000 (Illumina, San Diego, CA, USA) instrument with PE100 reads and an 8 bp index read to multiplexing. With the version three chemistry, the first 26 bp of Read 1 consist of the cell barcode and the UMI, and the last 74 bp on the read are not used. Read two contains the single cell transcripts.

SNAP-Seq data pre-processing and quality control-

Digital gene expression matrices (DGEs) in sparse matrix representation we obtained using 10x Genomics' Cell Ranger v3.0.2 software suite. Briefly,. bcl files obtained from the UCLA Broad Stem Cell Research Center sequencing core were demultiplexed and converted to fastq files using the mkfastq function in Cell Ranger which wraps Illumina's bcl2fastq v2.19.1.403. The counts function in Cell Ranger was used to generate DGEs from the fastq files. Briefly, the resulting fastq files are aligned to a 10x supplied mm10 reference genome (mm10-3.0.0) using STAR and reads are identified as either exonic, intronic, or intergenic using the supplied 10x Genomics GTF file. To determine cell barcodes, the counts function in Cell Ranger implements an algorithm based on EmptyDrops (***Lun et al., 2019***). Only reads which align to exonic regions were used in the resulting DGE. The count values for each cell were normalized by the total number of UMIs in that cell and then

multiplied by 10,000 and log transformed. Single cells were identified from background ambient mRNA using thresholds of at least 200 genes and a maximum mitochondrial fraction of 10%.

Identification of adipocyte clusters

The Seurat R package version 3.0.0.9000 (https://github.com/satijalab/seurat) was used to project all sequenced cells onto two dimensions using t-SNE/UMAP and Louvain clustering was used to assign clusters. The optimal number of PCs used for t-SNE dimensionality reduction and Louvain clustering were determined using the Jackstraw permutation approach and a grid-search of the parameters. Similarly, the density used to assign clusters was identified using a parameter grid search.

Identification of marker genes of individual adipocyte clusters

We defined cell cluster specific marker genes from our 10x Genomics dataset using the FindConservedMarkers function in Seurat across all the samples. Briefly, a Wilcoxon Rank Sum Test is run within each sample and a meta p-value across all samples is computed to assess the significance of each gene as a marker for a particular cluster. Within each sample, the cells are split into two groups: single cells from the cell type of interest and all other single cells. To be considered in the analysis, the gene had to be expressed in at least 10% of the single cells form one of the groups and there had to be at least a 0.25 log fold change in gene expression between the groups. This process was conducted within each sample separately, and then a meta p-value was assessed from the p-values across all samples. Multiple testing was corrected using the Benjamini-Hochberg method on the meta p-values and genes with an FDR < 0.05 were defined as cell type specific marker genes.

Resolving cell identities of the cell clusters

Two methods were used to aid in resolving the identities of the cell type clusters. First, KEGG, Reactome, BIOCARTA, GO Biological Processes, and Hallmark gene sets were obtained from MSigDB. To identify pathways which had significant enrichment of our cell type marker genes, we used a hypergeometric test, followed by multiple testing correction with the Benjamini–Hochberg method. We also adapted the method proposed by ***Zywitza et al. (2018)*** to get a single cell level score for each pathway. Briefly, the expression of each gene was linearly transformed to (0,1) and the average gene expression of all genes for each gene set was computed to represent the score for that gene set. We then identified the top scoring gene sets which were representative of each cell type. The GEO accession number for the sequencing data is GSE133486.

RNAScope fluorescence in situ hybridization (FISH)

Inguinal white adipose tissue (iWAT) from CL-treated WT mice (Jackson Laboratory, #000664) was fixed in 10% formalin overnight, embedded with paraffin, and sectioned into unstained, 5-µm-thick sections. Sections were baked at 60˚C for 1 hr, deparaffinized, and baked again at 60˚C for another hour prior to pre-treatment. The standard pre-treatment protocol was followed for all sectioned tissues. In situ hybridization was performed according to manufacturers' instructions using the RNAscope Multiplex Fluorescent Reagent Kit v2 (#323136, Advanced Cell Diagnostics [ACD], Newark, CA). Opal fluorophore reagent packs (Akoya Biosciences, Menlo Park, CA) for Opal 520 (FP1487001KT), Opal 570 (FP1488001KT), and Opal 620 (FP1495001KT) were used at a 1:1000 dilution in TSA buffer provided in the RNAscope Multiplex Fluorescent Reagent Kit v2. Probes targeting mm-Adrb3 (#495521, ACD) in channel 1, mm-Ucp1 (#455411-C2, ACD) in channel 2, and mm-Ppargc1b (#402131-C4, ACD) in channel four were used. Slides were mounted with ProLong Diamond Antifade Mountant with DAPI (P36966, Life Technologies). Fluorescent signals were captured with the 40x objective lens on a laser scanning confocal microscope (LSM880; Zeiss).

Real time qPCR

Total RNA was isolated using TRIzol reagent (Invitrogen) and reverse transcribed with the iScript cDNA synthesis kit (Biorad). cDNA was quantified by real-time PCR using SYBR Green Master Mix (Diagenode) on a QuantStudio six instrument (Themo Scientific, CA). Gene expression levels were determined by using a standard curve. Each gene was normalized to the housekeeping gene 36B4 and was analyzed in duplicate. Primers used for real-time PCR are in ***Supplementary file 2***.

Western blotting

Whole cell lysate or tissue lysate was extracted using RIPA lysis buffer (Boston Bioproducts) supplemented with complete protease inhibitor cocktail (Roche). Proteins were diluted in Nupage loading dye (Invitrogen), heated at 95˚C for 5 min, and run on 4–12% NuPAGE Bis-Tris Gel (Invitrogen). Proteins were transferred to hybond ECL membrane (GE Healthcare) and blotted with IL10Rα (AF-474-SP, R and D Systems), αTubulin (CP06, Calbiochem), Actin (A2066, Sigma-Aldrich).

Cellular and mitochondrial respiration

Mitochondria were isolated from fresh tissues and immediately used in a XF24 analyzer as previously described (***Rogers et al., 2011***). Briefly, mitochondria were isolated in MSHE+BSA buffer using a 800 g/8000 g dual centrifugation method and resuspended in MAS buffer. Protein concentration was determined using a Bradford Assay reagent (Bio-Rad) and 20 µg of protein were seeded per well by centrifugation. Coupling and electron flow assays were performed as described (***Rogers et al., 2011***). For the coupling assay, basal oxygen consumption rate (OCR) was measured in the presence of 10 mM succinate and 2 µM rotenone, and after sequential addition of 4 mM ADP (Complex V substrate), 2.5 µg/ml oligomycin (Complex V inhibitor), 4 µM FCCP (mitochondrial uncoupler) and 4 µM antimycin A (Complex III inhibitor). For electron flow assays, basal OCR was measured in presence of 10 mM pyruvate (Complex I substrate), 2 mM malate and 4 µM FCCP, and after sequential addition of 2 µM rotenone (Complex I inhibitor), 10 mM succinate (Complex II substrate), 4 µM antimycin A (Complex III inhibitor) and 1 mM TMPD containing 10 mM ascorbate (Complex IV substrate).

Statistics

All data are presented as mean ± SEM and analyzed using Microsoft Excel and Prism (Graphpad). Student's t test with Welch's correction was used for single variable comparison between two groups. One-way ANOVA followed by Dunnett post hoc test was used for multiple comparisons versus the control group. Two-way ANOVA followed by Bonferroni posttests was used to examine interactions between multiple variables. Statistical significance for CLAMS study was determined by multiple regression analysis (ANCOVA). $p<0.05$ was considered to be statistically significant and is presented as *$p<0.05$, **$p<0.01$, ***$p<0.001$, or ****$p<0.0001$.

Acknowledgements

We thank UCLA Broad Stem Cell Research Center Core for sequencing and Technology Center for Genomics and Bioinformatics for single cell sequencing. This work was supported by NIH grants R00DK114571 (PR), HL090533 (KR and PT), DK120851 and DK063491 (PT), DK104363 and UL1TR001881 (XY), and R01GM086372 (STS). A-C F is funded by the Tri-Service General Hospital, National Defense Medical Center, Taipei, Taiwan. The funders had no role in study design, data collection and interpretation, or the decision to submit the work for publication.

Additional information

Competing interests

Peter Tontonoz: Reviewing editor, *eLife*. The other authors declare that no competing interests exist.

Funding

Funder	Grant reference number	Author
National Institutes of Health	K99 DK114571	Prashant Rajbhandari
National Institutes of Health	DK063491	Peter Tontonoz
National Institutes of Health	DK120851	Peter Tontonoz
National Institutes of Health	HL090533	Karen Reue Peter Tontonoz

National Institutes of Health	DK104363	Xia Yang
National Institutes of Health	UK1TR001881	Xia Yang
National Institutes of Health	R01GM086372	Stephen T Smale

The funders had no role in study design, data collection and interpretation, or the decision to submit the work for publication.

Author contributions

Prashant Rajbhandari, Conceptualization, Formal analysis, Funding acquisition, Methodology, Writing—original draft, Writing—review and editing; Douglas Arneson, Data curation, Formal analysis, Investigation, Methodology, Writing—review and editing; Sydney K Hart, Luis C Santos, Stephen D Lee, Investigation; In Sook Ahn, Formal analysis, Investigation, Methodology; Graciel Diamante, An-Chieh Feng, Brandon J Thomas, Laurent Vergnes, Formal analysis, Investigation; Nima Zaghari, Software, Formal analysis, Investigation; Abha K Rajbhandari, Supervision, Investigation; Karen Reue, Funding acquisition, Investigation, Writing—review and editing; Stephen T Smale, Supervision, Funding acquisition, Writing—review and editing; Xia Yang, Formal analysis, Supervision, Funding acquisition, Methodology, Writing—review and editing; Peter Tontonoz, Conceptualization, Supervision, Funding acquisition, Writing—original draft, Project administration, Writing—review and editing

Author ORCIDs

Peter Tontonoz https://orcid.org/0000-0003-1259-0477

Ethics

Animal experimentation: This study was performed in strict accordance with the recommendations in the Guide for the Care and Use of Laboratory Animals of the National Institutes of Health. All of the animals were handled according to approved institutional animal care and use committee (IACUC) protocol (99-131) of the University of California, Los Angeles.

Decision letter and Author response

Decision letter https://doi.org/10.7554/eLife.49501.020
Author response https://doi.org/10.7554/eLife.49501.021

Additional files

Supplementary files

- Supplementary file 1. Top enriched pathways among DEGs of major cell types (FDR < 5%).
DOI: https://doi.org/10.7554/eLife.49501.014
- Supplementary file 2. QPCR primers used in this study.
DOI: https://doi.org/10.7554/eLife.49501.015
- Transparent reporting form DOI: https://doi.org/10.7554/eLife.49501.016

Data availability

Sequencing data have been deposited to GEO (GSE133486).

The following dataset was generated:

Author(s)	Year	Dataset title	Dataset URL	Database and Identifier
Tontonoz P, Rajbhandari P, Arneson D	2019	Single cell sequencing of stromal vascular fraction (SVF) under B3-adrenergic agonist stimulation and mature adipocytes under cold exposure and B3-adrenergic agonist stimulation	https://www.ncbi.nlm.nih.gov/geo/query/acc.cgi?acc=GSE133486	NCBI Gene Expression Omnibus, GSE133486

References

Arneson D. 2019. dropSeqPipeDropEST. *GitHub*. 3d357a0. https://github.com/darneson/dropSeqPipeDropEST

Bachman ES, Dhillon H, Zhang CY, Cinti S, Bianco AC, Kobilka BK, Lowell BB. 2002. betaAR signaling required for diet-induced thermogenesis and obesity resistance. *Science* **297**:843–845. DOI: https://doi.org/10.1126/science.1073160, PMID: 12161655

Bapat SP, Myoung Suh J, Fang S, Liu S, Zhang Y, Cheng A, Zhou C, Liang Y, LeBlanc M, Liddle C, Atkins AR, Yu RT, Downes M, Evans RM, Zheng Y. 2015. Depletion of fat-resident treg cells prevents age-associated insulin resistance. *Nature* **528**:137–141. DOI: https://doi.org/10.1038/nature16151, PMID: 26580014

Bartness TJ, Liu Y, Shrestha YB, Ryu V. 2014. Neural innervation of white adipose tissue and the control of lipolysis. *Frontiers in Neuroendocrinology* **35**:473–493. DOI: https://doi.org/10.1016/j.yfrne.2014.04.001, PMID: 24736043

Benjamini Y, Hochberg Y. 1995. Controlling the false discovery rate: a practical and powerful approach to multiple testing. *Journal of the Royal Statistical Society: Series B* **57**:289–300. DOI: https://doi.org/10.2307/2346101

Blondel VD, Guillaume J-L, Lambiotte R, Lefebvre E. 2008. Fast unfolding of communities in large networks. *Journal of Statistical Mechanics: Theory and Experiment* **2008**:P10008. DOI: https://doi.org/10.1088/1742-5468/2008/10/P10008

Bosma M, Schuler W, Bosma G. 1988. The scid mouse mutant. *Current Topics in Microbiology and Immunology* **137**:197–202. DOI: https://doi.org/10.1007/978-3-642-50059-6_29, PMID: 3416632

Burl RB, Ramseyer VD, Rondini EA, Pique-Regi R, Lee YH, Granneman JG. 2018. Deconstructing adipogenesis induced by β3-Adrenergic receptor activation with Single-Cell expression profiling. *Cell Metabolism* **28**:300–309. DOI: https://doi.org/10.1016/j.cmet.2018.05.025, PMID: 29937373

Camell CD, Sander J, Spadaro O, Lee A, Nguyen KY, Wing A, Goldberg EL, Youm Y-H, Brown CW, Elsworth J, Rodeheffer MS, Schultze JL, Dixit VD. 2017. Inflammasome-driven catecholamine catabolism in macrophages blunts lipolysis during ageing. *Nature* **550**:119–123. DOI: https://doi.org/10.1038/nature24022

Cannon B, Nedergaard J. 2004. Brown adipose tissue: function and physiological significance. *Physiological Reviews* **84**:277–359. DOI: https://doi.org/10.1152/physrev.00015.2003, PMID: 14715917

Carter S, Miard S, Caron A, Sallé-Lefort S, St-Pierre P, Anhê FF, Lavoie-Charland E, Blais-Lecours P, Drolet MC, Lefebvre JS, Lacombe J, Deshaies Y, Couet J, Laplante M, Ferron M, Bossé Y, Marette A, Richard D, Marsolais D, Picard F. 2018. Loss of OcaB prevents Age-Induced fat accretion and insulin resistance by altering B-Lymphocyte transition and promoting energy expenditure. *Diabetes* **67**:1285–1296. DOI: https://doi.org/10.2337/db17-0558, PMID: 29496744

Chechi K, Carpentier AC, Richard D. 2013. Understanding the Brown adipocyte as a contributor to energy homeostasis. *Trends in Endocrinology & Metabolism* **24**:408–420. DOI: https://doi.org/10.1016/j.tem.2013.04.002, PMID: 23711353

Chen J, Cheung F, Shi R, Zhou H, Lu W, Candia J, Kotliarov Y, Stagliano KR, Tsang JS, Consortium C. 2018. PBMC fixation and processing for Chromium single-cell RNA sequencing. *Journal of Translational Medicine* **16**:198. DOI: https://doi.org/10.1186/s12967-018-1578-4

Cohen P, Levy JD, Zhang Y, Frontini A, Kolodin DP, Svensson KJ, Lo JC, Zeng X, Ye L, Khandekar MJ, Wu J, Gunawardana SC, Banks AS, Camporez JP, Jurczak MJ, Kajimura S, Piston DW, Mathis D, Cinti S, Shulman GI, et al. 2014. Ablation of PRDM16 and beige adipose causes metabolic dysfunction and a subcutaneous to visceral fat switch. *Cell* **156**:304–316. DOI: https://doi.org/10.1016/j.cell.2013.12.021, PMID: 24439384

Duncan RE, Ahmadian M, Jaworski K, Sarkadi-Nagy E, Sul HS. 2007. Regulation of lipolysis in adipocytes. *Annual Review of Nutrition* **27**:79–101. DOI: https://doi.org/10.1146/annurev.nutr.27.061406.093734, PMID: 17313320

Hagberg CE, Li Q, Kutschke M, Bhowmick D, Kiss E, Shabalina IG, Harms MJ, Shilkova O, Kozina V, Nedergaard J, Boucher J, Thorell A, Spalding KL. 2018. Flow cytometry of mouse and human adipocytes for the analysis of Browning and cellular heterogeneity. *Cell Reports* **24**:2746–2756. DOI: https://doi.org/10.1016/j.celrep.2018.08.006, PMID: 30184507

Han X, Wang R, Zhou Y, Fei L, Sun H, Lai S, Saadatpour A, Zhou Z, Chen H, Ye F, Huang D, Xu Y, Huang W, Jiang M, Jiang X, Mao J, Chen Y, Lu C, Xie J, Fang Q, et al. 2018. Mapping the mouse cell atlas by Microwell-Seq. *Cell* **172**:1091–1107. DOI: https://doi.org/10.1016/j.cell.2018.02.001, PMID: 29474909

Harms M, Seale P. 2013. Brown and beige fat: development, function and therapeutic potential. *Nature Medicine* **19**:1252–1263. DOI: https://doi.org/10.1038/nm.3361, PMID: 24100998

Hepler C, Shan B, Zhang Q, Henry GH, Shao M, Vishvanath L, Ghaben AL, Mobley AB, Strand D, Hon GC, Gupta RK. 2018. Identification of functionally distinct fibro-inflammatory and adipogenic stromal subpopulations in visceral adipose tissue of adult mice. *eLife* **7**:e39636. DOI: https://doi.org/10.7554/eLife.39636, PMID: 30265241

Jaworski K, Sarkadi-Nagy E, Duncan RE, Ahmadian M, Sul HS. 2007. Regulation of triglyceride metabolism. IV. hormonal regulation of lipolysis in adipose tissue. *American Journal of Physiology-Gastrointestinal and Liver Physiology* **293**:G1–G4. DOI: https://doi.org/10.1152/ajpgi.00554.2006, PMID: 17218471

Kong X, Banks A, Liu T, Kazak L, Rao RR, Cohen P, Wang X, Yu S, Lo JC, Tseng YH, Cypess AM, Xue R, Kleiner S, Kang S, Spiegelman BM, Rosen ED. 2014. IRF4 is a key thermogenic transcriptional partner of PGC-1α. *Cell* **158**:69–83. DOI: https://doi.org/10.1016/j.cell.2014.04.049, PMID: 24995979

Lee KY, Luong Q, Sharma R, Dreyfuss JM, Ussar S, Kahn CR. 2019. Developmental and functional heterogeneity of white adipocytes within a single fat depot. *The EMBO Journal* **38**:e99291. DOI: https://doi.org/10.15252/embj.201899291, PMID: 30530479

Lun ATL, Riesenfeld S, Andrews T, Dao TP, Gomes T, Marioni JC, participants in the 1st Human Cell Atlas Jamboree. 2019. EmptyDrops: distinguishing cells from empty droplets in droplet-based single-cell RNA sequencing data. *Genome Biology* **20**:63. DOI: https://doi.org/10.1186/s13059-019-1662-y, PMID: 30902100

Macosko EZ, Basu A, Satija R, Nemesh J, Shekhar K, Goldman M, Tirosh I, Bialas AR, Kamitaki N, Martersteck EM, Trombetta JJ, Weitz DA, Sanes JR, Shalek AK, Regev A, McCarroll SA. 2015. Highly parallel Genome-wide expression profiling of individual cells using nanoliter droplets. *Cell* **161**:1202–1214. DOI: https://doi.org/10.1016/j.cell.2015.05.002, PMID: 26000488

Mina AI, LeClair RA, LeClair KB, Cohen DE, Lantier L, Banks AS. 2018. CalR: a Web-Based analysis tool for indirect calorimetry experiments. *Cell Metabolism* **28**:656–666. DOI: https://doi.org/10.1016/j.cmet.2018.06.019, PMID: 30017358

Patsouris D, Qi P, Abdullahi A, Stanojcic M, Chen P, Parousis A, Amini-Nik S, Jeschke MG. 2015. Burn induces Browning of the subcutaneous white adipose tissue in mice and humans. *Cell Reports* **13**:1538–1544. DOI: https://doi.org/10.1016/j.celrep.2015.10.028, PMID: 26586436

Petruzzelli M, Schweiger M, Schreiber R, Campos-Olivas R, Tsoli M, Allen J, Swarbrick M, Rose-John S, Rincon M, Robertson G, Zechner R, Wagner EF. 2014. A switch from white to Brown fat increases energy expenditure in cancer-associated cachexia. *Cell Metabolism* **20**:433–447. DOI: https://doi.org/10.1016/j.cmet.2014.06.011, PMID: 25043816

Petukhov V, Guo J, Baryawno N, Severe N, Scadden DT, Samsonova MG, Kharchenko PV. 2018. dropEst: pipeline for accurate estimation of molecular counts in droplet-based single-cell RNA-seq experiments. *Genome Biology* **19**:78. DOI: https://doi.org/10.1186/s13059-018-1449-6

Pirzgalska RM, Seixas E, Seidman JS, Link VM, Sánchez NM, Mahú I, Mendes R, Gres V, Kubasova N, Morris I, Arús BA, Larabee CM, Vasques M, Tortosa F, Sousa AL, Anandan S, Tranfield E, Hahn MK, Iannacone M, Spann NJ, et al. 2017. Sympathetic neuron-associated macrophages contribute to obesity by importing and metabolizing norepinephrine. *Nature Medicine* **23**:1309–1318. DOI: https://doi.org/10.1038/nm.4422, PMID: 29035364

Rajbhandari P, Thomas BJ, Feng AC, Hong C, Wang J, Vergnes L, Sallam T, Wang B, Sandhu J, Seldin MM, Lusis AJ, Fong LG, Katz M, Lee R, Young SG, Reue K, Smale ST, Tontonoz P. 2018. IL-10 signaling remodels adipose chromatin architecture to limit thermogenesis and energy expenditure. *Cell* **172**:218–233. DOI: https://doi.org/10.1016/j.cell.2017.11.019, PMID: 29249357

Rogers GW, Brand MD, Petrosyan S, Ashok D, Elorza AA, Ferrick DA, Murphy AN. 2011. High throughput microplate respiratory measurements using minimal quantities of isolated mitochondria. *PLOS ONE* **6**:e21746. DOI: https://doi.org/10.1371/journal.pone.0021746, PMID: 21799747

Rosen ED, Spiegelman BM. 2014. What we talk about when we talk about fat. *Cell* **156**:20–44. DOI: https://doi.org/10.1016/j.cell.2013.12.012, PMID: 24439368

Saely CH, Geiger K, Drexel H. 2012. Brown versus white adipose tissue: a mini-review. *Gerontology* **58**:15–23. DOI: https://doi.org/10.1159/000321319, PMID: 21135534

Saraiva M, O'Garra A. 2010. The regulation of IL-10 production by immune cells. *Nature Reviews Immunology* **10**:170–181. DOI: https://doi.org/10.1038/nri2711, PMID: 20154735

Schäffler A, Schölmerich J. 2010. Innate immunity and adipose tissue biology. *Trends in Immunology* **31**:228–235. DOI: https://doi.org/10.1016/j.it.2010.03.001, PMID: 20434953

Schreiber R, Diwoky C, Schoiswohl G, Feiler U, Wongsiriroj N, Abdellatif M, Kolb D, Hoeks J, Kershaw EE, Sedej S, Schrauwen P, Haemmerle G, Zechner R. 2017. Cold-Induced thermogenesis depends on ATGL-Mediated lipolysis in cardiac muscle, but not Brown adipose tissue. *Cell Metabolism* **26**:753–763. DOI: https://doi.org/10.1016/j.cmet.2017.09.004, PMID: 28988821

Sell H, Habich C, Eckel J. 2012. Adaptive immunity in obesity and insulin resistance. *Nature Reviews Endocrinology* **8**:709–716. DOI: https://doi.org/10.1038/nrendo.2012.114, PMID: 22847239

Song NJ, Choi S, Rajbhandari P, Chang SH, Kim S, Vergnes L, Kwon SM, Yoon JH, Lee S, Ku JM, Lee JS, Reue K, Koo SH, Tontonoz P, Park KW. 2016. Prdm4 induction by the small molecule butein promotes white adipose tissue Browning. *Nature Chemical Biology* **12**:479–481. DOI: https://doi.org/10.1038/nchembio.2081, PMID: 27159578

Song W, Luo Q, Zhang Y, Zhou L, Liu Y, Ma Z, Guo J, Huang Y, Cheng L, Meng Z, Li Z, Zhang B, Li S, Yee SW, Fan H, Li P, Giacomini KM, Chen L. 2019. Organic cation transporter 3 (Oct3) is a distinct catecholamines clearance route in adipocytes mediating the beiging of white adipose tissue. *PLOS Biology* **17**:e2006571. DOI: https://doi.org/10.1371/journal.pbio.2006571, PMID: 30653498

Stoeckius M, Hafemeister C, Stephenson W, Houck-Loomis B, Chattopadhyay PK, Swerdlow H, Satija R, Smibert P. 2017. Simultaneous epitope and transcriptome measurement in single cells. *Nature Methods* **14**:865–868. DOI: https://doi.org/10.1038/nmeth.4380, PMID: 28759029

Tabula Muris Consortium, Overall coordination, Logistical coordination, Organ collection and processing, Library preparation and sequencing, Computational data analysis, Cell type annotation, Writing group, Supplemental text writing group, Principal investigators. 2018. Single-cell transcriptomics of 20 mouse organs creates a tabula muris. *Nature* **562**:367–372. DOI: https://doi.org/10.1038/s41586-018-0590-4, PMID: 30283141

Takahashi A, Adachi S, Morita M, Tokumasu M, Natsume T, Suzuki T, Yamamoto T. 2015. Post-transcriptional Stabilization of Ucp1 mRNA Protects Mice from Diet-Induced Obesity. *Cell Reports* **13**:2756–2767. DOI: https://doi.org/10.1016/j.celrep.2015.11.056

Tong A-J, Liu X, Thomas BJ, Lissner MM, Baker MR, Senagolage MD, Allred AL, Barish GD, Smale ST. 2016. A Stringent Systems Approach Uncovers Gene-Specific Mechanisms Regulating Inflammation. *Cell* **165**:165–179. DOI: https://doi.org/10.1016/j.cell.2016.01.020

van der Maaten L, Hinton G. 2008. Visualizing data using t-SNE. *Journal of Machine Learning Research* **9**:2579–2605.

Villanueva CJ, Vergnes L, Wang J, Drew BG, Hong C, Tu Y, Hu Y, Peng X, Xu F, Saez E, Wroblewski K, Hevener AL, Reue K, Fong LG, Young SG, Tontonoz P. 2013. Adipose subtype-selective recruitment of TLE3 or Prdm16 by pparγ specifies lipid storage versus thermogenic gene programs. *Cell Metabolism* **17**:423–435. DOI: https://doi.org/10.1016/j.cmet.2013.01.016, PMID: 23473036

Vitali A, Murano I, Zingaretti MC, Frontini A, Ricquier D, Cinti S. 2012. The adipose organ of obesity-prone C57BL/6J mice is composed of mixed white and Brown adipocytes. *Journal of Lipid Research* **53**:619–629. DOI: https://doi.org/10.1194/jlr.M018846, PMID: 22271685

Wajchenberg BL. 2000. Subcutaneous and visceral adipose tissue: their relation to the metabolic syndrome. *Endocrine Reviews* **21**:697–738. DOI: https://doi.org/10.1210/edrv.21.6.0415, PMID: 11133069

Wang QA, Tao C, Gupta RK, Scherer PE. 2013. Tracking adipogenesis during white adipose tissue development, expansion and regeneration. *Nature Medicine* **19**:1338–1344. DOI: https://doi.org/10.1038/nm.3324, PMID: 23995282

Wernstedt Asterholm I, Tao C, Morley TS, Wang QA, Delgado-Lopez F, Wang ZV, Scherer PE. 2014. Adipocyte inflammation is essential for healthy adipose tissue expansion and remodeling. *Cell Metabolism* **20**:103–118. DOI: https://doi.org/10.1016/j.cmet.2014.05.005, PMID: 24930973

Zechner R, Kienesberger PC, Haemmerle G, Zimmermann R, Lass A. 2009. Adipose triglyceride lipase and the lipolytic catabolism of cellular fat stores. *Journal of Lipid Research* **50**:3–21. DOI: https://doi.org/10.1194/jlr.R800031-JLR200, PMID: 18952573

Zhang X, Lan Y, Xu J, Quan F, Zhao E, Deng C, Luo T, Xu L, Liao G, Yan M, Ping Y, Li F, Shi A, Bai J, Zhao T, Li X, Xiao Y. 2019. CellMarker: a manually curated resource of cell markers in human and mouse. *Nucleic Acids Research* **47**:D721–D728. DOI: https://doi.org/10.1093/nar/gky900, PMID: 30289549

Zywitza V, Misios A, Bunatyan L, Willnow TE, Rajewsky N. 2018. Single-Cell transcriptomics characterizes cell types in the subventricular zone and uncovers molecular defects impairing adult neurogenesis. *Cell Reports* **25**:2457–2469. DOI: https://doi.org/10.1016/j.celrep.2018.11.003, PMID: 30485812

APPENDIX E

Enhanced In Vivo Delivery of Stem Cells using Microporous Annealed Particle Scaffolds

NANO · MICRO small
www.small-journal.com

Enhanced In Vivo Delivery of Stem Cells using Microporous Annealed Particle Scaffolds

Jaekyung Koh, Donald R. Griffin, Maani M. Archang, An-Chieh Feng, Thomas Horn, Michael Margolis, David Zalazar, Tatiana Segura, Philip O. Scumpia, and Dino Di Carlo**

Delivery to the proper tissue compartment is a major obstacle hampering the potential of cellular therapeutics for medical conditions. Delivery of cells within biomaterials may improve localization, but traditional and newer void-forming hydrogels must be made in advance with cells being added into the scaffold during the manufacturing process. Injectable, in situ cross-linking microporous scaffolds are recently developed that demonstrate a remarkable ability to provide a matrix for cellular proliferation and growth in vitro in three dimensions. The ability of these scaffolds to deliver cells in vivo is currently unknown. Herein, it is shown that mesenchymal stem cells (MSCs) can be co-injected locally with microparticle scaffolds assembled in situ immediately following injection. MSC delivery within a microporous scaffold enhances MSC retention subcutaneously when compared to cell delivery alone or delivery within traditional in situ cross-linked nanoporous hydrogels. After two weeks, endothelial cells forming blood vessels are recruited to the scaffold and cells retaining the MSC marker CD29 remain viable within the scaffold. These findings highlight the utility of this approach in achieving localized delivery of stem cells through an injectable porous matrix while limiting obstacles of introducing cells within the scaffold manufacturing process.

Stem cell therapies hold promise for many intractable diseases through a variety of mechanisms. These mechanisms include the promotion of tissue repair, replacement of mutated or missing factors, and modulation of the immune system.[1–4] Mesenchymal stem cells (MSCs) represent a particularly attractive stem cell therapeutic candidate as they are multipotent cells with the capacity to migrate to injured or inflamed organs to induce tissue repair through secreted factors[5] and differentiate into functional tissue.[6] However, clinical translation has been challenging due to poor homing, survival, and engraftment of transplanted stem cells to a disease site.[7,8] Moreover, loss of control by the engrafted cells in a disrupted biological environment limits the ability to harness the stem cells for meaningful therapeutic outcomes.[5,9]

Localized delivery of stem cells using biomaterials can mitigate these issues.[10–13] An ideal material should not only enable minimally invasive delivery by injection, and retain cells after transplantation to achieve sustained function, but also create an artificial stem cell niche in situ for higher efficacy and longer maintenance of the therapy.[14,15] Specifically, the biomaterial should provide suitable biophysical and biochemical microenvironmental cues for enhanced control of cell function in vivo.[16,17]

Dr. J. Koh, M. M. Archang, T. Horn, M. Margolis, D. Zalazar, Prof. D. Di Carlo
Department of Bioengineering
University of California, Los Angeles
Los Angeles, CA 90095, USA
E-mail: dicarlo@ucla.edu
Prof. D. R. Griffin
Department of Biomedical Engineering
University of Virginia
Charlottesville, VA 22904, USA
Dr. A.-C. Feng
Department of Microbiology, Immunology, and Molecular Genetics
David Geffen School of Medicine
University of California, Los Angeles
Los Angeles, CA 90095, USA
Prof. T. Segura
Department of Biomedical Engineering, Neurology, Dermatology
Duke University
Durham, NC 27708, USA
The ORCID identification number(s) for the author(s) of this article can be found under https://doi.org/10.1002/smll.201903147.

DOI: 10.1002/smll.201903147

Dr. P. O. Scumpia
Division of Dermatology
Department of Medicine
David Geffen School of Medicine
University of California, Los Angeles
Los Angeles, CA 90095, USA
E-mail: PScumpia@mednet.ucla.edu
Dr. P. O. Scumpia
Department of Dermatology
VA Greater Los Angeles Healthcare System
Los Angeles, CA 90073, USA
Prof. D. Di Carlo
Department of Mechanical and Aerospace Engineering
University of California, Los Angeles
Los Angeles, CA 90095, USA
Prof. D. Di Carlo
California NanoSystems Institute (CNSI)
University of California, Los Angeles
Los Angeles, CA 90095, USA
Prof. D. Di Carlo
Jonsson Comprehensive Cancer Center
University of California, Los Angeles
Los Angeles, CA 90095, USA

However, current injectable biomaterials suffer from ineffective modulation or lack of porosity for mass transport, cell motility, proliferation, cell–cell adhesion, or new tissue formation.[14,15,18]

To this end, void forming hydrogels were created to facilitate expansion of cells within the hydrogel coupled with the degradation of porogens in the hydrogel matrix.[19] While these hydrogels display tremendous promise, a major limitation of this approach is that cells need to be supplied at the time of manufacture of the hydrogel, which represents a significant manufacturing and application hurdle as cells need to survive from the time of manufacture to the time of delivery. Acute medical conditions that require immediate therapeutics may be less amenable to this approach. Approaches where therapeutics can be mixed with the delivery vehicle immediately before application to form a scaffold in situ within tissue may overcome the manufacturing limitation.

We originally created microporous annealed particle (MAP) scaffolds as a way to combine microporosity and injectability, which showed a tremendous potential to heal wounds.[20] We and others with similar technology have shown that in vitro, cells use these microporous scaffolds to expand and proliferate in three dimensions around the microparticles.[20–25] These findings suggested that cells can be mixed with hydrogel immediately before delivery, and this can be used as a cellular delivery platform that can overcome some of the limitations of current hydrogel technologies.

Here, we present data demonstrating delivery of stem cells in a microporous, injectable scaffold enhances their retention in tissue, without requiring the integration of the stem cells during the microparticle building block manufacturing process (**Figure 1**A). When subcutaneously implanted without cells, we obtained additional evidence that subcutaneous delivery of MAP scaffolds by themselves resulted in tremendous cellular integration, new blood vessel formation, and an absence of foreign body formation around the implant, and collagen deposition and vascularization deep into the scaffold volume. Seeding MAP scaffolds with mesenchymal stem cells immediately before subcutaneous delivery results in enhanced maintenance

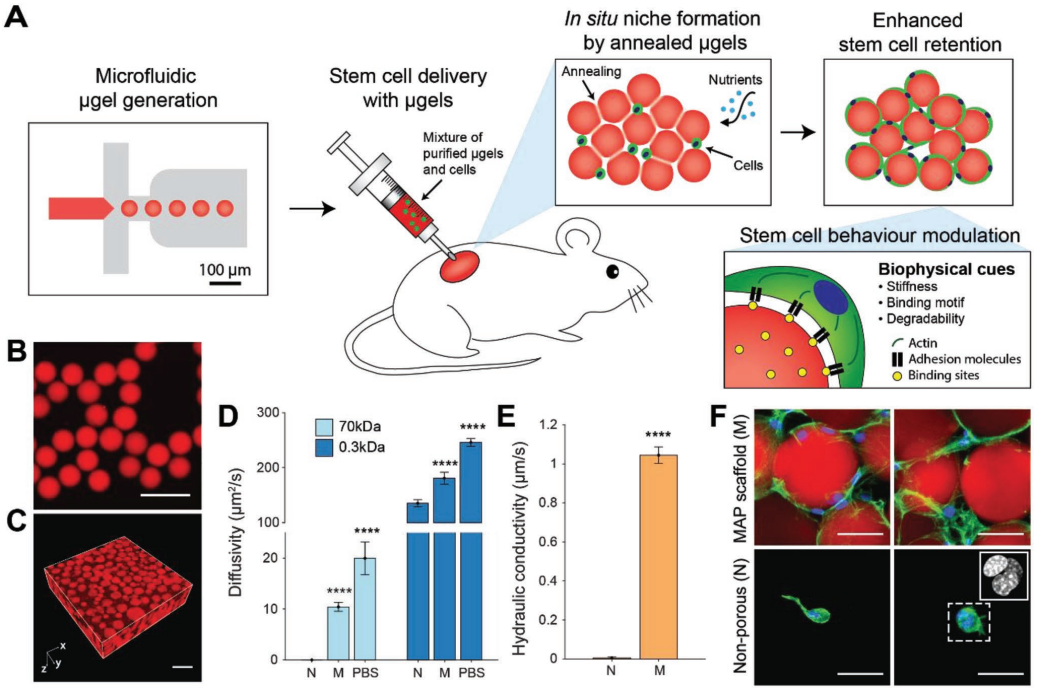

Figure 1. Mesenchymal stem cell (MSC) delivery and in situ niche creation strategy using annealed monodisperse hydrogel particles. A) An artificial stem cell niche is created in situ by annealing a suspension of injectable monodisperse hydrogel particles. Highly monodisperse particle building blocks enable the generation of a pore network in a highly controllable manner, which promotes the transport of oxygen and nutrients as well as cell migration. The biophysical properties of building blocks are modulated to enhance the functions of the transplanted MSCs. B) Monodisperse hydrogel particles or μgels produced by the microfluidic device. Scale bar: 200 μm. C) Tissue scaffold assembled from monodisperse μgels. Scale bar: 200 μm. D) Diffusivity of 70 kDa dextran and 0.3 kDa FITC in nonporous scaffolds (N), MAP scaffolds (M) and PBS ($n = 4$–7). Data are presented as average ± s.d. Statistical significance based on one-way ANOVA followed by Tukey's HSD post hoc test (significance compared to N, ****$p < 0.0001$). E) Hydraulic conductivity of PBS through the nonporous scaffold (N) and MAP scaffold (M) at atmospheric pressure ($n = 3$). Data are presented as average ± s.d. Statistical significance based on standard two-tailed Student *t*-test (****$p < 0.0001$). F) Fluorescent images of MSCs in vitro cultured in microporous scaffolds and nonporous scaffolds at week 2. Blue, nucleus; Green, actin; Red, gel. Scale bar: 50 μm.

of MSCs when compared to MSCs delivered in PBS or nonporous hydrogels and allows for MSCs to quickly migrate, adhere, and proliferate, leading to enhanced maintenance of transplanted cells in vivo. Moreover, we show that the material properties can be tuned to promote the maintenance of the stem cell population while integrating with surrounding tissues through vascularization. We anticipate that this approach can be easily translated and generally applied to delivery of other treatment-appropriate therapeutic cells, given cell production can be independent of biomaterial production, and molecularly and biophysically tailored niches can be created.

We hypothesized that covalently linked assemblies of monodisperse hydrogel particles would produce an interconnected pore space beneficial for the transport of oxygen and nutrients and may overcome diffusion limitations of conventional nonporous hydrogels. To test whether this is indeed the case, highly monodisperse (CV < 5%) microscale hydrogel particles were generated using a microfluidic approach (Figure S1, Supporting Information). These particles were enzymatically annealed in vitro to generate MAP scaffolds (M) (Figure 1B,C). To assess transport by diffusion, we performed fluorescence recovery after photobleaching (FRAP) using fluorescein (0.3 kDa) and dextran-conjugated fluorescein (70 kDa) (Figure 1D and Figure S2, Supporting Information). The fluorescent intensity recovery was on the order of tens of seconds in MAP scaffolds, resulting in a calculated diffusivity for 70 kDa dextran ≈50% of that in PBS, while no diffusion was detected into the hydrogel particles in the same timeframe. Given the relatively large hydrodynamic diameter of 70 kDa dextran that is comparable to the nanoscale pores in the gel mesh network, steric hindrance severely limits diffusion within nanoporous hydrogels.[26,27] In fact, the observation of diffusion in macroscale gels revealed that the diffusivity was 50-fold lower than that in PBS (0.42 $\mu m^2\ s^{-1}$), in agreement with previous reports.[28] For 0.3 kDa fluorescein molecules, MAP scaffolds again demonstrated a significantly enhanced diffusivity compared to chemically matched nonporous gels (Figure 1D).

Higher convective flux of fluid also resulted from the interconnected pore network of the scaffolds. To measure hydraulic conductivity, nonporous scaffolds and MAP scaffolds were placed on top of a membrane with 5 μm pores in a custom-designed device, which allowed for precise gravity-driven flow (Figure S3, Supporting Information). While only limited permeation was observed through the nonporous scaffold resulting in a conductivity of $\approx 1.6 \times 10^{-3}\ \mu m\ s^{-1}$ at atmospheric pressure, the interconnected porosity of MAP scaffolds yielded ≈600-fold enhancement of the conductivity ($\approx 1\ \mu m\ s^{-1}$) (Figure 1E), which was comparable to physiologic convection in the extracellular fluid.[29] This not only indicates that the pores are interconnected throughout the scaffold, but also suggests that nutrients and waste can be transported by convection,[30] which may be beneficial for cell survival and proliferation in a macroscale biomaterial formed from MAP gel in vitro and in vivo.

As a proof of concept as to whether microporous scaffold implants can support stem cells in vivo, we first assessed whether scaffolds subcutaneously injected result in a foreign body response that would limit nutrient delivery to cells within the scaffold (Figure S4, Supporting Information). To our surprise, not only did the MAP scaffolds display no foreign body response (Figure S4B, Supporting Information), they supported the ingrowth of both PECAM (CD31) expressing blood vessels (Figure S4C, Supporting Information), and collagen I and III expressing fibroblasts (Figure S4B, Supporting Information) through the majority of the scaffold. By contrast, chemically identical traditional (i.e., nanoporous) hydrogels elicited a significant collagen I-rich fibrotic encapsulation without significant integration within the scaffold (Figure S4A, Supporting Information). We considered the findings a positive indication that MAP scaffolds would support nutrient delivery to co-injected stem cells in vivo leading to enhanced survival and proceeded to test this hypothesis.

Given the increased potential for enhanced nutrient transport and tissue formation in MAP scaffolds, we next tested whether MAP scaffolds do indeed support cell survival. MSCs incorporated in MAP scaffolds showed highly interconnected and spread morphology through the void spaces between hydrogel building blocks (**Figures** 1F and **2**A). On the other hand, MSCs in nonporous gels possessed a round morphology with limited spreading and connection between cells (Figures 1F and 2A). Although cells can degrade the hydrogel matrix locally to infiltrate, the time course for degradation prevents cells from migrating to occupy the space throughout the scaffold. In fact, multiple cells were confined to a small area (Figure 1F inset).

The ability to spread and migrate throughout the MAP scaffold led to more rapid proliferation, with increased void volume in MAP scaffolds leading to significantly higher proliferation rate. To correlate the microscale pore network with cell growth and proliferation, the intensity of red fluorescent protein (RFP) produced by RFP-transfected MSCs (RFP-MSCs) was measured for each scaffold over a two-week period. While the expansion of cells incorporated in nonporous gels yielded only a 2.3-fold increase, the expansion of RFP-MSCs in MAP scaffolds yielded a 17-fold increase (Figure 2B). Enhanced proliferation was confirmed through the analysis of nucleus density, in which much lower number of cell-free regions were observed in MAP scaffolds (Figure 2C).

Building off of these in vitro results and acellular MAP scaffold support of robust endogenous cell ingrowth in vivo (Figure S4, Supporting Information), we hypothesized that MAP scaffolds would enhance the retention of MSCs in tissue when compared with PBS or nonporous scaffolds in vivo. MSCs expressing RFP (RFP-MSCs) were injected subcutaneously in C57BL/6 mice, an immunocompetent mouse strain, to recapitulate MSC survival in the presence of a functional immune system. The fluorescent intensity was measured over a two-week period (Figure 2D,E). RFP fluorescence intensity remained the highest for cells co-delivered in MAP scaffolds compared to PBS and nonporous scaffolds at the end of one week (Figure 2F). Likewise, the cell area, which was defined by the area above a radiant efficiency of 2×10^7, was also significantly higher in MAP scaffolds (Figure 2G). The half-life of MSCs for each case calculated from the RFP intensity decay over time was 6.13 days for MAP scaffolds, 2.35 days for nonporous gel, and 1.91 days for PBS. Combined, these results support that the formation of a microporous scaffold in situ promotes cell proliferation and survival in vivo, perhaps due to enhanced transport, cell distribution and connectivity throughout the scaffold, as identified in vitro.

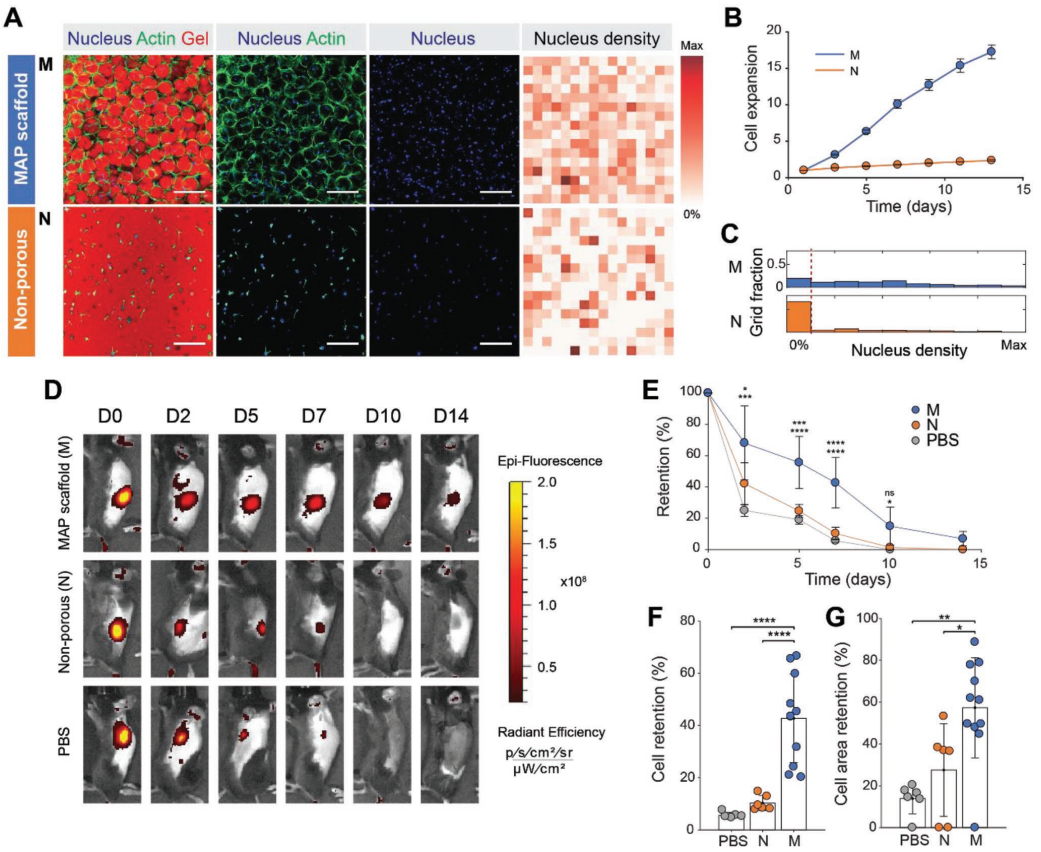

Figure 2. Controlled microporosity generated by MAP scaffolds facilitates the highest proliferation in vitro and retention in vivo. A) Fluorescent images of MSCs growing in MAP scaffolds (M), and nonporous scaffolds (N) following two weeks of in vitro culture. Corresponding heat map of nucleus density in the fields of view. Darker red color indicates a region with a higher number of nuclei. (Blue, nucleus; Green, actin; Red, gel). Scale bar: 200 μm. B) Cell proliferation of fluorescently transfected MSCs measured by increase in fluorescence intensity over time ($n = 4$). C) Histograms of nucleus density for five scaffold conditions ($n = 4$ scaffolds per condition). The red dashed line indicates the threshold for no nuclei in a region. D) Representative fluorescence IVIS images of MSCs producing RFP that were subcutaneously injected into C57BL/6 mice with MAP scaffold (M), nonporous scaffold (N) and PBS at 0, 2, 5, 7, 10, and 14 days post-implantation. E) Integrated fluorescent intensity at each time point ($n = 6$–11). F) Comparison of cell retention at day 7 relative to day 0. G) Comparison of cell area at day 7 relative to day 0. Cell area was defined as an area with radiant efficiency higher than 2×10^7. Each point represents an individual mouse. All data are presented as average ± s.d. Statistical significance based on one-way ANOVA followed by Tukey's HSD post hoc test (*$p < 0.05$, **$p < 0.01$, ***$p < 0.001$, and ****$p < 0.0001$); n.s. indicates not significant.

Since the in vivo fluorescence studies suggest that MAP scaffolds improved the retention of the subcutaneously delivered MSCs, we next wished to confirm the retention of MSCs within the MAP hydrogel. We also wished to test whether MSC retention in the injected scaffold could be improved through modulation of material properties of the building blocks, such as degradability, stiffness, and cell-binding motif amount, as these parameters were shown to play a critical role in cell delivery with other biomaterials.[31–33] To arrive at a final set of microgel parameters for in vivo experiments, different weight percent, stoichiometry, crosslinker types and cell binding motif (RGD) concentrations were screened (**Figure 3**A and Table S1, Supporting Information). Two soft building blocks were designed to have storage moduli of 500 Pa with enzymatically degradable (SoD1; corresponding to the same/original formulation of MAP hydrogel used in Figure 2) and nondegradable (SoN1) crosslinkers and a standard RGD concentration (0.5×10^{-3} M) to isolate the effect of MMP-triggered degradability. Stiff building blocks were designed using the nondegradable formulation, decoupling degradability from stiffness. We avoided simultaneous modulation of stiffness with MMP-degradable crosslinkers since we observed that stiffness and degradability were difficult to independently control. For example, doubling the crosslinking concentration of degradable crosslinkers

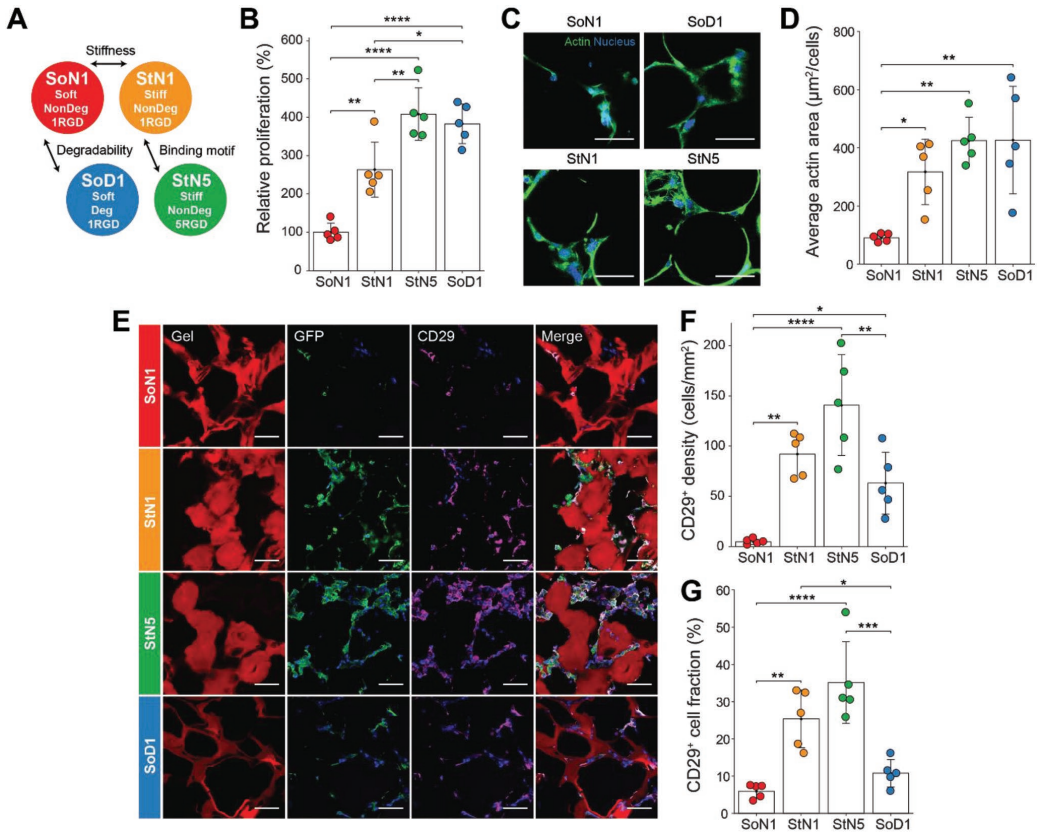

Figure 3. Modulating MAP scaffold material properties affect MSC function. A) Four MAP gel formulations manufactured to study the effect of degradability, stiffness and binding motif concentration. B) Relative cell expansion in vitro at 7 days ($n = 5$). C) Representative fluorescent images of MSC growth in vitro following two weeks (Blue, nucleus; Green, actin). Scale bar: 50 µm. D) Average actin area normalized by the number of cells for in vitro culture ($n = 5$). E) Representative fluorescent images of GFP-producing MSCs in MAP scaffolds subcutaneously injected into C57BL/6 mice following two weeks (Red, gel; Blue, nucleus; Green, GFP; Magenta, CD29). Scale bar: 50 µm. F) $CD29^+$ cells per area in scaffolds at week 2 ($n = 5$). G) Ratio of CD29+ cells to all cells in the scaffolds at week 2 ($n = 5$). Each dot in the plots represents an individual mouse. All data are presented as average ± s.d. Statistical significance based on one-way ANOVA followed by Tukey's HSD post hoc test (*$p < 0.05$, **$p < 0.01$, ***$p < 0.001$, and ****$p < 0.0001$).

resulted in higher stiffness but also resulted in a significant loss of degradability (Figure S5A, Supporting Information). In fact, the degree of cell spreading through local degradation is reduced for cells encapsulated in 10 wt% degradable gel (Figure S5B, Supporting Information), which contrasts with increasing spread cell morphology on a stiffer 2D substrate.[34] In our system, the crosslinking density of the stiffer microgel building blocks was increased to achieve a storage modulus of 2500 Pa while maintaining RGD concentration (StN1) such that the effect of stiffness could be investigated independently from degradability or adhesive ligand concentration. Importantly, due to in situ assembly of cells into micropores formed within the annealed MAP scaffolds, increasing the stiffness of hydrogel building blocks did not result in changes in confinement of cells. To investigate the effect of cell binding motif concentration, the RGD concentration within the stiff non-enzymatically degradable hydrogel formulation was increased fivefold (StN5), without changing the storage modulus (Figure S6A, Supporting Information). Although these four distinctive compositions (SoN1, StN1, StN5, SoD1; Figure 3A) had different swelling ratios in an aqueous buffer, we used microfluidic droplet generation to tune the pre-swollen building block size, such that each microgel type was similar in size after swelling (Figure S6B, Supporting Information). This was important to preserve the microporous structure of the MAP scaffolds and decouple potential effects of material properties from microporosity. By manufacturing microgel particles with well-controlled material properties we could create MAP scaffolds with orthogonally controlled properties to study the effect of microenvironmental cues on stem cells.

Indeed, all three material properties tested affected in vitro MSC proliferation (Figure 3B). SoD1 showed a higher expansion rate than SoN1, indicating that material degradability plays a role when material stiffness is low. Stiff gel building blocks also led to higher proliferation, which is in agreement with previous work that indicated that MSCs spread more and proliferate more readily on stiffer 2D substrates.[24,35] MSC expansion was further enhanced on these stiff scaffolds by incorporating higher RGD concentration. For the enzymatically non-degradable gel conditions, more RGD sites on the surface may be beneficial to promote growth as cells have more difficulty in degrading and revealing new RGD binding sites. In fact, StN5 was observed to promote slightly larger actin spread area per cell than StN1, indicating that the high RGD enhanced binding of cells to the substrate and spreading (Figure 3C,D).

To investigate the in vivo response to the four types of MAP scaffolds, MSCs expressing GFP (GFP-MSCs) were subcutaneously injected in C57BL/6 mice along with the different hydrogel formulations and scaffolds were excised two weeks after implantation. Since MSCs expresses the stem cell marker CD29,[36,37] we examined whether GFP-MSCs retaining CD29, and any recruited myeloid cells were present within the different MAP scaffolds. In all MAP scaffolds, injected MSCs were identified by the colocalization of CD29 and GFP (Figure 3E) and negative staining for CD11b. The number of cells with CD29 staining in the scaffold were counted to calculate the density and fraction of cells retaining stem cell markers (Figure S7, Supporting Information). The density of $CD29^+$ cells was the highest in StN5 scaffolds (Figure 3F), corresponding to the results of our in vitro cell proliferation experiments. The lower in vivo preservation of MSCs in SoD1, degradable gels, than in vitro may be due to the degradable formulation losing physical integrity more rapidly once implanted and exposed to proteases. Stiffer gels also resulted in $CD29^+$ cells occupying a larger fraction of the total cells present in scaffolds (Figure 3G). For the highest performing scaffold, StN5, we also observed GFP-producing MSCs in tissue cross-sections after subcutaneous implantation for a longer time period of 56 days (Figure S8, Supporting Information). Among cells extensively occupying the scaffold, GFP-positive cells that survived for two months were identified. Over this two month period, the scaffold also maintained an interconnected porous structure without significant degradation. The intensity of fluorophores conjugated to the gels did not significantly change from day 14 to day 56 (Figure S9, Supporting Information), indicating that the gel matrix or fluorophores were not degraded. Therefore, the scaffold is expected to maintain its physical properties for 56 days. Overall, the stiffer gels with higher RGD (StN5) retained the implanted stem cell population at higher levels compared to other formulations, and cells and scaffold were both maintained up to 56 days after implantation.

Microporosity of the implanted MSC-containing MAP scaffolds also induced cell migration, in-growth of host tissue, and vascularization important for improved clinical function. The integration of the MAP scaffolds was evaluated by the number of cells near the boundary between the surrounding tissue and MAP scaffold (**Figure 4**A,B). The density of cells within a 200 µm region outside of and neighboring the scaffold was about 1580 cells mm^{-2}. Within a region ≈100 µm deep into the scaffold boundary, the cell density was similar to the surrounding tissue, indicating that all four types of MAP scaffolds integrated well with the tissue. Cell density gradually decreased in all MAP scaffolds up to a distance of 1.5 mm, with SoN1 showing the lowest cell density in the scaffold core. The other formulations remained cellular (≈500 cells mm^{-2}) throughout the scaffold, even at depths of 1.5 mm from the implant interface. This value is above the initial seeding density (≈125 cells mm^{-2} given that the tissue sectioning was ≈25 µm in thickness). Since MSC retention cannot account for the increase in cell numbers and MSCs produce factors that recruit other cell types,[38] this indicates that MAP scaffolds likely induced the migration of endogenous cells deep into the scaffold and maintained these cells over weeks overcoming transport limitations of conventional hydrogels. The SoD1 formulation resulted in a greater number of cells in the periphery of the scaffold, suggesting more cell migration and tissue ingrowth into the scaffold corresponding to scaffold degradation over time.

Next, we examined the recruitment of specific cell types into the different formulations of MAP hydrogel. Since MSCs produce factors that actively recruit myeloid cells,[39] we examined whether modulating different hydrogel parameters resulted in a differential ability for MSCs to attract myeloid cells. Indeed, MSCs implanted in all of the hydrogel scaffolds recruited CD11b myeloid cells, without significant differences between the different formulations (Figure S10, Supporting Information). While biomaterial-induced immune responses often lead to foreign body encapsulation,[40] we examined the location of the $CD11b^+$ cells and whether they were forming multinucleated/fused cells consistent with foreign body encapsulation. While the majority of the $CD11b^+$ myeloid cells were present within the peripheral aspects of the hydrogel, neither multinucleation nor encapsulation were evident to any of the formulations. These findings suggest that the scaffold-MSC implants were similarly able to recruit myeloid cells, without resulting in a foreign body response that often results in material rejection.

Since we observed blood vessel structures within subcutaneously implanted MAP scaffolds without MSCs (Figure S4, Supporting Information), we next wished to evaluate whether different formulations of MAP scaffolds with MSCs resulted in differential formation of blood vessels by examining the endothelial cell markers (PECAM-1). Indeed, we found cells expressing PECAM-1 within all four types of MAP scaffolds (Figure 4C). There were significantly higher numbers of PECAM-1-expressing cells within StN1, StN5, and SoD1 scaffolds compared to the SoN1 scaffolds (Figure 4D,E), which may correspond to the ability of these same scaffolds to retain the injected $CD29^+$ cells at higher levels as MSCs present in the scaffold may secrete angiogenic factors such as vascular endothelial growth factor (VEGF).[41,42]

The application of stem cell-based therapies has been limited by low retention rate of transplanted cells and lack of efficient control of the cell state and function. Biomaterial-enhanced delivery of stem cell therapies offers a potential solution to overcome this, but nonporous or nanoporous materials do not allow for sufficient incorporation of cells into the hydrogel, requiring significant degradation for cell proliferation and migration, and yielding low transport of nutrients which may limit incorporated cell survival. Void forming hydrogels

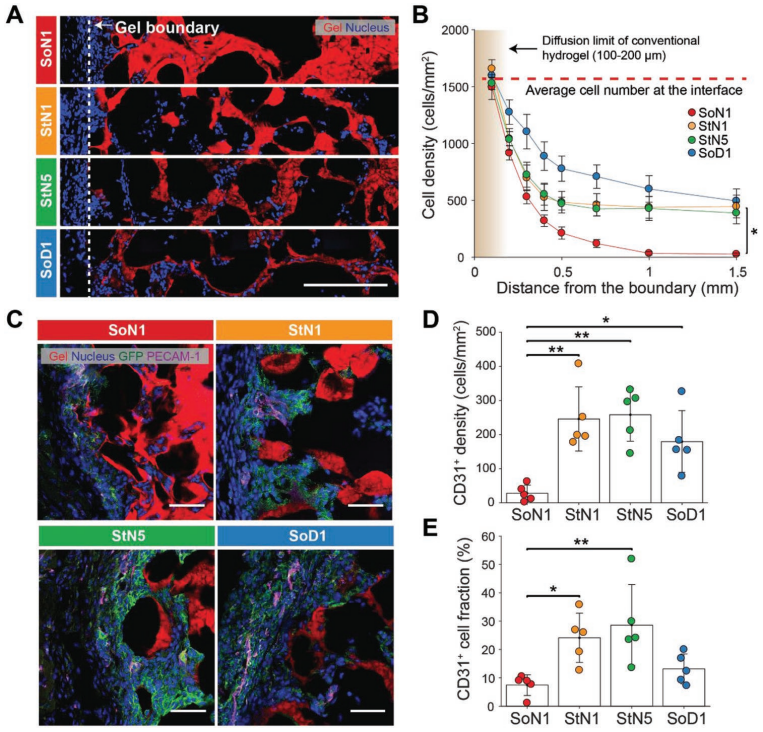

Figure 4. Tissue ingrowth and vascularization into microparticle scaffolds. A) Representative images of tissue slices following two weeks of implantation of MSCs with corresponding building block materials. The dotted line indicates a boundary with the surrounding tissue. Scale bar: 200 µm. B) Number of cells per area as a function of the distance from the interface between the MAP scaffold and the tissue (n = 5). Data presented as average ± s.e.m. Statistical significance performed using one-way ANOVA with a Dunnett post hoc multiple comparison test (*p < 0.05). C) Representative images of platelet endothelial cell adhesion molecule (PECAM-1) and GFP immunostaining of the scaffolds following two weeks indicating the presence of implanted GFP-MSCs and endothelial cells growing in from surrounding tissue. Scale bar: 50 µm. D) CD31$^+$ cells per area in scaffolds at week 2 (n = 5). E) Ratio of CD31+ cells to all cells in the scaffolds at week 2 (n = 5). Each dot in the plots in (D,E) represents an individual mouse. Data are presented as average ± s.d. Statistical significance based on one-way ANOVA followed by Tukey's HSD post hoc test (*p < 0.05 and **p < 0.01).

offer an advantage, as they provide a scaffold that can be rapidly degraded while cells proliferate and expand. However, these hydrogels require the cellular therapeutics to be populated into the scaffold during manufacture, representing a major hurdle to their use as this could affect stem cell function, viability, and long-term storage, requiring great care during manufacture and deployment,[19] ultimately resulting in higher costs for therapies. This study demonstrates increased in vivo maintenance of mesenchymal stem cells co-injected with a modular microporous scaffold made through the in situ crosslinking of flowable monodisperse hydrogel particles. The stem cells can be mixed with hydrogel particle building blocks immediately before injection/deployment, decoupling the manufacturing of scaffolds from the culture of therapeutic cells. Assemblies of spherical hydrogel building blocks created interconnected microscale void spaces which enhanced nutrient transport, and promoted cell migration and cell-cell connections, inducing more than ≈7-times higher proliferation than chemically identical nonporous hydrogels in vitro and ≈3-times enhanced half-life of MSCs in a subcutaneous murine implantation model. Furthermore, the possibility of independent modulation of material properties of the building blocks, including stiffness and adhesive ligand composition, can be performed with different cell types, allowing tuning of conditions appropriate for many different populations of therapeutic cells for specific downstream applications in vivo (e.g., delivery to heart, bone, skin, nerves, etc.). MSCs represent a promising therapeutic cell population for tissue/organ regeneration, with local therapy showing some positive effects in human disease.[43] Deployment of a high concentration of MSCs within a regenerative scaffold material immediately before delivery to tissue may improve their efficacy and overcome a manufacturing hurdle of other scaffold materials that require stem cells to be incorporated during scaffold synthesis. Overall, we show that cell delivery in conjunction with an in situ-formed microporous niche promotes the survival of delivered cells and should enhance cell therapies in regenerative medicine and immunologic applications.

Experimental Section

Microfluidic Device Fabrication: Microfluidic devices were fabricated using soft lithography as previously described.[20] Briefly, master molds were fabricated on mechanical grade silicon wafers (University wafer) using KMPR 1050 photoresist (Microchem). Devices were molded from the masters using poly(dimethyl)siloxane (PDMS) Sylgard 184 kit (Dow Corning). The base and crosslinker were mixed at a 10:1 mass ratio, poured over the mold, and degassed prior to curing for overnight at 65 °C. Channels were sealed by treating the PDMS mold and a glass microscope slide (VWR) with oxygen plasma at 500 mTorr and 80 W for 30 s. The channels were functionalized by injecting 100 µL of Aquapel (88 625-47 100, Aquapel) and reacting for 30 s until washed by Novec 7500 (9 802 122 937, 3M). The channels were dried by air suction and kept in the oven at 65 °C until used.

Microgel Production: Monodisperse microgels were produced as follows. Two aqueous solutions were prepared: i) 4 Arm-PEG VS MW 20000 (PTE-200VS, NOF) at 8%, 10%, 20%, and 24% (w/v) in 0.3 M triethyloamine (TEOA) pH 8.25, pre-reacted with K-peptide (Ac-FKGGERCG-NH2), Q-peptide (Ac-NQEQVSPLGGERCG-NH2) at a final concentration of 250×10^{-6} M and with RGD peptide (Ac-RGDSPGERCG-NH2) at a final concentration of 500×10^{-6} M or 2.5×10^{-3} M and ii) an 8×10^{-3} M di-cysteine modified Matrix Metalloprotease (MMP) (Ac-GCRDGPQGIWGQDRCG-NH2) (Genscript) or 6×10^{-3}, 18×10^{-3}, or 20×10^{-3} M poly(ethylene glycol) dithiol MW 1000 (717 142-1G, Sigma-Aldrich) pre-reacted with 10×10^{-6} M Alexa-fluor 488 or 568-maleimide (Life Technologies). Please see the Table S1 (Supporting Information) for the composition according to MAP gel types. These pre-gel solutions were sterile-filtered through a 0.2 µm polyethersulfone (PES) membrane in a leur-lok syringe filter, injected into the microfluidic device and pinched off by oil phase (0.1% Pico-Surf in Novec 7500, SF-000149, Sphere Fluidics) (Figure S1A, Supporting Information). The flow rate for aqueous solutions was 1–12 µL min^{-1} and for oil solutions was 4–400 µL min^{-1} to fine-tune the size of droplets (Figure S1B, Supporting Information). Gels were collected from the device into a tube in oil phase, incubated overnight at room temperature in dark. Microgels in oil phase were vortexed with 20% 1H,1H,2H,2H-Perfluoro-1-octanol (PFO) (370 533-25G, Sigma-Aldrich) in Novec 7500 for 10 s. Microgels were then mixed with 1:1 mixture of HEPES buffer (100×10^{-3} M HEPES, 40×10^{-3} M NaCl pH 7.4) and hexane followed by centrifugation at 10 000 rpm to separate microgels from oil for five times. Microgels were incubated in sterile-filtered 70% ethanol solution at 4 °C at least overnight for sterilization. Before in vivo or in vitro experiment, microgels were washed with HEPES buffer with 10×10^{-3} M $CaCl_2$ for five times.

Annealing of Microgels: Equal volumes of two microgel solutions were incubated in HEPES-buffered saline (pH 7.4) containing FXIII (10 U mL^{-1}) or thrombin (2 U mL^{-1}) respectively at 4 °C overnight. The two solutions were centrifuged at 10 000 rpm for 5 min and supernatants were removed to concentrate the microgels. These concentrated solutions were thoroughly mixed with each other by pipetting up and down, pipetted into a desired location and kept at 37 °C for 90 min to anneal the microgels into a MAP scaffold.

Rheology Techniques for Measuring the Storage Modulus of MAP Building Blocks: The storage modulus of an 8 mm disc gel was measured using an Anton paar physica mcr 301 Rheometer. 40 µL of pre-gel solutions (20 µL of PEG with peptides, 20 µL of crosslinker) were pipetted onto sterile siliconized (Sigmacote; SL2-25ML, Sigma-Aldrich) slide glass, covered with another glass with 1 mm spacer and incubated at 37 °C for 2 h. Disc gels were swollen to equilibrium in PBS overnight before being measured. An amplitude sweep (0.01–10% strain) was performed to find the linear amplitude range for each. An amplitude within the linear range was chosen to run a frequency sweep (0.5–5 Hz). At least, four disc-gels were measure for each condition.

Diffusion Measurement using Photobleaching in MAP Scaffold: MAP gels were incubated with 100×10^{-6} M 70 kDa dextran-FITC (FD70S-100MG, Sigma-Aldrich) solution in PBS or a 100×10^{-9} M fluorescein solution in PBS. 20 µL of microgels were pipetted and annealed in a 3 mm diameter PDMS well on a glass coverslip to form a MAP scaffold. Fluorescence recovery after photobleaching was conducted using a Leica TCS SP5 confocal microscope. A 20× dry objective and argon laser were used for bleaching and imaging. For pore diffusivity measurements, bleaching was performed with 30% laser power and 100% transmission, with imaging at 15% transmission to limit additional bleaching. For the single-phase bleaching measurements in nonporous hydrogel and PBS, 70% laser power and 100% transmission were used for bleaching, with 6% transmission used for imaging. After bleaching for 8 s, at least 50 images were taken with the interval of 390 ms (Figure S2, Supporting Information). A circle of 100 µm diameter centered on the bleach spot was taken as the analysis region of interest (ROI) in all cases using ImageJ. The diffusivity was calculated via the approach of Soumpasis[44] Equation (1)

$$D = \frac{0.224w^2}{t_{1/2}} \tag{1}$$

where w is the ROI radius, $t_{1/2}$ is the halftime calculated by fitting the mean intensity of the ROI in time to an exponential Equation (2)

$$F(t) = a + \frac{b}{2^{t/t_{1/2}}} \tag{2}$$

where a and b were obtained from the fitted curve.

Diffusion Measurement in Nonporous Hydrogel using Fluorescent Intensity Profile: 8 mm disc gels were prepared as previously described in the rheology technique section. Gels were swollen in PBS overnight and placed between two slide glasses in PBS with 100×10^{-6} M 70 kDa dextran-FITC (FD70S-100MG, Sigma-Aldrich). The fluorescent images of gels (FITC) were taken every day and the intensity profiles over time were used to calculate the diffusivity using Fick's law.

Gel Degradation Experiment: 10 µL of pre-gel solutions (5 µL of PEG with peptides, 5 µL of crosslinker pre-reacted with 10×10^{-6} M Alexa-fluor 488-maleimide) were pipetted onto sterile siliconized (Sigmacote; SL2-25ML, Sigma-Aldrich) slide glass, covered with another glass with 1 mm spacer and incubated at 37 °C for 2 h. The final concentrations of PEG and crosslinkers were 5 wt% 4-Arm PEG-VS with 4×10^{-3} M PEG-dithiol (5%ND), 5 wt% 4-Arm PEG-VS with 4×10^{-3} M MMP-cleavable dithiol (5%D) and 10 wt% 4-Arm PEG-VS with 8×10^{-3} M MMP-cleavable dithiol (10%D). Gels were swollen to equilibrium in PBS overnight before being transferred to a 24-well insert with fluorescent-blocking membrane (08-772-147, Fisher Scientific); one gel per a well. The insert was inserted into a 24 well-plate with 1 mL of 1% TryPLE (12 604 013, Gibco) in PBS. The fluorescent level at the bottom of the plate was measured by the plate-reader (BioTek Cytation5) at 37 °C for 12 h.

Hydraulic Conductivity Measurement in the Scaffold: A custom-designed device was designed using Autodesk Inventor 3D CAD software, and printed in Watershed XC 11 122 Normal-Resolution Stereolithography build in 0.004" layers from Proto Labs, Inc. (Figure S3, Supporting Information). For the MAP scaffold, 25 µL of microgel building blocks (5 wt% crosslinked with MMP-cleavable dithiol) was casted on top of a 5 µm pore size cellulose membrane (SMWP01300, Fisher Scientific) in the bottom plane of the device and annealed followed by the overnight incubation in PBS. For the nonporous scaffold, 10 µL of pre-gel solution (5 wt% PEG with 4×10^{-3} M MMP-cleavable dithiol) was casted on top of the membrane in the device and incubated at 37 °C for 2 h followed by the overnight incubation in PBS. Then 1 mL of PBS with blue food dye was injected into the device and the permeated volume over time was measured. The hydraulic conductivity was calculated based on Darcy's law[45]

$$k = \frac{aL}{AT} \times \ln\left(\frac{h_1}{h_2}\right) \tag{3}$$

where, a is the inner cross-sectional area of the graduated tube (cm^2), L is the test sample thickness (cm), A is the test sample cross-sectional area (cm^2). T is the time elapsed between the initial head and the final head (s), h_1 is the initial head across the test specimen (cm), and h_2 is the final head across the test specimen (cm).

Mesenchymal Stem Cell Culture in Flasks: Strain C57BL/6 Mouse Mesenchymal Stem Cells with RFP (MUBMX-0 1201, Cyagen

Biosciences) and strain C57BL/6 Mouse Mesenchymal Stem Cells with GFP (MUBMX-0 1101, Cyagen Biosciences) were maintained in Mouse Mesenchymal Stem Cell Growth Medium (MUXMX-90 011, Cyagen Biosciences) according to manufacturer's specifications to retain stemness. Cells between passages 4–6 were used. Cells were maintained at lower than 80% confluency in culture.

Mesenchymal Stem Cell In Vitro Culture on the MAP Scaffold: MSCs labelled with RFP (MUBMX-0 1201, Cyagen Biosciences) were dissociated by trypsin and centrifuged down to remove medium. 60 µL of MAP in HEPES-buffered saline (pH 7.4) containing FXIII (10 U mL^{-1}) and 10×10^{-3} M $CaCl_2$ was combined as mixed thoroughly with 60 µL of MAP microgel building blocks in HEPES-buffered saline (pH 7.4) containing thrombin (2 U mL^{-1}) with a positive displacement pipette (MICROMAN, Gilson, Inc.). Cells were resuspended and spiked in MAP building blocks at 1000 cells μL^{-1} concentration. These MAP gels were kept on ice to prevent annealing as well as maintaining the MSC viability. 20 µL of MAP gels with MSCs at 1000 cells μL^{-1} was pipetted into silicone isolators (GBL664206-25EA, Sigma-Aldrich) in a tissue culture plate (08-772-50, Thermo Fisher Scientific) and incubated for 90 min at 37 °C followed by adding a complete cell culture medium. Cells were grown in 5% CO_2 and 37 °C and 1 mL of medium was changed every 3–4 days. The fluorescent intensity from RFP was detected using a plate-reader (BioTek Cytation5). In each sample, at least 6 points of RFP intensity were measured (Ex: 545, Em: 605) using the area scanning function. At day 14, samples were gently washed with PBS twice, fixed with 4% PFA overnight at 4 °C followed by Hoechst (1/500) (Thermo Fisher Scientific) and phalloidin 647 (1/500) (Thermo Fisher Scientific) staining at room temperature for 4 h. Then the scaffolds were gently washed twice with PBS and kept at 4 °C until imaged.

Mesenchymal Stem Cell In Vitro Culture on the Nonporous Scaffold: PEG-VS scaffolds (5 wt% $r = 0.8$ MMP-1 crosslinker, 250×10^{-6} M K, 250×10^{-6} M Q, 500×10^{-6} M RGD) were used to encapsulate MSCs (1000 cells μL^{-1}). Gels were formed for 15 min (TEOA 0.3M, pH 8.25) before being placed into appropriate media. The fluorescent intensity detection and staining was performed as for MAP scaffold in vitro experiments.

In Vivo Imaging System (IVIS) Experiments: Strain C57BL/6J mice (The Jackson Laboratory) were anesthetized using continuous application of aerosolized isofluorane (3 vol%) throughout the duration of the procedure. 60 µL of MAP in HEPES-buffered saline (pH 7.4) containing FXIII (10 U mL^{-1}) and 10×10^{-3} M CaCl2 was combined as mixed thoroughly with 60 µL of MAP building blocks in HEPES-buffered saline (pH 7.4) containing thrombin (2 U mL^{-1}) with a positive displacement pipette (MICROMAN, Gilson, Inc.). 100 µL of MAP building blocks with one million MSCs expressing RFP (MUBMX-0 1201, Cyagen Biosciences) was injected subcutaneously into mice via 25-gauge needles. As controls, 100 µL of PBS with one million MSCs expressing RFP and 40 µL of pre-gel solution (5 wt% PEG with 4×10^{-3} M MMP-cleavable dithiol, swelling ratio 2.5) with one million MSCs expressing RFP were injected using the same method. Two injection sites on opposing sides of the back per mouse were used to avoid potential signal overlap during imaging. To monitor cell viability and distribution, the RFP fluorescence was measured using a Perkin Elmer IVIS Lumina II on days 0, 2, 5, 7, 10, and 14. Before imaging, mice were anesthetized with 3% isofluorane/air. For each image acquisition, a gray scale body surface image was collected, followed by an overlay of the fluorescent (Ex: 535, Em: 600) and their radiant efficiency were quantified using Living Image software (Caliper LifeSciences). All animal experiments were performed according to established animal protocols.

Subcutaneous MSC Injection Model: Strain C57BL/6J mice (The Jackson Laboratory) were anesthetized using continuous application of aerosolized isofluorane (3 vol%) throughout the duration of the procedure. 60 µL of MAP in HEPES-buffered saline (pH 7.4) containing FXIII (10 U mL^{-1}) and 10×10^{-3} M $CaCl_2$ was combined as mixed thoroughly with 60 µL of MAP building blocks in HEPES-buffered saline (pH 7.4) containing thrombin (2 U mL^{-1}) with a positive displacement pipette (MICROMAN, Gilson, Inc.). 2.4 µL of MSC suspension was then added and mixed thoroughly. 100 µL of MAP building blocks with MSC GFP (MUBMX-0 1101, Cyagen Biosciences) at 5000 cells μL^{-1} was injected subcutaneously into mice via 25-gauge needles. Four injection sites on the back per mouse were used to accommodate all four test conditions (SoD1, SoN1, StN1, and StN5). Mice were sacrificed at week 2 and MAP scaffolds were excised and immediately fixed in 4% PFA for 2 h before flash frozen in OCT compound (Tissue-Tek). These OCT tissue blocks were kept at -80 °C until sectioned at 25 µm thickness using cryostat (Leica CM1950) and collected onto 25 × 75 mm charged slides (1358W, Globe Scientific). Sections were dried at room temperature overnight and kept at −20 °C until stained. All animal experiments were performed according to established animal protocols.

Tissue Section Immunofluorescence: Slides containing tissue sections were washed and blocked using 10% normal goat serum (50062Z, Invitrogen) for 2 h at room temperature and then stained with primary antibodies overnight at 4 °C. Primary antibody dilutions were prepared as in the Table S2 (Supporting Information). Sections were incubated in secondary antibodies with 1/500 diluted Hoechst for 2 h at room temperature, and subsequently washed with PBS. Secondary antibody dilutions were prepared as in the Table S2 (Supporting Information). Sections were mounted in Antifade Gold mounting medium (9071S, Cell Signaling Technology) and imaged using Leica Confocal SP-5 with 63× water immersion objective lens or Nikon Ti Eclipse with 10× objective lens.

Computational Analysis of Tissue Images: Images were analyzed using a MATLAB code. Briefly, the code defines the region of an injected MAP scaffold region using the TRITC channel. It divides the region into two: a periphery region of interest (ROI) (200 µm into and out of the scaffold) and core ROI (inside of the periphery region) (Figure S7, Supporting Information). For ROI regions, the code reads the Cy5 channel intensity profiles and defines regions of protein expression using a threshold (identical for all sample images). The ratio of cells with protein expression was calculated by the ratio of cells having a nuclear stain also in the protein expression region for each ROI. The density of cells was calculated by the total number of cells under the protein expression mask divided by the area of the ROI. The cell density as a function of the distance from the interface was calculated by counting the number of cells in a subregion of the scaffold that was divided by distance (Figure S7E, Supporting Information). It was verified that the quantification by this method was insensitive to imaging conditions: exposure time and number of scans, although the imaging condition was kept same for all samples (Figure S11, Supporting Information). Tissue slice areas with physical defects from imperfect tissue sectioning were excluded manually in the analysis.

Ethics Statement: The mouse studies described in this manuscript were performed under the written approval of the UCLA Animal Research Committee (ARC) in accordance to all federal, state, and local guidelines. All studies were carried out under strict accordance to the guidelines in The Guide for the Care and Use of Laboratory Animals of the National Institutes of Health and the accreditation and guidelines of the Association for the Assessment and Accreditation of Laboratory Animal Care (AALAC). The protocol/permit/project license number assigned by the IACUC/ethics committee that approved under UCLA ARC Protocol Number 2010-011-31. All injections were performed under isofluorane anesthesia and all efforts were made to minimize animal pain and discomfort.

Statistical Analysis: All values are depicted as mean ± standard deviation unless stated. Statistical comparisons were performed using GraphPad Prism 8.0 or MATLAB version R2016b (MathWorks, Inc.). The significance between two groups was analyzed by a two-tailed Student *t*-test. The significance between multiple groups was analyzed by a one-way ANOVA. Values were considered to be significantly different when $p < 0.05$.

Supporting Information

Supporting Information is available from the Wiley Online Library or from the author.

Acknowledgements

This work was supported by the Presidential Early Career Award for Scientists and Engineers (N00014-16-1-2997). J.K. was supported by the Kwanjeong Educational Foundation, Korea. P.O.S. was supported by the Mentored Clinical Scientist Development Award (K08-AR066545) through NIAMS. M.A. was supported by NIH NIGMS training grant (GM008042). The authors would like to thank Weikun Xiao and Dr. Stephanie Seidlits for technical assistance and comments, Dr. Jason Lee at the Crump Institute in California NanoSystems Institute (CNSI) for discussions and assistant for IVIS, Dr. Matt Schibler and Dr. Laurent Bentolila at Advanced Light Microscopy/Spectroscopy in CNSI for confocal imaging consultation, Dr. Westbrook Weaver, Joseph de Rutte, Dr. Maria Antfolk and Wei Yang for helpful discussions. J.K., D.R.G., T.S., P.O.S., and D.D.C. conceived the study and designed the experiment. J.K., M.A. performed in vitro studies, J.K., D.R.G., A.F., P.O.S. performed in vivo studies. J.K., T.H., M.M., D.Z. characterized the MAP scaffold. J.K. designed and fabricated the microfluidic device. J.K., D.D.C. analyzed and interpreted the data. J.K., P.O.S. and D.D.C. wrote the manuscript with input from all the authors.

Note: An error in ref. [24] was corrected on September 25, 2019 after initial online publication.

Conflict of Interest

The authors have a financial interest in Tempo Therapeutics, which aims to commercialize MAP technology.

Keywords

hydrogel microparticles, injectable microporous scaffolds, microfluidics, stem cell delivery, tissue engineering

Received: June 18, 2019
Revised: July 25, 2019
Published online: August 13, 2019

[1] B. Parekkadan, J. M. Milwid, *Annu. Rev. Biomed. Eng.* **2010**, *12*, 87.
[2] A. Trounson, C. McDonald, *Cell Stem Cell* **2015**, *17*, 11.
[3] C. Tran, M. S. Damaser, *Adv. Drug Delivery Rev.* **2015**, *82–83*, 1.
[4] J. Ankrum, J. M. Karp, *Trends Mol. Med.* **2010**, *16*, 203.
[5] J. Galipeau, L. Sensébé, *Cell Stem Cell* **2018**, *22*, 824.
[6] P. J. Mishra, D. Banerjee, *Methods Mol. Biol.* **2017**, *1554*, 201.
[7] E. Eggenhofer, V. Benseler, A. Kroemer, F. C. Popp, E. K. Geissler, H. J. Schlitt, C. C. Baan, M. H. Dahlke, M. J. Hoogduijn, *Front. Immunol.* **2012**, *3*, 1.
[8] J. S. Elman, R. M. Murray, F. Wang, K. Shen, S. Gao, K. E. Conway, M. L. Yarmush, B. A. Tannous, R. Weissleder, B. Parekkadan, *PLoS One* **2014**, *9*, e89882.
[9] S. H. Ranganath, O. Levy, M. S. Inamdar, J. M. Karp, *Cell Stem Cell* **2012**, *10*, 244.
[10] C. M. Madl, S. C. Heilshorn, H. M. Blau, *Nature* **2018**, *557*, 335.
[11] J. A. Burdick, R. L. Mauck, S. Gerecht, *Cell Stem Cell* **2016**, *18*, 13.
[12] S. W. Lane, D. a Williams, F. M. Watt, *Nat. Biotechnol.* **2014**, *32*, 795.
[13] L. Cai, R. E. Dewi, S. C. Heilshorn, *Adv. Funct. Mater.* **2015**, *25*, 1344.
[14] N. Mitrousis, A. Fokina, M. S. Shoichet, *Nat. Rev. Mater.* **2018**, *3*, 441.
[15] R. Dimatteo, N. J. Darling, T. Segura, *Adv. Drug Delivery Rev.* **2018**, *127*, 167.
[16] J. W. Shin, D. J. Mooney, *Cell Stem Cell* **2016**, *18*, 16.
[17] M. P. Lutolf, P. M. Gilbert, H. M. Blau, *Nature* **2009**, *462*, 433.
[18] X. Tong, F. Yang, *Adv. Healthcare Mater.* **2018**, *7*, 1701065.
[19] N. Huebsch, E. Lippens, K. Lee, M. Mehta, S. T. Koshy, M. C. Darnell, R. Desai, C. M. Madl, M. Xu, X. Zhao, O. Chaudhuri, C. Verbeke, W. S. Kim, K. Alim, *Nat. Mater.* **2015**, *14*, 1269.
[20] D. R. Griffin, W. M. Weaver, P. O. Scumpia, D. Di Carlo, T. Segura, *Nat. Mater.* **2015**, *14*, 737.
[21] E. Sideris, D. R. Griffin, Y. Ding, S. Li, W. M. Weaver, D. Di Carlo, T. Hsiai, T. Segura, *ACS Biomater. Sci. Eng.* **2016**, *2*, 2034.
[22] L. R. Nih, E. Sideris, S. T. Carmichael, T. Segura, *Adv. Mater.* **2017**, *29*, 1606471.
[23] N. J. Darling, E. Sideris, N. Hamada, S. T. Carmichael, T. Segura, *Adv. Sci.* **2018**, *5*, 1801046.
[24] J. M. de Rutte, J. Koh, D. Di Carlo, *Adv. Funct. Mater.* **2019**, *29*, 1900071.
[25] A. S. Caldwell, G. T. Campbell, K. M. T. Shekiro, K. S. Anseth, *Adv. Healthcare Mater.* **2017**, *6*, 1.
[26] N. N. Kumar, M. Gautam, J. J. Lochhead, D. J. Wolak, V. Ithapu, V. Singh, R. G. Thorne, *Sci. Rep.* **2016**, *6*, 1.
[27] J. Li, D. J. Mooney, *Nat. Rev. Mater.* **2016**, *1*, 16071.
[28] A. P. Wong, R. Perez-Castillejos, J. Christopher Love, G. M. Whitesides, *Biomaterials* **2008**, *29*, 1853.
[29] A. Wood, *Biocontrol Sci. Technol.* **2006**, *16*, 495.
[30] A. Sannino, P. A. Netti, M. Madaghiele, V. Coccoli, A. Luciani, A. Maffezzoli, L. Nicolais, *J. Biomed. Mater. Res., Part A* **2006**, *79A*, 229.
[31] A. J. Keung, S. Kumar, D. V. Schaffer, *Annu. Rev. Cell Dev. Biol.* **2010**, *26*, 533.
[32] Y. Sun, C. S. Chen, J. Fu, *Annu. Rev. Biophys.* **2012**, *41*, 519.
[33] F. Gattazzo, A. Urciuolo, P. Bonaldo, *Biochim. Biophys. Acta, Gen. Subj.* **2014**, *1840*, 2506.
[34] M. Guo, A. F. Pegoraro, A. Mao, E. H. Zhou, P. R. Arany, Y. Han, D. T. Burnette, M. H. Jensen, K. E. Kasza, J. R. Moore, F. C. Mackintosh, J. J. Fredberg, D. J. Mooney, J. Lippincott-Schwartz, D. A. Weitz, *Proc. Natl. Acad. Sci. USA* **2017**, *c*, 201705179.
[35] J. Lee, A. A. Abdeen, K. A. Kilian, *Sci. Rep.* **2014**, *4*, 20.
[36] S. Ma, N. Xie, W. Li, B. Yuan, Y. Shi, Y. Wang, *Cell Death Differ.* **2014**, *21*, 216.
[37] M. Jurewicz, S. Yang, A. Augello, J. G. Godwin, R. F. Moore, J. Azzi, P. Fiorina, M. Atkinson, M. H. Sayegh, R. Abdi, *Diabetes* **2010**, *59*, 3139.
[38] L. da Silva Meirelles, A. M. Fontes, D. T. Covas, A. I. Caplan, *Cytokine Growth Factor Rev.* **2009**, *20*, 419.
[39] R. Romieu-Mourez, M. Francois, M.-N. Boivin, M. Bouchentouf, D. E. Spaner, J. Galipeau, *J. Immunol.* **2009**, *182*, 7963.
[40] O. Veiseh, J. C. Doloff, M. Ma, A. J. Vegas, H. H. Tam, A. R. Bader, J. Li, E. Langan, J. Wyckoff, W. S. Loo, S. Jhunjhunwala, A. Chiu, S. Siebert, K. Tang, J. Hollister-Lock, S. Aresta-Dasilva, M. Bochenek, J. Mendoza-Elias, Y. Wang, M. Qi, D. M. Lavin, M. Chen, N. Dholakia, R. Thakrar, I. Lacík, G. C. Weir, J. Oberholzer, D. L. Greiner, R. Langer, D. G. Anderson, *Nat. Mater.* **2015**, *14*, 643.
[41] K. C. Rustad, V. W. Wong, M. Sorkin, J. P. Glotzbach, M. R. Major, J. Rajadas, M. T. Longaker, G. C. Gurtner, *Biomaterials* **2012**, *33*, 80.
[42] J. S. Kim, Y. Jung, S. H. Kim, J. S. Shin, S. H. Kim, C. G. Park, *Xenotransplantation* **2019**, *26*, 1.
[43] Z. Chen, L. Chen, C. Zeng, W. E. Wang, *Stem Cells Int.* **2018**, *2018*, 7045245.
[44] D. M. Soumpasis, *Biophys. J.* **1983**, *41*, 95.
[45] M. Aboufoul, A. Garcia, *Mater. Struct.* **2017**, *50*, 1.

APPENDIX F

IL-10 Signaling Remodels Adipose Chromatin Architecture to Limit Thermogenesis and Energy Expenditure

Article

Cell

IL-10 Signaling Remodels Adipose Chromatin Architecture to Limit Thermogenesis and Energy Expenditure

Graphical Abstract

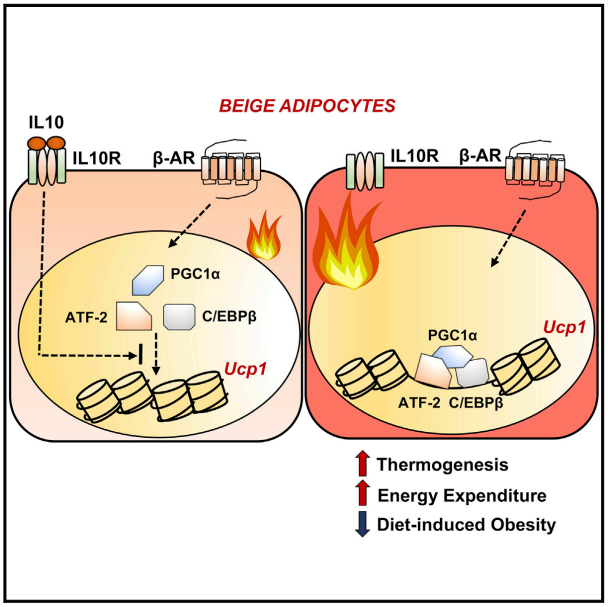

Authors

Prashant Rajbhandari, Brandon J. Thomas, An-Chieh Feng, ..., Karen Reue, Stephen T. Smale, Peter Tontonoz

Correspondence

ptontonoz@mednet.ucla.edu

In Brief

An anti-inflammatory cytokine suppresses adipocyte thermogenesis to limit energy expenditure.

Highlights

- Mice lacking IL-10 have increased energy expenditure and adipose thermogenesis
- IL-10 acts on IL-10Rα in adipose tissue to antagonize adrenergic tone
- IL-10Rα knockdown promotes the browning of subcutaneous white adipose tissue
- IL-10 affects chromatin structure and C/EBPβ and ATF occupancy at thermogenic genes

Rajbhandari et al., 2018, Cell *172*, 218–233
January 11, 2018
https://doi.org/10.1016/j.cell.2017.11.019

CellPress

Cell

Article

IL-10 Signaling Remodels Adipose Chromatin Architecture to Limit Thermogenesis and Energy Expenditure

Prashant Rajbhandari,[1,9] Brandon J. Thomas,[4,9] An-Chieh Feng,[4] Cynthia Hong,[1] Jiexin Wang,[1] Laurent Vergnes,[5] Tamer Sallam,[6] Bo Wang,[1] Jaspreet Sandhu,[1] Marcus M. Seldin,[4,5] Aldons J. Lusis,[4,5] Loren G. Fong,[6] Melanie Katz,[7] Richard Lee,[7] Stephen G. Young,[6] Karen Reue,[2,5] Stephen T. Smale,[2,4,8] and Peter Tontonoz[1,2,3,8,10,*]

[1]Department of Pathology and Laboratory Medicine
[2]Molecular Biology Institute
[3]Howard Hughes Medical Institute
[4]Department of Microbiology, Immunology, and Molecular Genetics
[5]Department of Human Genetics
[6]Department of Medicine, Division of Cardiology
David Geffen School of Medicine, University of California, Los Angeles, Los Angeles, CA 90095, USA
[7]Ionis Pharmaceuticals, Carlsbad, CA 92008, USA
[8]Senior author
[9]These authors contributed equally
[10]Lead Contact
*Correspondence: ptontonoz@mednet.ucla.edu
https://doi.org/10.1016/j.cell.2017.11.019

SUMMARY

Signaling pathways that promote adipose tissue thermogenesis are well characterized, but the limiters of energy expenditure are largely unknown. Here, we show that ablation of the anti-inflammatory cytokine IL-10 improves insulin sensitivity, protects against diet-induced obesity, and elicits the browning of white adipose tissue. Mechanistic studies define bone marrow cells as the source of the IL-10 signal and adipocytes as the target cell type mediating these effects. IL-10 receptor alpha is highly enriched in mature adipocytes and is induced in response to differentiation, obesity, and aging. Assay for transposase-accessible chromatin sequencing (ATAC-seq), ChIP-seq, and RNA-seq reveal that IL-10 represses the transcription of thermogenic genes in adipocytes by altering chromatin accessibility and inhibiting ATF and C/EBPβ recruitment to key enhancer regions. These findings expand our understanding of the relationship between inflammatory signaling pathways and adipose tissue function and provide insight into the physiological control of thermogenesis that could inform future therapy.

INTRODUCTION

White adipose tissue (WAT) stores energy in times of nutritional excess, and its dysfunction contributes to metabolic disorders such as type 2 diabetes (Rosen and Spiegelman, 2014). BAT is specialized to dissipate stored chemical energy in the form of heat, and BAT mass inversely correlates with body mass index and has been ascribed a potential anti-obesity function (van Marken Lichtenbelt et al., 2009; Virtanen et al., 2009). Recent studies have revealed the ability of certain WAT depots to activate thermogenesis upon exposure to cold and hormonal stimuli (Ohno et al., 2012; Tiraby and Langin, 2003). A subpopulation of cells in inguinal WAT (iWAT) known as "beige" cells expresses UCP1 and carries out thermogenesis (Wu et al., 2012). UCP1 is crucial for thermogenesis in both brown and beige adipocytes, and its activity contributes to regulation of energy balance (Feldmann et al., 2009).

Immune-adipose crosstalk has pronounced effects on the expansion and activation of beige adipose tissue. Several studies have highlighted the importance of anti-inflammatory (type II) cytokines in regulating adipose thermogenesis. Production of interleukin-4 (IL-4)/IL-13 by eosinophils upon stimulation by cold or exercise activates thermogenesis (Qiu et al., 2014; Rao et al., 2014). Activation of type 2 innate lymphoid (IL-C2) cells by IL-33 acts via IL-4Rα in pre-adipocytes to promote beige fat biogenesis (Lee et al., 2015). Recently, IL-33 was shown to license adipocytes for uncoupled respiration by regulating the splicing of UCP1 (Odegaard et al., 2016).

IL-10 is a type II cytokine with anti-inflammatory properties and its loss is associated with autoimmune pathologies (Couper et al., 2008). IL-10 is secreted by multiple immune cells, including macrophages, dendritic cells, B cells, and T cells (Saraiva and O'Garra, 2010). It signals through a receptor complex of IL-10Rα and IL-10Rβ to trigger the activation of signal transducer and activator of transcription 3 (STAT3) (Moore et al., 2001). STAT3 is essential for the anti-inflammatory activity of IL-10 (Lang et al., 2002), which are believed to be primarily due to repression of transcription. However, the precise mechanisms by which IL-10 regulates gene expression remain very poorly understood (Murray, 2005; Murray and Smale, 2012).

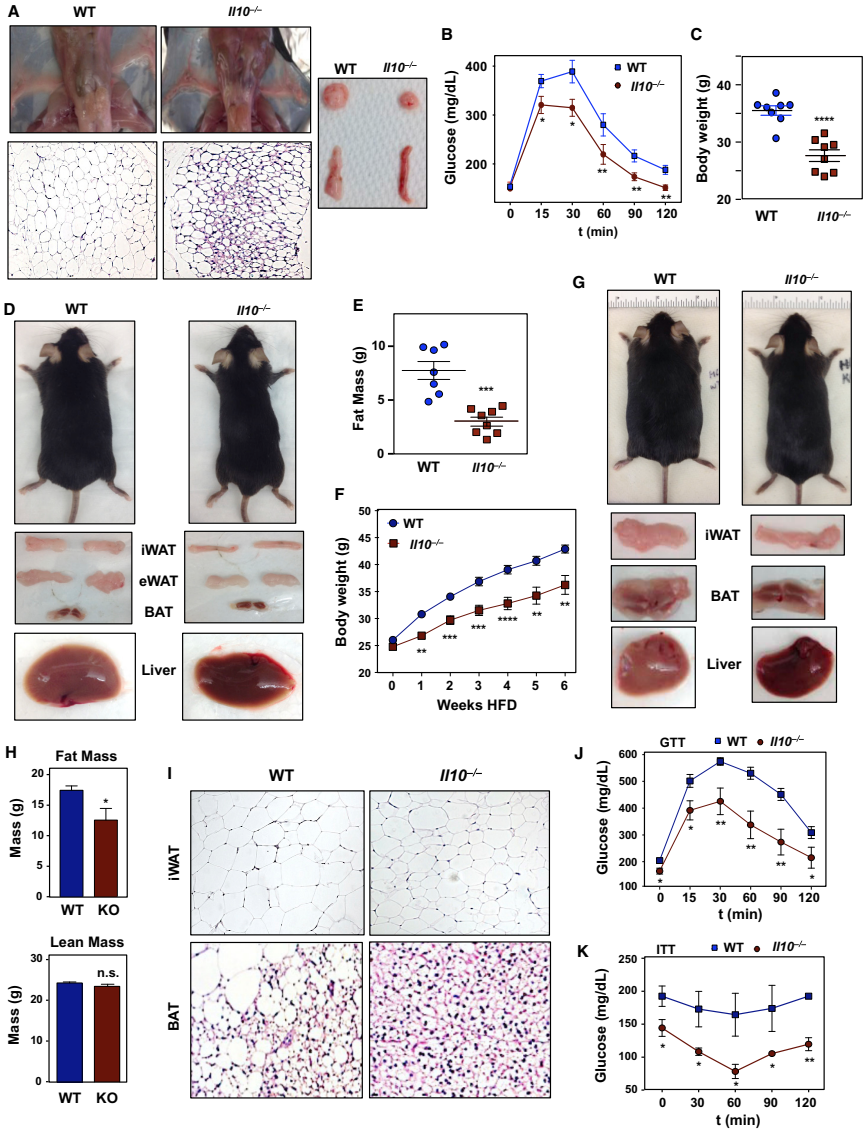

Figure 1. IL-10-Deficient Mice Are Protected against Obesity

(A) Representative images of 10-week-old chow-fed WT and *Il10*$^{-/-}$ mice showing gross adipose tissue appearance and histology (H&E).

(B) Intraperitoneal (i.p.) glucose tolerance test performed on 10-week-old chow-fed mice. N = 7. Comparisons at each time point were made against WT control mice by repeated measures ANOVA.

(C) Body weight of 32-week-old chow-fed WT and *Il10*$^{-/-}$ mice. N = 8, 8.

(D) Gross appearance of representative 32-week-old chow-fed mice and their tissue.

(E) Body fat mass of 32-week-old chow-fed mice determined by EchoMRI. N = 7, 8.

(legend continued on next page)

The role of IL-10 in adipose biology and energy homeostasis is largely unknown. Some studies have suggested that IL-10 might create an anti-inflammatory milieu by promoting the activity of M2 macrophages (Gao et al., 2013; Hong et al., 2009; Lumeng et al., 2007; Xie et al., 2014). However, loss-of-function studies have not supported an anti-obesity role for IL-10 (den Boer et al., 2006; Mauer et al., 2014; Miller et al., 2011). Furthermore, ablation of IL-10 does not cause insulin resistance (Kowalski et al., 2011). Here, we delineate a function for IL-10 signaling in directing transcriptional responses that limit thermogenesis. We show that bone-marrow-derived IL-10 acts on adipocytes via IL-10Rα to repress thermogenic gene expression by altering the chromatin landscape at transcriptional regulatory regions. These findings identify the IL-10 axis as a regulator of thermogenesis and expand our understanding of the links between immune signaling and adipose tissue function.

RESULTS

Ablation of IL-10 Protects Mice from Diet-Induced Obesity

To dissect the role of IL-10 in systemic metabolic homeostasis, we analyzed young *Il10*$^{-/-}$mice (10 weeks of age) on a C57BL/6 background. IL-10 deficiency on this genetic background is associated with a relatively low incidence of colitis (Keubler et al., 2015). There was no overt evidence of systemic inflammation in *Il10*$^{-/-}$ mice, and they had comparable body weights and colon morphology to wild-type (WT) controls (Figures S1A–S1C). However, on visual inspection, iWAT from *Il10*$^{-/-}$ mice appeared redder than that from littermate controls. Histological analysis also revealed smaller adipocytes and increased numbers of cells with multilocular lipid droplets (Figure 1A). Serum triglycerides were lower, and serum-free fatty acids were elevated in *Il10*$^{-/-}$ mice (Figure S1D). We further found that *Il10*$^{-/-}$ mice exhibited markedly improved glucose tolerance despite similar basal glucose levels (Figures 1B and S1D). Interestingly, ablation of IL-10 did not have a marked influence on serum pro-inflammatory cytokine levels or total or activated M1 macrophage populations in adipose tissues (Figures S1E and S1F).

Next, we addressed how this phenotype progressed with age. Chow-fed *Il10*$^{-/-}$ mice at 8 months of age were grossly leaner than controls and had less total body mass and fat mass (Figures 1C–1E). Furthermore, the size and weight of individual adipose depots were reduced (Figure S1G). Livers of *Il10*$^{-/-}$ mice also appeared to be protected from hepatic steatosis (Figure 1D). We further assessed how IL-10 ablation would affect the development of diet-induced obesity. Mice of 10 weeks of age were fed a high-fat diet (HFD; 60% calories from fat) for 6 weeks. After this regimen, *Il10*$^{-/-}$ mice were grossly leaner and gained less weight than WT mice (Figures 1F and 1G). MRI analysis of body composition confirmed reduced body fat with no difference in lean mass (Figure 1H). *Il-10*$^{-/-}$ mice were also protected from diet-induced hepatic steatosis, and the size and weight of individual adipose depots were reduced (Figures 1G–1I and S1H). Liver and serum triglyceride and cholesterol levels were reduced in *Il10*$^{-/-}$ mice (Figure S1I), and the mice had improved glucose tolerance and insulin tolerance (Figures 1J and 1K). Assessment of AKT phosphorylation in response to insulin suggested that adipose tissue insulin sensitivity was preferentially increased in the absence of IL-10 (Figure S1J).

Colon morphology and histology revealed no apparent signs of colitis in *Il10*$^{-/-}$ mice (Figures S1K and S1L), although we noted a small increase in the basal levels of *Mcp1* and *Il-12p40* in colon tissue (Figure S1M). With the exception of IL-10, WT and *Il10*$^{-/-}$ mice had comparable levels of most pro-inflammatory cytokines in serum (Figure S1N). There was a modest decrease in both serum and adipose MCP-1 in HFD-fed *Il10*$^{-/-}$ mice (Figures S1O and S1P), in line with their protection against diet-induced obesity (Kanda et al., 2006; Sartipy and Loskutoff, 2003).

Increased Energy Expenditure in IL-10-Deficient Mice

Next, we probed the influence of IL-10 expression on energy homeostasis. Chow-fed mice at 10 weeks of age were individually housed in metabolic chambers for 72 hours. Oxygen consumption rate (VO_2) energy expenditure (EE) and food consumption were higher in *Il10*$^{-/-}$ mice compared to WT controls (Figures 2A–2C and S2A). Metabolic cage studies performed on an independent cohort of HFD-fed mice revealed similar elevations in VO_2 and EE in mice lacking IL-10 (Figures S2B and S2C).

To examine if the increase in EE in *Il10*$^{-/-}$ mice might reflect altered mitochondrial activity, we isolated mitochondria from iWAT and measured rates of oxygen consumption (OCR). Mitochondrial respiration was sequentially measured with substrate present (basal respiration) and in the presence of ADP (complex V respiration) or FCCP (maximal respiration). We observed increases in basal, complex V, and maximal respiration in *Il10*$^{-/-}$ mice (Figures 2D and S2D). We then assessed the activity of complexes I-IV by performing an electron flow assay. The activity of all complexes was augmented in *Il10*$^{-/-}$ mitochondria (Figures 2E and S2D).

Increased Adipose Thermogenesis in IL-10-Deficient Knockout Mice

To address whether the loss of IL-10 affected adipose gene expression, we performed RNA sequencing (RNA-seq) on iWAT from chow-fed, 10-week-old mice. Remarkably, as depicted in Figure 2F, genes linked to adipocyte thermogenesis

(F) Body weight of mice fed chow diet for 10 weeks and then on a 60% high-fat diet (HFD) for 6 weeks. N = 16, 12. Statistical analysis was performed using Student's t test.
(G) External and gross tissue appearance of representative 6-week-old mice that were HFD-fed.
(H) Fat and lean mass of mice in (F). Statistical analysis was performed using Student's t test.
(I) Representative histology of iWAT and BAT from mice in (F).
(J) An i.p. glucose tolerance test (GTT) was performed on WT and *Il10*$^{-/-}$ mice fed chow diet for 10 weeks and then on a 60% HFD for 6 weeks. N = 7.
(K) An i.p. insulin tolerance test (ITT) was performed on mice in (J). N = 7. Comparisons at each time point were made against WT control mice by repeated measures ANOVA. *p < 0.05, **p < 0.01, ***p < 0.001, ****p < 0.0001, ns, not significant.
Error bars represent SEM. See also Figure S1.

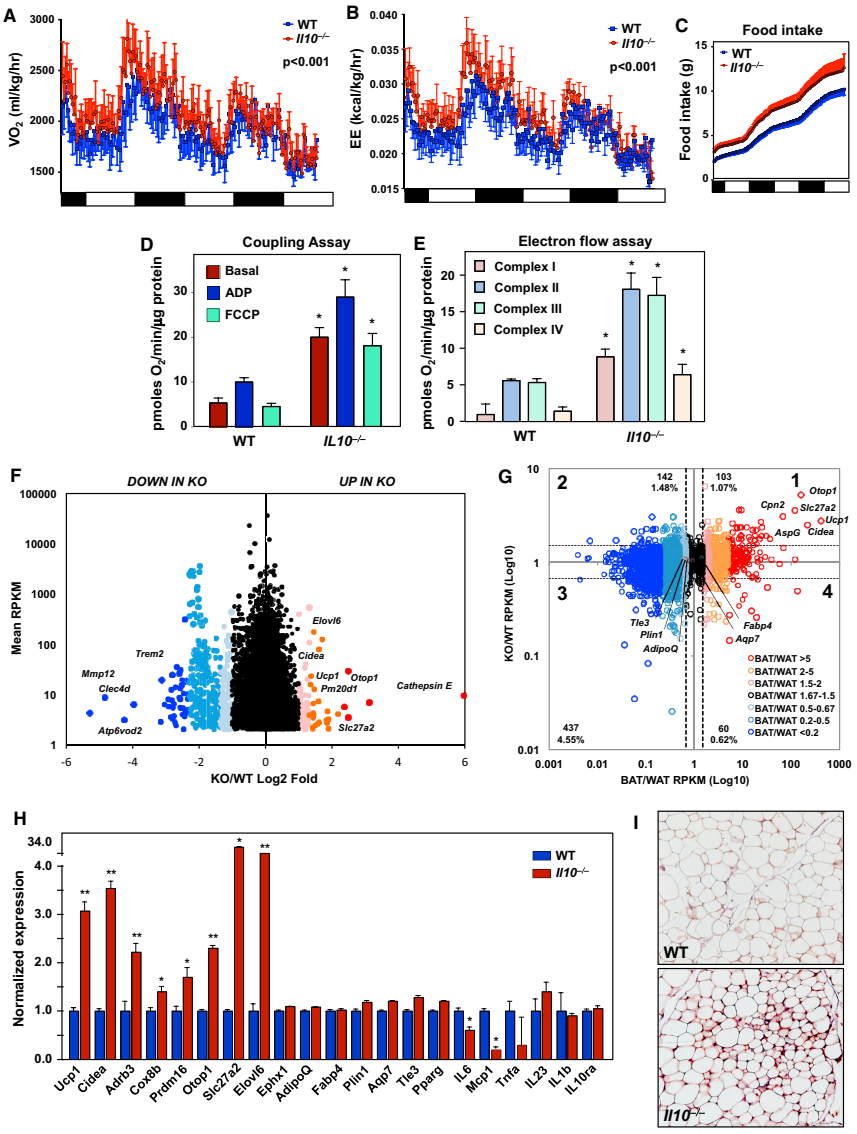

Figure 2. IL-10 Deficiency Promotes Energy Expenditure and Adipose Tissue Browning

(A–C) Energy expenditure (EE) (kCal/kg/hr) (A), VO_2 (mL/kg/hr) (B), and food intake (g) (C) of chow-fed 10-week-old WT and *Il10*$^{-/-}$ mice was analyzed by Columbus Oxymax metabolic chambers. 12-hr light/dark cycles; 72-hr total duration; and each light/dark bar represents 12 hr duration. N = 7. Statistical analysis was performed using two-way ANOVA and ANCOVA.

(D and E) Average oxygen consumption rate (OCR) of mitochondria isolated from iWAT in mitochondrial coupling (D) and electron flow assays (E). Samples were treated with different substrates or inhibitors to obtain specific respiration states as indicated. Data are the average of six internal replicates and are representative of two experiments. Statistical analysis was performed using Student's t test.

(legend continued on next page)

were highly upregulated in iWAT from *Il10*$^{-/-}$ mice compared to controls. Such genes included *Ucp1*, *Cidea*, and *Pm20d1* (Long et al., 2016). Conversely, genes selectively expressed in WAT and those associated with obesity, including *Mmp12*, *Trem2*, *Celec4d*, and *Atp6v0d2*, were downregulated. We further analyzed the correlation between the gene expression signatures of WT and *Il10*$^{-/-}$ iWAT and reference BAT and WAT from public datasets (Seale et al., 2007). The data plot in Figure 2G is divided into four quadrants with different shades of red and blue representing the BAT/WAT ratio as a function of knockout (KO)/WT ratio. The large cluster of genes between the horizontal dotted lines show that vast majority of genes were similarly expressed between WT and KO mice. However, the substantial number of genes clustered in quadrant one indicated that the profile of *Il10*$^{-/-}$ iWAT more closely resembled BAT than did that of WT. Real-time PCR confirmed that markers of adipose browning were increased in *Il10*$^{-/-}$ mice, whereas inflammatory markers were reduced or unchanged (Figures 2H and S1O), with the exception of mild increases in the low basal levels of *Tnfa*, *Mcp1*, and *Il-12p40* in colon (Figure S1M). We also found increased UCP-1 protein in adipose tissue of *Il10*$^{-/-}$ mice (Figure 2I). Expression of previously identified "beige markers" was generally not different, except for a mild enrichment in the TMEM26+ cell population in *Il10*$^{-/-}$ mice (Figures S2E and S2F). Thermogenic gene expression in BAT was similar between groups (Figure S2G).

To rule out a contribution of subclinical colonic inflammation to the metabolic phenotype of *Il10*$^{-/-}$ mice, we treated them with the broad-spectrum antibiotic enrofloxacin starting at 4 weeks of age (Hoentjen et al., 2003; Madsen et al., 2000). After 7 weeks of antibiotic *Il10*$^{-/-}$ mice still had increased adipose thermogenic gene expression (Figure S2H). Thus, the improved metabolic phenotype of *Il10*$^{-/-}$ mice could not be linked with the development of colitis or obvious systemic inflammation.

Adrenergic signaling is enhanced in mice housed at ambient temperature (23°C) compared to thermoneutrality (30°C). We noted that genes induced in response to cold, such as *Cpn2*, *Otop1*, and *Pm20d1* (Long et al., 2016) were upregulated in *Il10*$^{-/-}$ mice maintained at 23°C (Figures 2F and 2G). This finding raised the possibility that either increased production of β-adrenergic agonist or increased response to the same level of agonist might contribute to the phenotype of *Il10*$^{-/-}$ mice. To address this, we housed 4-week-old mice at 30°C for 7 weeks. Thermoneutral housing attenuated the differences in thermogenic gene expression between WT and *Il10*$^{-/-}$ mice (Figure S2I), suggesting that the phenotype was dependent on active beta-adrenergic signaling. To rule out the possibility that *Il10*$^{-/-}$ mice were producing more β-adrenergic agonists, perhaps because they were perceiving cold due to changes in skin or fur, we measured body temperature and catecholamine levels and observed no differences between groups (Figures S2J and S2K). Further, *Il10*$^{-/-}$ mice exposed to cold (5°C) for 6–24 hr showed a more robust increase in thermogenic genes compared to controls (Figure S2L). These findings suggest that IL-10 affects the downstream response to β-adrenergic agonists.

Bone Marrow IL-10 Production Determines the Thermogenic Phenotype

To determine the source of the IL-10 signal leading to these metabolic effects, we performed bone-marrow transplantation (BMT) studies. We reconstituted lethally irradiated *Il10*$^{-/-}$ mice with either WT (WT➡KO) or *Il10*$^{-/-}$ bone-marrow (KO➡KO) (Figure S3A). Genotyping of blood 7 weeks post-BMT showed that the WT allele was fully reconstituted in *Il10*$^{-/-}$ mice (Figure S3A). Following the transplant WT➡KO mice gained more weight and accumulated more fat mass than KO➡KO controls (Figures 3A and 3B). The iWAT depot was larger in WT➡KO mice compared to KO➡KO controls (Figure 3C). WT➡KO mice also had higher blood glucose levels and were less glucose tolerant (Figures S3B and S3D). Importantly, neither group showed apparent signs of colitis (Figure S3C). We performed calorimetry to investigate whether the thermogenic phenotype of IL-10-deficient mice was rescued by WT bone marrow. WT➡KO mice had reduced VO_2 and EE compared to KO➡KO mice (Figure 3E). Consistent with this finding, thermogenic gene expression and mitochondrial respiration were repressed in WT➡KO mice (Figures 3F–3H and S3D).

IL-10-IL-10R Axis Represses Adipocyte Thermogenesis

To explore if IL-10 could act on adipose tissue directly, we characterized IL-10Rα expression in fat. *Il10ra* was highly enriched in the mature adipocyte fraction of iWAT and *Il10ra*, but not *Il10rb*, was induced during differentiation (Figures 4A, 4B, and S4A). Furthermore, *Il10ra* was increased in response to HFD, genetic obesity, and aging (Figures 4C and S4B). Interestingly, *Il10ra* was also regulated over the time course of mice exposed to cold. *Il10ra* was induced acutely, but fell as thermogenic gene expression increased (Figures S4C and S4D). We also found that cold exposure and HFD feeding led to an increase in serum IL-10 (Figure S4D). IL-10Rα levels were higher in WAT compared to other metabolic tissues such as liver and muscle (Figure S4E).

Meta-analysis of published data from the Metabolic Syndrome in Men (METSIM) study (N = ~10,000) and >100 strains of high-fat/fructose fed mice from the hybrid mouse diversity panel

(F) Scatterplot of gene expression differences between WT and *Il10*$^{-/-}$ mice as determined by RNA sequencing of iWAT. Genes with at least 4 RPKM are shown. The log2 ratio of KO/WT expression (x axis) is shown as a function of max RPKM (y axis), with select genes indicated with vertical text. Shades of blue correspond to genes downregulated in the *Il10*$^{-/-}$ mice, and shades of red indicate upregulation in *Il10*$^{-/-}$ mice. N = 9, 11.

(G) Scatterplot of the gene expression ratio in *Il10*$^{-/-}$ to WT mice versus BAT to WAT (Seale et al., 2007). Genes are color-coded based on the expression ratio of BAT to WAT, and the dash lines represent the cutting range of the gene expression ratio, 0.67 and 1.5 accordingly. Genes that are strongly upregulated in *Il10*$^{-/-}$ mice are enriched in BAT-selective genes (red annotated genes). WAT-selective genes (black annotated genes) with similar expression in *Il10*$^{-/-}$, and WT mice were either weakly repressed or similar in BAT.

(H) Real-time analysis of gene expression in iWAT from WT and *Il10*$^{-/-}$ mice. N = 9, 11.

(I) Immunohistochemical staining for UCP1 in iWAT. *p < 0.05, **p < 0.01.

Error bars represent SEM. See also Figure S2.

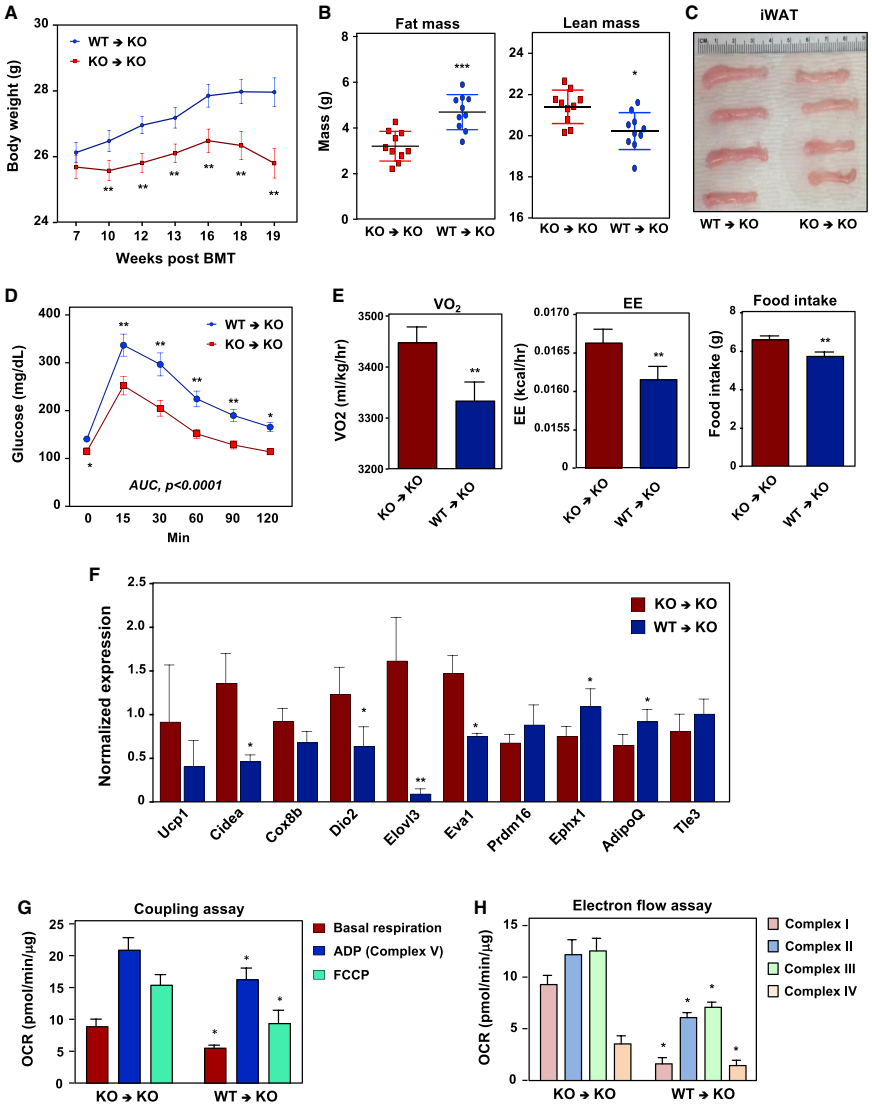

Figure 3. Bone-Marrow-Derived IL-10 Inhibits Thermogenesis

(A) Body weight of lethally irradiated chow-fed *Il10*$^{-/-}$ mice reconstituted with WT (WT→KO) or *Il10*$^{-/-}$ (KO→KO) bone marrow 7 weeks post-transplant. N = 10. Statistical analysis was performed using Student's t test.

(B) Body fat and lean mass of WT→KO and KO→KO mice determined by EchoMRI.

(C) Gross appearance of iWAT 19 weeks post-BMT.

(D) An i.p. GTT was performed on WT→KO and KO→KO mice. N = 10. Comparisons at each time point were made by repeated measures ANOVA.

(E) EE, VO_2, and food intake were analyzed by metabolic chambers. 12-hr light/dark cycles; 72-hr total duration; and each light/dark bar represents 12-hr duration. N = 10 per group. Statistical analysis was performed using two-way ANOVA and ANCOVA.

(F) Gene expression in iWAT determined by real-time PCR. N = 9. Statistical analysis was performed using Student's t test.

(legend continued on next page)

(Laakso et al., 2017; Parks et al., 2013) showed robust correlation of *IL10Ra* with fat mass and insulin resistance (Figures 4F and 4G). We also identified *Il10ra* as a direct PPARγ target gene. *Il10ra* expression was induced in response to PPARγ activation, and analysis of published chromatin immunoprecipitation sequencing (ChIP-seq) data revealed robust enrichment of PPARγ at the enhancer region of the *Il10ra* gene locus in adipocytes (Figure S4F) (Siersbæk et al., 2012).

Next, we assessed whether the IL-10Rα pathway was functional in adipocytes. We confirmed that IL-10 activated STAT3 phosphorylation (Figure S4G). We then proceeded to knock down IL-10Rα in iWAT with an adenoviral vector expressing a specific small hairpin RNA (shRNA). Partial knockdown of IL-10Rα protein was sufficient to increase thermogenic gene expression (Figures 4D and 4E). We also performed acute knockdown studies *in vivo* using an antisense oligonucleotide (ASO) targeting IL-10Rα. Importantly, we observed knockdown of IL-10Rα expression in fat, but not liver or muscle, in response to ASO treatment (Figure 4H). Acute IL-10Rα depletion by ASO caused weight loss, a reduction in fat but not lean mass, and a reduction in WAT weight (Figures 4I–4K). Neither control ASO- nor IL-10Rα ASO-treated mice showed signs of colitis (Figure S4H). Furthermore, expression of thermogenic genes was increased in iWAT of IL-10RαASO-treated mice (Figure 4K).

Treatment of iWAT acutely *ex vivo* with IL-10 decreased UCP1 protein and its corresponding mRNA (Figures 5A and 5B). To establish that these effects were due to direct actions of IL-10 on adipocytes and did not require other cell types, we studied primary beige adipocytes differentiated *in vitro*. Treatment of these cells with IL-10 also led to a robust downregulation of thermogenic genes (Figure S5A). To facilitate our analysis of IL-10 signaling in cultured adipocytes, we established an immortalized brown-like preadipocyte cell line that expressed IL-10Rα and was capable of inducing thermogenic genes in response to stimuli (iBAd cells). IL-10 signaling was operative in these cells as indicated by induction of the canonical IL-10-responsive gene *Socs3* (Figure 5C). Reciprocal with the induction of *Socs3*, we observed a decrease in *Ucp1* levels and decreased mitochondrial respiration upon IL-10 treatment (Figure S5B). Pretreatment of the cells with an IL-10Rα antibody or small interfering RNA (siRNA)-mediated knockdown of STAT3 blunted the effects of IL-10 (Figures S5C and S5D).

We then assessed global gene expression in differentiating iBAd cells in the presence or absence of IL-10. Genes induced in vehicle-treated cells more than 5-fold on day 5 (D5) of differentiation compared to D0 were plotted as a heat-map (Figure 5D). Thermogenic genes such as *Ucp1*, *Cidea*, and *Pppargc1α* were among the highest induced genes on D5. Moreover, these same genes were also among the most highly inhibited by IL-10 (Figure 5D). Pathway analysis revealed that brown fat cell differentiation and lipid metabolic processes were compromised by IL-10 (Figure 5E). Blockade of the browning program by IL-10 was further validated by plotting the RNA-seq vehicle (NT)/IL-10 expression ratio as a function of WAT/BAT expression ratio (Sun et al., 2013). 70% of the genes inhibited by IL-10 were brown-selective genes, suggesting a high specificity for the browning program (Figure 5F).

IL-10 Alters Chromatin Architecture at Thermogenic Genes

The primary mode of IL-10 action in macrophages is believed to be inhibition of transcription, although the underlying mechanisms are unclear. We found that IL-10 inhibited the abundance of primary transcripts of thermogenic genes and the expression of putative enhancer RNAs (eRNAs) from *Ucp1* (Figure 5G), indicating that IL-10 was acting to block transcription. To test whether IL-10-dependent repression of transcription was due to action at DNA regulatory regions, we performed genome-wide assay for transposase-accessible chromatin sequencing (ATAC-seq) on differentiated iBAd cells. ATAC-Seq peaks correspond to genomic regions sensitive to cleavage by transposase because of their open chromatin configuration (Buenrostro et al., 2013). Using a parallel approach to the RNA-seq analysis of Figure 5D, we identified 3,174 ATAC peaks that were enriched more than 5-fold on D5 compared to D0 in vehicle-treated cells and represented them as a heatmap (Figure 6A). Peaks indicative of open chromatin appearing at D5 included those at the enhancer/promoter regions of thermogenic genes such as *Ucp1 and Cidea*, consistent with the induction of these genes during differentiation. In line with the inhibitory effects of IL-10 on thermogenic gene repression, IL-10 markedly reduced ATAC peak enrichment at thermogenic genes (Figure 6A).

To qualitatively assess the changes in ATAC-seq peaks, we plotted the data as a bedgraph. As shown in Figure 6B, on D5 of brown differentiation a discreet set of new peaks emerged (peaks 1 and 3), indicative of newly opened chromatin at regulatory regions of the *Ucp1* locus. Remarkably, IL-10 treatment caused an almost complete loss of these differentiation-dependent peaks, indicating that the chromatin remained closed in response to IL-10 signaling. These changes in ATAC peaks were consistent with the RNA-seq data showing a decreased *Ucp1* transcript in IL-10-treated cells and increased transcript in IL-10-deficient mice. Importantly, there were a number of prominent ATAC peaks at the *Ucp1* locus that were not affected by IL-10 (e.g., peak 2), indicating that IL-10 was selectively altering chromatin at specific sites (Figure 6B). Specificity was further confirmed by aligning the adipocyte results with ATAC-seq data from *Il-10*$^{-/-}$ bone-marrow-derived macrophages treated with and without IL-10. Most of the peaks present at the *Ucp1* locus in adipocytes were absent in macrophages. ATAC-seq peak quantification at the *Ucp1* locus further validated the repressive effects of IL-10 at peaks 1 and 3, but not 2 (Figure 6C).

IL-10 treatment also altered chromatin configuration at the regulatory regions of a battery of other thermogenic genes, including *Cidea*, *Ppargc1α*, and *Elovl3* (Figures 6B and S6E).

(G and H) Average oxygen consumption rate (OCR) in coupling (G) and electron flow (H) assays of mitochondria isolated from iWAT of WT→KO and KO→KO mice. Data are the average of six internal replicates and are representative of two experiments. Statistical analysis was by Student's t test. *$p < 0.05$, **$p < 0.01$, ***$p < 0.001$.

Error bars represent SEM. See also Figure S3.

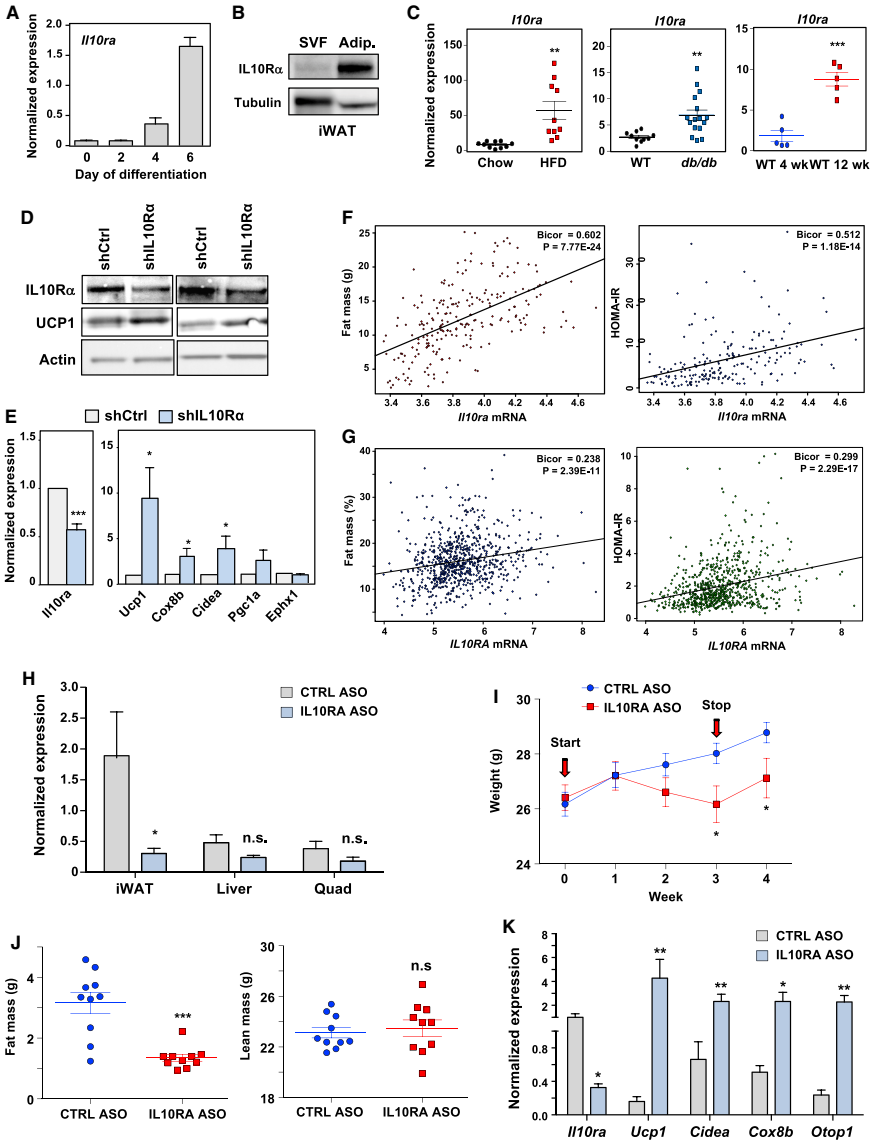

Figure 4. Adipose IL-10Rα Knockdown Increases Thermogenic Gene Expression

(A) Real-time PCR analysis of *Il10ra* mRNA during the differentiation of primary iWAT stromal vascular fraction (SVF). Cells were stimulated to differentiate with dexamethasone (1 μM), IBMX (0.5 mM), insulin (5 μg/mL), and rosiglitazone (20 nM) for 2 days, followed by insulin and rosiglitazone for 5 days.

(B) Immunoblot analysis of IL-10Rα expression in SVF and adipocyte fraction of iWAT from chow-fed 10-week-old mice.

(C) *Il10ra* mRNA from iWAT of 12-week-old chow or HFD-fed mice, 12-week-old WT or *db/db* mice, and 4- and 12-week-old chow-fed WT mice. Statistical analysis was performed using Student's t test. N = 5–15.

(legend continued on next page)

Furthermore, examination of ATAC signals at genes whose expression was not altered by IL-10, including *Fabp4 and Ephx1*, showed that the ATAC peaks were virtually unchanged by IL-10 (Figure S5E). The expected increase in ATAC signals at the *Socs3* locus served as a positive control for IL-10 transcriptional effects (Figure S5E). Finally, we plotted the ratio of vehicle/IL-10 from our ATAC-seq data as a function of gene expression (RNA-seq). Changes in ATAC peaks did not always correlate with transcript abundance, suggesting that changes in chromatin configuration do not necessarily translate into transcriptional regulation. However, we found a small cluster of genes in the quadrant 2 of the plot shown in Figure 6D with particularly high ATAC-/RNA-seq correlation. This cluster included thermogenic genes, such as *Ucp1*, *Pppargc1α*, and *Cidea*, further underscoring the specificity of IL-10 action.

To extend our results to beige adipocytes, we performed ATAC-seq on adipocytes differentiated from primary SVFs from iWAT of 10-week-old mice. We found that IL-10 altered chromatin accessibility at thermogenic genes (*Ucp1*, *Cidea*, and *Cox8b*) in primary beige adipocytes (Figure S6A). We isolated mature adipocytes from iWAT and performed ATAC-seq to further establish the physiological relevance of our findings. Consistent with the upregulation of thermogenic genes (Figure 2), regulatory regions of *Ucp1*, *Cidea*, *Cox8b*, *Adrb3*, and *Pm20d1* were in a more open chromatin configuration in *Il10*$^{-/-}$compared to WT iWAT adipocytes (Figures 6E, 6F, and S6B). Thus, results from three different models indicated that IL-10 affects chromatin architecture and thermogenic gene transcription in a cell-autonomous manner.

IL-10 Alters Transcription Factor Occupancy at Thermogenic Genes

Thermogenic gene transcription is orchestrated by multiple transcriptional regulators (Harms and Seale, 2013). To investigate if IL-10 affected accessibility at sites of transcription factor binding, we performed *in silico* analysis. We plotted all the ATAC-seq data peaks from D0 and D5 as a function of fold induction to assess the percentage of peaks showing a change in accessibility during differentiation. About 10% of the ATAC peaks show an increase of 5-fold or higher on D5 (Figure S7A). Furthermore, the distribution of ATAC peaks that were highly enriched during BAT differentiation favored intergenic regions that could possibly contain enhancer elements (Figures S7B and S7C). We separated the ATAC peaks into 10 equivalently sized bins to assess the peak strength (reads per kilobase per million mapped reads [RPKM]) within each category of samples (D0, D5, and D5+IL-10). Next, we quantitatively assess transcription factor binding sites in the intergenic/enhancer regions where ATAC peaks were enriched. Motifs associated with the binding of canonical thermogenic transcription factors such as CREB/ATF, C/EBPs, and NFIs were highly enriched on D5 (Figure S7D). By contrast, AP-1 (Fos/Jun) motifs were highly downregulated. To further investigate the effect of IL-10 on transcription factor enrichment, we analyzed the same regions from Figure S7D and divided the motifs into three groups based on the level of IL-10 inhibition. IL-10 caused a substantial loss of enrichment for motifs associated with thermogenesis-linked transcription factors (Figure 7A).

To complement these *in silico* analyses, we directly tested the functional relevance of the transcription factor motifs identified by ATAC-seq. We performed directed qChIP-PCR analysis on the regulatory regions of *Ucp1* gene locus. The boxed peaks in Figure 7D contain sequences that regulate chromatin dynamics through histone modification and recruitment of transcription regulators such as C/EBPs, PGC1α, and CREB/ATF. We found that IL-10 treatment compromised active enhancer histone methylation mark H3K4me1 as well as recruitment of C/EBPβ, PGC1α, and ATF-2 to *Ucp1* regulatory peaks 1 and 3, but not to the constitutively present peak 2 (Figure 7B). In accordance with these ChIP data, IL-10 treatment caused a marked reduction in the ATF-2 phosphorylation and protein levels of PGC1α in adipocytes (Figure 7C).

To further investigate the involvement of C/EBPβ in the actions of IL-10, we performed genome-wide Chip-seq. Motif analysis showed that the C/EBPβ consensus site was highly enriched in our peak analysis, and peak annotation showed that IL-10 treatment did not cause global changes in C/EBPβ DNA occupancy (Figures S7E and S7F). However, gene ontology analysis revealed that IL-10 antagonized C/EBPβ enrichment selectively at gene loci associated with the brown differentiation program (Figure 7D). For example, IL-10 blunted the recruitment of C/EBPβ to regulatory regions of *Elovl6*, *Lpl*, and *Ppargc1α*, without affecting recruitment to *Pparg* (Figures 7E and S7G).

DISCUSSION

Although multiple signaling pathways that can stimulate adipose tissue browning have been characterized, the physiologic limiters of energy expenditure programs are not well defined. Here, we have outlined an unexpected role for IL-10 in the modulation of adipocyte thermogenesis. Loss of IL-10 in mice increased energy expenditure and protected against diet-induced obesity, and did so in the absence of overt systemic

(D) Immunoblot analysis of protein from iWAT of 10-week-old mice injected with 2 × 10^9 plaque-forming units (PFUs) of the adenovirus-expressing control shRNA (shCtrl) or the shRNA targeting IL-10Rα for 72 hr. Each lane represents an individual animal.
(E) Gene expression in iWAT transduced with shCtrl or shIL-10Rα adenovirus. Data represent the average of 8–10 mice/group. Statistical analysis was performed using Student's t test.
(F and G) Correlation trait plots of IL-10Rα expression and fat mass and HOMA-IR data from the HMDP (F) and the METSIM (G) studies. All correlations were assessed from the midweight bicorrelation coefficient and corrected p value using the R package WGCNA (Langfelder and Horvath, 2008).
(H) *Il10ra* expression in tissues from ctrl or IL-10Rα ASO-treated mice.
(I) Body weight of 12-week-old mice treated with ctrl or IL-10Rα ASO for 3 weeks.
(J) Fat mass and lean mass of mice in (I).
(K) Gene expression in iWAT from mice treated with ctrl or IL-10Rα ASO. N = 10 per group. *p < 0.05, **p < 0.01, ***p < 0.001, ****p < 0.0001, ns, not significant. Error bars represent SEM. See also Figure S4.

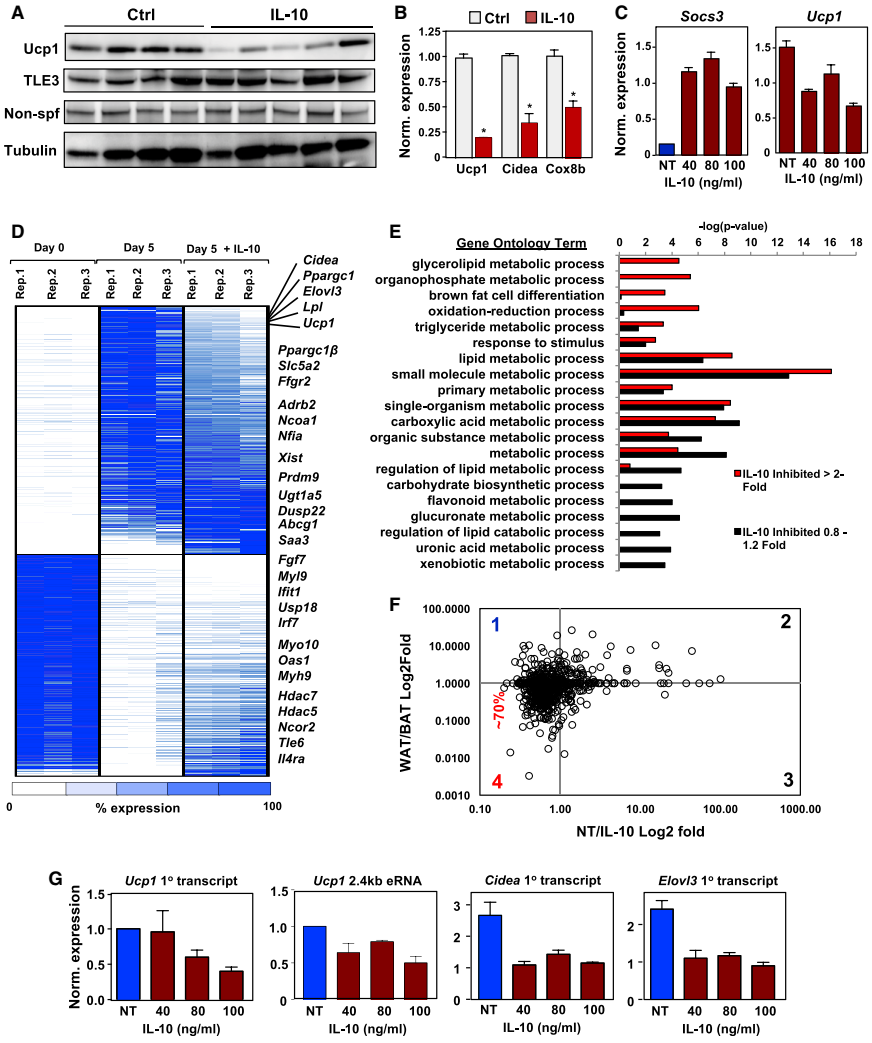

Figure 5. IL-10 Directly Acts on Adipocyte IL-10Rα to Inhibit Thermogenesis

(A) Immunoblot analysis of protein extracts from iWAT of 10-week-old mice treated *ex vivo* with vehicle (ctrl) or 100 ng/mL IL-10. N = 4–6. Results are representative of three independent experiments.

(B) Real-time PCR analysis of gene expression in iWAT of 10-week-old mice treated *ex vivo* with control (NT) or 100 ng/mL IL-10 for 1 hr. N = 4–6.

(C) Gene expression in brown differentiated iBAd cells treated with recombinant IL-10 for 16 hr.

(D) Heatmap representation of genes that changed >3-fold ($p < 0.01$) by RNA-seq on day 5 (D5) of differentiation of iBAd cells. Each sample is shown in triplicate and compared to expression at day 0 (D0). Genes are grouped as either induced upon differentiation (top) or repressed during differentiation (bottom). The far-right column shows the effect of 100 ng/mL IL-10 treatment on gene expression at D5. Genes are ranked based on IL-10 inhibition, with selected genes shown in the text at right.

(E) Genes induced upon differentiation were divided based on their response to IL-10, either inhibited >2-fold (red bars) or not affected (black bars), and gene ontology analysis was performed with –log10 (p value) plotted (x axis) as a function of classification meeting a p value of < 0.001.

(legend continued on next page)

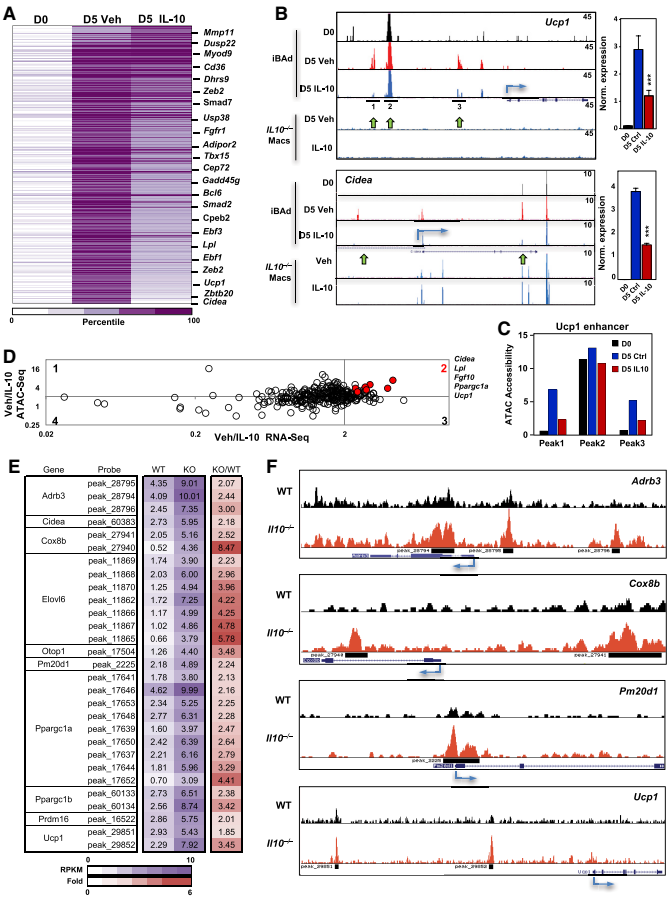

Figure 6. IL-10 Signaling Remodels Chromatin Architecture at Thermogenic Genes

(A) Heatmap analysis of ATAC-seq performed on D0 and D5 of iBAd cell differentiation with and without 100 ng/mL IL-10 for 16 hr for all called peaks demonstrating >5-fold induction (N = 3,174 sites). Peaks were assigned to the nearest gene, and the selected genes are shown.

(B) ATAC-seq bedgraph panels of the *Ucp1* and *Cidea* loci showing peak locations relative to the transcription start site (TSS). Panels compare ATAC signals between iBAd cells to signals from *Il10*$^{-/-}$ bone-marrow-derived macrophages (macs) treated with and without 30 ng/mL IL-10. Adjacent to the ATAC panel is real-time PCR analysis of gene expression.

(C) ATAC peak strength (y axis) for selected peaks within the *Ucp1* locus under the indicated conditions.

(D) Correlation plot of ATAC-seq and RNA-seq data.

(E) Merged heatmap analysis of ATAC-seq performed on adipocytes derived from 10-week-old mice showing enhanced chromatin accessibility in *Il10*$^{-/-}$ mice at peaks annotated to BAT-selective genes. N = 2.

(F) ATAC-seq bedgraph panels of the indicated gene loci showing peak locations relative to the TSS. *p < 0.05, **p < 0.01, ***p < 0.001.

Error bars represent SEM. See also Figure S6.

or adipose inflammation. We further showed that IL-10 acts directly on adipocytes to repress thermogenic genes by altering the chromatin landscape. These findings expand our understanding of the complexity of regulatory links between immune and inflammatory signaling and adipocyte metabolism. They further suggest that blockade of IL-10 receptor signaling in fat could represent a tractable approach to de-repress thermogenic gene expression in a therapeutic context.

Adipose tissue inflammation is widely regarded to be a contributory factor in the development of metabolic dysfunction (Lumeng and Saltiel, 2011). However, paradoxical increases in insulin resistance in mice depleted of various pro-inflammatory signals, and the development of age-related obesity upon anti-inflammatory ablation, suggest a more complex relationship between the immune system, adipocytes, and systemic metabolism (Bapat et al., 2015; Wallenius et al., 2002; Wernstedt Asterholm et al., 2014). Several pro-inflammatory molecules have been shown to impair insulin action and lipid storage in mouse models, leading to the suggestion that inhibition of adipose tissue inflammation might be beneficial in the setting of diabetes (Shoelson et al., 2006). Inflammation is also linked with increased energy expenditure in patients with cachexia and inflammatory bowel disease (Barot et al., 1981; Moldawer et al., 1987). The cytokine IL-6 is induced in response to exercise and cancer cachexia has been associated with browning and energy expenditure (Knudsen et al., 2014; Petruzzelli et al., 2014). Similarly, nuclear factor κB (NF-κB) is induced in cancer cachexia and is known to promote energy expenditure (Tang et al., 2010; Tisdale, 1997). In contrast, IL-1β and tumor necrosis factor alpha (TNF-α) have been reported to negatively regulate adipose thermogenesis and to

(F) RNA-seq data from the *in-vitro*-differentiated WAT/BAT ratio (Sun et al., 2013) plotted as a function of RNA-seq data from the NT/IL-10 ratio.

(G) Real-time PCR analysis of primary mRNA transcripts and *Ucp1* eRNA in iBAd cells on D5 with and without IL-10 for 16 hr. *p < 0.05, **p < 0.01, ***p < 0.001, ****p < 0.0001, ns, not significant.

Error bars represent SEM. See also Figure S5.

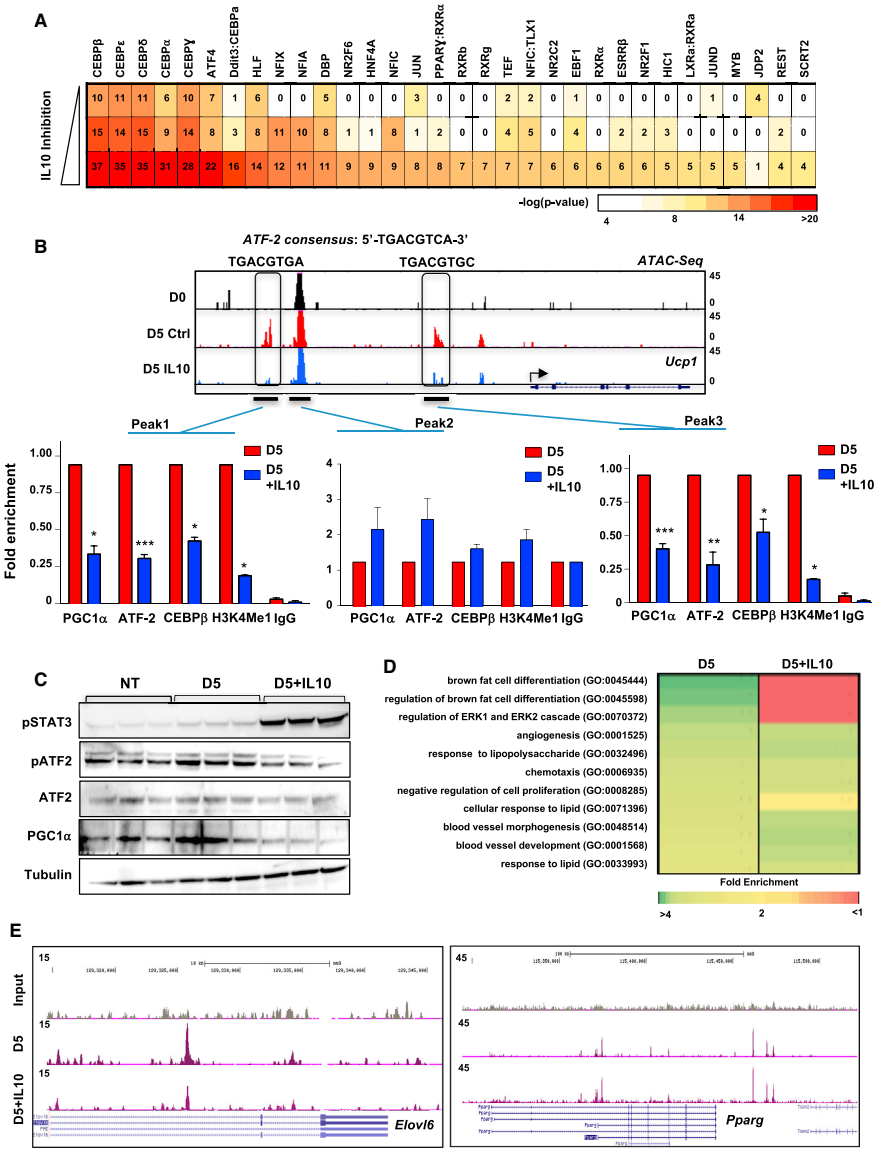

Figure 7. IL-10 Limits the Recruitment of Thermogenic Transcriptional Regulators

(A) TF motif analysis of ten bins containing 3,174 ATAC peaks demonstrating the highest fold induction during maturation separated into three groups of 1,058 peaks based on the degree of IL-10 inhibition.

(B) ChIP-qPCR was performed for indicated proteins on iBAd cells treated with and without 100 ng/mL IL-10 for 16 hr.

(C) Immunoblot analysis of proteins from differentiated iBAd cells treated with and without IL-10 for 16 hr.

(legend continued on next page)

cause desensitization to catecholamines (Goto et al., 2016; Nisoli et al., 2000). Thus, the effects of individual cytokine pathways on thermogenesis are likely to depend on a range of variables, including the source of the cytokine, the duration of the exposure, and the cell type(s) responding to it.

The ability of IL-10 to counter the pro-inflammatory actions of other cytokines is well documented (Saraiva and O'Garra, 2010). Contrary to the expectation that loss of IL-10 might exacerbate adipose inflammation, we did not observe this. Our finding that IL-10-deficient mice had increased thermogenic gene expression even when maintained on an antibiotic that prevents colitis indicates that bowel inflammation is not the driver of their metabolic phenotype. Multiple lines of evidence suggest that adipocyte-intrinsic effects of IL-10 signaling are an important determinant of thermogenesis; however, we acknowledge that we cannot exclude the possibility that secondary changes in the activities of other cytokine pathways might also contribute to the phenotype of IL-10-deficient mice.

Several prior studies have addressed metabolism in IL-10-deficient mice, with differing results. Clementi et al. and den Boer et al. found that *Il10*$^{-/-}$ mice fed HFD had increased hepatic triglycerides but no change in insulin sensitivity (Clementi et al., 2009; den Boer et al., 2006). In better agreement with our data, Miller et al. (2011) reported that *Il10*$^{-/-}$ mice fed high fat diet for 12 weeks were protected from hepatic steatosis, and Faulkner et al. (2013) reported that *Il10*$^{-/-}$ mice on HFD had reduced adiposity and increased insulin sensitivity. Potential factors that might influence these differing results include dietary composition, subtle differences in genetic background of the *Il10*$^{-/-}$ mice, and vivarium conditions. Given that IL-10 is known to engage in crosstalk with many other pathways, including IL-6 and Toll-like receptor (TLR) signaling, it seems likely that the basal activities of such pathways could also be an important variable in the metabolic consequences of IL-10 deletion.

We have built on prior work in macrophages to dissect the actions of IL-10 in a different cell type, where it acts on a largely distinct set of transcriptional target genes. ATAC- and RNA-seq revealed that chromatin at the regulatory regions of thermogenic genes remained closed during browning in the presence of IL-10. Importantly, this effect was selective for the thermogenic program, as the chromatin structure adipocyte genes not related to browning was not altered. Thus, IL-10 is not a general inhibitor of adipocyte transcription, but rather a specific modifier of thermogenesis. We also identified specific transcription factors whose interactions with regulatory regions of thermogenic genes were dependent on IL-10 signaling. ATAC accessibility at ATF/CREB and C/EBP motifs was enriched during browning, and the presence of IL-10 antagonized accessibility at these motifs. Consistent with the changes in accessibility at these motifs, directed ChIP analysis showed reduced occupancy of C/EBPβ, ATF-2, and its cofactor PGC-1α at *Ucp1* regulatory regions in the presence of IL-10. Furthermore, genome-wide ChIP-seq analysis revealed selective changes in the recruitment of C/EBPβ to regulatory regions of thermogenic genes. Finally, we found that AFT-2 activation and expression of PGC-1α itself were also repressed in response to IL-10.

Our data are most consistent with the model that IL-10 acts on pre-existing mature adipocytes to enact a change in gene expression that alters their thermogenic activity. IL-10Rα is enriched in white and beige adipocytes and is upregulated during differentiation and in obesity. Thus, hematopoietic-derived IL-10 could act on white adipocytes to maintain adiposity and on beige adipocytes to limit thermogenesis. However, it is also possible that a change in IL-10 signaling might affect the recruitment of beige precursors, especially in a chronic context. For example, in *Il10*$^{-/-}$ mice beige adipocytes could experience sustained adrenergic signaling that would be expected to lead to their maintenance and enrichment (Altshuler-Keylin et al., 2016). We did observe an increase in the frequency of TMEM26+ cells in iWAT of *Il10*$^{-/-}$ mice, although we did not observe robust increases in the expression of classic beige marker genes (Wu et al., 2012). Future lineage tracing studies will be required to directly test the effects of the IL-10 axis on beige progenitor recruitment and expansion.

Our results suggest that IL-10 signaling provides a brake that limits thermogenic gene expression. Since *Il10ra* is a direct target of PPARγ, it seems reasonable to hypothesize that the IL-10 axis could serve to facilitate lipid storage and maintain adiposity. Given the central role that IL-10 plays in inflammation and immunity, IL-10 signaling might function as a mechanism to conserve energy in the setting of acute systemic demands such as infection. IL-10Rα expression is further elevated in response to obesity and aging, implying that changes in the activity of the IL-10 axis are relevant in these contexts. Finally, our data suggest that blockade of IL-10 signaling in adipose tissue might have beneficial effects in the setting of obesity and insulin resistance. The observation that acute knockdown of IL-10Rα expression in iWAT induces thermogenic gene expression supports further research into the therapeutic utility of targeting the adipose IL-10 axis.

STAR★METHODS

Detailed methods are provided in the online version of this paper and include the following:

- KEY RESOURCES TABLE
- CONTACT FOR REAGENT AND RESOURCE SHARING
- EXPERIMENTAL MODEL AND SUBJECT DETAILS
  - Mice
  - Cell Culture
- METHOD DETAILS
  - Bone marrow transplantation studies
  - Antibiotic Treatment
  - Cold exposure studies
  - Thermoneutral condition studies

(D) Gene ontology analysis of the C/EBPβ ChIP-seq data.

(E) ChIP-seq bedgrah showing C/EBPβ peaks on the indicated genes in D5 differentiated iBAd cells treated with and without IL-10 for 16 hr. Input served as a control of C/EBPβ enrichment. Statistical analysis was performed using Student's t test. *p < 0.05, **p < 0.01, ***p < 0.001, ****p < 0.0001, ns, not significant. Error bars represent SEM. See also Figure S7.

SUPPLEMENTAL INFORMATION

Supplemental Information includes seven figures and two tables and can be found with this article online at https://doi.org/10.1016/j.cell.2017.11.019.

AUTHOR CONTRIBUTIONS

P.R., B.J.T, A.-C.F., J.S., C.H., L.V., T.S., J.W., B.W., and L.G.F. performed the experiments. M.M.S. and A.J.L. performed the HMDP and the METSIM correlation meta-analysis. M.K. and R.L. designed and validated the IL-10Rα ASO. P.R., S.G.Y., K.R., S.T.S., and P.T. designed the experiments and interpreted the data. P.R. and P.T. wrote the manuscript. P.T. and S.T.S. supervised the study.

ACKNOWLEDGMENTS

We thank the UCLA Broad Stem Cell Research Center Core for sequencing. This work was supported by grants from the NIH (F32DK104484 to P.R.; T32AI007323 and T32GM008042 to B.J.T.; HL128822 to T.S.; F32DK109601 to B.W.; HL090533 to K.R., S.G.Y., and P.T.; GM086372 to S.T.S.; and DK063491 P.T.). A-C. F. is funded by the Tri-Service General Hospital, National Defense Medical Center, Taipei, Taiwan.

Received: February 10, 2017
Revised: September 12, 2017
Accepted: November 9, 2017
Published: December 14, 2017

REFERENCES

Altshuler-Keylin, S., Shinoda, K., Hasegawa, Y., Ikeda, K., Hong, H., Kang, Q., Yang, Y., Perera, R.M., Debnath, J., and Kajimura, S. (2016). Beige adipocyte maintenance is regulated by autophagy-induced mitochondrial clearance. Cell Metab. *24*, 402–419.

Bapat, S.P., Myoung Suh, J., Fang, S., Liu, S., Zhang, Y., Cheng, A., Zhou, C., Liang, Y., LeBlanc, M., Liddle, C., et al. (2015). Depletion of fat-resident Treg cells prevents age-associated insulin resistance. Nature *528*, 137–141.

Barot, L.R., Rombeau, J.L., Steinberg, J.J., Crosby, L.O., Feurer, I.D., and Mullen, J.L. (1981). Energy expenditure in patients with inflammatory bowel disease. Arch. Surg. *116*, 460–462.

Benjamini, Y., and Hochberg, Y. (1995). Controlling the false discovery rate: a practical and powerful approach to multiple testing. J. R. Stat. Soc. Series B *57*, 289–300.

Buenrostro, J.D., Giresi, P.G., Zaba, L.C., Chang, H.Y., and Greenleaf, W.J. (2013). Transposition of native chromatin for fast and sensitive epigenomic profiling of open chromatin, DNA-binding proteins and nucleosome position. Nat. Methods *10*, 1213–1218.

Buenrostro, J.D., Wu, B., Chang, H.Y., and Greenleaf, W.J. (2015). ATAC-seq: a method for assaying chromatin accessibility genome-wide. Curr. Protoc. Mol. Biol. *109*, 21.29.1–9.

Church, C.D., Berry, R., and Rodeheffer, M.S. (2014). Isolation and study of adipocyte precursors. Methods Enzymol. *537*, 31–46.

Clementi, A.H., Gaudy, A.M., van Rooijen, N., Pierce, R.H., and Mooney, R.A. (2009). Loss of Kupffer cells in diet-induced obesity is associated with increased hepatic steatosis, STAT3 signaling, and further decreases in insulin signaling. Biochim. Biophys. Acta *1792*, 1062–1072.

Couper, K.N., Blount, D.G., and Riley, E.M. (2008). IL-10: the master regulator of immunity to infection. J. Immunol. *180*, 5771–5777.

den Boer, M.A., Voshol, P.J., Schröder-van der Elst, J.P., Korsheninnikova, E., Ouwens, D.M., Kuipers, F., Havekes, L.M., and Romijn, J.A. (2006). Endogenous interleukin-10 protects against hepatic steatosis but does not improve insulin sensitivity during high-fat feeding in mice. Endocrinology *147*, 4553–4558.

Faulkner, J.L., Gomolak, J.R., and Didion, S.P. (2013). Interleukin-10 deficiency limits the development of obesity and insulin resistance produced by a high fat diet. FASEB J. *27* (*Suppl 1*), 1183.6.

Feldmann, H.M., Golozoubova, V., Cannon, B., and Nedergaard, J. (2009). UCP1 ablation induces obesity and abolishes diet-induced thermogenesis in mice exempt from thermal stress by living at thermoneutrality. Cell Metab. *9*, 203–209.

Gao, M., Zhang, C., Ma, Y., Bu, L., Yan, L., and Liu, D. (2013). Hydrodynamic delivery of mIL10 gene protects mice from high-fat diet-induced obesity and glucose intolerance. Mol. Ther. *21*, 1852–1861.

Goto, T., Naknukool, S., Yoshitake, R., Hanafusa, Y., Tokiwa, S., Li, Y., Sakamoto, T., Nitta, T., Kim, M., Takahashi, N., et al. (2016). Proinflammatory cytokine interleukin-1β suppresses cold-induced thermogenesis in adipocytes. Cytokine *77*, 107–114.

Harms, M., and Seale, P. (2013). Brown and beige fat: development, function and therapeutic potential. Nat. Med. *19*, 1252–1263.

Heinz, S., Benner, C., Spann, N., Bertolino, E., Lin, Y.C., Laslo, P., Cheng, J.X., Murre, C., Singh, H., and Glass, C.K. (2010). Simple combinations of lineage-determining transcription factors prime cis-regulatory elements required for macrophage and B cell identities. Mol. Cell *38*, 576–589.

Hoentjen, F., Harmsen, H.J., Braat, H., Torrice, C.D., Mann, B.A., Sartor, R.B., and Dieleman, L.A. (2003). Antibiotics with a selective aerobic or anaerobic spectrum have different therapeutic activities in various regions of the colon in interleukin 10 gene deficient mice. Gut *52*, 1721–1727.

Hong, E.G., Ko, H.J., Cho, Y.R., Kim, H.J., Ma, Z., Yu, T.Y., Friedline, R.H., Kurt-Jones, E., Finberg, R., Fischer, M.A., et al. (2009). Interleukin-10 prevents diet-induced insulin resistance by attenuating macrophage and cytokine response in skeletal muscle. Diabetes *58*, 2525–2535.

Hummasti, S., and Tontonoz, P. (2006). The peroxisome proliferator-activated receptor N-terminal domain controls isotype-selective gene expression and adipogenesis. Mol. Endocrinol. *20*, 1261–1275.

Kanda, H., Tateya, S., Tamori, Y., Kotani, K., Hiasa, K., Kitazawa, R., Kitazawa, S., Miyachi, H., Maeda, S., Egashira, K., and Kasuga, M. (2006). MCP-1 contributes to macrophage infiltration into adipose tissue, insulin resistance, and hepatic steatosis in obesity. J. Clin. Invest. *116*, 1494–1505.

Keubler, L.M., Buettner, M., Häger, C., and Bleich, A. (2015). A Multihit model: colitis lessons from the interleukin-10-deficient mouse. Inflamm. Bowel Dis. *21*, 1967–1975.

Knudsen, J.G., Murholm, M., Carey, A.L., Biensø, R.S., Basse, A.L., Allen, T.L., Hidalgo, J., Kingwell, B.A., Febbraio, M.A., Hansen, J.B., and Pilegaard, H. (2014). Role of IL-6 in exercise training- and cold-induced UCP1 expression in subcutaneous white adipose tissue. PLoS ONE *9*, e84910.

Kowalski, G.M., Nicholls, H.T., Risis, S., Watson, N.K., Kanellakis, P., Bruce, C.R., Bobik, A., Lancaster, G.I., and Febbraio, M.A. (2011). Deficiency of haematopoietic-cell-derived IL-10 does not exacerbate high-fat-diet-induced inflammation or insulin resistance in mice. Diabetologia *54*, 888–899.

Laakso, M., Kuusisto, J., Stančáková, A., Kuulasmaa, T., Pajukanta, P., Lusis, A.J., Collins, F.S., Mohlke, K.L., and Boehnke, M. (2017). The Metabolic Syndrome in Men study: a resource for studies of metabolic and cardiovascular diseases. J. Lipid Res. *58*, 481–493.

Lang, R., Patel, D., Morris, J.J., Rutschman, R.L., and Murray, P.J. (2002). Shaping gene expression in activated and resting primary macrophages by IL-10. J. Immunol. *169*, 2253–2263.

Langfelder, P., and Horvath, S. (2008). WGCNA: an R package for weighted correlation network analysis. BMC Bioinformatics *9*, 559.

Lee, M.W., Odegaard, J.I., Mukundan, L., Qiu, Y., Molofsky, A.B., Nussbaum, J.C., Yun, K., Locksley, R.M., and Chawla, A. (2015). Activated type 2 innate lymphoid cells regulate beige fat biogenesis. Cell *160*, 74–87.

Long, J.Z., Svensson, K.J., Bateman, L.A., Lin, H., Kamenecka, T., Lokurkar, I.A., Lou, J., Rao, R.R., Chang, M.R., Jedrychowski, M.P., et al. (2016). The secreted enzyme PM20D1 regulates lipidated amino acid uncouplers of mitochondria. Cell *166*, 424–435.

Lumeng, C.N., and Saltiel, A.R. (2011). Inflammatory links between obesity and metabolic disease. J. Clin. Invest. *121*, 2111–2117.

Lumeng, C.N., Bodzin, J.L., and Saltiel, A.R. (2007). Obesity induces a phenotypic switch in adipose tissue macrophage polarization. J. Clin. Invest. *117*, 175–184.

Madsen, K.L., Doyle, J.S., Tavernini, M.M., Jewell, L.D., Rennie, R.P., and Fedorak, R.N. (2000). Antibiotic therapy attenuates colitis in interleukin 10 gene-deficient mice. Gastroenterology *118*, 1094–1105.

Mauer, J., Chaurasia, B., Goldau, J., Vogt, M.C., Ruud, J., Nguyen, K.D., Theurich, S., Hausen, A.C., Schmitz, J., Brönneke, H.S., et al. (2014). Signaling by IL-6 promotes alternative activation of macrophages to limit endotoxemia and obesity-associated resistance to insulin. Nat. Immunol. *15*, 423–430.

Miller, A.M., Wang, H., Bertola, A., Park, O., Horiguchi, N., Ki, S.H., Yin, S., Lafdil, F., and Gao, B. (2011). Inflammation-associated interleukin-6/signal transducer and activator of transcription 3 activation ameliorates alcoholic and nonalcoholic fatty liver diseases in interleukin-10-deficient mice. Hepatology *54*, 846–856.

Moldawer, L.L., Georgieff, M., and Lundholm, K. (1987). Interleukin 1, tumour necrosis factor-alpha (cachectin) and the pathogenesis of cancer cachexia. Clin. Physiol. *7*, 263–274.

Moore, K.W., de Waal Malefyt, R., Coffman, R.L., and O'Garra, A. (2001). Interleukin-10 and the interleukin-10 receptor. Annu. Rev. Immunol. *19*, 683–765.

Murray, P.J. (2005). The primary mechanism of the IL-10-regulated antiinflammatory response is to selectively inhibit transcription. Proc. Natl. Acad. Sci. USA *102*, 8686–8691.

Murray, P.J., and Smale, S.T. (2012). Restraint of inflammatory signaling by interdependent strata of negative regulatory pathways. Nat. Immunol. *13*, 916–924.

Nisoli, E., Briscini, L., Giordano, A., Tonello, C., Wiesbrock, S.M., Uysal, K.T., Cinti, S., Carruba, M.O., and Hotamisligil, G.S. (2000). Tumor necrosis factor alpha mediates apoptosis of brown adipocytes and defective brown adipocyte function in obesity. Proc. Natl. Acad. Sci. USA *97*, 8033–8038.

Odegaard, J.I., Lee, M.W., Sogawa, Y., Bertholet, A.M., Locksley, R.M., Weinberg, D.E., Kirichok, Y., Deo, R.C., and Chawla, A. (2016). Perinatal licensing of thermogenesis by IL-33 and ST2. Cell *166*, 841–854.

Ohno, H., Shinoda, K., Spiegelman, B.M., and Kajimura, S. (2012). PPARγ agonists induce a white-to-brown fat conversion through stabilization of PRDM16 protein. Cell Metab. *15*, 395–404.

Parks, B.W., Nam, E., Org, E., Kostem, E., Norheim, F., Hui, S.T., Pan, C., Civelek, M., Rau, C.D., Bennett, B.J., et al. (2013). Genetic control of obesity and gut microbiota composition in response to high-fat, high-sucrose diet in mice. Cell Metab. *17*, 141–152.

Parks, B.W., Sallam, T., Mehrabian, M., Psychogios, N., Hui, S.T., Norheim, F., Castellani, L.W., Rau, C.D., Pan, C., Phun, J., et al. (2015). Genetic architecture of insulin resistance in the mouse. Cell Metab. *21*, 334–346.

Petruzzelli, M., Schweiger, M., Schreiber, R., Campos-Olivas, R., Tsoli, M., Allen, J., Swarbrick, M., Rose-John, S., Rincon, M., Robertson, G., et al. (2014). A switch from white to brown fat increases energy expenditure in cancer-associated cachexia. Cell Metab. *20*, 433–447.

Qiu, Y., Nguyen, K.D., Odegaard, J.I., Cui, X., Tian, X., Locksley, R.M., Palmiter, R.D., and Chawla, A. (2014). Eosinophils and type 2 cytokine signaling in macrophages orchestrate development of functional beige fat. Cell *157*, 1292–1308.

Rao, R.R., Long, J.Z., White, J.P., Svensson, K.J., Lou, J., Lokurkar, I., Jedrychowski, M.P., Ruas, J.L., Wrann, C.D., Lo, J.C., et al. (2014). Meteorin-like is a hormone that regulates immune-adipose interactions to increase beige fat thermogenesis. Cell *157*, 1279–1291.

Rogers, G.W., Brand, M.D., Petrosyan, S., Ashok, D., Elorza, A.A., Ferrick, D.A., and Murphy, A.N. (2011). High throughput microplate respiratory measurements using minimal quantities of isolated mitochondria. PLoS ONE *6*, e21746.

Rosen, E.D., and Spiegelman, B.M. (2014). What we talk about when we talk about fat. Cell *156*, 20–44.

Sallam, T., Jones, M.C., Gilliland, T., Zhang, L., Wu, X., Eskin, A., Sandhu, J., Casero, D., Vallim, T.Q., Hong, C., et al. (2016). Feedback modulation of cholesterol metabolism by the lipid-responsive non-coding RNA LeXis. Nature *534*, 124–128.

Saraiva, M., and O'Garra, A. (2010). The regulation of IL-10 production by immune cells. Nat. Rev. Immunol. *10*, 170–181.

Sartipy, P., and Loskutoff, D.J. (2003). Monocyte chemoattractant protein 1 in obesity and insulin resistance. Proc. Natl. Acad. Sci. USA *100*, 7265–7270.

Seale, P., Kajimura, S., Yang, W., Chin, S., Rohas, L.M., Uldry, M., Tavernier, G., Langin, D., and Spiegelman, B.M. (2007). Transcriptional control of brown fat determination by PRDM16. Cell Metab. *6*, 38–54.

Shoelson, S.E., Lee, J., and Goldfine, A.B. (2006). Inflammation and insulin resistance. J. Clin. Invest. *116*, 1793–1801.

Siersbæk, M.S., Loft, A., Aagaard, M.M., Nielsen, R., Schmidt, S.F., Petrovic, N., Nedergaard, J., and Mandrup, S. (2012). Genome-wide profiling of peroxisome proliferator-activated receptor γ in primary epididymal, inguinal, and brown adipocytes reveals depot-selective binding correlated with gene expression. Mol. Cell. Biol. *32*, 3452–3463.

Stancáková, A., Javorský, M., Kuulasmaa, T., Haffner, S.M., Kuusisto, J., and Laakso, M. (2009). Changes in insulin sensitivity and insulin release in relation to glycemia and glucose tolerance in 6,414 Finnish men. Diabetes *58*, 1212–1221.

Sun, L., Goff, L.A., Trapnell, C., Alexander, R., Lo, K.A., Hacisuleyman, E., Sauvageau, M., Tazon-Vega, B., Kelley, D.R., Hendrickson, D.G., et al. (2013). Long noncoding RNAs regulate adipogenesis. Proc. Natl. Acad. Sci. USA *110*, 3387–3392.

Tang, T., Zhang, J., Yin, J., Staszkiewicz, J., Gawronska-Kozak, B., Jung, D.Y., Ko, H.J., Ong, H., Kim, J.K., Mynatt, R., et al. (2010). Uncoupling of

inflammation and insulin resistance by NF-kappaB in transgenic mice through elevated energy expenditure. J. Biol. Chem. *285*, 4637–4644.

Tiraby, C., and Langin, D. (2003). Conversion from white to brown adipocytes: a strategy for the control of fat mass? Trends Endocrinol. Metab. *14*, 439–441.

Tisdale, M.J. (1997). Biology of cachexia. J. Natl. Cancer Inst. *89*, 1763–1773.

Tong, A.J., Liu, X., Thomas, B.J., Lissner, M.M., Baker, M.R., Senagolage, M.D., Allred, A.L., Barish, G.D., and Smale, S.T. (2016). A stringent systems approach uncovers gene-specific mechanisms regulating inflammation. Cell *165*, 165–179.

van Marken Lichtenbelt, W.D., Vanhommerig, J.W., Smulders, N.M., Drossaerts, J.M., Kemerink, G.J., Bouvy, N.D., Schrauwen, P., and Teule, G.J. (2009). Cold-activated brown adipose tissue in healthy men. N. Engl. J. Med. *360*, 1500–1508.

Villanueva, C.J., Waki, H., Godio, C., Nielsen, R., Chou, W.L., Vargas, L., Wroblewski, K., Schmedt, C., Chao, L.C., Boyadjian, R., et al. (2011). TLE3 is a dual-function transcriptional coregulator of adipogenesis. Cell Metab. *13*, 413–427.

Villanueva, C.J., Vergnes, L., Wang, J., Drew, B.G., Hong, C., Tu, Y., Hu, Y., Peng, X., Xu, F., Saez, E., et al. (2013). Adipose subtype-selective recruitment of TLE3 or Prdm16 by PPARγ specifies lipid storage versus thermogenic gene programs. Cell Metab. *17*, 423–435.

Virtanen, K.A., Lidell, M.E., Orava, J., Heglind, M., Westergren, R., Niemi, T., Taittonen, M., Laine, J., Savisto, N.J., Enerbäck, S., and Nuutila, P. (2009). Functional brown adipose tissue in healthy adults. N. Engl. J. Med. *360*, 1518–1525.

Wallenius, V., Wallenius, K., Ahrén, B., Rudling, M., Carlsten, H., Dickson, S.L., Ohlsson, C., and Jansson, J.O. (2002). Interleukin-6-deficient mice develop mature-onset obesity. Nat. Med. *8*, 75–79.

Wernstedt Asterholm, I., Tao, C., Morley, T.S., Wang, Q.A., Delgado-Lopez, F., Wang, Z.V., and Scherer, P.E. (2014). Adipocyte inflammation is essential for healthy adipose tissue expansion and remodeling. Cell Metab. *20*, 103–118.

Wu, M., Neilson, A., Swift, A.L., Moran, R., Tamagnine, J., Parslow, D., Armistead, S., Lemire, K., Orrell, J., Teich, J., et al. (2007). Multiparameter metabolic analysis reveals a close link between attenuated mitochondrial bioenergetic function and enhanced glycolysis dependency in human tumor cells. Am. J. Physiol. Cell Physiol. *292*, C125–C136.

Wu, J., Boström, P., Sparks, L.M., Ye, L., Choi, J.H., Giang, A.H., Khandekar, M., Virtanen, K.A., Nuutila, P., Schaart, G., et al. (2012). Beige adipocytes are a distinct type of thermogenic fat cell in mouse and human. Cell *150*, 366–376.

Xie, L., Fu, Q., Ortega, T.M., Zhou, L., Rasmussen, D., O'Keefe, J., Zhang, K.K., and Chapes, S.K. (2014). Overexpression of IL-10 in C2D macrophages promotes a macrophage phenotypic switch in adipose tissue environments. PLoS ONE *9*, e86541.

Zambelli, F., Pesole, G., and Pavesi, G. (2009). Pscan: finding over-represented transcription factor binding site motifs in sequences from co-regulated or co-expressed genes. Nucleic Acids Res. *37*, W247–W252.

STAR★METHODS

KEY RESOURCES TABLE

REAGENT or RESOURCE	SOURCE	IDENTIFIER
Antibodies		
UCP1	Abcam	Cat# ab10983 RRID:AB_2241462
PGC1α	Santa Cruz	Cat# sc-13067 RRID:AB_2166218
ATF-2	Santa Cruz	Cat# sc-6233 RRID:AB_2058437
pATF-2	Santa Cruz	Cat# sc-8398 RRID:AB_626709
C/EBPβ	Santa Cruz	Cat# sc-150 RRID:AB_2260363
Tubulin	Millipore	Cat# CP06 RRID:AB_2617116
STAT3	Cell Signaling	Cat# 9139 RRID:AB_331757
pSTAT3 (Tyr705)	Cell Signaling	Cat# 9131 RRID:AB_331586
Actin	Sigma	Cat# A2066 RRID:AB_476693
AKT	Cell Signaling	Cat# 9272 RRID:AB_329827
pAKT (Ser473)	Cell Signaling	Cat# 4060 RRID:AB_2315049
IL10Rα	R&D	AF-474-SP
H3K4ME1	Abcam	Cat# ab8895 RRID:AB_306847
ON-TARGETplus mouse STAT3 siRNA SMARTpool	Dharmacon	L-040794-01-0005
Non-targeting POOL	Dharmacon	D-001810-03-05
CD11b	Tonbo	60-0112-U100
CD11c	Tonbo	35-0114-U100
F4/80	Tonbo	20-4801-U025
TMEM26	Imgenex	IMG-6633A
DAPI	Molecular Probes	D1306
B220	BD Bioscience	561880
Ter119	eBioscience	25-5921-81
CD137	eBioscience	12-1371-81
IL10Rα generation 2.5 antisense oligonucleotide (ASO)	Ionis Pharmaceutical	939570
DMEM	Corning	MT-10-013-CM
FBS	Omega Scientific	FB11
DMEM/F12 Glutamax	Thermo Fischer	10565-018
Trypsin	Corning	MT-25-053-CI
Penicillin/Streptomycin	Corning	MT-30-002-CI
Lipofectamine 2000	Thermo Fischer	11668027
Bacterial and Virus Strains		
Adenovirus: IL10Rα shRNA	This paper	N/A
Retrovirus: IL10Rα	This paper	N/A
Chemicals, Peptides, and Recombinant Proteins		
3-isobutyl-1-methylxanthine	Sigma	I-7018
Dexamethasone	Sigma	D-2915
Rosiglitazone	Sigma	R-2408
T3 (3,3′,5-Triiodo-L-thyronine)	Sigma	T-2877
Isoproterenol	Sigma	I-6504
Forskolin	Sigma	F3917
Indomethacin	Sigma	I-7378

(*Continued on next page*)

Continued

REAGENT or RESOURCE	SOURCE	IDENTIFIER
Insulin	Thermo Fischer	12585-014
Recombinant mouse IL10	Peprotech	210-10
Glucose	Sigma	G8769-100ML
Adenosine	Sigma	A9251-1G
Ascorbic acid	Sigma	A4544
Electrophoresis grade delipidated BSA	Sigma	A7030
Sodium Metabisulfite	Sigma	S9000
Collagenase D	Roche	11088882001
Collagenase B	Roche	11 088 831 001
Dispase II	Roche	04942078001
Enroflox® 100 (Enrofloxacin)	Norbrook	NDC-55529-152-04
Red Blood Cell (RBC) lysis buffer	Sigma	R7757
Humulin® R U-100 (Human Insulin for ITT)	Lilly	002-8215-01
Puromycin	Sigma	P9620
Hygromycin	Sigma	H0654
Polybrene	Millipore	TR-1003-G
RIPA buffer	Boston BioProducts	BP-115-500ml
IsoFlo (Isoflurane)	Zoetis	N/A
Formalin	Fischer	23-305-510
Critical Commercial Assays		
TruSeq Stranded Total RNA Library Prep Kit	Illumina	RS-122-2102
Nextera Tn5 Transposase kit	Illumina	FC-121-1030
Kapa LTP Library Preparation Kit	KR0453	KR0453
Wako L-Type Triglyceride Assay M Enzyme Color A	Wako	461-08992
Wako NEFA-HR	Wako	991-34891
Wako Cholesterol E Test	Wako	439-17501
Milliplex Kit	Millipore	MCYTOMAG-70K-09 M
3-CAT Research ELISA	Rocky MTN Diagnositics	BA E-5600
BCA protein assay kit	Pierce	23225
Vectastain Elite ABC kit	Vectastain	PK-6100
Deposited Data		
All sequencing data	This paper	GEO: GSE94654
Experimental Models: Cell Lines		
iWAT primary preadipocytes	This paper	N/A
iWAT immortalized preadipocytes	This paper	N/A
BAT immortalized preadipocytes	This paper	N/A
iBAd-BAT immortalized preadipocytes expressing IL10Rα	This paper	N/A
Phoenix-ECO cells (Retrovirus packaging)	ATCC	CRL-3214
Experimental Models: Organisms/Strains		
Mouse: *Il10*$^{-/-}$: B6129P2-*Il10*^{tm1cgn}/J	Jackson Lab	02251
Mouse: WT: C57BL/6J	Jackson Lab	000664
Oligonucleotides		
Mouse qPCR Primers, see Table S1	N/A	N/A
ChIP-qPCR Primers, see Table S2	N/A	N/A
CACCGGGCCAGCTGTATAGACATCTC GAAAGATGTCTATACAGCTGGCCC-Lacz shRNA	This paper	N/A
CACCGCATCTTAGTCATATCTATGCCGAA GCATAGATATGACTAAGATGC- IL10Rα shRNA	This paper	N/A

(*Continued on next page*)

Continued

REAGENT or RESOURCE	SOURCE	IDENTIFIER
Recombinant DNA		
pENTR/U6 plasmid IL10Rα	This paper	N/A
pBLOCK-IT adenovirus vector IL10Rα shRNA	This paper	N/A
Retroviral pBABE-puro IL10Rα	This paper	N/A
pENTR223.1 mouse IL10Rα	Harvard Plasmids	MmCD00081028
Software and Algorithms		
Prism6	GraphPad	N/A
ImageJ	https://imagej.nih.gov/ij/	N/A
HOMER	http://homer.ucsd.edu/homer/	N/A
MACS2	http://liulab.dfci.harvard.edu/MACS/Download.html	N/A
Pscan	http://159.149.160.88/pscan/	N/A
Samtools	https://github.com/samtools/samtools	N/A
SeqMonk	https://www.bioinformatics.babraham.ac.uk/projects/seqmonk/	N/A
Bowtie2	http://bowtie-bio.sourceforge.net/bowtie2/index.shtml	N/A
Tophat	http://tophat.cbcb.umd.edu	N/A
Bioconductor DESeq2	http://bioconductor.org/packages/release/bioc/html/DESeq.html	N/A
MS Excel 2016	Microsoft	N/A
Other		
High Fat Diet (HFD; 60% kcal fat)	Research Diets	N/A
TissueLyzer	QIAGEN	N/A
Metabolic Chamber-Comprehensive Lab Animal Monitoring System (CLAMS)	Columbus Instruments	N/A
Mouse MRI machine	EchoMRI	N/A
FACS machine	BD Bioscience	BD FACSVERSE
Applied Biosystem (ABI) qPCR machine	Thermo Fischer	QuantStudio 6 Flex System
100 μm cell strainer	Falcon	352360
70 μm cell strainer	Falcon	352350
BioCoat 6-well collagen I plate	Fisher	08-772-69
Syber Green Master Mix	Diagenode	DMMLD2D600

CONTACT FOR REAGENT AND RESOURCE SHARING

Further information and requests for resources and reagents should be directed to and will be fulfilled by the Lead Contact, Peter Tontonoz (ptontonoz@mednet.ucla.edu).

EXPERIMENTAL MODEL AND SUBJECT DETAILS

Mice

Breeding pairs of *Il10*$^{-/-}$ mice and WT controls were acquired from Jackson Laboratory and colony maintained in pathogen-free barrier-protected environment (12:12 h light/dark cycle, 22°C-24°C) at UCLA animal facility. Male mice were used for all experiments. Experimental mice were sacrificed at ages mentioned in figure legends for histological, protein, and gene expression analysis. All the mutant strains used in this study were backcrossed to a C57BL/6 background as stated by Jackson inventory. Animal experiments were conducted in accordance with the UCLA Institutional Animal Care and Research Advisory Committee.

Cell Culture

Murine white and brown preadipocytes were cultured in Dulbecco's modified Eagle's medium (DMEM) supplemented 10% fetal bovine serum (FBS). For *in vitro* brown/beige adipocyte differentiation, preadipocytes were grown to confluence in DMEM

with 10% FBS plus insulin (5 μg/ml) and T3 (1 nM). Confluent cells were induced to differentiate with dexamethasone (1 μM), IBMX (0.5 mM), insulin (5 μg/ml), indomethacin (125 nM) and Rosiglitazone (1 μM) for 2 days, followed by insulin, T3 and Rosiglitazone alone. On the fourth day, cells were pretreated for overnight (~16h) with and without 100 ng/ml IL10 and next day treated with 10 μM isoproterenol or forskolin for 5-6 h. White and brown preadipocytes were isolated and immortalized as previously described (Villanueva et al., 2013) and below. Brown preadipocytes IL10Rα expressing stable cells (iBAD) were generated using the pBabe retroviral system (Hummasti and Tontonoz, 2006) and described below.

METHOD DETAILS

Bone marrow transplantation studies

Ten week old *Il10*$^{-/-}$ mice (n = 3-4) were euthanized using isoflurane. Mice were dunked in 70% EtOH and fur/skin was removed from legs. Quadriceps and hamstring were removed to expose pelvic joints. Hair and muscles were removed and legs were kept in ice-cold PBS during processing of other legs. Tissues were then removed from legs to expose tibia and femur. After all the legs were collected, tibiae and femurs were separated and kept in PBS/DMEM solution. Bones were picked with forceps and using 23G subQ gauge needles PBS/DMEM solution was pushed through to oust bone marrow onto 2-3ml DMEM solution on a Petri dish. Using 18 gauge needles bone marrow chunks were broken apart by gently aspirating. Bone marrow solution was strained onto 50 mL conical tube using cell strainer (70 μm) to remove any debris. Petri dish was rinsed with 1-2 mL PBS/DMEM to collect residual bone marrow. The solution was spun down for 5 min at room temperature (RT) at 1200 rpm. RBC lysis buffer was added to the pellet for 5min and spun down again. Pellets were washed three times and bone marrow cells were counted and stored on ice for later injection into recipient mice. For bone marrow transplantation (BMT) studies, recipient WT or *Il10*$^{-/-}$ mice (10 weeks of age) were lethally irradiated with 900 rads and transplanted with 3 × 10^6 bone marrow cells from above donor mice (*Il10*$^{-/-}$) via tail vein injection. After injection mice were place in immunocompromised room in autoclaved cages supplemented with sterilized water and chow feed. Mice were kept on antibiotics regiment (see below) for 6 weeks and then moved to experimental facility and maintained in normal chow diet. Mice weights and body composition were measured every week. Mice were subjected to metabolic studies as indicated in figures and figure legends.

Antibiotic Treatment

Antibiotic treatment was performed as previously described (Hoentjen et al., 2003; Madsen et al., 2000) with modifications. Weaned (3 week old) WT or *Il10*$^{-/-}$ mice were treated with 660 mg/L broad spectrum antibiotic enrofloxacin (Enroflox® 100, Norbrook, equivalent to ciprofloxacin). Antibiotic was added to drinking water every week for 7 weeks dosed at ~100 mg/kg/day.

Cold exposure studies

For 4°C cold exposure experiment, WT or *Il10*$^{-/-}$ mice at 8-10 weeks of age were singly or doubly housed at 4°C room in a non-bedded cage with access to food and water for the time points indicated in figure legend. At the end of the experiment, iWATs were resected for gene expression analysis.

Thermoneutral condition studies

For thermoneutral experiment, WT and *Il10*$^{-/-}$ mice at 4 weeks of age were housed (4/cage with bedding) in 30°C room with 12h light:dark cycle for 7 weeks on a regular chow diet. After 7 weeks, various tissues including iWATs were resected for gene analysis.

High fat diet studies

For diet study, 10 weeks of age *Il10*$^{-/-}$ and WT mice were fed a 60% high-fat diet (Research Diets) for the indicated times. Mice weights and body composition were measured every week and food was replaced weekly.

Cytokines and Lipid Measurement

On the day of harvest, mice were fasted for 6 h and euthanized using isoflurane. Blood was drawn by cardiac puncture and kept in clot activator commercial tube (Terumo CAPIJET, T-MG) and placed on ice. Blood was spun down at 8000 rpm for 5 mins at 4°C table-top centrifuge and serum was collected and stored at −80°C. Liver lipids were isolated using Folch extraction method and as previously described (Sallam et al., 2016). Serum cytokines were measured using Milliplex mouse cytokine Magnetic kit (Millipore) and serum lipids were measured using Wako L-Type TG M, Wako NEFA-HR, or Wako Cholesterol E Test kit according to manufactures' instructions.

Serum and Adipose Catecholamine Measurement

Serum samples were collected as described above. Adipose tissue homogenates were collected as previously described (Qiu et al., 2014). Briefly, resected adipose tissues were flash frozen in liquid nitrogen and stored at −80°C until further analysis. 600 μL of homogenization buffer (0.01N HCl, 1mM EDTA, 4mM $Na_2S_2O_5$) was added to 100-300 mg of tissue and were homogenized using TissueLyzer for 1min at 30 MHz. Cellular debris was cleared by centrifugation at 13000 rpm for 15 min at 4°C. 50 μL of serum and 200 μL of cleared adipose homogenate was used to measure catecholamine levels using 3-CAT Research ELISA (Labor Diagnostika Nord GmBH & Co.) according to manufacturer's instructions.

Measurement of Core Temperature

Core body temperature of WT and *Il10*$^{-/-}$ mice was measured at room temperature using rectal probe (BAT-10) purchased from Physitemp.

Glucose Tolerance Test (GTT) and Insulin Tolerance Test (ITT)

For glucose tolerance tests, mice were fasted for 6 h and challenged with an intraperitoneally (i.p.) injection of glucose (2 g/kg). For insulin tolerance tests, mice were fasted for 6 hr and given an i.p. injection of insulin (1 U/kg). Blood glucose levels were monitored using the ACCUCHEK active glucometer (Roche) at times indicated in figure legends.

Indirect Calorimetry and Body Composition Measurements

Indirect calorimetry was performed using a Columbus Instruments Comprehensive Lab Animal Monitoring System (CLAMS, Columbus Instruments). Animals were placed individually in chambers for 3 consecutive days at ambient temperature (26.5°C) with 12 hr light/dark cycles. Animals had free access to food and water. Respiratory measurements were made in 20 min intervals after initial 7-9 hr acclimation period. Energy expenditure was calculated from VO2 and RER using the Lusk equation, EE in Kcal/hr = (3.815 + 1.232 X RER) X VO2 in ml/min. Food intake was measured in metabolic chambers. Body composition (fat and lean mass) was determined using EchoMRI Body Composition Analyzer

Ex vivo iWAT IL10 treatment

For *ex vivo* iWAT IL10 treatment, 10 week old WT mice were housed at cold room (4-6°C) for 6 h and iWATs were isolated and minced, placed in KREB's Ringer Buffer (12 mM HEPES, 121 mM NaCl, 4.9 mM KCl, 1.2 mM $MgSO_4$, 0.33 mM $CaCl_2$) supplemented with 0.1% glucose and incubated with and without 100 ng/ml IL10 for 30 mins-1h at 37°C.

Construction of Adenovirus (Ad) expressing IL10Rα shRNA

Invitrogen's Gateway cloning strategy was used to generate mouse IL10Rα shRNA adenovirus. shRNA targeting mouse IL10Rα was designed using Invitrogen Block-iT RNAi Designer. Forward and reverse shRNA oligonucleotides were synthesized by Integrated DNA Techonologies (IDT) and diluted to 200 uM and annealed and ligated into gateway entry plasmid pENTR/U6 vector (Invitrogen). To generate mammalian expression constructs, we used LR recombination between IL10Rα containing pENTR/U6 and pAD-BLOCK-iT to generate AD-shIL10Rα. Viruses were amplified, purified, and tittered by Viraquest.

Adenovirus IL10Rα shRNA injection into iWAT

For the IL10Rα shRNA adenovirus delivery to fat pads, $2X10^9$ PFU of adenovirus was percutaneously injected into each inguinal fat depot of anesthetized WT mice at 8-10 weeks of age. In each mouse, Ad-IL10Rα shRNA was injected into iWAT on one side, and Ad-Lacz shRNA (control) was injected into the contralateral side as a control. 4-5 days after the injection, iWATs were resected for gene expression analysis.

Acute IL10Rα antisense oligonucleotide (ASO) studies

For acute ASO studies, WT mice at 8-10 weeks of age were i.p. injected with control or IL10Rα ASO (CCTTTCTACAGATATG) at 25mg/kg for twice a week for 3 weeks. Body weight was measured weekly and body composition was determined by EchoMRI analysis. At the end of ASO treatment, various tissues were resected and weighted and subjected to gene expression analysis.

Tissue hematoxylin and eosin (H&E) staining and immunohistochemistry

Tissues (4-5 microns thickness) were placed in cassettes and submerged in 10% formalin solution overnight. Tissue cassettes were washed with tap water for 15 minutes and stored in 70% EtOH at room temperature. Paraffin embedment and H&E staining was performed at the Translational Pathology Core Laboratory (TPCL) at UCLA. Vectastain Elite ABC kit was used for UCP1 and MCP1 immunohistochemistry as per manufacturer's instructions.

Cellular and Mitochondrial Respiration assay

Cell were seeded in a XF24 plate, differentiated, and analyzed in a XF24 analyzer (Seahorse Bioscience/Agilent) as described (Wu et al., 2007). Briefly, oxygen consumption rate (OCR) was measured before and after the sequential injection of 0.75 μM oligomycin, 1 μM FCCP, and 1 μM of rotenone/myxothiazol. Mixing, waiting, and measurement times were 5, 2, and 2 min, respectively. Measures were normalized by total protein. In another set of experiments, mitochondria were isolated from fresh tissues and immediately used in a XF24 analyzer as previously described (Rogers et al., 2011). Briefly, mitochondria were isolated in MSHE+BSA buffer using a 800 g/8000 g dual centrifugation method and resuspended in MAS buffer. Protein concentration was determined using a Bradford Assay reagent (Bio-Rad) and 20 μg of protein were seeded per well by centrifugation. Coupling and electron flow assays were performed as described (Rogers et al., 2011). For the coupling assay, basal oxygen consumption rate (OCR) was measured in the presence of 10 mM succinate and 2 μM rotenone, and after sequential addition of 4 mM ADP (Complex V substrate), 2.5 μg/ml oligomycin (Complex V inhibitor), 4 μM FCCP (mitochondrial uncoupler) and 4 μM antimycin A (Complex III inhibitor). Coupled respiration was calculated as the difference between basal and response to oligomycin. Uncoupled respiration was the difference

between oligomycin and antimycin A injections. For electron flow assays, basal OCR was measured in presence of 10 mM pyruvate (Complex I substrate), 2 mM malate and 4 μM FCCP, and after sequential addition of 2 μM rotenone (Complex I inhibitor), 10 mM succinate (Complex II substrate), 4 μM antimycin A (Complex III inhibitor) and 1mM TMPD containing 10 mM ascorbate (Complex IV substrate). Complex III respiration corresponds to the antimycin A-sensitive respiration.

Construction of immortalized beige/brown preadipocytes expressing IL10Rα (iBAd) cells

Mouse IL10Rα in gateway cloning vector pENTR223.1 was purchased from Harvard Plasmids. To generate mammalian expression construct, pENT223.1 mIL10Rα was LR recombined into gateway retrovirus vector pBabe-puro. pBABE-mIL10Rα was transfected into retrovirus packaging Pheonix E cells for 48hrs. Target cells (immortalized beige/brown preadipocytes) were plated at 50% confluency 24hrs post-transfection. 48 h after transfection media from transfected Phoenix-E cells were harvested and spun down for 5min at 5000 rpm to pellet cells and debris. Retrovirus containing supernatant was carefully removed and plated onto target cells with 1:1000 polybrene for overnight. Next day, media was replaced with regular growth media and cells were incubated for additional 24 h. 4.5 μg/ml puromycin selection was performed to select for cells stably expressing mIL10Rα.

Isolation of and immortalization of primary white and brown adipocytes

Male mice (8-10 week old) were euthanized in isoflurane chamber. Mice were sprayed thoroughly with 70% EtOH. 100-300 mg of inguinal WAT (iWAT) or BAT were dissected and placed on sterile 6-well tissue culture plate with ice-cold 1XPBS. Fat pads were blotted on a napkin to removed excess liquid. Tissues were cut with scissors and minced using blade. Minced fat pads (600-800 mg) were placed in a15ml conical tube containing 3 mL of digestion buffer (PBS, 1.5 U/ml Collagenase D (iWAT) or collagenase B (BAT), 2.4 U/ml Dispase II, 10 mM $CaCl_2$) and incubated at 37°C for 45 min with gentle shaking. Inside tissue culture hood, 10-15 mL of plating media DMEM/F12 with glutamax supplemented with 15%FBS and 1% pen/strep was added to digested solution and slowly resuspended 5 times. The digestion mixture was passed through 100 μm cell strainer and centrifuged at 500 x g for 10 mins at room temperature. Supernatant was carefully decanted and pellet resuspended in 10 mL of plating media and passed through 40 μm cell strainer. Filtered suspension was spun down again at 500 x g for 10 mins at room temperature. Supernatant was decanted and pellet resuspended in 6ml plating media and plated onto collagen-coated plates. After overnight incubation, media was changed every other day until the cells reached 70% confluency (~3-4 days post-harvest). White and brown stromal vascular fractions (SVF) were with differentiated into beige/brown adipocytes using protocol mentioned above or immortalized. For immortalization, retrovirus-expressing largeT-antigen in pBABE-hygromycin vector was generated as mentioned above. Virus was added to target cells and selected with 600 μg/ml hygromycin to make immortalized cells.

ATAC-Seq in cells

ATAC-Seq libraries were prepared from 100,000 cells using the Nextera Tn5 Transposase and DNA library preparation kit (Illumina) as described (Buenrostro et al., 2015) with slight modifications. Libraries were single-end sequenced (50bp) on an Illumina HiSeq 2000. Reads were mapped to the mouse genome (NCBI37/mm9) using Bowtie2. Reads were removed from the subsequent analysis if they were duplicated, mapped to mitochondrial genome, or aligned to unmapped contiguous sequences. Peak calling was performed using MACS2 using parameters callpeak–nomodel -g mm–keep-dup all -q 0.01–llocal 10000. The reads were converted to reads per thousand base pairs peak per million mapped reads (RPKM) by dividing by the total number of reads per sample.

ATAC-Seq in mature adipocytes

Adipocyte nuclei isolation from chow-fed 10 week old WT and *Il10*$^{-/-}$ mice was performed as previously described with modifications (Church et al., 2014). WT and *Il10*$^{-/-}$ mice iWAT (~100-200 mg) was isolated and minced and digested in Krebs Ringer Henseleit Buffer (1M HEPES, 2M NaCl, 1 M KCL, 1 M $CaCl_2$, 1 M $MgCl_2$, 1M K_2HPO4, pH 7.4) supplemented with 5mM glucose, 0.1 μM adenosine, 0.1 mg/ml ascorbic acid, 4% electrophoresis grade delipidated BSA and collagenase D for 45 mins saking at 180 rpm at 37°C. Adipocyte suspension were filtered through 100 μm nylon mesh and washed with buffer. 250,000 cells from the filtered adipocyte suspension were subjected to ATAC-Seq procedure as described above.

RNA-Seq

Total RNA was prepared as described (Tong et al., 2016). Strand-specific libraries were generated from 500 ng total RNA using the TruSeq Stranded Total RNA Library Prep Kit (Illumina). cDNA libraries were single-end sequenced (50bp) on an Illumina HiSeq 2000 or 4000. Reads were aligned to the mouse genome (NCBI37/mm9) with TopHat v1.3.3 and allowed one alignment with up to two mismatches per read. mRNA RPKM values were calculated using Seqmonk's mRNA quantitation pipeline. All RPKMs represent an average from three biological replicates for in-vitro studies, and pooled RNA representation for tissue samples where equal amounts of RNA were pooled from 11 *Il10*−/− animals and 9 WT animals prior to library construction. A gene was included in the analysis if it met all of the following criteria: The maximum RPKM reached 4 at any time point, the gene length was > 200bp, and for in-vitro studies was induced at least 3-fold from Day 0 samples, and the expression was significantly different from the basal ($p < 0.01$) as determined by the DESeq2 package in R Bioconductor. P values were adjusted using the Benjamini-Hochberg procedure of multiple hypothesis testing (Benjamini and Hochberg, 1995).

Chromatin immunoprecipitation (ChIP) and ChIP-Seq

ChIP experiments were performed according to standard protocols (Villanueva et al., 2011, 2013). Lysed cells were sonicated using a Bioruptor (Diagenode) according to the manufacturer's protocol, and chromatin was immunoprecipitated with antibodies against PGC1α (H-300 sc-13067, Santa Cruz Biotechnology), ATF-2 (C-19 sc-187, Santa Cruz Biotechnology), C/EBPβ (sc-150, Santa Cruz Biotechnology), and IgG (PP64, Millipore) overnight at 4°C in the presence of Protein A beads (GE Healthcare). DNA enrichment was quantified by real-time PCR (ABI QuantStudio) using SYBR Green Master Mix (Diagenode). Primers used for these studies are list in Table S2. Occupancy was quantified using a standard curve and normalized to input DNA. ChIP-Seq libraries were prepared using the Kapa LTP Library Preparation Kit (Kapa Biosystems). ChIP-Seq was performed as described (Tong et al., 2016). Reads were aligned to the mouse genome (NCBI37/mm9) with Bowtie2. Uniquely mapped reads were used for peak calling and annotation using HOMER (Heinz et al., 2010). Peaks were called if they passed a false discovery rate of 0.01 and were enriched over input. Peaks were annotated to the nearest TSS.

Gene Expression Analysis

Total RNA was isolated using TRIzol reagent (Invitrogen) and reverse transcribed with the iScript cDNA synthesis kit (Biorad). cDNA was quantified by real-time PCR using SYBR Green Master Mix (Diagenode) on an ABI QuantStudio instrument. Gene expression levels were determined by using a standard curve. Each gene was normalized to the housekeeping gene 36B4 and was analyzed in duplicate. Primers used for real-time PCR are listed in Table S1.

Protein Analysis

Whole cell lysate or tissue lysate was extracted using RIPA lysis buffer (Boston Bioproducts) supplemented with complete protease inhibitor cocktail (Roche). Proteins were diluted in Nupage loading dye (Invitrogen), heated at 95°C for 5 min, and run on 4–12% NuPAGE Bis-Tris Gel (Invitrogen). Proteins were transferred to hybond ECL membrane (GE Healthcare) and blotted with commercial antibodies mentioned in the figure legends and the Key Resources Table.

Mouse and human population-based investigation of IL10Rα

Hybrid mouse diversity panel data was analyzed from 106 inbred strains fed a High-fat high-sucrose diet for 8 weeks as previously described (Parks et al., 2013, 2015). Mouse adipose tissue global expression was analyzed using Affymetrix HT_MG430A arrays and overlaid with phenotypic measurements. Human adipose tissue expression arrays using Affymetrix U219 microarray and phenotypic data was analyzed from the Metabolic Syndrome in Men (METSIM) study (Laakso et al., 2017; Stancáková et al., 2009). All correlations were assessed from the midweight bicorrelation coefficient and corrected p value using the R package WGCNA (Langfelder and Horvath, 2008).

QUANTIFICATION AND STATISTICAL ANALYSES

Motif Analysis

MACS2 called ATAC peak regions were used for motif analysis. JASPAR2016 Position Weight Matrices were used to identify binding sites in ChIP-Seq and ATAC peaks using Pscan-ChIP (Zambelli et al., 2009)

Statistics

All data are presented as mean ± SEM and analyzed using Microsoft Excel and Prism (Graphpad). Student's t test was used for single variable comparison between two groups. One-way ANOVA followed by Dunnett post hoc test was used for multiple comparisons versus the control group. Two-way ANOVA followed by Bonferroni posttests was used to examine interactions between multiple variables. Statistical significance for CLAMS study was determined by using two-way ANOVA repeated-measures and multiple regression analysis (ANCOVA). Data are presented as ± SEM $p < 0.05$ was considered to be statistically significant and is presented as * $p < 0.05$, ** $p < 0.01$, *** $p < 0.001$, or **** $p < 0.0001$.

DATA AND SOFTWARE AVAILABILITY

The accession number for the genome-wide sequencing dataset reported in this paper is GEO: GSE94654

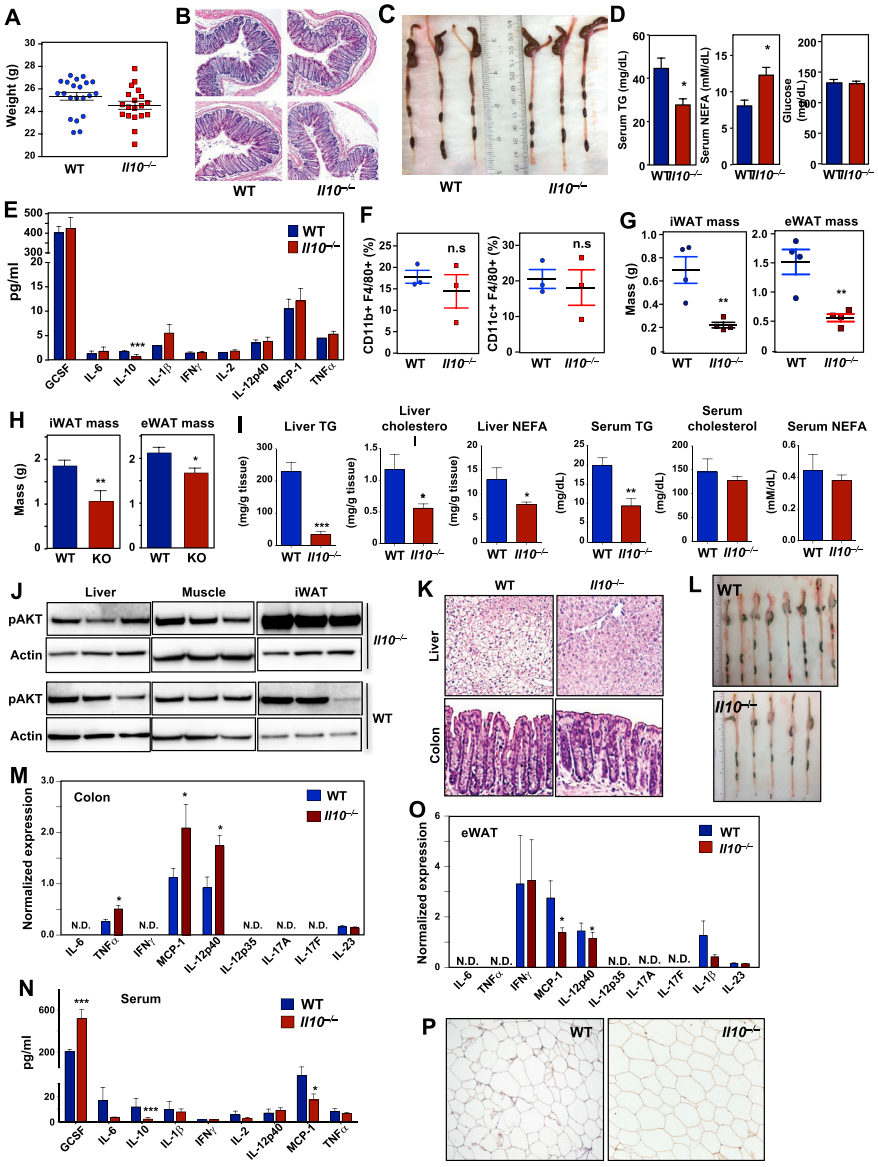

Figure S1. Protection against Age-Related Obesity and Absence of Systemic Inflammation in *IL-10*$^{-/-}$ Mice, Related to Figure 1

(A) Body weight of 10 week old chow-fed WT and *Il10*$^{-/-}$ mice, N = 20 per group.

(B) Representative colon histology from 10 week-old chow-fed WT and *Il10*$^{-/-}$ mice.

(C) Gross appearance of colon tissue from 10 weeks-old chow-fed mice.

(D) Serum triglyceride (TG), non-esterified fatty acid (NEFA), and blood glucose levels of chow-fed 10 week-old mice.

(E) Serum cytokines levels of 10-week-old chow-fed WT and *Il10*$^{-/-}$ mice measured by multiplex immunoassay.

(legend continued on next page)

(F) FACS analysis of macrophage population from stromal vascular fraction isolated from iWAT.
(G) Weight of iWAT and eWAT from 32-week-old chow-fed WT and *Il10*$^{-/-}$ mice, N = 4 per group.
(H) Weight of iWAT and eWAT from from HFD-fed WT and *Il10*$^{-/-}$ mice. N = 7 per group.
(I) Liver and serum lipid levels in HFD-fed WT and *Il10*$^{-/-}$ mice. N = 5 per group.
(J) Immunoblot analysis of pAKT in the indicated tissues from 5 weeks HFD-fed WT and *Il10*$^{-/-}$ mice injected with 3 U/kg insulin for 30 min.
(K) Representative histology of liver and colon from 6 week HFD-fed WT and *Il10*$^{-/-}$ mice.
(L) Gross appearance of colon tissue from 6 week HFD-fed mice.
(M) Real-time PCR analysis of gene expression in colons from chow-fed 10 week-old WT and *Il10*$^{-/-}$ mice.
(N) Serum cytokines levels of WT and *Il10*$^{-/-}$ mice fed chow diet for 10 weeks and then 60% high-fat diet (HFD) for 6 weeks measured by multiplex immunoassay. N = 16, 12.
(O) Real-time PCR analysis of gene expression in eWAT from chow-fed 10 week-old mice.
(P) MCP1 immunohistochemistry in WAT of 6 week HFD-fed WT and *Il10*$^{-/-}$ mice.

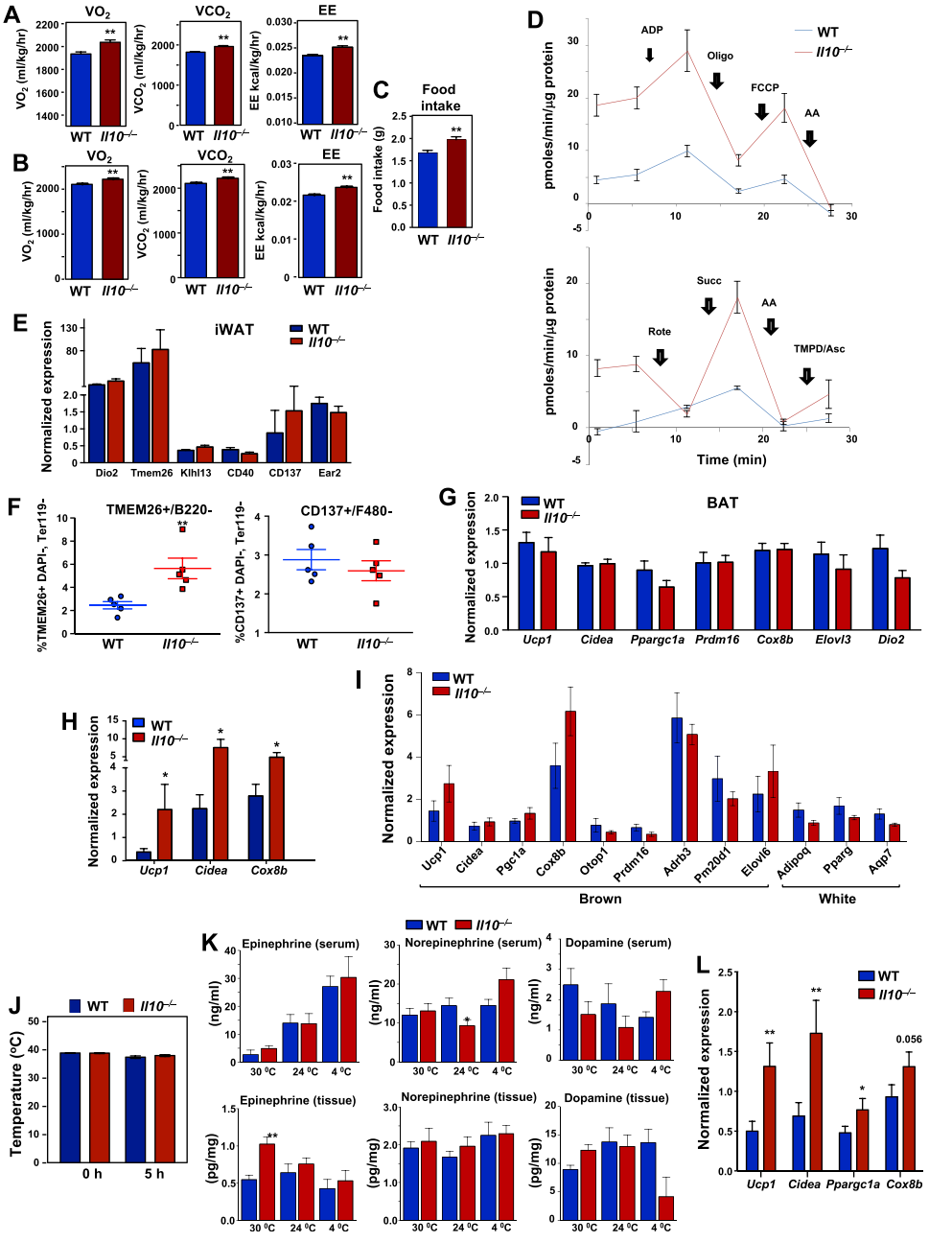

(legend on next page)

Figure S2. Increased Energy Expenditure and Adipose Mitochondrial Respiration in *IL-10*$^{-/-}$ Mice, Related to Figure 2

(A and B) Energy expenditure (EE) rate (kCal/kg/hr), VCO2 (ml/kg/hr), VO2 (ml/kg/hr) of chow-fed 10-week-old WT and *Il10*$^{-/-}$ mice (A) and 6-week HFD-fed mice (B) were analyzed by Columbus Oxymax metabolic chambers. 12 h light/dark cycles, 72 h total duration, each light/dark bar represents 12 h duration. N = 7 per group.

(C) Food intake of HFD-fed mice analyzed by Columbus Oxymax metabolic chambers.

(D) Seahorse trace plot showing coupling (right) and electron flow (left) analysis on iWAT from chow-fed 10 week-old WT and *Il10*$^{-/-}$ mice.

(E) Real-time PCR analysis of gene expression in iWAT from chow-fed 10 week-old WT and *Il10*$^{-/-}$ mice.

(F) FACS analysis of cells population in iWAT of chow-fed mice. N = 5 per group. Immune cell markers B220 and F480 were gated to exclude immune cell populations in the SVFs.

(G) Real-time PCR analysis of gene expression in BAT from chow-fed 10 week-old mice.

(H) Real-time PCR analysis of gene expression in 10 week-old WT and *Il10*$^{-/-}$ mice treated with enrofloxacin for 7 weeks at 100mg/kg/day. N = 8-10 per group.

(I) Real-time PCR analysis of gene expression in chow-fed 11 week-old WT and *Il10*$^{-/-}$ mice housed at 30°C for 7 weeks. N = 8-10 per group.

(J) Average body temperature of fasted chow-fed 10-week-old WT and *Il10*$^{-/-}$ mice measured at 0 h and 5 h in the absence of food.

(K) Serum and iWAT catecholamine levels measured by ELISA in chow-fed WT mice maintained at 30°C for 7 weeks, 24°C for 10 weeks, and 4°C for 24 h. N = 5 per group.

(L) Real-time PCR analysis of gene expression in iWAT from chow-fed 11 week-old WT and *Il10*$^{-/-}$ mice housed at 5°C for 6-24 h. N = 8-10 per group. Statistical analysis was performed using Student's t test. *$p < 0.05$, **$p < 0.01$.

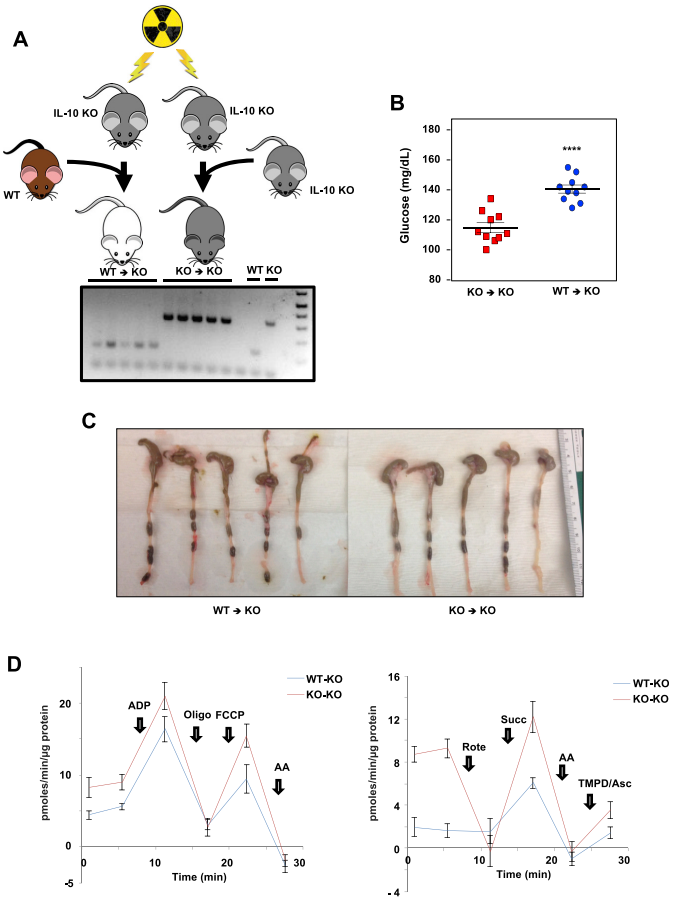

Figure S3. Bone Marrow IL-10 Production Affects Mitochondrial Respiration, Related to Figure 3

(A) Cartoon representation of bone marrow transplantation experiment and genotyping of WT➡KO and KO➡KO mice for WT or *IL10*$^{-/-}$ alleles.

(B) Fasting blood glucose levels of WT➡KO and KO➡KO mice. N = 10,per group.

(C) Gross appearance of colon tissue from WT➡KO and KO➡KO mice.

(D) Seahorse trace plots showing coupling (right) and electron flow (left) analysis on iWAT from chow-fed WT➡KO and KO➡KO mice. Statistical analysis was performed using Student's t test. ****p < 0.0001.

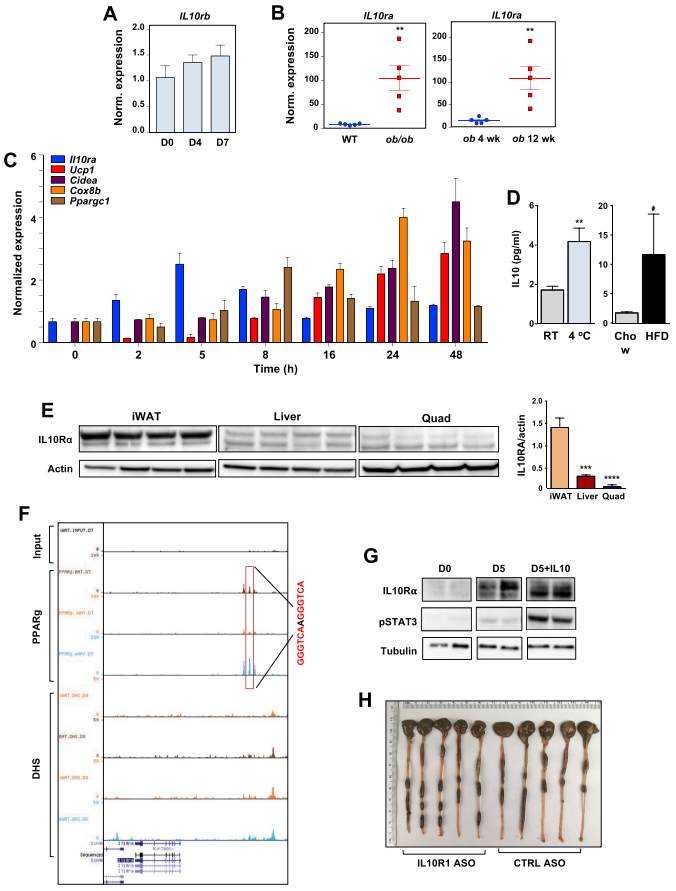

Figure S4. Regulation of IL-10Rα Expression in WAT, Related to Figure 4

(A) Real-time PCR analysis of *Il10rb* mRNA during the differentiation of primary stromal vascular fraction (SVF) derived from WT chow-fed 10 week-old mice.

(B) *Il10ra* expression in iWAT from chow-fed 12 week -old WT and *ob*/*ob* mice, and 4- and 12 week-old *ob*/*ob* mice.

(C) Real-time PCR analysis of gene expression in iWAT from chow-fed 10 week-old WT mice exposed to cold (5˚C) for the indicated times.

(D) Serum IL10 levels in chow-fed RT and 6 h cold-exposed (left) and chow-fed and HFD-fed WT mice (right). N = 5/group.

(E) Immunoblot analysis (left) and quantification (right) of IL10Rα protein in iWAT, liver, and muscle of chow-fed WT mice.

(F) Bedgraph showing PPARγ and DNase hypersensitivity (DHS) ChIP-Seq peaks on the enhancer region of *Il10ra* gene locus from previously published data (Siersbæk et al., 2012).

(G) Immunoblot showing activation of STAT3 (pSTAT3) in day 5 (D5) differentiated brown preadipocytes treated with 100 ng/ml IL10.

(H) Gross appearance of colon tissue from Ctrl or IL10Rα ASO-treated mice. Statistical analysis was performed using Student's t test. *$p < 0.05$, **$p < 0.01$, ***$p < 0.001$, ****$p < 0.0001$.

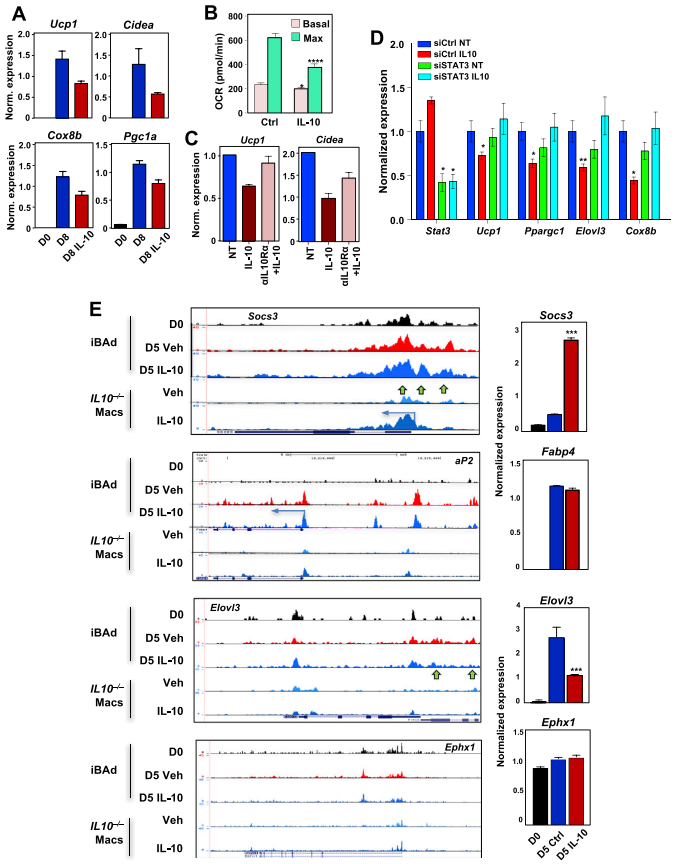

Figure S5. IL-10-STAT3 Axis Inhibits Thermogenic Gene Expression and Chromatin Accessibility, Related to Figure 5

(A) Real-time PCR analysis of gene expression on D0 and D8 in brown/beige-differentiated primary stromal vascular fraction (SVF) cells derived from WT chow-fed 10 week-old mice.

(B) Oxygen consumption rate (OCR) in D5 differentiated iBAd cells treated with and without IL10.

(C) Gene expression in D5 differentiated iBAd cells treated with and without IL10 and IL10Rα-neutralizing antibody.

(D) Gene expression in Ctrl or STAT3 siRNA-transfected iBAD cells treated with and without IL10.

(E) ATAC-Seq bedgraph panels of gene loci showing peak locations relative to the TSS (blue arrow). Green arrows indicate peaks differentially affected by vehicle or IL10 treatment. mRNA expression is shown at right. Statistical analysis was performed using Student's t test. *p < 0.05, **p < 0.01.

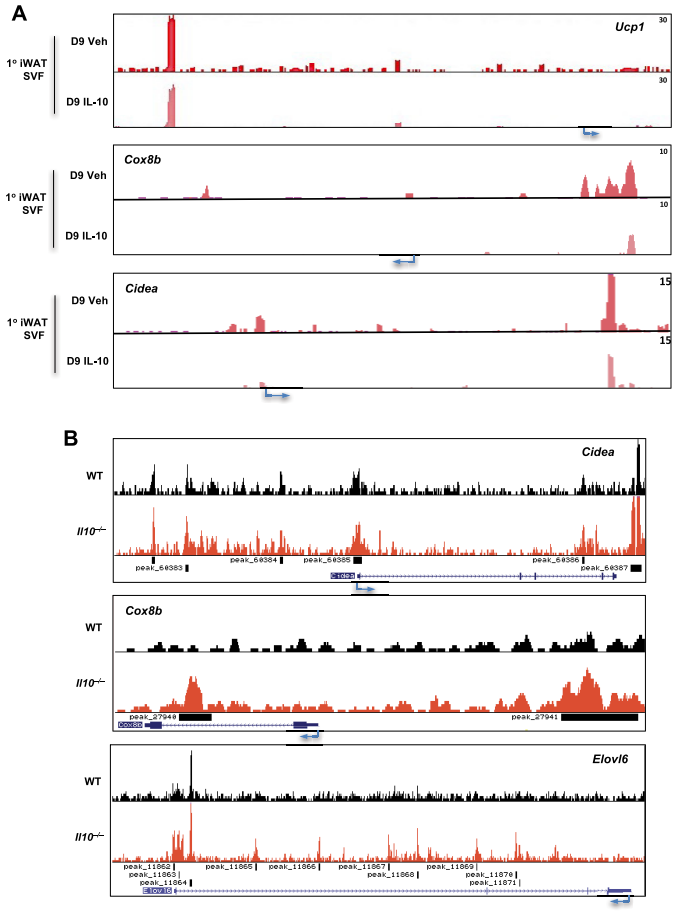

Figure S6. Direct Inhibition of Chromatin Accessibility by IL-10 in Primary Adipocytes, Related to Figure 6

(A) ATAC-Seq was performed on D9 of beige-differentiated primary (1°) iWAT SVF treated with and without 100ng/ml IL10 treatement followed by 10 μM forskolin treatment. Bedgraph panels from indicated thermogenic gene loci show peak locations relative to the TSS (blue arrow).

(B) ATAC-Seq was performed on mature iWAT adipocytes derived from 10 week-old chow-fed *Il10*$^{-/-}$ and WT mice. Bedgraph panels from indicated thermogenic gene loci show peak locations relative to the TSS (blue arrow). N = 2.

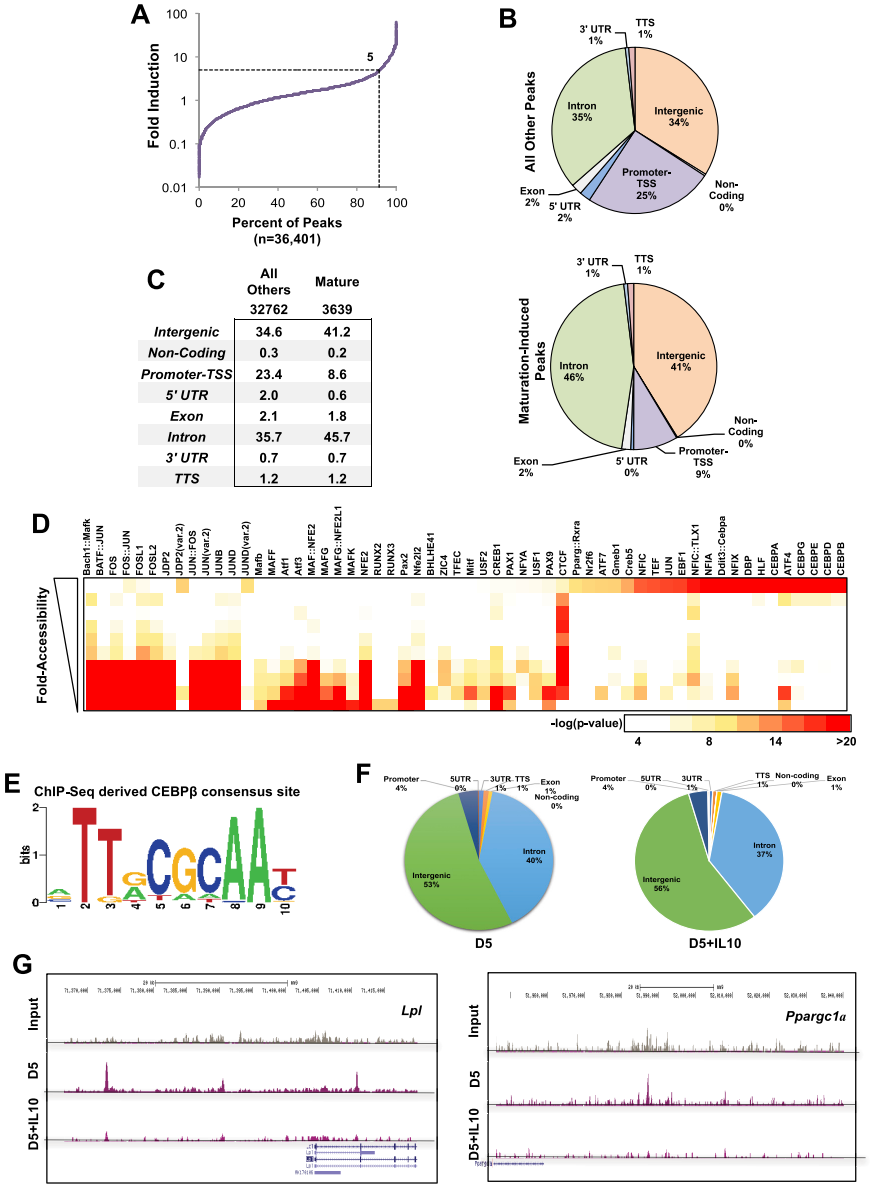

Figure S7. IL-10 Inhibits Recruitment of C/EBPβ to Thermogenic Enhancers, Related to Figure 7

(A) Graph showing ATAC peaks plotted as a function of fold induction in accessibility during brown differentiation. 10% of peaks showed a 5-fold or greater increase.

(B) Localization of all called ATAC peaks, grouped as either maturation-induced (D5 versus D0) or all others. The data reveal an enrichment of intronic and intergenic localized peaks.

(legend continued on next page)

(C) Quantification of the ATAC peak pie chart from B.
(D) ATAC peaks were ranked by order of increasing fold accessibility and used to perform transcription factor (TF) motif analysis using the ChIP-Pscan JASPAR 2016 database (Zambelli et al., 2009). The –log(p value) is plotted for each TF identified as indicted by the legend with red values indicating high significance of detection. The –log(p value) is plotted for each TF identified as indicted by the legend with red values indicating high significance of detection.
(E) C/EBPβ consensus site derived using PSCAN from the ChIP-Seq data.
(F) Pie chart of C/EBPβ distribution derived from ChIP-Seq data.
(G) ChIP-Seq bedgrah showing C/EBPβ peaks on the indicated genes in D5 differentiated cells treated with and without IL10. Input served as a control for C/EBPβ enrichment.